



# Theoretical and Numerical Analysis of Super-Resolution Without Grid

Quentin Denoyelle

## ► To cite this version:

Quentin Denoyelle. Theoretical and Numerical Analysis of Super-Resolution Without Grid. General Mathematics [math.GM]. PSL Research University, 2018. English. NNT: 2018PSLED030 . tel-02002504

HAL Id: tel-02002504

<https://tel.archives-ouvertes.fr/tel-02002504>

Submitted on 31 Jan 2019

**HAL** is a multi-disciplinary open access archive for the deposit and dissemination of scientific research documents, whether they are published or not. The documents may come from teaching and research institutions in France or abroad, or from public or private research centers.

L'archive ouverte pluridisciplinaire **HAL**, est destinée au dépôt et à la diffusion de documents scientifiques de niveau recherche, publiés ou non, émanant des établissements d'enseignement et de recherche français ou étrangers, des laboratoires publics ou privés.

# THÈSE DE DOCTORAT

de l'Université de recherche Paris Sciences et Lettres  
PSL Research University

Préparée à l'Université Paris-Dauphine

Theoretical and Numerical Analysis of Super-Resolution  
without Grid

École Doctorale de Dauphine — ED 543

Spécialité **Sciences**

## COMPOSITION DU JURY :

Gabriel Peyré  
CNRS - Ecole Normale Supérieure  
Directeur de thèse

Laure Blanc-Féraud  
CNRS - I3S  
Présidente du jury

Claire Boyer  
Sorbonne Université  
Membre du jury

Vincent Duval  
INRIA Paris  
Membre du jury

Cédric Herzet  
INRIA Rennes  
Membre du jury

Charles Soussen  
Centrale Supélec  
Membre du jury

**Soutenue le 09.07.2018  
par Quentin Denoyelle**

Dirigée par **Gabriel Peyré**



# Contents

<b>General Introduction (English)</b>	vii
<b>Introduction Générale (Français)</b>	xxv
<b>I Sparse Super-Resolution of Positive Measures</b>	1
<b>1 Asymptotic Analysis of Support Recovery</b>	3
1.1 Introduction . . . . .	4
1.2 A Primer on Certificates for Super-Resolution . . . . .	8
1.3 A Result of Non-Degeneracy for $\eta_V$ . . . . .	18
1.4 The $(2N - 1)$ -Vanishing Derivatives Pre-Certificate . . . . .	26
1.5 Transfer Theorem . . . . .	30
<b>2 Non-Degeneracy of <math>\eta_W</math></b>	35
2.1 Introduction . . . . .	36
2.2 $\eta_W$ for a Convolution Operator . . . . .	40
2.3 $\eta_W$ for Laplace-like Operators . . . . .	49
2.4 The Case of Several Clusters of Spikes . . . . .	56
<b>3 Separation and Robustness of BLASSO</b>	65
3.1 Introduction . . . . .	66
3.2 Separation Influence on Robustness of Super-Resolution . . . . .	68
3.3 Sketch of Proof . . . . .	70
3.4 Preliminaries . . . . .	73
3.5 Building a Candidate Solution . . . . .	80
3.6 Convergence of $\eta_{\lambda,t}$ to $\eta_W$ . . . . .	87
<b>II Numerical Grid-Less BLASSO Solving</b>	91
<b>4 The Sliding Frank-Wolfe BLASSO Solver</b>	93
4.1 Introduction . . . . .	94
4.2 The SFW Algorithm . . . . .	100

4.3	The SFW Algorithm versus Other Solvers . . . . .	115
4.4	Study of the Laplace Transform Numerical Inversion . . . . .	131
<b>5</b>	<b>Super-Resolution Microscopy</b>	<b>139</b>
5.1	Introduction . . . . .	140
5.2	Modelling of the 3D recovery problem . . . . .	152
5.3	Numerical Results . . . . .	165
	<b>Conclusion</b>	<b>181</b>
	<b>Bibliography</b>	<b>183</b>

## Remerciements

Je souhaite tout d'abord remercier les rapporteurs de cette thèse, Martin Burger et Carlos Fernandez-Granda, et les membres du jury (tout particulièrement Cédric Herzet et Charles Soussen) pour le temps accordé à la lecture de ce manuscrit.

Je remercie également Gabriel et Vincent, mes directeurs de thèse, pour leur bienveillance et leur disponibilité tout au long de ces années passées ensemble. Cela a été un vrai plaisir de travailler avec vous et vous m'avez énormément appris. Vous êtes les meilleurs !

Merci à Emmanuel de m'avoir initié à la microscopie par fluorescence, d'avoir répondu à mes nombreuses questions ainsi que pour les relectures de ce manuscrit.

Merci à Gilles, Thomas et Maxime pour leur aide et pour leurs efforts dans la mise en place d'un cluster au top au Ceremade dont j'ai pu activement profiter et sans lequel cette thèse serait nettement moins illustrée.

Un grand merci à mes "soeurs" et "frères" de thèse que j'ai pu côtoyer avec plaisir pendant toutes ces années, Jonathan, Lénaïc, Aude, Paul, Gwendoline. Je n'oublie pas tous les doctorants du Ceremade, en particulier Raphaël, Camille et Marco qui ont commencé en même temps que moi et Maxime et Luca. Merci également au Ceremade, à l'équipe Mokaplan et au DMA de m'avoir accueilli.

À mes amis pour leur soutien sans faille tout au long de ces années.

Et enfin à mes parents et mon frère ainsi que toute ma famille, sans qui je ne serais jamais arrivé là où j'en suis.



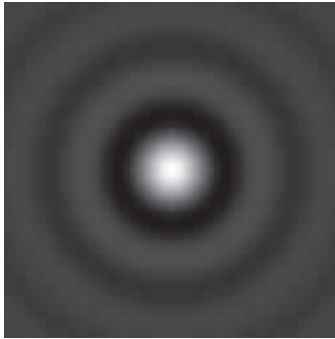
# **General Introduction (English)**

This thesis studies the theory, algorithms and applications of sparse spikes super-resolution. Super-resolution is the problem of enhancing the level of details of a given observed signal. The underlying high resolution information captured is altered by the physical limitations of the system of acquisition and by random perturbations. For example, it is involved in fields as diverse as astronomy, medical imaging, geophysics or radar imagery. One of the most recent and important application of super-resolution concerns fluorescent microscopy in Biology where experimenters try to overcome the diffraction phenomenon (200nm lateral limit resolution) by localizing precisely the positions of fluorophores (fluorescent molecules attached to proteins) in a sample. The fluorophores can be mathematically modeled as spikes (*i.e.* a measure composed of a sum of Dirac masses with positive amplitudes). Therefore, from an altered and noisy version of these spikes, the aim is to recover the closest possible estimation of their true positions and amplitudes. This inverse problem is often called the sparse spikes super-resolution. Because two fluorophores can be separated by a distance well below 200nm, one needs to develop theoretical and numerical tools that can deal with this challenging problem. Our approach, in this thesis, is to consider an optimization problem called the BLASSO which is a continuous version of the well-known LASSO. It consists in the minimization of a sum the quadratic error between the altered current estimate and the observations plus a regularization term (the total variation norm for measures) enforcing sparsity. While there exist many theoretical guarantees for the recovery of such measures both in the noiseless and noisy case, the question of the super-resolution in presence of noise when solving the BLASSO is an open problem. We show, in 1D, that the non-degeneracy of what we call the  $(2N - 1)$ -vanishing derivatives pre-certificate (denoted  $\eta_W$ ) assures the recovery of a unique measure composed of the same number of spikes as the original measure, when the spikes of the initial measure are separated by a distance  $t \rightarrow 0$ . This recovery is possible only if the noise level drops faster than  $t^{2N-1}$ . On the numerical standpoint, we provide a grid-less algorithm, that we call the Sliding Frank-Wolfe (SFW) algorithm, to solve the BLASSO (optimization problem on measures) based on the Frank-Wolfe algorithm but with an added step where the amplitudes and positions are moved continuously. It is inspired by [24]. A similar, but different version of this algorithm has recently been studied in [22] where the authors show that it reaches state of the art numerical performance in several applications, including fluorescent microscopy in 2D. We prove that if there is a unique discrete measure solution of the BLASSO, then the SFW recovers this measure in a finite number of steps improving drastically the only known convergence result for this class of algorithm (weak-\* convergence with an error of  $O(1/k)$  in the objective function). Finally we apply our algorithm to the fluorescent microscopy problem in a 3D designed setup close of experimental conditions and we compare three different models of acquisition. We observe a typical spatial resolution of less than 20nm along the three axis, which is a state of the art resolution.

## Sparse Spikes Super-Resolution

The sparse spikes super-resolution setting is of utmost importance and is routinely encountered in many imaging scenarios: in Astronomy, the stars can be considered as point sources of light. In Biology, fluorescent proteins in cells can also be seen as spikes. Moreover in these two applications, the acquisition process induces an alteration of the ideal source signal. A classical way of measuring whether a particular application is in the range of the sparse spikes super-resolution framework is to use a two-point resolution criterion.

In resolution theory, a two-point resolution criterion defines the ability of a system to resolve two points of equal intensities. As a point source produces a diffraction pattern which is centered about the geometrical image point of the point source, there are many resolution criteria depending on the size of the pattern. One of the most common is Rayleigh resolution criterion [I22] which states that two points are resolved by a system if the central maximum of the intensity diffraction of one point source coincides with the first minimum (if it exists) of the intensity diffraction pattern of the other point. This defines a distance that only depends on the system and which is called the Rayleigh length. A celebrated example in Physics and Astronomy is the Airy disk which is the diffraction pattern obtained when a light source hits a small circular aperture, see Figure I. The observed



(a) Airy disk

Figure 1: Diffraction pattern obtain at infinity or at the focal plane of the optical system when a light source at infinity illuminates a small circular aperture (Fraunhofer diffraction).

pattern is given by a function depending on  $J_1$  the Bessel function of the first kind of order one and in this case the Rayleigh length is:

$$\Delta_R = 1.22 \frac{\lambda_\ell}{d},$$

where  $\lambda_\ell$  is the wavelength and  $d$  the diameter of the aperture. For diffraction patterns such as those given by Gaussians, there is no minimum of intensity around the central maximum. That is why we prefer to use the separation criterion which

states that a system can resolve two point sources if their diffraction patterns do not overlap such that the resulting observation has only one central maximum. One denotes by  $\Delta_S$  this limit distance. See Figure 2 for an illustration of this criterion. We refer to [47] for more details about resolution theory.

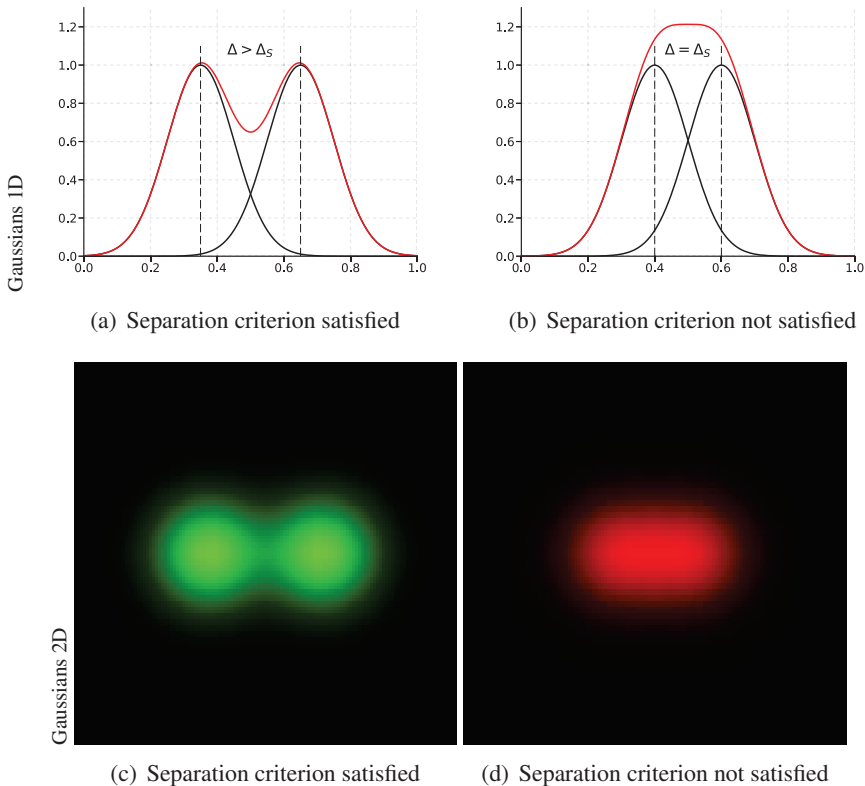


Figure 2: Illustration of our separation criterion for diffraction patterns given by Gaussian impulse response in 1D and 2D. For a Gaussian with variance  $\sigma^2$ , one has  $\Delta_S = \sigma$ .

The challenge of sparse spike super-resolution in signal processing thus consists in developing robust theoretical and numerical techniques that enable to separate two or more point sources separated by a distance well under the length  $\Delta_S$  (with possibly no theoretical limit) in presence of noise. Providing such tools is the main goal of this thesis. As we argue in this thesis, from a theoretical but also practical perspective, the question of super-resolution is a signal-to-noise scaling problem: how should the signal-to-noise ratio increase as a function of the number of spikes and their respective distances.

## Mathematical Modelling

### Sparse Signal Modelling

In many applications already highlighted, the source signal that one aims at recovering from altered and noisy observations can be modeled by a collection of spikes or point sources.

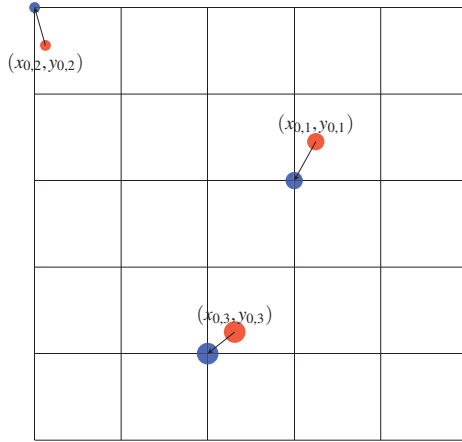


Figure 3: Illustration of the sparsity of a point source signal. Points  $(x_{0,i}, y_{0,i})$  for  $i \in \{1, \dots, 3\}$  in  $[0, 1]^2$  (red spots) with amplitudes  $a_{0,i}$  encoded by the diameter of the spots. A uniform grid of  $[0, 1]^2$  with  $6 \times 6$  points is displayed. For each  $(x_{0,i}, y_{0,i})$ , one associates its closest neighborhood on the grid (blue spots). The goal is to recover the amplitudes of these blue spots. Only a fraction of the points on the grid have non-zero amplitudes hence the sparsity.

This type of source signals is qualified as *sparse*. To illustrate the concept of sparsity in the particular case of spikes, let us consider a collection of positions  $(x_{0,1}, y_{0,1}), \dots, (x_{0,N}, y_{0,N})$  in  $[0, 1]^2$  with associated positive amplitudes  $a_{0,1}, \dots, a_{0,N}$ . One can see this example as a collection of stars in a portion of the sky with different magnitudes ( $a_{0,i}$ ). If one uses a uniform grid with  $K^2$  points to discretize  $[0, 1]^2$  and associate to each  $(x_{0,i}, y_{0,i})$  for  $i \in \{1, \dots, N\}$  its closest neighborhood on the grid, then the goal is to recover a vector  $\tilde{a}_0 \in \mathbb{R}^{K^2}$  with only  $N$  non-zero coefficients corresponding to the  $a_{0,i}$ . Provided that the grid is thin enough to capture sufficient details, this means that  $N \ll K^2$  so that  $\tilde{a}_0$  is a sparse vector. See Figure 3 for an illustration of this example. Sparsity can then be used beneficially in the recovery process.

A grid is convenient to illustrate the concept of sparsity in the case of a point source signal and is from the start a finite dimensional problem (in the end, a computer can only store a finite amount of data). However the appropriate mathematical object to represent a collection of spikes are sums of Dirac masses with amplitudes. The mathematical framework where Dirac masses best fit in are Radon

measures. Indeed a Dirac mass  $\delta_x$  can be seen as a linear form over a space of continuous functions (hence a Radon measure), corresponding to point-wise evaluation

$$\delta_x : \varphi \in \mathcal{C}_0 \mapsto \varphi(x).$$

As a result, one can express the collection of spikes in  $[0, 1]^2$  of the previous example as

$$m_{a_0, \bar{x}_0} \stackrel{\text{def.}}{=} \sum_{i=1}^N a_{0,i} \delta_{(x_{0,i}, y_{0,i})},$$

where  $\bar{x}_0 = ((x_{0,1}, y_{0,1}), \dots, (x_{0,N}, y_{0,N})) \in ([0, 1]^2)^N$ .  $m_{a_0, \bar{x}_0}$  is a Radon measure

$$m_{a_0, \bar{x}_0} : \varphi \in \mathcal{C}_0 \mapsto \sum_{i=1}^N a_{0,i} \varphi(x_{0,i}, y_{0,i}),$$

and it is now the sparse source signal that one aims to recover.

More generally, in the following and from now on, one denotes as  $X$  the domain of positions of the Dirac masses. Depending on the context,  $X$  can be either  $\mathbb{R}^d$  (or a compact connected subset of  $\mathbb{R}^d$ ) or  $\mathbb{T}^d$  (the  $d$ -dimensional torus) for different values of  $d \in \mathbb{N}^*$ .

Let us denote by  $\mathcal{M}(X)$  the space of bounded Radon measures on  $X$  which can be seen as the topological dual of the space  $\mathcal{C}_0(X, \mathbb{R})$  of continuous functions on  $X$  that vanish at infinity (see Definition 3 for a more accurate statement).

## Imaging Operator

The source signal  $m_{a_0, \bar{x}_0} \in \mathcal{M}(X)$  that one aims at recovering is altered through the acquisition process. For example when a telescope takes a picture of a portion of the sky,  $m_{a_0, \bar{x}_0}$  is convolved with the point spread function (PSF) of the optical system. That is the only information that one has access to. This alteration process is modeled by the action of a linear operator  $\Phi$  defined on  $\mathcal{M}(X)$ , taking values in a separable Hilbert space  $\mathcal{H}$  and having the following form

$$\Phi : m \in \mathcal{M}(X) \mapsto \int_X \varphi(x) dm(x) \in \mathcal{H}. \quad (1)$$

$\varphi$ , which one calls in the following the kernel of  $\Phi$ , is a continuous function defined on  $X$  and taking values in  $\mathcal{H}$ . The choice of  $\varphi$  and  $\mathcal{H}$  depends on the application. In the following, one uses the term *observations* to denote:

$$y_0 \stackrel{\text{def.}}{=} \Phi m_{a_0, \bar{x}_0},$$

or its noisy version. See Figure 4 for an example of observations in the case of a Gaussian convolution on  $\mathbb{R}$ .

A few examples of setups which are covered by the model (1) includes:

- i)  $X = \mathbb{T}$ ,  $\mathcal{H} = L^2(\mathbb{T})$  and  $\varphi(x) = \frac{\sin(2\pi f_c(\cdot-x))}{\sin(\pi(\cdot-x))}$  which corresponds to a convolution by the Dirichlet kernel with cutoff frequency  $f_c$ ,

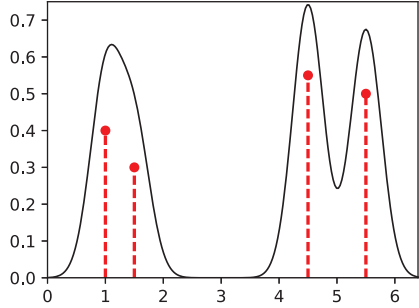


Figure 4: In red the spikes of the initial measure  $m_{a_0, \bar{x}_0}$  and in black the observations  $y_0 = \Phi m_{a_0, \bar{x}_0}$  for a Gaussian convolution *i.e.*  $\varphi(x) = e^{-\frac{(x-\bar{x})^2}{2\sigma^2}} \in L^2(\mathbb{R})$ .

ii)  $X = \mathbb{T}$ ,  $\mathcal{H} = \mathbb{R}^{2f_c+1}$  and

$$\varphi(x) = \begin{pmatrix} 1 \\ \sqrt{2}\cos(2\pi x) \\ \vdots \\ \sqrt{2}\cos(2\pi f_c x) \\ \sqrt{2}\sin(2\pi x) \\ \vdots \\ \sqrt{2}\sin(2\pi f_c x), \end{pmatrix} \in \mathbb{R}^{2f_c+1}$$

which is in some sense equivalent to (i) by taking the Fourier coefficients of the observations,

- iii)  $X = \mathbb{R}$ ,  $\mathcal{H} = L^2(\mathbb{R})$  and  $\varphi(x) = e^{-\frac{(x-\bar{x})^2}{2\sigma^2}} \in L^2(\mathbb{R})$  which corresponds to a Gaussian convolution with variance  $\sigma^2$ ,
- iv)  $X = [\varepsilon, x_b]$  for  $0 < \varepsilon < x_b$ ,  $\mathcal{H} = L^2(\mathbb{R}_+)$  and  $\varphi(x) = s \mapsto e^{-sx} \in L^2(\mathbb{R}_+)$  which corresponds to a Laplace transform (see Chapter 2). Note that this kernel is not translation invariant,
- v)  $X = [\varepsilon, x_b]$  for  $0 < \varepsilon < x_b$ ,  $\mathcal{H} = \mathbb{R}^K$  and  $\varphi(x) = (e^{-s_k x})_{1 \leq k \leq K} \in \mathbb{R}^K$  which corresponds to a discretized Laplace transform (see Chapter 2). This kernel is also not translation invariant,
- vi)  $X = \mathbb{R}^2$ ,  $\mathcal{H} = L^2(\mathbb{R}^2)$  and  $\varphi(x, y) = (u, v) \mapsto e^{-\frac{(u-x)^2}{2\sigma_x^2}} e^{-\frac{(v-y)^2}{2\sigma_y^2}} \in L^2(\mathbb{R}^2)$  which corresponds to a Gaussian convolution in 2D,
- vii) Chapter 5 studies several examples in  $\mathbb{R}^3$  built on a 2D discretized Gaussian convolution.

To summarize, from the observations  $y_0 = \Phi m_{a_0, \bar{x}_0}$  or  $y = y_0 + w$ , where  $w \in \mathcal{H}$  represents some noise, the aim of the sparse spikes super-resolution problem is to recover some object  $m$  “close” (for some measure of similarity which is typically problem-dependent) of the source sparse signal  $m_{a_0, \bar{x}_0}$ . This is an ill-posed inverse problem because  $\Phi$  is ill-posed in general. Following the classical approach of regularization theory, a sparsity prior should thus be used to regularize the inversion process.

## State of the Art

The theory and practice of super-resolution can be roughly split in three parts:

- Theory: choice of a method and theoretical study of its performance.
- Algorithms: design of an exact or approximate solver and study of its approximation performance.
- Applications: countless subtlety and adaptation needs to be done to account for real life problems, and we focus on in this thesis in particular on fluorescent microscopy imaging.

These three parts are addressed in this thesis. Part I is devoted to the first item and Part II to the last two.

## Theory

There are two main categories of theoretical approaches for the super-resolution problem: Prony’s based and variational methods.

**Prony’s Based Methods.** Prony’s method [44], MUSIC (MULTiple SIgnal Classification) [130], ESPRIT (Estimation of Signal Parameters by Rotational Invariance Techniques) [96] or Matrix Pencil [89] enables to recover exactly the signal parameters for Fourier measurements in the noiseless case, because they do not need to perform any discretization. There exist many extensions of Prony’s based methods. While these methods were not primarily designed to deal with noise, extensions have been developed in [28, 39]. Stability to noise is known to hold under a minimum separation distance [106]. There exists also a Prony method in a multivariate setup, see [116]. And extensions to non-bandlimited signals with finite rate of innovation have been formulated [147, 48].

Prony’s based methods are better than LASSO (see below) for 1D Fourier measurements. In other configurations, the comparison is less clear and sometimes it may even be impossible to extend these methods.

**Variational Methods.** Variational approaches are more resilient because they do not impose any particular structure on the forward operator  $\Phi$ , they can be adapted to virtually any type of noise and they do not require the knowledge of the number of sources. The idea to solve the previous sparse spikes deconvolution problem (find  $m$  "close" of  $m_{a_0, \bar{x}_0}$  given only  $y$ ) consists in minimizing among all source signals possible the sum of a term measuring the error with respect to the observations (in all this thesis, it is the quadratic error) and a regularization term enforcing sparsity.

We now detail the two main class of variational methods we focus on in this thesis.

**LASSO.** In a finite dimensional setting, *i.e.* when the positions of the spikes must lie on a grid  $\mathcal{G} \subset X$  (see Figure 3 for example), one obtains the LASSO [142] or Basis-pursuit problem, which is a  $\ell^1$  regularized inversion, defined by solving

$$\min_{a \in \mathbb{R}^{|\mathcal{G}|}} \underbrace{\frac{1}{2} \|\Phi_{\mathcal{G}} a - y\|_{\mathcal{H}}^2}_{\text{fidelity term}} + \underbrace{\lambda \|a\|_1}_{\text{sparsity enforcing term}}, \quad (2)$$

where  $\Phi_{\mathcal{G}} a \stackrel{\text{def.}}{=} \Phi m_{a, x_{\mathcal{G}}}$  and  $x_{\mathcal{G}}$  is the collection of points of  $\mathcal{G}$ . It retains both the features of subset selection (by setting to zero some coefficients, thanks to the property of the  $\ell^1$  norm to favor sparse solutions) and ridge regression (by shrinking the other coefficients).

$\ell^1$  regularization techniques were first introduced in geophysics (see [37, 105, 127]) for seismic prospecting. Indeed, the density changes in the underground can be modeled as a sparse spikes train.  $\ell^1$  reconstruction property provides solutions with few non-zero coefficients and can be solved efficiently with convex optimization methods. Donoho theoretically studied and justified these techniques in [49]. In signal processing, the basis pursuit method [34] uses the  $\ell^1$  norm to decompose signals into overcomplete dictionaries.

Because a grid is used, in order to capture with a high precision the position of the spikes of  $m_{a_0, \bar{x}_0}$ , one needs to choose a grid with potentially a very small step size. However this approach impairs the theoretical (an numerical, see below) recovery properties because it leads to the phenomenon known as basis mismatch [35, 51] and highly correlated atoms. It was proven recently in [55, 56] that in a low noise regime, the LASSO on thin grid estimates twice the number of spikes of the initial measure  $m_{a_0, \bar{x}_0}$ .

These limitations of such a discrete LASSO method can be somehow alleviated by considering a grid-free setting that we now detail.

**BLASSO.** Following recent works (see for instance [17, 24, 30, 42, 54]), the sparse super-resolution method that we consider in this thesis is an infinite-dimensional counterpart to (2), which can also be understood as a limit (for the topology of measure) of the LASSO as the grid refined. This inverse problem

solved over the space of Radon measures is called in [42] the BLASSO (B for Beurling). The continuous “grid-free” setting makes the mathematical analysis easier and allows us to make precise statement about the location of the recovered spikes locations.

Therefore, the optimization problem (2) becomes:

$$\min_{m \in \mathcal{M}(X)} \frac{1}{2} \|\Phi m - y\|_{\mathcal{H}}^2 + \lambda |m|(X). \quad (\mathcal{P}_\lambda(y))$$

There are several differences between the LASSO and the BLASSO  $\mathcal{P}_\lambda(y)$ :

1. one optimizes over  $\mathcal{M}(X)$  rather than  $\mathbb{R}^{\#\mathcal{G}}$  and  $\Phi_{\mathcal{G}}a = \Phi m_{a,x_g}$  for any  $a \in \mathbb{R}^{\#\mathcal{G}}$  is replaced by  $\Phi m$  for any  $m \in \mathcal{M}(X)$ , which make  $\mathcal{P}_\lambda(y)$  an optimization problem over a non-reflexive Banach space rather than a finite dimensional vector space,
2. the  $\ell^1$  norm used in the regularization term (only valid in a finite dimensional setting) is replaced by its infinite dimensional counterpart *i.e.* the total variation norm defined by:

$$\forall m \in \mathcal{M}(X), \quad |m|(X) \stackrel{\text{def.}}{=} \sup_{\psi \in \mathcal{C}_0} \left\{ \int_X \psi dm ; \|\psi\|_{\infty,X} \leq 1 \right\}.$$

It is the dual norm of  $\|\cdot\|_{\infty,X}$  on  $\mathcal{C}_0$  and it indeed generalizes the  $\ell^1$  norm to the continuous setting of measures because:

$$\forall a_0 \in \mathbb{R}^N, \forall \bar{x}_0 \in X^N, \quad |m_{a_0,\bar{x}_0}|(X) = \|a_0\|_1,$$

As a result, similarly to the  $\ell^1$  norm which favors solutions with only few non-zero coefficients, the use of the total variation norm in  $\mathcal{P}_\lambda(y)$  favors sparse measures *i.e.* composed of Dirac masses.

The regularization parameter  $\lambda > 0$  should be adapted to the noise level  $\|w\|_{\mathcal{H}}$ . Note there exists a variant of the BLASSO that estimates in the same time the initial measure and the noise level, see [23]. In the noiseless case  $w = 0$ , one can make  $\lambda \rightarrow 0$  in  $\mathcal{P}_\lambda(y)$  and then end up with the following problem:

$$\min_{m \in \mathcal{M}(X)} \{|m|(X) ; \Phi m = y_0\}. \quad (\mathcal{P}_0(y_0))$$

It is a generalization of the classical basis pursuit

$$\min_{a \in \mathbb{R}^{\#\mathcal{G}}} \{\|a\|_1 ; \Phi_{\mathcal{G}}a = y_0\},$$

defined originally in [34] in a finite dimensional setting, and written here over the space of Radon measures. One refers to this problem as the *basis pursuit for measures*. This is the problem studied in [30], in the case where  $\Phi$  is an ideal

low-pass filter on the torus (see Example 1). The authors show that  $m_{a_0, \bar{x}_0}$  is the unique solution of  $\mathcal{P}_0(y_0)$  if  $\Delta(\bar{x}_0) \geq \frac{C}{f_c}$  for some  $0 < C \leq 1.87$  where

$$\Delta(\bar{x}_0) \stackrel{\text{def.}}{=} \min_{i \neq j} |\bar{x}_{0,i} - \bar{x}_{0,j}|. \quad (3)$$

is the minimum separation distance between the spikes. In [65], the author proved that  $C \leq 1.26$ . And from [54], necessarily  $C \geq \frac{1}{2}$ .

From this last statement, one deduces that super-resolution is impossible in general by solving  $\mathcal{P}_0(y_0)$  (or  $\mathcal{P}_\lambda(y)$ ) without any assumption on the sign of the amplitudes. Even if one can recover exactly the position of the spikes (if  $\Delta(\bar{x}_0)$  is large enough) in the continuous domain, super-resolution is the recovery of two or more spikes that are possibly infinitely close. However the picture is completely different when considering positive measures. For positive spikes (i.e.  $a_{0,i} > 0$ ), exact recovery of  $m_{a_0, \bar{x}_0}$  without noise (i.e. for  $\mathcal{P}_0(y_0)$ ) holds whatever  $\Delta(\bar{x}_0) > 0$  (provided sum injectivity assumption), see for instance [42]. Therefore the appropriate framework to study super-resolution are positive measures. Most of the time it is the setup that we choose in this thesis.

The last result of [42] cited above is only valid in the noiseless case. The super-resolution problem in presence of noise for the BLOSSO is an open question. That is the main topic of our work. In [24], it is shown that if the solution of  $\mathcal{P}_0(y_0)$  is unique then the measures recovered by  $\mathcal{P}_\lambda(y)$  converge in the weak-\* sense to the solution of  $\mathcal{P}_0(y_0)$  when  $\lambda \rightarrow 0$  and  $\|w\|_{\mathcal{H}}^2 / \lambda \rightarrow 0$ . In [29], the authors provide a reconstruction error using the  $L^1$  norm of an ideal low-pass filtered version of the recovered measures. The arguments used are refinements of [27]. In [7, 64], error bounds are given on the locations of the recovered spikes with respect to those of the input measure  $m_{a_0, \bar{x}_0}$ . However, those works provide little information about the structure of the measures recovered by  $\mathcal{P}_\lambda(y)$ . That point is addressed in [54] where the authors show that if the vanishing derivatives pre-certificate (see Section 1.2 for more details)  $\eta_V \stackrel{\text{def.}}{=} \Phi^* p_V$ , where  $p_V$  is the unique solution of

$$\inf \left\{ \|p\|_{\mathcal{H}} ; \forall i = 1, \dots, N, (\Phi^* p)(\bar{x}_{0,i}) = \text{sign}(a_{0,i}), (\Phi^* p)'(\bar{x}_{0,i}) = 0 \right\},$$

is non-degenerate *i.e.*

$$\forall x \in X \setminus \bigcup_{i=1}^N \bar{x}_{0,i}, \quad |\eta_V(x)| < 1 \quad \text{and} \quad |\eta_V''(\bar{x}_{0,i})| \neq 0,$$

then there exists a unique solution of  $\mathcal{P}_\lambda(y)$  with the exact same number of spikes as the original measure provided that  $\lambda$  and  $\|w\|_{\mathcal{H}} / \lambda$  are small enough. Note that one can easily see that if  $\|\eta_V\|_{\infty, X} \leq 1$  then  $\eta_V$  is a *certificate* (also called dual certificate) for  $m_{a_0, \bar{x}_0}$ , because it satisfies all the requirements except  $\|\eta_V\|_{\infty, X} \leq 1$ , assuring that  $m_{a_0, \bar{x}_0}$  is solution of  $\mathcal{P}_0(y_0)$ . Indeed, a certificate for a discrete measure and for the problem  $\mathcal{P}_0(y_0)$  is a continuous function in the image of  $\Phi^*$  that interpolates the sign of the amplitudes at the positions of the spikes and is lower

than 1 in uniform norm (also called *source condition* in the literature [26]). The intuition behind the definition of  $\eta_V$  is that the minimal  $L^2$ -norm property together with the interpolation of the signs with zero derivatives may favor  $\|\eta_V\|_{\infty,X} \leq 1$ .

Section 1.4 defines the  $(2N - 1)$ -vanishing derivatives pre-certificate denoted  $\eta_W \stackrel{\text{def.}}{=} \Phi^* p_W$ . It is the limit of  $\eta_V$  when the  $N$  spikes (all positive) of  $m_{a_0,\bar{x}_0}$  cluster at some point in the domain.  $p_W$  is the unique solution of

$$\inf \left\{ \|p\|_{\mathcal{H}} ; (\Phi^* p)(0) = 1, (\Phi^* p)'(0) = 0, \dots, (\Phi^* p)^{(2N-1)}(0) = 0 \right\}.$$

Since  $\eta_V$  controls the stability of the support in a low noise regime, one can guess that  $\eta_W$  plays a similar role (as a limit of  $\eta_V$ ) but when the spikes collapse at some point.

## Algorithms

There are different solvers depending on the approximation schemes of the BLASSO which can be divided in three main categories:

- Fixed spatial discretization.
- Fixed spectral discretization and SDP formulation.
- Adaptive discretization via optimization over the space of measures.

**Fixed spatial discretization.** This approach leads to the LASSO. The typical solvers are proximal methods. They rely on the fact that the LASSO has an Hilbertian structure. Iterative Hard Thresholding (IHT) [19, 20] or Iterative Soft Thresholding (IST) [41, 38] are algorithms which are part of the family of Iterative Shrinkage-Thresholding Algorithms (ISTA). Their rates of convergence have been largely studied in the literature [41, 50, 66]. Even if ISTA is simple to implement, it is in general slow to converge (the error in the objective function is typically in  $O(1/k)$ ). FISTA [9] gives a better non-asymptotic rate of convergence ( $O(1/k^2)$ ). With discrete grids, in order to achieve a sharp localization of the spikes of the initial measure, one needs to have a sufficiently small grid step size. But when the size of the grid  $\#\mathcal{G}$  increases it makes each iteration slower and a more correlated dictionaries which in turn deteriorate the constant of convergence. So that in practice, we often obtain a small cluster of non-zero weights in the neighborhood of each true spike.

**Fixed spectral discretization and SDP formulation.** Following [30], one can reformulate the BLASSO in the case of a low pass filter ( $X = \mathbb{T}$ ) into a semi-definite program (SDP). In this case, one uses interior point methods to solve the SDP followed by a root finding step. One of the drawback of this method is that the root finding step may pose stability issues. Moreover the overall complexity of an interior point method for the SDP is polynomial in  $O(f_c^{2d})$  where  $d$  is

the dimension of the domain  $X$ . This has led to recent developments [32] where the authors use a relaxed low rank SDP formulation of the BLASSO in order to use a greedy method (see below). Finally these methods can only be applied to certain type of forward operators (typically Fourier measurements) where Frank-Wolfe and greedy methods and proximal methods can be used for a larger class of operators  $\Phi$ .

**Adaptive discretization via optimization over the space of measures.** In order to directly solve the BLASSO, one needs to design algorithms that do not use any Hilbertian structure and can instead deals with measures. Solvers that are particularly well-fitted for this task are the Frank-Wolfe algorithm and greedy methods. One can first cite the Matching Pursuit (MP) algorithm [109] which adds new spikes by finding ones that best correlate with the residual, or the Orthogonal Matching Pursuit (OMP) algorithm [144].

The Frank-Wolfe (FW) algorithm [69] also called the Conditional Gradient Method (CGM) [104] is also adapted because it can minimizes a differentiable function over a weakly compact and convex set (see Section 4.2.1 for more details). It has been proven that the rate of convergence of this algorithm in the objective function is  $O(1/k)$ . In [24], the authors proposed to consider the Frank-Wolfe algorithm for the BLASSO but where a final update (at the end of each main iteration) is performed thanks to a gradient descent on a non-convex optimization problem. It is the starting point of the Sliding Frank-Wolfe algorithm (SFW) that we propose in Chapter 4. A similar version of this modified Frank-Wolfe algorithm has also been used lately [32] for an SDP relaxation, promoting low rank matrices, of the BLASSO using Lasserre's hierarchy, leading to an overall complexity of  $O(f_c^d \log(f_c))$  per iteration (instead of a complexity polynomial in  $f_c^{2d}$  for SDP).

## Application to Fluorescence Microscopy

The ability to recover high resolution images from blurred and noisy measurements is a difficult challenge in imaging sciences. For example in Biology, key events in cellular trafficking occur at the cell surface and high resolution images are needed to capture them. The domain of fluorescence microscopy has recently seen the arrival of new imaging techniques, which overcome the diffraction phenomenon of standard optical microscopes that have a typical lateral resolution to 200nm and 500nm in depth.

Our interest turns to the PALM/STORM methods (Photoactivation Localization Microscopy and Stochastic Optical Reconstruction Microscopy) [16, 132, 124] which consist in turning on and off stochastically sparse subset of fluorophores in a sample. The authors of these methods were awarded a Chemistry nobel prize in 2014<sup>1</sup>. The fluorophores are fluorescent molecules attached to typically proteins that can be seen as spikes. When individual random fluorophores are activated and

---

<sup>1</sup>[https://www.nobelprize.org/nobel\\_prizes/chemistry/laureates/2014/](https://www.nobelprize.org/nobel_prizes/chemistry/laureates/2014/)

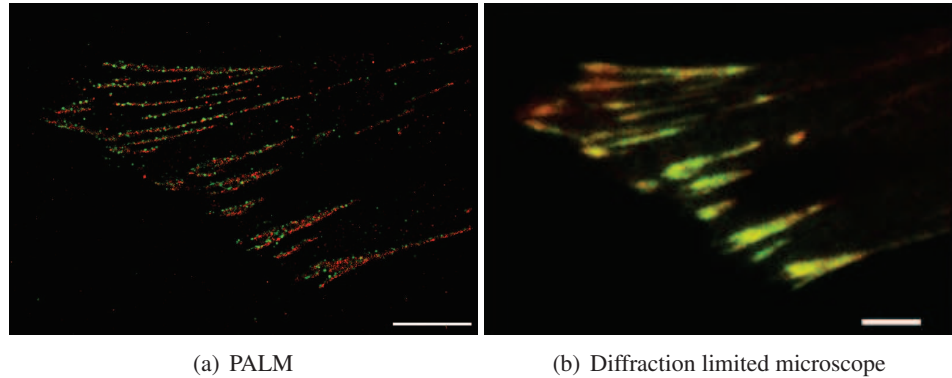


Figure 5: Comparison of PALM versus a classical diffraction limited microscope for the imaging of two proteins : tdEos-paxillin (green) and PsCFP20-zyxin (red). It demonstrates that these two focal adhesion proteins have very little over-lap when visualized with super-resolution. In contrast, when the same field is visualized with a diffraction limited method, the two proteins appear almost completely colocalized. Bar is 2 microns. *Images obtained from the Cell Image Library <http://www.cellimagelibrary.org/images/38602>.*

fluoresce, an image is recorded. A few thousands images, each containing just a few fluorophores, are collected. For each snapshot, a recovery is performed to obtain the coordinates of the fluorophores. The PSF of the system can often be approximated by a 2D Gaussian, thus if the fluorophores are separated enough, the centers of the spots give a nanometer precision on the real positions of the molecules, hence the breaking of the diffraction limit. PALM/STORM can then achieve a resolution of 20 nm [16, 8, 67]. All the coordinates obtained from all the snapshots are finally assembled to form the final super-resolve image. See Figure 5 for an example of an image obtained thanks to PALM.

The recovery step where the position of the fluorophores are obtained corresponds typically to the solving of sparse spikes inverse problem. Being able to locate with a high precision more and more fluorophores on each single snapshot is crucial because it would enhance the temporal resolution of the acquisition (the time needed to collect all the data) and therefore observe rapidly occurring events in the cell. As a result this application requires high performance numerical schemes. The *Single Molecule Localization Microscopy* (SMLM) contest<sup>2</sup> compares different numerical methods and grid-less techniques perform the best [22].

In this thesis, one proposes to use our grid-less algorithm introduced in Chapter 4 to study the recovery of fluorophores in a 3D volume (see Chapter 5). The PALM/STORM methods only capture lateral information and most of the experimental techniques and numerical schemes tackle only the 2D problem which is far less challenging than the 3D framework. To obtain depth information in addition

<sup>2</sup><http://bigwww.epfl.ch/smlm/>

to lateral information, we combine the PALM/STORM model with three different approaches:

- MA-TIRF (Multi-Angle Total Internal Reflection Fluorescence) [126, 21] consists in exciting the fluorophores with a laser under different angles.
- Double-Helix [121] consists in a point spread function (PSF) composed of two Gaussians that rotates with the depth.
- Astigmatism [90] consists in a PSF composed of a Gaussian whose horizontal and vertical size vary with the depth.

The PALM+MA-TIRF does not exist yet on the market but the Morpheme team (CNRS/INRIA/UCA) at the Institute of Biology Valrose (iBV) is currently working on it. This work is the result of a collaboration with Emmanuel Soubies who was part of the Morpheme team until recently.

## Main Contributions

**Chapter 1.** Chapter 1 studies the recovery of the support for the BLASSO first with no assumption on the sign of the amplitudes and secondly for positive amplitudes. In the first case, we provide in Section 1.2 (in the general setting where  $X$  has dimension  $d$ ), thanks to a convergence result between pre-certificates, a new proof using a constructive approach similar to the one developed in Chapter 3 of the main result of [54] (Theorem 2) on the support recovery for  $\mathcal{P}_\lambda(y)$  in a low noise regime. In Section 1.3, we show that the vanishing derivatives pre-certificate  $\eta_V$ , controlling the stability of the support in a low noise regime, is non-degenerate if the spikes of the initial measure are separated enough.

In a second time, when considering the particular case of positive measures (main setup of this thesis), we provide a novel pre-certificate called the  $(2N - 1)$ -vanishing derivatives pre-certificate, and denoted  $\eta_W$ , which arises naturally in the study of the recovery of the support of positive spikes that cluster at some point in the one dimensional domain  $X$ . It is defined in Section 1.4. We show that  $\eta_V$  converges towards  $\eta_W$ . In Section 1.5, we prove that the non-degeneracy of  $\eta_W$  is transferred to  $\eta_V$  when the spikes of the initial measures are close enough. It means in particular that one can perform the recovery of the support in a low noise regime (but with an unknown size with respect to separation between the spikes) when the spikes of the initial measure collapse at some point.

**Chapter 2.** The previous chapter showed that  $\eta_W$  controls the recovery of the support for the super-resolution problem (spikes collapsing at some point) in presence of noise. The crucial property of  $\eta_W$  involved in this matter is its  $(2N - 1)$ -non-degeneracy (defined in Section 1.5). This chapter discusses the non-degeneracy for several different imaging operators  $\Phi$ . In Section 2.2, we show that  $\eta_W$  is always locally non-degenerate when  $\Phi$  is a convolution operator. In the particular

case of a Gaussian convolution, we provide a formula for  $\eta_W$  and one deduces its non-degeneracy. In Section 2.3, one turns to  $\eta_W$  for Laplace measurements. We show, by providing formulas, that  $\eta_W$  is non-degenerate when  $\Phi$  is the un-normalized and  $L^2$ -normalized Laplace transform. This particular setup is of high interest to us because the MA-TIRF fluorescent microscopy model uses a Laplace-like transform for depth information recovery in the 3D volume of a sample. Finally in Section 2.4, one extends the definition of  $\eta_W$  to the case of several clusters of spikes and shows that if the clusters are separated enough then the non-degeneracy of the  $\eta_W$  (for several clusters) only depends on the non-degeneracy of the classical  $\eta_W$  (single cluster). This result justifies our choice of defining  $\eta_W$  for only one cluster of spikes.

**Chapter 3.** Chapter I proved that the non-degeneracy of  $\eta_W$  assures the recovery of the support of the initial measures in a low noise regime when the distance between the spikes  $t \rightarrow 0$ . However this result has limited practical interest because it does not tell anything on the tradeoff between the noise level and the distance between the spikes  $t$ . In this chapter, one studies precisely this dependency answering for the first time to the open question of super-resolution in presence of noise (in a low noise regime). We prove that if  $\eta_W$  is non-degenerate, if the regularization parameter  $\lambda$  and the noise  $w$  are in a domain whose size is proportional to  $t^{2N-1}$ , where  $N$  is the number of spikes of the initial measure, and if the ratio  $\|w\|_{\mathcal{H}}/\lambda$  is small enough then the BLASSO has a unique solution composed of the same number of spikes as the initial measure. Moreover the recovered amplitudes and positions converge toward those of the initial measure if the noise level drops to 0 faster than  $t^{2N-1}$ .

We also show that the non-degeneracy of  $\eta_W$  is almost a sharp condition.

**Chapter 4.** We propose a grid-less algorithm to solve the BLASSO (the domain  $X$  is  $d$  dimensional). We call it the Sliding Frank-Wolfe (SFW) algorithm. It is a modification of the algorithm detailed in [24]. It is based on the Frank-Wolfe algorithm and it adds iteratively new spikes to the recovered measure. The difference with the classical Frank-Wolfe algorithm is that the amplitudes and positions are moved before adding a new spike, using beneficially the continuous nature of the domain  $X$ . This update is performed in the same time for the amplitudes and positions contrary to what is proposed in [24] and later in [22]. This difference is crucial in our proof of its convergence speed. The algorithm is detailed in Section 4.2.1. Our main theoretical contribution in this chapter is that the SFW algorithm converges towards the unique solution of the BLASSO in a finite number of iterations if  $\eta_V$  is non-degenerate. This implies (in dimension 1) as a corollary that the SFW algorithm solves the super-resolution problem in presence of noise in a finite number of steps by recovering the unique measure solution of the BLASSO (and composed of the same number of spikes as the initial measure) if  $\eta_W$  is  $(2N-1)$ -non-degenerate. This convergence result dramatically improves the

standard weak-\* convergence (with an error in the objective function of  $O(1/k)$ ) of the Frank-Wolfe algorithm.

In Section 4.3, one compares numerically the SFW algorithm with FISTA and OMP and we show that it outperforms them in a Optimal Transport based metric but also in a metric based on detection indices.

In Section 4.4, one studies the properties of the numerical inversion of the Laplace transform using our algorithm by solving the BLASSO. In particular we show that one obtains better results when normalizing the kernel and that the size of the interval containing the discretization points of the Laplace transform influence the ability to recover spikes near or far from the origin. This provides crucial information for the experimentalists in order to design new imaging techniques based on the MA-TIRF model (Chapter 5).

**Chapter 5.** We use our algorithm to solve the BLASSO for three different 3D models to recover fluorophores positions in a cell. These models are based on the PALM/STORM technic which is known to improve the lateral resolution to as low as 20nm but offers no estimation of depth. In Section 5.2, we detail a mathematical framework, close of the one encountered by experimenters, modeling the acquisition of data for the models PALM+Double-Helix, PALM+MA-TIRF and PALM+Astigmatism. One provides the forward operators  $\Phi$  for these three cases. In the particular case of the Double-Helix and Astigmatism, one gives a formulation that deals with several camera mounted in parallel and acquiring data in the same time from several focal planes.

In Section 5.3, one uses our algorithm to solve the BLASSO for these three models in a designed framework close of experimental conditions, providing a new way (grid-less approach) to tackle this 3D problem. We show that the best performance is attained by the PALM+Double-Helix model followed by the PALM+MA-TIRF model and finally the PALM+Astigmatism model. The peak performance is attained in all cases when  $K = 4$  (4 TIRF angles or 4 focal planes). For the Double-Helix and Astigmatism, we show that considering at least two focal planes ( $K = 2$ ) instead of one (standard in the literature) improves significantly the recovery performance. The resolution attained for both models is under 20 nm in all dimensions. It provides valuable information for the experimenters because theses methods does not exist on the market yet (PALM+Double-Helix with  $K > 1$  has even never been tested).



# **Introduction Générale (Français)**

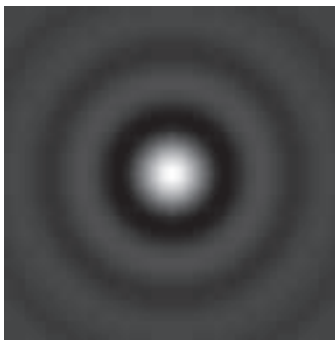
Cette thèse étudie la théorie, les algorithmes et les applications de la super-résolution de sources ponctuelles. La super-résolution consiste à améliorer le niveau de détails d'un signal observé donné. L'information de haute résolution sous-jacente capturée est altérée à cause des limitations physiques du système d'acquisition et par des perturbations aléatoires. C'est un problème que l'on rencontre par exemple dans des champs aussi diverses que l'astronomie, l'imagerie médicale, la géophysique ou l'imagerie radar. Une des applications les plus récentes de la super-résolution de sources ponctuelles concerne la microscopie par fluorescence en Biologie où les expérimentateurs essayent de dépasser le phénomène de diffraction (résolution latérale limite de 200nm) en localisant précisément la position de fluorophores (molécules fluorescentes attachées aux protéines) dans un échantillon. Les fluorophores peuvent être modélisés mathématiquement par des sources ponctuelles (c'est-à-dire une mesure composée d'une somme de masses de Dirac ayant des amplitudes positives). Ainsi, à partir d'une version altérée et bruitée de ces masses de Dirac, l'objectif est de reconstruire une estimation la plus précise possible de leurs positions et amplitudes. Comme deux fluorophores peuvent être séparés d'une distance bien inférieure à la limite de diffraction de 200nm, ce problème difficile requiert le développement d'outils théoriques et numériques performants. Notre approche, dans cette thèse, consiste à étudier un problème d'optimisation appelé le BLASSO et qui est une version continue du LASSO bien connu des statisticiens. Le BLASSO revient à minimiser la somme de l'erreur quadratique entre la version estimée et altérée du signal source et les données observationnelles, et d'un terme de régularisation (la norme de la variation totale des mesures) qui va favoriser les solutions parcimonieuses. Bien qu'il existe de nombreuses garanties théoriques pour la reconstruction de telles mesures à la fois dans le cadre sans bruit et avec bruit, la question de la super-résolution en présence de bruit pour le BLASSO est un problème ouvert. Nous avons montré, en dimension 1, que la non dégénérescence de ce que nous appelons le pré-certificat aux  $2N - 1$  dérivées nulles (noté  $\eta_W$ ) est une condition suffisante (et presque nécessaire) pour la reconstruction d'une unique mesure composée du même nombre de masses de Dirac que la mesure initiale lorsque ces dernières sont séparées par une distance  $t \rightarrow 0$ . Nous avons prouvé que cette reconstruction n'est valide que si le niveau de bruit diminue plus rapidement que  $t^{2N-1}$ . D'un point de vue numérique, nous fournissons un algorithme sans grille, que nous appelons l'algorithme SFW, qui résout le BLASSO (qui est un problème d'optimisation sur les mesures), basé sur l'algorithme de Frank-Wolfe mais avec une étape supplémentaire où les amplitudes et les positions des masses de Dirac sont déplacées continûment. Cet algorithme est inspiré par [24]. Une version proche de cet algorithme a récemment été étudiée dans [22] où les auteurs montrent que l'algorithme fournit un nouvel état de l'art dans plusieurs applications comme la microscopie par fluorescence 2D. Nous avons démontré dans le cas où une unique mesure discrète est solution du BLASSO, alors l'algorithme SFW reconstruit cette mesure en un nombre fini d'itérations. Ceci améliore significativement la seule garantie théorique de convergence connue jusqu'alors (convergence faible-\* avec une erreur en  $O(1/k)$  en la

fonction objective). Enfin nous avons appliqué notre algorithme au problème de la microscopie par fluorescence dans un cadre 3D en simulant précisément les conditions expérimentales et nous avons comparé trois modèles différents d'acquisition des données. Les résultats montrent une résolution spatiale de moins de 20nm selon les trois axes.

## La super-résolution de sources ponctuelles

Le cadre de la super-résolution de sources ponctuelles est rencontré de manière régulière dans de nombreux problèmes d'imagerie. En astronomie, les étoiles peuvent être considérées comme des sources ponctuelles de lumière. En biologie, les protéines fluorescentes dans les cellules peuvent également être vues comme des sources ponctuelles. Pour ces deux applications, le processus d'acquisition des données induit une altération du signal source idéal.

Une manière classique de déterminer si une application donnée entre dans le cadre de la super-résolution de sources ponctuelles est d'utiliser un critère de séparation de deux points. En théorie de la résolution, un critère de séparation de deux points définit la capacité d'un système de séparer deux points de même intensité. Un des critères les plus connus est le critère de Rayleigh [122] qui dit que deux points sont séparés par un système optique si le maximum d'intensité du motif de diffraction d'un des deux points source coincide avec le premier minimum (s'il existe) de l'intensité du motif de diffraction de l'autre point source. Ce critère définit une distance qui ne dépend que du système optique et qui est appelée la longueur de Rayleigh. Un exemple connu en physique et en astronomie est la tache d'Airy qui est le motif de diffraction obtenu quand une source de lumière rencontre une petite ouverture circulaire, voir la figure 6.



(a) Tache d'Airy

Figure 6: Motif de diffraction obtenu à l'infini ou au plan focal d'un système optique quand une source de lumière à l'infini illumine une petite ouverture circulaire (diffraction de Fraunhofer).

Le motif observé est donné par une fonction dépendant de la fonction de Bessel

$J_1$  et dans ce cas la longueur de Rayleigh est donnée par

$$\Delta_R \stackrel{\text{def.}}{=} 1.22 \frac{\lambda_\ell}{d},$$

où  $\lambda_\ell$  est la longueur d'onde et  $d$  le diamètre de l'ouverture. Pour les motifs de diffraction comme ceux donnés par des gaussiennes, il n'y a pas de minimum d'intensité autour du maximum central. C'est pourquoi nous préférons utiliser le critère de séparation qui dit qu'un système peut séparer deux sources ponctuelles si leurs motifs de diffraction ne se superposent pas de sorte que l'observation résultante n'a qu'un seul maximum central. Nous notons  $\Delta_S$  cette longueur limite. Voir la figure 7 pour une illustration de ce critère. Nous référerons à [47] pour plus de détails sur la théorie de la résolution.

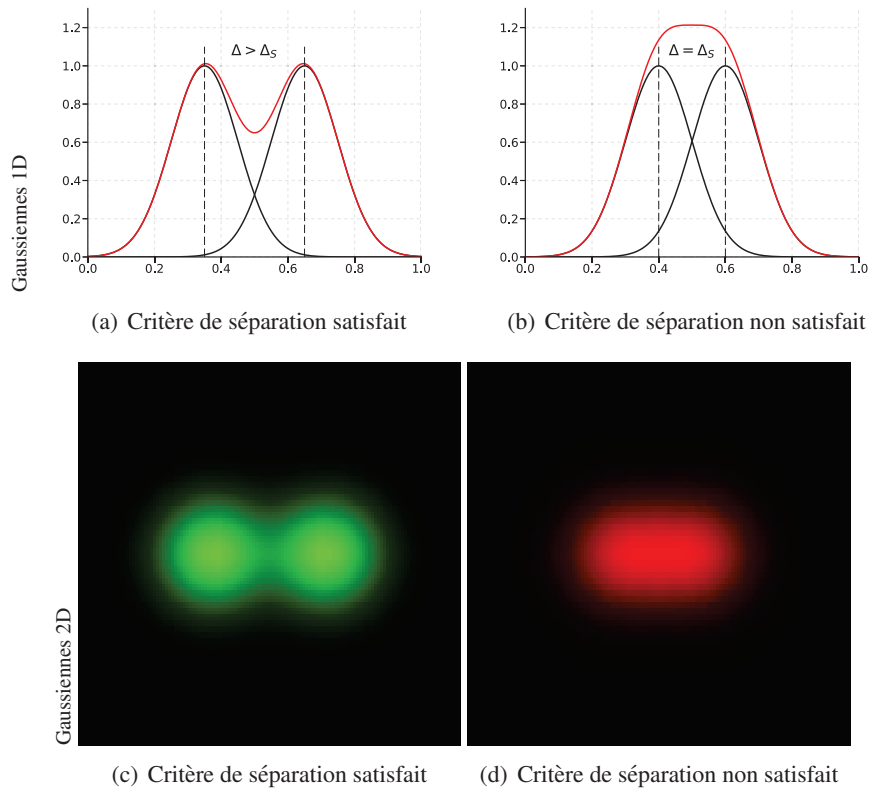


Figure 7: Illustration de notre critère de séparation pour les motifs de diffraction donnés par des gaussiennes en 1D et 2D. Pour une gaussienne de variance  $\sigma^2$ , on a  $\Delta_S = \sigma$ .

Le défi de la super-résolution de sources ponctuelles consiste donc à développer des techniques théoriques et numériques robustes permettant de séparer deux (voire plus) sources ponctuelles séparées par une distance en dessous de  $\Delta_S$  et dont les

données observationnelles sont contaminées par des perturbations aléatoires (bruit). Fournir de tels outils est le principal objectif de cette thèse. Comme nous l'argumentons dans cette thèse, la question de la super-résolution, à la fois d'un point de vue théorique et numérique, est un problème de détermination du comportement du rapport signal sur bruit : comment doit se comporter ce ratio en fonction du nombre de sources ponctuelles et de leurs distances respectives.

## Modélisation mathématiques

### Modélisation de signaux parcimonieux

Dans beaucoup d'applications (certaines déjà mentionnées), le signal source que l'on veut reconstruire à partir d'observations altérées et bruitées peut être modélisé par une collection de sources ponctuelles.

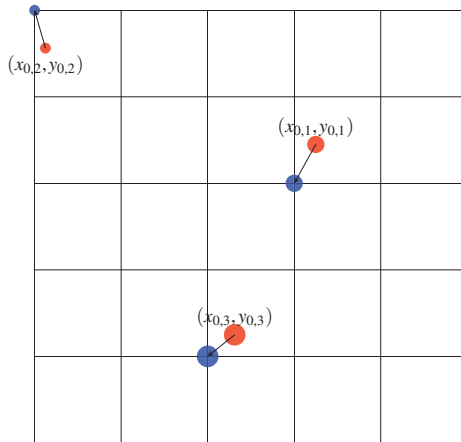


Figure 8: Illustration de la parcimonie d'un signal composé de sources ponctuelles donné par les points  $(x_{0,i}, y_{0,i})$  pour  $i \in \{1, \dots, 3\}$  dans  $[0, 1]^2$  (rouges) dont les amplitudes  $a_{0,i}$  sont encodées par le diamètre des disques. Une grille uniforme de  $[0, 1]^2$  composée de  $6 \times 6$  points est représentée. Pour chaque  $(x_{0,i}, y_{0,i})$ , on lui associe son voisin le plus proche sur la grille (points bleus). Le but est de reconstruire ces points bleus. Seulement une fraction des points sur la grille a des amplitudes non nulles d'où la parcimonie.

Ce type de signaux est qualifié de *parcimonieux*. Pour illustrer le concept de la parcimonie dans le cas particulier des sources ponctuelles, considérons un ensemble de positions  $(x_{0,1}, y_{0,1}), \dots, (x_{0,N}, y_{0,N})$  dans  $[0, 1]^2$  avec des amplitudes positives associées notées  $a_{0,1}, \dots, a_{0,N}$ . On peut se représenter cette exemple comme un ensemble d'étoiles dans une partie du ciel ayant des magnitudes  $(a_{0,i})$ . Si on utilise une grille uniforme composée de  $K^2$  points pour discréteriser le domaine  $[0, 1]^2$  et que l'on associe à chaque  $(x_{0,i}, y_{0,i})$  pour  $i \in \{1, \dots, N\}$  son plus proche voisin sur la grille, alors l'objectif est de retrouver un vecteur  $\tilde{a}_0 \in \mathbb{R}^{K^2}$  avec seule-

ment  $N$  coefficients non nuls correspondant aux  $a_{0,i}$ . Si la grille est assez fine pour capturer suffisamment de détails, cela signifie que  $N \ll K^2$  de sorte que  $\tilde{a}_0$  est un vecteur parcimonieux (peu de coefficients non nuls). Voir la figure 8 pour une illustration de cet exemple. La parcimonie peut alors être utilisée avantageusement dans le processus de reconstruction.

Une grille est pratique pour illustrer le concept de parcimonie dans le cas de signaux à sources ponctuelles. De plus, dès le départ c'est un problème de dimension finie (un ordinateur ne peut stocker qu'une quantité finie de données). Cependant les objets mathématiques appropriés pour représenter une collection de sources ponctuelles sont les sommes de masses de Dirac qui sont des mesures de Radon. En effet la masse de Dirac  $\delta_x$  peut être vue comme la forme linéaire sur l'espace des fonctions continues correspondant à l'évaluation en  $x$

$$\delta_x : \varphi \in \mathcal{C}_0 \mapsto \varphi(x).$$

Par conséquent, on peut exprimer la collection de sources ponctuelles dans  $[0, 1]^2$  du précédent exemple comme

$$m_{a_0, \bar{x}_0} \stackrel{\text{def.}}{=} \sum_{i=1}^N a_{0,i} \delta_{(x_{0,i}, y_{0,i})},$$

où  $\bar{x}_0 = ((x_{0,1}, y_{0,1}), \dots, (x_{0,N}, y_{0,N})) \in ([0, 1]^2)^N$ .  $m_{a_0, \bar{x}_0}$  est une mesure de Radon

$$m_{a_0, \bar{x}_0} : \varphi \in \mathcal{C}_0 \mapsto \sum_{i=1}^N a_{0,i} \varphi(x_{0,i}, y_{0,i}),$$

et c'est désormais le signal source parcimonieux que l'on souhaite reconstruire.

Plus généralement, dans la suite et à partir de maintenant, on notera  $X$  le domaine des positions des masses de Dirac. Selon le contexte,  $X$  peut-être soit  $\mathbb{R}^d$  (ou un sous ensemble compact d'intérieur non vide de  $\mathbb{R}^d$ ) ou  $\mathbb{T}^d$  (le tore de dimension  $d$ ) pour différentes valeurs de  $d \in \mathbb{N}^*$ .

On note  $\mathcal{M}(X)$  l'espace des mesures de Radon bornées sur  $X$  et qui peut-être vu comme le dual topologique de l'espace  $\mathcal{C}_0(X, \mathbb{R})$  des fonctions continues sur  $X$  qui tendent vers 0 à l'infini (voir la définition 3 pour un énoncé plus précis).

### Opérateur modélisant le processus d'acquisition

Le signal source  $m_{a_0, \bar{x}_0} \in \mathcal{M}(X)$  que l'on souhaite reconstruire est altéré par le processus d'acquisition. Par exemple quand un télescope prend une image d'une partie du ciel,  $m_{a_0, \bar{x}_0}$  est convolée avec la réponse impulsionnelle du système optique. Le résultat de cette altération correspond à la seule information à laquelle on a accès. Nous modélisons ce processus par l'action d'un opérateur linéaire  $\Phi$  défini sur  $\mathcal{M}(X)$ , prenant ses valeurs dans un espace de Hilbert séparable  $\mathcal{H}$  et ayant la forme suivante

$$\Phi : m \in \mathcal{M}(X) \mapsto \int_X \varphi(x) dm(x) \in \mathcal{H}. \quad (4)$$

La fonction  $\varphi$ , que l'on appelle dans la suite le noyau de  $\Phi$ , est une fonction continue définie sur  $X$  et prenant ses valeurs dans  $\mathcal{H}$ . Le choix de  $\varphi$  et  $\mathcal{H}$  dépend de l'application considérée. Dans la suite, on utilise le terme *observations* pour signifier les données collectées et représentant l'élément

$$y_0 \stackrel{\text{def.}}{=} \Phi m_{a_0, \bar{x}_0} \in \mathcal{H},$$

ou sa version bruitée ( $y = y_0 + w$  où  $w$  est du bruit). Voir la figure 9 pour un exemple d'observations dans le cas d'une convolution par une gaussienne sur  $\mathbb{R}$ .

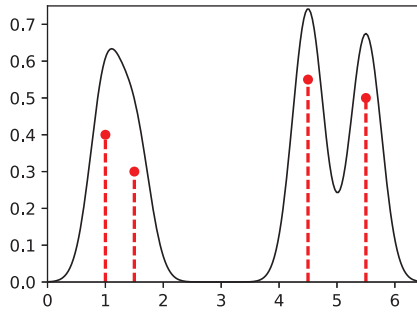


Figure 9: En rouge les masses de Dirac de la mesure initiale  $m_{a_0, \bar{x}_0}$  et en noir les observations  $y_0 = \Phi m_{a_0, \bar{x}_0}$  pour une convolution par une gaussienne c'est-à-dire  $\varphi(x) = e^{-\frac{|x|}{2\sigma^2}} \in L^2(\mathbb{R})$ .

Plusieurs exemples importants sont couverts par le modèle (I):

i)  $X = \mathbb{T}$ ,  $\mathcal{H} = L^2(\mathbb{T})$  et  $\varphi(x) = \frac{\sin(2\pi f_c(-x))}{\sin(\pi(-x))}$  ce qui correspond à une convolution par le noyau de Dirichlet ayant une fréquence de coupure  $f_c$ ,

ii)  $X = \mathbb{T}$ ,  $\mathcal{H} = \mathbb{R}^{2f_c+1}$  et

$$\varphi(x) = \begin{pmatrix} 1 \\ \sqrt{2} \cos(2\pi x) \\ \vdots \\ \sqrt{2} \cos(2\pi f_c x) \\ \sqrt{2} \sin(2\pi x) \\ \vdots \\ \sqrt{2} \sin(2\pi f_c x), \end{pmatrix} \in \mathbb{R}^{2f_c+1}$$

est équivalent à (II),

iii)  $X = \mathbb{R}$ ,  $\mathcal{H} = L^2(\mathbb{R})$  et  $\varphi(x) = e^{-\frac{(x-x_0)^2}{2\sigma^2}} \in L^2(\mathbb{R})$  ce qui correspond à une convolution par une gaussienne de variance  $\sigma^2$ ,

- iv)  $X = [\varepsilon, x_b]$  pour  $0 < \varepsilon < x_b$ ,  $\mathcal{H} = L^2(\mathbb{R}_+)$  et  $\varphi(x) = s \mapsto e^{-sx} \in L^2(\mathbb{R}_+)$  ce qui correspond à une transformée de Laplace (voir chapitre 2). On remarque en particulier que ce noyau n'est pas invariant par translation,
- v)  $X = [\varepsilon, x_b]$  pour  $0 < \varepsilon < x_b$ ,  $\mathcal{H} = \mathbb{R}^K$  et  $\varphi(x) = (e^{-s_k x})_{1 \leq k \leq K} \in \mathbb{R}^K$  ce qui correspond à une transformée de Laplace discrétisée (voir chapitre 2). Ce noyau est aussi invariant par translation,
- vi)  $X = \mathbb{R}^2$ ,  $\mathcal{H} = L^2(\mathbb{R}^2)$  et  $\varphi(x, y) = (u, v) \mapsto e^{-\frac{(u-x)^2}{2\sigma_x^2}} e^{-\frac{(v-y)^2}{2\sigma_y^2}} \in L^2(\mathbb{R}^2)$  ce qui correspond à une convolution par une gaussienne en 2D,
- vii) le chapitre 5 étudie plusieurs exemples dans  $\mathbb{R}^3$  construits à partir d'une convolution discrétisée par une gaussienne 2D.

Pour résumer, à partir des observations  $y_0 = \Phi m_{a_0, \bar{x}_0}$  ou  $y = y_0 + w$ , le but de la super-résolution de sources ponctuelles est de reconstruire un certain  $m \in \mathcal{M}(X)$  "proche" (pour une certaine distance) du signal source parcimonieux  $m_{a_0, \bar{x}_0}$ . C'est un problème inverse mal posé car  $\Phi$  n'est pas inversible. En suivant l'approche classique de la théorie de la régularisation, nous allons utiliser un a priori parcimonieux pour régulariser le processus d'inversion.

## Etat de l'art

La théorie et la pratique de la super-résolution peuvent être grossièrement divisées en trois parties:

- théorie : choix d'une méthode et étude théorique de ses performances,
- algorithmes : création d'une méthode de résolution exacte ou approximée et étude de ses performances d'approximation,
- applications : un grand nombre de subtilités et d'adaptations doit être pris en compte pour rendre compte des problèmes de la vie courante, et nous nous concentrerons dans cette thèse sur le problème de la microscopie par fluorescence.

Ces trois parties sont abordées dans cette thèse. La partie I concerne le premier point et la partie II concerne elle les deux derniers.

## Théorie

Il y a deux principales catégories d'approches théoriques pour le problème de la super-résolution : celle basée sur la méthode de Prony et celle basée sur les méthodes variationnelles.

**Méthodes basées sur Prony.** La méthode de Prony [44], MUSIC (MULTiple SIgnal Classification) [130], ESPRIT (Estimation of Signal Parameters by Rotational Invariance Techniques) [96] ou Matrix Pencil [89] permettent de reconstruire exactement les paramètres du signal dans le cas de mesures de Fourier et en l'absence de bruit car elle n'exige pas de discrétiliser le domaine. Bien que ces techniques n'ont pas été conçues à la base pour gérer une contamination des observations par du bruit, il existe des extensions qui en sont capables, voir [28, 39]. La stabilité au bruit est satisfaite sous une condition de séparation minimale [106]. Il existe également une méthode de Prony dans un cadre multivarié, voir [116].

Les méthodes basées sur Prony ont de meilleures performances que le LASSO dans le cas 1D pour des mesures de Fourier. Dans d'autres configurations, la comparaison est moins évidente et parfois il peut même être impossible de les étendre.

**Méthodes variationnelles.** Les approches variationnelles sont plus résiliantes car elles n'imposent pas de conditions particulières sur l'opérateur  $\Phi$  modélisant le processus d'acquisition des données. De plus, elles peuvent potentiellement s'adapter à n'importe quel type de bruit et n'exigent pas de connaître le nombre de sources ponctuelles. L'idée pour résoudre le problème de la super-résolution de sources ponctuelles présenté précédemment est de minimiser parmi tous les signaux sources possibles la somme d'un terme mesurant l'erreur par rapport aux observations (dans toute cette thèse, on considérera l'erreur quadratique) et d'un terme de régularisation favorisant la parcimonie.

**LASSO.** Dans un contexte de dimension finie, c'est-à-dire quand les positions des masses de Dirac sont prescrites sur une grille  $\mathcal{G} \subset X$  (voir la figure 8 pour un exemple), on obtient le LASSO [142] qui est défini par

$$\min_{a \in \mathbb{R}^{|\mathcal{G}|}} \underbrace{\frac{1}{2} \|\Phi_{\mathcal{G}} a - y\|_{\mathcal{H}}^2}_{\text{terme de fidélité}} + \underbrace{\lambda \|a\|_1}_{\text{terme favorisant la parcimonie}}, \quad (5)$$

où  $\Phi_{\mathcal{G}} a \stackrel{\text{def.}}{=} \Phi m_{a, x_{\mathcal{G}}}$  et  $x_{\mathcal{G}}$  est le vecteur des points de la grille  $\mathcal{G}$ .

Les techniques de régularisation  $\ell^1$  ont d'abord été introduites en géophysique (voir [37, 105, 127]) pour la prospection sismique car les changements de densité dans le sous-sol peuvent être modélisés par une somme de sources ponctuelles. La reconstruction basée sur la régularisation  $\ell^1$  fournit des solutions avec peu de coefficients non nuls et peut être résolue efficacement avec des méthodes numériques d'optimisation convexe. Donoho a étudié et justifié théoriquement ces techniques dans [49]. En traitement du signal, la méthode de la poursuite de base [34] utilise la norme  $\ell^1$  pour décomposer des signaux sur des dictionnaires redondants.

Puisqu'une grille est utilisée, cela signifie qu'il faut potentiellement la choisir de sorte que le pas soit très petit pour capturer avec grande précision la position des masses de Dirac de  $m_{a_0, \bar{x}_0}$ . Cependant cette approche a un effet négatif sur les propriétés de reconstructions théoriques (et numériques) car cela engendre le

phénomène de l'inadéquation de la base [35, 51] ainsi que des atomes fortement corrélés. Récemment, il a été prouvé dans [55, 56] que dans un régime de petit bruit, le LASSO sur une grille fine estime le double des masses de Dirac de la mesure initiale  $m_{a_0, \bar{x}_0}$ .

Ces limitations liées à l'approche discrète du LASSO peuvent être levées en considérant dès le départ un cadre sans grille. Nous le détaillons dans le paragraphe suivant.

**BLASSO.** Inspiré par de récents travaux (voir par exemple [17, 24, 30, 42, 54]), la méthode de super-résolution parcimonieuse que nous considérons dans cette thèse est un homologue de dimension infinie du LASSO (2). Elle peut être interprétée comme la limite (pour la topologie sur les mesures) du LASSO lorsque la grille se raffine. Ce problème inverse défini sur l'espace des mesures de Radon est appelé dans [42] le BLASSO (B pour Beurling). Le cadre sans grille simplifie l'analyse mathématique (au prix du passage à la dimension infinie) et permet potentiellement de faire des prédictions précises sur la position des masses de Dirac reconstruites.

Ainsi, le problème d'optimisation (2) devient

$$\min_{m \in \mathcal{M}(X)} \frac{1}{2} \|\Phi m - y\|_{\mathcal{H}}^2 + \lambda |m|(X). \quad (\mathcal{P}_\lambda(y))$$

Il y a plusieurs différences entre le LASSO et le BLASSO  $\mathcal{P}_\lambda(y)$

1. on optimise sur  $\mathcal{M}(X)$  plutôt que sur  $\mathbb{R}^{\#G}$  et  $\Phi_g a = \Phi m_{a, x_g}$  pour tout  $a \in \mathbb{R}^{\#G}$  est remplacé par  $\Phi m$  pour tout  $m \in \mathcal{M}(X)$ , ce qui fait de  $\mathcal{P}_\lambda(y)$  un problème d'optimisation sur un espace de Banach non réflexif plutôt que sur un espace vectoriel de dimension finie,
2. la norme  $\ell^1$  utilisée comme terme de régularisation (et qui est uniquement utilisable en dimension finie) est remplacée par son homologue de dimension infinie c'est-à-dire la norme de la variation totale définie par

$$\forall m \in \mathcal{M}(X), \quad |m|(X) \stackrel{\text{def.}}{=} \sup_{\psi \in \mathcal{C}_0(X, \mathbb{R})} \left\{ \int_X \psi dm ; \|\psi\|_{\infty, X} \leq 1 \right\}.$$

C'est la norme duale de  $\|\cdot\|_{\infty, X}$  sur  $\mathcal{C}_0(X, \mathbb{R})$  et elle généralise bien la norme  $\ell^1$  au cadre continu des mesures car

$$\forall a_0 \in \mathbb{R}^N, \forall \bar{x}_0 \in X^N, \quad |m_{a_0, \bar{x}_0}|(X) = \|a_0\|_1.$$

Par conséquent, comme pour la norme  $\ell^1$  qui favorise les solutions avec peu de coefficients non nuls, la norme de la variation totale utilisée dans  $\mathcal{P}_\lambda(y)$  va favoriser les mesures parcimonieuses c'est-à-dire celles composées de masses de Dirac (ce sont les points extrémaux de la boule unité de  $\mathcal{M}(X)$  pour  $|\cdot|(X)$ ).

Le paramètre de régularisation  $\lambda > 0$  doit être adapté au niveau de bruit  $\|w\|_{\mathcal{H}}$ . Faisons remarquer avant de continuer qu'il existe une variante du BLASSO qui estime à la fois la mesure initiale et le niveau de bruit, voir [23]. Dans le cas sans bruit  $w = 0$ , on peut faire tendre  $\lambda \rightarrow 0$  dans  $\mathcal{P}_\lambda(y)$  et alors obtenir le problème suivant

$$\min_{m \in \mathcal{M}(X)} \{|m|(X) ; \Phi m = y_0\}. \quad (\mathcal{P}_0(y_0))$$

C'est une généralisation de la classique méthode de la poursuite de base

$$\min_{a \in \mathbb{R}^{\#\mathcal{G}}} \{\|a\|_1 ; \Phi \mathcal{G}a = y_0\},$$

introduite à l'origine dans [34] dans un contexte de dimension finie, et écrite ici sur l'espace des mesures de Radon. Dans la suite on fera référence au problème  $\mathcal{P}_0(y_0)$  comme la méthode de la poursuite de base pour les mesures. C'est le problème étudié dans [30], dans le cas où  $\Phi$  est le filtre passe-bas idéal sur le tore (voir l'exemple (1)). Les auteurs montrent que  $m_{a_0, \bar{x}_0}$  est l'unique solution de  $\mathcal{P}_0(y_0)$  si  $\Delta(\bar{x}_0) \geq \frac{C}{f_c}$  pour une certaine constante  $0 < C \leq 1.87$  où

$$\Delta(\bar{x}_0) \stackrel{\text{def}}{=} \min_{i \neq j} |\bar{x}_{0,i} - \bar{x}_{0,j}|. \quad (6)$$

est la distance minimale de séparation entre les masses de Dirac. Dans [65], l'auteur démontre que  $C \leq 1.26$ . De plus [54] prouve nécessairement que  $C \geq \frac{1}{2}$ .

D'après cette dernière relation, on en déduit que la super-résolution est impossible de manière générale lorsque l'on résout  $\mathcal{P}_0(y_0)$  (ou  $\mathcal{P}_\lambda(y)$ ) sans hypothèse sur le signe des amplitudes. En effet même si on peut retrouver exactement la position des masses de Dirac (si  $\Delta(\bar{x}_0)$  est suffisamment grand) dans le domaine continu des positions des sources ponctuelles, nous avons expliqué précédemment que la super-résolution consiste à essayer de reconstruire deux (ou plus) masses de Dirac possiblement infiniment proches. Cependant pour des masses de Dirac positives (c'est-à-dire  $a_{0,i} > 0$ ), la reconstruction exacte de  $m_{a_0, \bar{x}_0}$  pour le problème sans bruit (*i.e.* pour  $\mathcal{P}_0(y_0)$ ) est satisfaite peu importe  $\Delta(\bar{x}_0) > 0$ , voir par exemple [42]. Par conséquent le bon cadre pour étudier la super-résolution est celui des mesures positives. La plupart du temps dans cette thèse, nous nous placerons dans ce contexte. Le résultat de [42] cité au-dessus est uniquement vrai lorsqu'il n'y a pas de bruit contaminant les observations. Ainsi le problème de la super-résolution en présence de bruit est une question ouverte. C'est le principal sujet de notre travail.

Dans [24], il est montré que si la solution de  $\mathcal{P}_0(y_0)$  est unique alors les mesures solutions de  $\mathcal{P}_\lambda(y)$  convergent pour la topologie faible-\* vers la solution de  $\mathcal{P}_0(y_0)$  quand  $\lambda \rightarrow 0$  et  $\|w\|_{\mathcal{H}}^2 / \lambda \rightarrow 0$ . Dans [29], les auteurs fournissent une estimation de l'erreur en utilisant la norme  $L^1$  d'une version basse fréquence des mesures reconstruites. Les arguments utilisés sont un raffinement de [27]. Dans [7, 64], les majorations de l'erreur sont données en terme de localisation des

masses de Dirac reconstruites par rapport à celles de la mesure initiale. Cependant, ces travaux ne donnent que peu d'informations sur la structure des mesures reconstruites par  $\mathcal{P}_\lambda(y)$ . Cette question est adressée dans [54] où les auteurs montrent que si le pré-certificat aux dérivées nulles (voir la section 1.2 pour plus de détails)  $\eta_V \stackrel{\text{def.}}{=} \Phi^* p_V$ , où  $p_V$  est l'unique solution de

$$\inf \left\{ \|p\|_{\mathcal{H}} ; \forall i = 1, \dots, N, (\Phi^* p)(\bar{x}_{0,i}) = \text{sign}(a_{0,i}), (\Phi^* p)'(\bar{x}_{0,i}) = 0 \right\},$$

est non-dégénéré c'est-à-dire

$$\forall x \in X \setminus \bigcup_{i=1}^N \bar{x}_{0,i}, \quad |\eta_V(x)| < 1 \quad \text{and} \quad |\eta_V''(\bar{x}_{0,i})| \neq 0,$$

alors il existe une unique solution de  $\mathcal{P}_\lambda(y)$  avec exactement le même nombre de masse de Dirac que la mesure initiale  $m_{a_0, \bar{x}_0}$ , pourvu que  $\lambda$  et  $\|w\|_{\mathcal{H}} / \lambda$  soient suffisamment petits. Remarquons que l'on peut facilement montrer que si  $\|\eta_V\|_{\infty, X} \leq 1$  alors  $\eta_V$  est un *certificat* pour  $m_{a_0, \bar{x}_0}$ . Nous rappelons qu'un certificat pour une mesure discrète  $m_{a_0, \bar{x}_0}$  et pour  $\mathcal{P}_0(y_0)$  est une fonction continue dans l'image de  $\Phi^*$  qui interpole le signe des amplitudes à la position des masses de Dirac et qui est plus petite que 1 en norme infinie (condition également appelée condition source dans la littérature [26]). Or il se trouve que  $\eta_V$  satisfait toutes les conditions sauf  $\|\eta_V\|_{\infty, X} \leq 1$  qui assure alors que  $m_{a_0, \bar{x}_0}$  est solution de  $\mathcal{P}_0(y_0)$ . L'intuition derrière la définition de  $\eta_V$  est que la propriété de norme minimale  $L^2$  ainsi que les conditions d'interpolation avec dérivées nulles vont permettre d'obtenir  $\|\eta_V\|_{\infty, X} \leq 1$ .

La section 1.4 définie le pré-certificat aux  $(2N - 1)$  dérivées nulles que l'on note  $\eta_W \stackrel{\text{def.}}{=} \Phi^* p_W$ . C'est la limite de  $\eta_V$  quand les  $N$  masses de Dirac (toutes positives) de  $m_{a_0, \bar{x}_0}$  se rapprochent en un point du domaine.  $p_W$  est l'unique solution de

$$\inf \left\{ \|p\|_{\mathcal{H}} ; (\Phi^* p)(0) = 1, (\Phi^* p)'(0) = 0, \dots, (\Phi^* p)^{(2N-1)}(0) = 0 \right\}.$$

Puisque  $\eta_V$  contrôle la stabilité du support dans un régime de petit bruit, on peut imaginer que  $\eta_W$  va jouer un rôle similaire (en tant que limite de  $\eta_V$ ) lorsque les masses de Dirac se rapprochent les unes des autres.

## Algorithmes

Il y a plusieurs algorithmes en fonction des schémas d'approximation du BLASSO. On peut rassembler ces derniers en trois catégories :

- discréétisation spatiale fixe,
- discréétisation spectrale fixe et formulation SDP,
- discréétisation dynamique grâce à une optimisation sur l'espace des mesures.

**Discrétisation spatiale fixe.** Cette approche est celle qui mène au LASSO. La classe d’algorithme qui correspond à ce cas est la famille des méthodes proximales. Ces algorithmes reposent sur le fait que le LASSO a une structure hilbertienne. L’“Iterative Hard Thresholding” (IHT) [19, 20] ou l’“Iterative Soft Thresholding” (IST) [41, 38] sont des algorithmes qui font partie de la famille des algorithmes “Iterative Shrinkage-Thresholding” (ISTA). Leurs taux de convergence ont été abondamment étudiés dans la littérature [41, 50, 66]. Bien que ISTA soit simple à implémenter, sa convergence est relativement lente (l’erreur en la fonction objective est typiquement en  $O(1/k)$ ). FISTA [9] donne un meilleur taux de convergence non asymptotique en  $O(1/k^2)$ . Lorsque l’on travaille avec une grille, il est nécessaire qu’elle soit suffisamment fine pour obtenir une localisation suffisamment précise des masses de Dirac de la mesure initiale. Cependant quand la taille de la grille  $\#\mathcal{G}$  augmente, cela rend chaque itération plus lente et produit un dictionnaire plus corrélé ce qui détériore les constantes de convergence. Par conséquent, en pratique, on obtient souvent un petit groupe de coefficients non nuls dans un voisinage de chacune des masses de Dirac de la mesure initiale.

**Discrétisation spectrale fixe et formulation SDP.** En s’inspirant de [30], il est possible de reformuler le BLASSO dans le cas d’un filtre passe-bas ( $X = T$ ) en un problème SDP (semi-definite program). Dans ce cas, on utilise alors des méthodes de points intérieurs pour le résoudre puis une étape de calcul de racines d’un polynôme trigonométrique pour trouver les positions des masses de Dirac. Un des désavantages de cette approche est l’étape de calcul de racines qui peut rencontrer des soucis de stabilité. De plus la complexité d’une méthode de points intérieurs pour ce problème SDP est polynomiale en  $O(f_c^{2d})$  où  $d$  est la dimension du domaine  $X$ . Cet état de fait a mené à de récents développements [32] où les auteurs ont utilisé une relaxation de faible rang de la formulation SDP du BLASSO pour utiliser ensuite une méthode gloutonne (voir ci-dessous). Enfin cette approche ne peut être appliquée que pour certains types d’opérateur  $\Phi$  (mesures de Fourier) alors que l’algorithme de Frank-Wolfe (et les méthodes gloutonnes) et les méthodes proximales peuvent être employés pour des  $\Phi$  plus généraux.

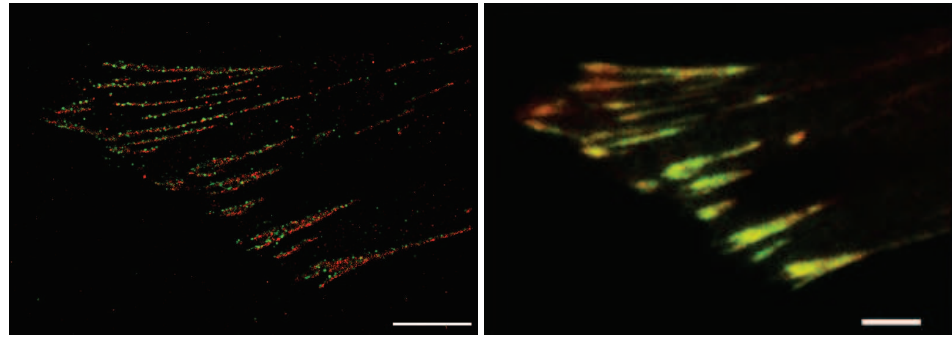
**Discrétisation dynamique grâce à une optimisation sur l’espace des mesures.** Afin de résoudre directement le BLASSO, on a besoin d’algorithmes qui n’utilisent pas une structure hilbertienne et peuvent à la place directement travailler avec des mesures. Les algorithmes qui conviennent particulièrement bien à cette tâche sont l’algorithme de Frank-Wolfe et les méthodes gloutonnes. On peut par exemple tout d’abord penser à l’algorithme Matching Pursuit (MP) [109] qui ajoute de nouvelles masses de Dirac en trouvant celles qui ont la meilleure corrélation avec le résidu, ou à l’Orthogonal Matching Pursuit (OMP) [44].

L’algorithme de Frank-Wolfe (FW) [69], également appelé méthode du gradient conditionnel (CGM) [104], est aussi adapté à cette situation car il permet de minimiser une fonction différentiable sur un ensemble convexe faiblement com-

pact d'un espace de Banach (voir la section 4.2.1 pour plus de détails). Il a été montré que le taux de convergence de cet algorithme (en la fonction objective) est en  $O(1/k)$  si la fonction objective est convexe et si sa différentielle est lipschitzienne [46]. Dans [24], les auteurs proposent d'appliquer FW au BLASSO avec en plus une mise à jour des paramètres du signal à chaque fin d'itération via la minimisation d'un problème non convexe. C'est le point de départ de l'algorithme Sliding Frank-Wolfe (SFW) que nous proposons dans le chapitre 4 de cette thèse. Une version similaire de cet algorithme de Frank-Wolfe modifié a été utilisée dans [32] pour une relaxation SDP, favorisant les matrices de rang faibles, du BLASSO grâce à la hiérarchie de Lasserre. Cette approche a une complexité en  $O(f_c^d \log(f_c))$  par itération (au lieu de polynomial en  $O(f_c^{2d})$  pour la version SDP classique utilisant une méthode de points intérieurs).

### Application à la microscopie par fluorescence

La reconstruction d'images de haute résolution à partir d'observations altérées et bruitées est un défi compliqué en traitement d'images. Par exemple en biologie, le domaine de la microscopie par fluorescence a récemment vu l'arrivée de nouvelles techniques d'imagerie qui permettent de dépasser la limite de diffraction des microscopes optiques (qui ont une résolution latérale d'environ 200nm et axiale de 500nm).



(a) PALM

(b) Microscope limité par la diffraction

Figure 10: Comparaison de PALM et d'un microscope optique classique pour l'imagerie de deux protéines : tdEos-paxillin (vert) and PsCFP20-zyxin (rouge). On remarque que ces deux protéines ne se chevauchent pas quand elles sont visualisées grâce à PALM. À l'inverse elles apparaissent presque co-localisées quand elles sont observées via le microscope optique. *Images obtenues à partir de <http://www.cellimagelibrary.org/images/38602>.*

Nous nous intéressons, dans cette thèse, aux méthodes PALM/STORM (Photoactivation Localization Microscopy et Stochastic Optical Reconstruction Microscopy) [16, 32, 24] qui consistent à activer et éteindre de manière aléatoire un sous ensemble restreint de fluorophores dans un échantillon. Les auteurs de ces

méthodes ont été récompensés d'un prix nobel de chimie en 2014<sup>3</sup>. Les fluorophores sont des molécules fluorescentes attachées typiquement à des protéines et peuvent être vus comme des sources ponctuelles de lumière (donc des masses de Dirac). Quand des fluorophores sont activés de manière aléatoire et émettent de la lumière, une image est enregistrée. Lors d'une acquisition, quelques milliers d'images sont enregistrées. Pour chacune d'entre elles, une reconstruction est effectuée afin d'obtenir les coordonnées (la localisation) des fluorophores. La PSF du système peut souvent être approximée par une gaussienne 2D, ainsi si les fluorophores sont suffisamment séparés le centre des taches donne une précision nanométrique sur la vraie position des molécules ce qui permet au bout du compte de dépasser largement la limite de résolution causée par la diffraction. Les techniques PALM/STORM permettent d'obtenir une résolution latérale de l'ordre de 20nm [16, 8, 67]. Toutes les coordonnées récupérées par les reconstructions sont alors rassemblées pour former une unique image super-résolue de l'échantillon observé. Voir la figure 10 pour un exemple d'image obtenue grâce à PALM.

L'étape de reconstruction correspond à la résolution d'un problème de super-résolution de sources ponctuelles. La localisation avec grande précision de plus en plus de fluorophores pour chaque image capturée est un point crucial car cela permet d'améliorer la résolution temporelle de l'acquisition (c'est-à-dire le temps total utilisé pour la collecte des données) et donc d'observer des événements qui se produisent dans des échelles de temps plus courtes. C'est pourquoi cette étape exige des méthodes numériques très performantes. Le challenge *Single Molecule Localization Microscopy* (SMLM)<sup>4</sup> compare différentes méthodes numériques et les techniques sans grille sont celles qui ont les meilleurs résultats à l'heure de l'écriture de ce manuscrit. Voir par exemple [22].

Dans cette thèse, nous proposons d'utiliser notre algorithme sans grille introduit au chapitre 4 pour étudier la reconstruction de fluorophores dans un volume 3D (voir le chapitre 5). Les méthodes PALM/STORM ne permettent de reconstruire qu'une information latérale et la plupart des techniques expérimentales et des schémas numériques ne s'intéressent qu'au problème 2D qui est bien plus facile que le problème 3D. Pour obtenir une information sur la profondeur, nous proposons de combiner PALM/STORM avec trois approches différentes :

- MA-TIRF (Multi-Angle Total Internal Reflection Fluorescence) [126, 21] qui consiste à exciter les fluorophores avec un laser suivant différents angles,
- la double hélice [121] qui produit une PSF composée de deux gaussiennes qui tournent avec la profondeur,
- l'astigmatisme [90] qui produit une PSF composée d'une gaussienne dont les dimensions horizontale et verticale changent avec la profondeur.

La technique PALM + MA-TIRF n'existe pas encore sur le marché mais l'équipe Morphème (CNRS/INRIA/UCA) à l'institut de biologie de Valrose (iBV) travaille

---

<sup>3</sup>[https://www.nobelprize.org/nobel\\_prizes/chemistry/laureates/2014/](https://www.nobelprize.org/nobel_prizes/chemistry/laureates/2014/)

<sup>4</sup><http://bigwww.epfl.ch/smlm/>

actuellement sur ce projet. Cette partie de la thèse est le résultat d'une collaboration avec Emmanuel Soubies (qui a fait parti de l'équipe Morpheme).

## Contributions principales

**Chapitre 1.** Nous étudions la reconstruction du support pour le BLASSO, dans un premier temps sans hypothèse sur le signe des amplitudes des masses de Dirac, puis dans un second temps pour des amplitudes positives. Dans le premier cas, nous fournissons dans la section 1.2 (lorsque le domaine  $X$  est de dimension  $d \in \mathbb{N}^*$ ) une nouvelle preuve du résultat principal de [54] (théorème 2) sur la reconstruction du support pour  $\mathcal{P}_\lambda(y)$  dans un régime de petit bruit, en utilisant une approche constructive similaire à celle développée dans le chapitre 3. Dans la section 1.3, nous démontrons que le pré-certificat aux dérivées nulles  $\eta_V$ , contrôlant la stabilité du support dans un régime de petit bruit, est non-dégénéré si les masses de Dirac de la mesure initiale sont suffisamment séparées.

Dans le second cas, nous définissons un nouveau pré-certificat appelé le pré-certificat aux  $(2N - 1)$  dérivées nulles, et noté  $\eta_W$ , apparaissant naturellement lors de l'étude de la reconstruction du support de mesures positives dont les masses de Dirac se rapprochent en un point du domaine  $X$  supposé ici de dimension 1. Cet objet est défini dans la section 1.4 où nous montrons que  $\eta_V$  converge vers  $\eta_W$ . Dans la section 1.5, nous prouvons que la non-dégénérescence de  $\eta_W$  est transférée à  $\eta_V$  quand les masses de Dirac de la mesure initiale sont suffisamment proches. Cela signifie en particulier que l'on peut effectuer la reconstruction du support dans un régime de petit bruit (mais dont la taille n'est pas connue par rapport à la distance séparant les masses de Dirac) quand les masses de Dirac se rapprochent infiniment en un point.

**Chapitre 2.** Le chapitre précédent montre que  $\eta_W$  contrôle la reconstruction du support pour le problème de la super-résolution en présence de bruit. La propriété centrale est sa  $(2N - 1)$  non dégénérescence (définie dans la section 1.5). Le chapitre 2 s'attelle à l'étude de cette non dégénérescence pour plusieurs exemples différents d'opérateur  $\Phi$  (modélisant le processus d'acquisition). Dans la section 2.2, nous démontrons que  $\eta_W$  est toujours localement non dégénéré si  $\Phi$  est un opérateur de convolution. Dans le cas particulier de la convolution par une gaussienne, nous fournissons une formule simple pour  $\eta_W$  dont on déduit sa non dégénérescence. Dans la section 2.3, on s'intéresse à  $\eta_W$  lorsque  $\Phi$  est une transformée de Laplace. Nous montrons, en fournissant des expressions, que  $\eta_W$  est non dégénéré quand  $\Phi$  est une transformée de Laplace non-normalisée et normalisée pour la norme  $L^2$ . Ces deux derniers cas nous intéressent particulièrement car ils sont impliqués dans le modèle MA-TIRF en microscopie par fluorescence. Enfin dans la section 2.4, nous étendons la définition de  $\eta_W$  au cas de plusieurs groupes de masses de Dirac qui se rapprochent en plusieurs points différents du domaine  $X$ . Nous démontrons que si ces points sont suffisamment éloignés alors la non

dégénérescence de  $\eta_W$  ne dépend que de la non dégénérescence de  $\eta_W$  pour un seul point de rapprochement. Ce résultat justifie rétrospectivement le choix de ne s'intéresser à  $\eta_W$  que pour un seul groupe de masses de Dirac.

**Chapitre 3.** Dans le chapitre [1], nous avons démontré que la non dégénérescence de  $\eta_W$  assure la reconstruction du support de la mesure initiale dans un régime de petit bruit quand la distance entre les masses de Dirac tend vers 0. Cependant ce résultat a peu d'intérêt en pratique car il ne donne aucune information sur le compromis qu'il y a entre le niveau de bruit et la distance minimale séparant les masses de Dirac  $t$ . Dans ce chapitre, nous faisons l'étude précise de cette dépendance et fournissons une réponse à la question ouverte de la super-résolution en présence de bruit. Nous prouvons que si  $\eta_W$  est non dégénéré, alors si le paramètre de régularisation  $\lambda$  et le bruit  $w$  sont dans un domaine dont la taille est proportionnelle à  $t^{2N-1}$ , où  $N$  est le nombre de masses de Dirac de la mesure initiale, et si le ratio  $\|w\|_{\mathcal{H}}/\lambda$  est suffisamment petit alors le BLASSO a une unique solution composée du même nombre de masses de Dirac que la mesure initiale. De plus les amplitudes et positions reconstruites convergent vers ceux de la mesure initiale si le niveau de bruit tend vers 0 plus vite que  $t^{2N-1}$ . Nous montrons également que la condition de non-dégénérescence de  $\eta_W$  est presque nécessaire.

**Chapitre 4.** Nous proposons un algorithme sans grille qui résout le BLASSO (le domaine est supposé être de dimension  $d \in \mathbb{N}^*$ ). Nous l'appelons l'algorithme Sliding Frank-Wolfe (SFW). C'est une modification de celui détaillé dans [24] et est basé sur l'algorithme de Frank-Wolfe. Il ajoute de manière itérative de nouvelles masses de Dirac à la mesure reconstruite. La différence fondamentale avec l'algorithme de FW est que les amplitudes et les positions sont déplacées avant chaque ajout de nouvelle masse de Dirac, via la minimisation d'un problème non convexe. Cette mise à jour est faite en même temps sur les amplitudes et les positions contrairement à ce qui est proposé dans [24] et plus tard dans [22]. Cette différence est importante car c'est l'ingrédient principal de l'étude de sa convergence. L'algorithme est détaillé dans la section [4.2.1].

Notre contribution théorique principale dans ce chapitre montre que l'algorithme SFW converge vers l'unique solution du BLASSO en un nombre fini d'itérations si  $\eta_V$  est non dégénéré. On en déduit en particulier en dimension 1 que l'algorithme est capable de résoudre numériquement le problème de la super-résolution en présence de bruit en temps fini en reconstruisant l'unique solution du BLASSO (composée du même nombre de masses de Dirac que la mesure initiale) si  $\eta_W$  est  $(2N - 1)$  non dégénéré. Ce résultat de convergence améliore significativement la convergence classique pour la topologie faible-\* (avec une erreur en la fonction objective en  $O(1/k)$ ) de l'algorithme de FW.

Dans la section [4.3], on compare l'algorithme SFW avec FISTA et OMP et nous montrons qu'il fournit de meilleures performances pour une métrique basée sur le transport optimal et également pour des métriques basées sur des indices de

détection.

Dans la section 4.4, nous étudions les propriétés de l'inversion numérique de la transformée de Laplace en utilisant notre algorithme pour résoudre le BLASSO. En particulier, nous montrons que l'on obtient de meilleurs résultats quand le noyau est normalisé et puis que la taille de l'intervalle contenant les points de discréttisation de la transformée de Laplace influence la capacité de reconstruire des masses de Dirac proches ou éloignées de l'origine. Cela procure aux expérimentateurs des indications très importantes pour la mise au point de nouvelles techniques d'imagerie basées sur le modèle MA-TIRF.

**Chapitre 5.** Nous utilisons notre algorithme pour résoudre le BLASSO pour trois modèles différents de reconstruction 3D de fluorophores dans une cellule. Ces modèles sont basées sur les techniques PALM/STORM qui sont connues pour améliorer la résolution latérale jusqu'à 20nm mais qui ne fournit pas d'estimation de la profondeur des fluorophores. Dans la section 5.2, nous détaillons un cadre mathématique qui est proche de celui rencontré par les expérimentateurs en pratique et que nous utilisons pour nos tests numériques. Nous modélisons mathématiquement les acquisitions pour les modalités PALM + double hélice, PALM + astigmatisme et PALM + MA-TIRF et nous prenons également en compte la possibilité pour l'expérimentateur d'installer plusieurs caméras en parallèle enregistrant les données simultanément à partir de plans focaux différents.

Dans la section 5.3, nous montrons que les meilleures performances sont obtenues par le modèle PALM + double hélice suivi de PALM + MA-TIRF et enfin de PALM + astigmatisme. Les meilleurs résultats pour chacune des modalités sont obtenus à chaque fois pour  $K = 4$  (4 angles TIRF et 4 plans focaux). Pour la double hélice et l'astigmatisme, nous montrons que considérer au moins deux plans focaux ( $K = 2$ ) au lieu d'un seul (ce qui est standard dans la littérature) améliore significativement les performances de reconstruction. La résolution atteinte pour chacun des modèles est en dessous de 20nm dans les 3 dimensions.

**Part I**

**Sparse Super-Resolution of  
Positive Measures**



## Chapter 1

# Asymptotic Analysis of Support Recovery

The recovery of the support of the BLASSO in a low noise regime is controlled by the non-degeneracy of the vanishing derivatives pre-certificate denoted  $\eta_V$ . We show, when no assumption is made on the sign of the amplitudes of the spikes, that it is non-degenerate provided that the Dirac masses are separated enough. In the case of positive spikes, there is no need for a separation. One can thus study the super-resolution problem which is the clustering of the spikes of the initial measure at some point in the domain. We prove that  $\eta_V$  converges towards a new pre-certificate called the  $(2N - 1)$  vanishing derivatives pre-certificate and denoted  $\eta_W$ . We then show that a particular notion of non-degeneracy for  $\eta_W$  is transferred to  $\eta_V$  when the spikes are close enough to each other. This leads to a first result of stability of the support in a low noise regime for the super-resolution problem when solving the BLASSO.

## 1.1 Introduction

Recall that one considers the following optimization problem

$$\min_{m \in \mathcal{M}(X)} \frac{1}{2} \|\Phi m - y\|_{\mathcal{H}}^2 + \lambda |m|(X), \quad (\mathcal{P}_\lambda(y))$$

where  $\Phi : \mathcal{M}(X) \rightarrow \mathcal{H}$  is a linear operator defined by  $\Phi m = \int_X \varphi(x) dm(x)$ , with  $\mathcal{M}(X)$  the space of Radon measures and  $\mathcal{H}$  a separable Hilbert space whose scalar product is denoted  $\langle \cdot, \cdot \rangle_{\mathcal{H}}$ . One has  $y = y_0 + w = \Phi m_{a_0, \bar{x}_0} + w$ . The noiseless version of  $\mathcal{P}_\lambda(y)$  is the basis pursuit for measures

$$\min_{m \in \mathcal{M}(X)} \{|m|(X) ; \Phi m = y_0\}. \quad (\mathcal{P}_0(y_0))$$

The main goal of this chapter is to provide an asymptotic analysis of  $\mathcal{P}_\lambda(y)$  of support recovery when the spikes of  $m_{a_0, \bar{x}_0}$  are positive.

### 1.1.1 BLASSO Performance Analysis

In order to quantify the recovery performance of the methods  $\mathcal{P}_0(y_0)$  and  $\mathcal{P}_\lambda(y)$ , the following two questions arise:

1. Does the solutions of  $\mathcal{P}_0(y_0)$  recover the input measure  $m_{a_0, \bar{x}_0}$  ?
2. How “close” is the solution of  $\mathcal{P}_\lambda(y)$  to the solution of  $\mathcal{P}_0(y_0)$  and what definition of close one has to use ?

When the amplitudes of the spikes are arbitrary complex numbers, the answers to the above questions require a large enough minimum separation distance  $\Delta(\bar{x}_0)$  between the spikes where:

$$\Delta(\bar{x}_0) \stackrel{\text{def.}}{=} \min_{i \neq j} d_X(\bar{x}_{0,i}, \bar{x}_{0,j}). \quad (1.1.1)$$

where  $d_X$  is a canonical distance on  $X$  *i.e.* for example:

$$\forall x, x' \in \mathbb{R}^d, \quad d_X(x, x') = \|x - x'\|, \quad (1.1.2)$$

when  $X = \mathbb{R}^d$ , or:

$$\forall x, x' \in \mathbb{T}^d, \quad d_X(x + \mathbb{Z}^d, x' + \mathbb{Z}^d) = \min_{k \in \mathbb{Z}^d} \|x - x' + k\|, \quad (1.1.3)$$

when  $X = \mathbb{T}^d$ .

The first question is addressed in [30] where the authors showed, in the case of  $\Phi$  being the ideal low-pass filter on the torus, *i.e.* when  $X = \mathbb{T}$ ,  $\mathcal{H} = L^2(\mathbb{T})$  and

$$\forall x \in X, \quad \varphi(x) = \psi(\cdot - x) \quad \text{where} \quad \psi(t) = \sum_{k=-f_c}^{f_c} e^{2i\pi kt},$$

that  $m_{a_0, \bar{x}_0}$  is the unique solution of  $\mathcal{P}_0(y_0)$  provided that  $\Delta(\bar{x}_0) \geq \frac{C}{f_c}$  where  $C > 0$  is a universal constant and  $f_c$  the cutoff frequency of the ideal low-pass filter. In the same paper, it is shown that  $C \leq 2$  when  $a_0 \in \mathbb{C}^N$  and  $C \leq 1.87$  when  $a_0 \in \mathbb{R}^N$ . In [65], the author proved that  $C \leq 1.26$ . And we know from [54] that necessarily  $C \geq \frac{1}{2}$ .

The second question receives partial answers in [7, 24, 29, 64]. In [24], it is shown that if the solution of  $\mathcal{P}_0(y_0)$  is unique then the measures recovered by  $\mathcal{P}_\lambda(y)$  converge in the weak-\* sense to the solution of  $\mathcal{P}_0(y_0)$  when  $\lambda \rightarrow 0$  and  $\|w\|_{\mathcal{H}}^2 / \lambda \rightarrow 0$ . In [29], the authors measure the reconstruction error using the  $L^1$  norm of an ideal low-pass filtered version of the recovered measures. In [7, 64], error bounds are given on the locations of the recovered spikes with respect to those of the input measure  $m_{a_0, \bar{x}_0}$ . However, those works provide little information about the structure of the measures recovered by  $\mathcal{P}_\lambda(y)$ . That point is addressed in [54] where the authors show that under the *Non Degenerate Source Condition* (see Section 5 for more details), there exists a unique solution to  $\mathcal{P}_\lambda(y)$  with the exact same number of spikes as the original measure provided that  $\lambda$  and  $\|w\|_{\mathcal{H}} / \lambda$  are small enough. Moreover in that regime, this solution converges to the original measure when the noise drops to zero.

The major information to recall when studying the recovery of measures  $m_{a_0, \bar{x}_0}$  composed of a sum of Dirac masses with no assumptions on  $a_0$  other than  $a_0 \in \mathbb{R}^N$  or  $a_0 \in \mathbb{C}^N$ , is that to guarantee the recovery of the support, the spikes must be separated enough. Thus destroying any hope to perform super-resolution (*i.e.* separate two or more point sources as close as possible).

### 1.1.2 BLASSO for Positive Spikes

For positive spikes (*i.e.*  $a_{0,i} > 0$ ), the picture is radically different, since exact recovery of  $m_{a_0, \bar{x}_0}$  without noise (*i.e.*  $(w, \lambda) = (0, 0)$ ) holds whatever  $\Delta(\bar{x}_0) > 0$  (provided sum injectivity assumption), see for instance [42]. This means that one can expect to solve, in this particular setting of positive measures, the problem of super-resolution mentioned in Section . To emphasize this ability, we choose from now on (in this framework of positive measures) to write  $m_{a_0, \bar{x}_0}$  as:

$$m_{a_0, t z_0} = \sum_{i=1}^N a_{0,i} \delta_{t z_{0,i}},$$

where for all  $i \in \{1, \dots, N\}$ ,  $t z_{0,i} \in X$  and  $a_{0,i} > 0$ . The parameter  $t > 0$  is used to bring closer as much as we want the spikes of  $m_{a_0, t z_0}$ . As mentioned above, one can then solve  $\mathcal{P}_0(y_{0,t})$  and recover  $m_{a_0, t z_0}$  when  $t \rightarrow 0$ . However the problem gets harder and harder because stability constants explode. As a result in presence of noise, there is a tradeoff between the noise level and  $t \rightarrow 0$  (the spikes infinitely close). We propose to investigate this relation in Chapter 1 and Chapter 3 in the context of support recovery, thus responding to the open problem of super-resolution with noise on the data:

- find a sufficient (and if possible necessary) condition on the noise level  $\|w\|_{\mathcal{H}}$  with respect to  $t$  to guarantee the recovery of two (or more) positive spikes separated by a distance proportional to  $t$  (with  $t \rightarrow 0$ ).

A recent work [113] shows that stable recovery is obtained if the signal-to-noise ratio grows faster than  $O(1/t^{2N})$ , closely matching optimal lower bounds of  $O(1/t^{2N-1})$  obtained by combinatorial methods, as also proved recently [45]. Our main contribution is to show that the same  $O(1/t^{2N-1})$  signal-to-noise scaling in fact guarantees a perfect support recovery of the spikes under a certain non-degeneracy condition on the filter. This extends, for positive measures, the initial results of [54] by providing an asymptotic analysis when  $t \rightarrow 0$ .

**MUSIC and related methods.** There is a large body of literature in signal processing on spectral methods to perform spikes location from low frequency measurements. One of the most popular methods is MUSIC (for MULTiple Signal Classification) [130] and we refer to [100] for an overview of its use in signal processing for line spectral estimation. In the noiseless case, exact reconstruction of the initial signal is guaranteed as long as there are enough observations compared to the number of distinct frequencies [106]. Stability to noise is known to hold under a minimum separation distance similar to the one of the BLASSO [106]. However, on sharp contrast with the behavior of the BLASSO, numerical observations (see for instance [39]), as well as a recent work of Demanet and Nguyen, show that this stability continues to hold regardless of the sign of the amplitudes  $a_{0,i}$ , as soon as the signal-to-noise ratio scales like  $O(1/t^{2N-1})$ . Note that this matches (when  $w$  is a Gaussian white noise) the Cramer-Rao lower bound achievable by any unbiased estimator [18]. This class of methods are thus more efficient than BLASSO for arbitrary measures, but they are restricted to operators  $\Phi$  that are convolutions with a low-pass filter, which is not the case of our analysis for the BLASSO.

### 1.1.3 Contributions

In Section 1.2, we prove a convergence result between pre-certificates (see Proposition 4) in a general setting (dimension  $d$  and low assumption on the kernel  $\varphi$ ) which leads to a new proof (constructive) of the main result of [54] (Theorem 2) on the support recovery in a low noise regime when solving the BLASSO.

In Section 1.3, Theorem 2 shows that the vanishing derivatives pre-certificate  $\eta_V$  is non-degenerate if the spikes of the initial measure are separated enough.

Section 1.4 defines a new pre-certificate for the study of the BLASSO in a 1 dimensional framework: the  $(2N-1)$ -vanishing derivatives pre-certificate  $\eta_W$ . It is a crucial object in this Thesis because it controls the recovery of the support in presence of noise when the spikes of the initial measure get closer and closer. We show that  $\eta_{V,t}$  converges towards  $\eta_W$  when the spikes collapse at 0 (see Proposition 9).

The main contribution of Section 1.5 is Theorem 3 which proves that any pre-certificate close enough of  $\eta_W$  is non-degenerate provided that  $\eta_W$  is itself non-

degenerate. The appropriate notion of degeneracy for  $\eta_W$  in order to obtain this result is also defined in this Section. One finally proves using the convergence of  $\eta_{V,t}$  towards  $\eta_W$  that one can perform the recovery of the support in a domain (unknown) in  $(\lambda, w)$  when the spikes of the initial measure collapse at 0 (see Proposition [10]).

## 1.2 A Primer on Certificates for Super-Resolution

In this Section, the goal is to set up some definitions for the rest of this thesis but also to present some tools introduced in [54] which are the starting point of what is presented in Part II of this thesis. Our main contribution in this Section consists in Proposition 4 where we prove a convergence result between pre-certificates. This leads to a new constructive proof of Theorem 1 (see Remark 2 at the end of this Section for the main differences between our approach here and the one of [54] (Theorem 2)). This new proof corresponds to a reasoning which is, in its core, similar to the one that we use later in Chapter 3 to prove our main contribution of Part II. As a result, we see this Section as a warm-up for what is coming next.

Before going any further, let us give some formal definitions that set up the general framework of this thesis.

### Measures.

**Definition 1** (Set  $X$  of positions of spikes). *The set of positions of spikes, denoted  $X$ , is supposed to be a set such that  $\overset{\circ}{X}$  is a smooth manifold of dimension  $d \in \mathbb{N}^*$ . In particular  $X$  is locally compact.*

Definition 1 covers the particular case of  $X = \mathbb{R}^d$ ,  $X = \mathbb{T}^d$  or any compact subset with non-empty interior of  $\mathbb{R}^d$ .

**Definition 2** (Continuous functions on  $X$ ). *We denote by  $\mathcal{C}_0(X, \mathcal{H})$  the set of continuous functions that vanish at infinity i.e.*

$$\forall \varepsilon > 0, \exists K \subset X \text{ compact}, \quad \sup_{x \in X \setminus K} \|\varphi(x)\|_{\mathcal{H}} \leq \varepsilon,$$

and by  $\mathcal{C}_0^k(X, \mathcal{H})$  the set of continuous functions that vanish at infinity and  $k$ -times differentiable on  $X$ . Note that when  $X$  is compact,  $\mathcal{C}_0(X, \mathcal{H})$  is just the set  $\mathcal{C}(X, \mathcal{H})$  of continuous functions on  $X$ .

Now we can define rigorously the space of real bounded Radon measures on  $X$  using the Riesz representation theorem.

**Definition 3** (Set  $\mathcal{M}(X)$  of Radon measures). *We denote by  $\mathcal{M}(X)$  the set of real bounded Radon measures on  $X$  which is the topological dual of  $\mathcal{C}_0(X, \mathbb{R})$  endowed with  $\|\cdot\|_{\infty, X}$  (the supremum norm for functions defined on  $X$ ). It is also the set of regular real Borel measures with finite total mass on  $X$ .*

See [123] for more details on Radon measures.

**Kernels.** This paragraph details the assumptions that we use in the following on the kernel  $\varphi$ . We recall that the operator modeling the alteration process of the acquisition of the source signal  $\Phi : \mathcal{M}(X) \rightarrow \mathcal{H}$  has the form:

$$\forall m \in \mathcal{M}(X), \quad \Phi m \stackrel{\text{def.}}{=} \int_X \varphi(x) dm(x), \quad (1.2.1)$$

For this to be valid and have a meaning but also to prove our results in the rest of this thesis, we need to make some assumptions concerning the kernel  $\varphi$ . Given the previous paragraph where we defined Radon measures, a readily requirement for  $\varphi$  is its belonging to  $\mathcal{C}_0(X, \mathcal{H})$ . We list in the following definition the other assumptions that an admissible kernel  $\varphi$  must verify.

**Definition 4** (Admissible kernels  $\varphi$ ). *We denote by  $\text{KER}^{(k)}$ , the set of admissible kernels of order  $k$ . A function  $\varphi : X \rightarrow \mathcal{H}$  belongs to  $\text{KER}^{(k)}$  if:*

- $\varphi \in \mathcal{C}^k(X, \mathcal{H})$ ,
- For all  $p \in \mathcal{H}$ ,  $x \in X \mapsto \langle \varphi(x), p \rangle_{\mathcal{H}}$  vanishes at infinity,
- for all  $0 \leq i \leq k$ ,  $\sup_{x \in X} \|D^i \varphi(x)\| < +\infty$ .

where  $D^i \varphi$  is the  $i$ -th differential of  $\varphi$ .

In the remaining of this Section, we take  $X$  as in Definition [I], we suppose that  $\varphi \in \text{KER}^{(2)}$  and we consider the BLASSO:

$$\min_{m \in \mathcal{M}(X)} \frac{1}{2} \|\Phi m - y\|_{\mathcal{H}}^2 + \lambda |m|(X), \quad (\mathcal{P}_{\lambda}(y))$$

where we recall the notation:

$$y \stackrel{\text{def.}}{=} \Phi m_{a_0, \bar{x}_0} + w \quad \text{with} \quad m_{a_0, \bar{x}_0} = \sum_{i=1}^N a_{0,i} \delta_{x_{0,i}}. \quad (1.2.2)$$

Moreover we make no assumption on the sign of the amplitudes  $a_0$  and  $x_0 \in \overset{\circ}{X^N}$ . The goal is to find sufficient conditions such that  $\mathcal{P}_{\lambda}(y)$  has a unique solution  $m_{a, \bar{x}}$  composed of exactly the same number of Dirac masses as  $m_{a_0, \bar{x}_0}$ .

First we start by giving the subdifferential of the total variation norm in the next Proposition (see [54] for a proof).

**Proposition 1** (Subdifferential of  $|\cdot|(X)$ ). *The total variation norm  $|\cdot|(X)$  is convex and lower semi-continuous with respect to the weak-\* topology so its subdifferential is non-empty at any  $m \in \mathcal{M}(X)$  and is given by:*

$$\partial|m|(X) = \left\{ \eta \in \mathcal{C}_0(X, \mathbb{R}); \|\eta\|_{\infty, X} \leq 1 \quad \text{and} \quad \int_X \eta dm = |m|(X) \right\}.$$

In particular for a discrete measure  $m_{a, \bar{x}}$ , one has:

$$\partial|m_{a, \bar{x}}|(X) = \left\{ \eta \in \mathcal{C}_0(X, \mathbb{R}); \|\eta\|_{\infty, X} \leq 1 \quad \text{and} \quad \forall i, \eta(x_i) = \text{sign}(a_i) \right\}.$$

From Proposition [I], we can then characterize discrete measures solutions of the BLASSO. This is the aim of the next Proposition.

**Proposition 2.** A discrete measure  $m_{a,\bar{x}} = \sum_{i=1}^n a_i \delta_{x_i}$  is solution of  $\mathcal{P}_\lambda(y)$  if and only if:

$$\|\eta_\lambda\|_{\infty,X} \leq 1 \quad \text{and} \quad \forall i, \eta(x_i) = \text{sign}(a_i). \quad (1.2.3)$$

where

$$\eta_\lambda \stackrel{\text{def.}}{=} \Phi^* p_\lambda \quad \text{with} \quad p_\lambda \stackrel{\text{def.}}{=} \frac{1}{\lambda} (y - \Phi m_{a,\bar{x}}), \quad (1.2.4)$$

*Proof.* Applying the Fermat's rule leads to  $m_{a,\bar{x}}$  solution of  $\mathcal{P}_\lambda(y)$  if and only if:

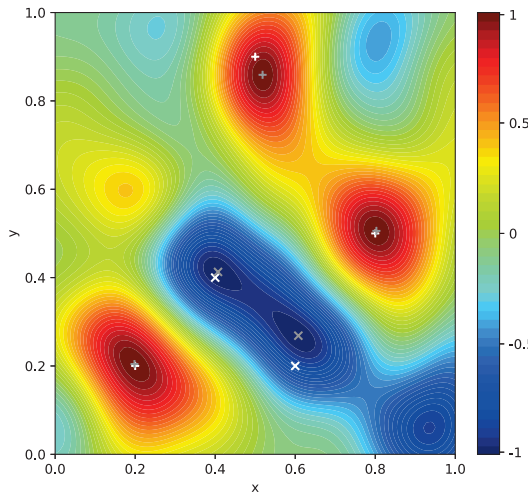
$$\eta_\lambda \stackrel{\text{def.}}{=} \Phi^* p_\lambda \in \partial|m_{a,\bar{x}}|(X). \quad (1.2.5)$$

Then using the expression of the subdifferential of the total variation norm for a discrete measure  $m_{a,\bar{x}}$  given in Proposition 1, gives the expected result.  $\square$

We recall that the adjoint of  $\Phi$  i.e.  $\Phi^* : \mathcal{H} \rightarrow \mathcal{C}_0(X, \mathbb{R})$  is given by:

$$\forall p \in \mathcal{H}, \quad \forall x \in X, \quad (\Phi^* p)(x) = \langle \varphi(x), p \rangle_{\mathcal{H}}.$$

See Figure 1.1 for an example of  $\eta_\lambda$  in a 2D setting. In particular it illustrates the statement of Proposition 2.



(a)  $\eta_\lambda$  in 2D for a Gaussian with  $\sigma = 0.1$

Figure 1.1: Illustration of  $\eta_\lambda$  for a Gaussian convolution in  $\mathbb{R}^2$ . White (rest. gray) markers corresponds to the spikes of  $m_{a_0, \bar{x}_0}$  (resp.  $m_{a, \bar{x}}$ ). A "+" (resp "x") is for a positive (resp. negative) spikes.  $m_{a, \bar{x}}$  is a solution of  $\mathcal{P}_\lambda(y)$  and we see that  $\|\eta_\lambda\|_{\infty,X} \leq 1$ .

*Remark 1.* If  $\eta_\lambda$  satisfies  $\|\eta_\lambda\|_{\infty,X} \leq 1$  and for all  $i \in \{1, \dots, n\}$ ,  $\eta_\lambda(x_i) = \text{sign}(a_i)$  then one obtains  $\nabla \eta_\lambda(x_i) = 0$ . The converse is of course wrong but the conditions:

$$\forall i \in \{1, \dots, n\}, (\lambda \eta_\lambda)(x_i) = \lambda \text{sign}(a_i) \quad \text{and} \quad \nabla(\lambda \eta_\lambda)(x_i) = 0, \quad (1.2.6)$$

are much more tractable than:

$$\forall i \in \{1, \dots, n\}, (\lambda \eta_\lambda)(x_i) = \lambda \text{sign}(a_i) \quad \text{and} \quad \|\eta_\lambda\|_{\infty,X} \leq 1,$$

because  $\|\eta_\lambda\|_{\infty,X} \leq 1$  involves an “infinite” number of inequalities.

We have characterized the solutions of  $\mathcal{P}_\lambda(y)$  using  $\eta_\lambda$ , which in turn satisfies some linear equations (1.2.6). Our approach is to show that a measure  $m_{a,\bar{x}}$  built by solving these linear equations for a given  $(\lambda, w)$  has its  $\eta_\lambda$  verifying the optimality condition (1.2.5) (provided some assumptions).

First note that  $m_{a_0,\bar{x}_0}$  is a solution of the BLASSO when  $(\lambda, w) = (0, 0)$ . Moreover in this case, one has:

$$\forall i \in \{1, \dots, N\}, (\lambda \eta_\lambda)(x_{0,i}) = \lambda \text{sign}(a_{0,i}) \quad \text{and} \quad \nabla(\lambda \eta_\lambda)(x_{0,i}) = 0.$$

Therefore we may parametrize, using the Implicit Function Theorem, the solutions of Equations 1.2.6 in a neighborhood  $V$  of  $(0, 0)$  in  $\mathbb{R} \times \mathcal{H}$  by a function  $g \in \mathcal{C}^1(V, \mathbb{R}^N \times X^N)$ , such that for all  $(\lambda, w) \in V$ ,  $(a, \bar{x}) = g(\lambda, w)$  if and only if  $\eta_\lambda$  (for  $m_{a,\bar{x}}$ ) satisfies the Equations 1.2.6. This is shown in the next proposition.

But before continuing, we detail a few notations that we use very often in the remaining of this thesis. Given  $\bar{x} = (x_1, \dots, x_N) \in X^N$ , we denote by  $\Phi_{\bar{x}} : \mathbb{R}^N \rightarrow \mathcal{H}$  the linear operator such that:

$$\forall a \in \mathbb{R}^N, \quad \Phi_{\bar{x}}(a) \stackrel{\text{def}}{=} \sum_{i=1}^N a_i \varphi(x_i), \quad (1.2.7)$$

and by  $\Gamma_{\bar{x}} : (\mathbb{R}^N \times \underbrace{\mathbb{R}^N \times \cdots \times \mathbb{R}^N}_d) \rightarrow \mathcal{H}$  the linear operator defined by:

$$\forall (a, b_1, \dots, b_d) \in \mathbb{R}^N \times (\mathbb{R}^N)^d, \quad \Gamma_{\bar{x}} \begin{pmatrix} a \\ b_1 \\ \vdots \\ b_d \end{pmatrix} \stackrel{\text{def}}{=} \sum_{i=1}^N \left( a_i \varphi(x_i) + \sum_{j=1}^d b_{j,i} \partial_j \varphi(x_i) \right). \quad (1.2.8)$$

One can also write

$$\Gamma_{\bar{x}} = \left( \Phi_{\bar{x}} \ (\Phi_{\bar{x}})^{(1)} \right) \quad (1.2.9)$$

where  $(\Phi_{\bar{x}})^{(1)}$  (also denoted sometimes  $\Phi_{\bar{x}}'$ ) stacks all the first order derivatives of  $\varphi$  for the different positions  $x_i$  (one can also define in the same way  $(\Phi_{\bar{x}})^{(k)}$  for  $k \geq 1$ ).

**Proposition 3.** Suppose that  $\Gamma_{\bar{x}_0}$  has full column rank. Then there exists neighborhoods  $V$  and  $U$  of respectively  $(0,0)$  in  $\mathbb{R} \times \mathcal{H}$  and  $(a_0, x_0)$  in  $\mathbb{R}^N \times X^N$ , and  $g \in \mathcal{C}^1(V, U)$  such that:

$$\begin{aligned} (a, \bar{x}, \lambda, w) \in U \times V \text{ and Equations (1.2.6)} &\text{ are satisfied} \\ \Leftrightarrow \\ (\lambda, w) \in U \text{ and } (a, \bar{x}) = g(\lambda, w). \end{aligned}$$

*Proof.* Consider:

$$E(a, \bar{x}, \lambda, w) = \left( \Phi_{\bar{x}}^*(y - \Phi m_{a, \bar{x}}) - \lambda \operatorname{sign}(a), (\Phi_{\bar{x}}^*)^{(1)}(y - \Phi m_{a, \bar{x}}) \right), \quad (1.2.10)$$

$$= \Gamma_{\bar{x}}^* \left( y - \Gamma_{\bar{x}} \begin{pmatrix} a \\ 0 \end{pmatrix} \right) - \lambda \begin{pmatrix} \operatorname{sign}(a) \\ 0 \end{pmatrix}. \quad (1.2.11)$$

Then it is a  $\mathcal{C}^1$  function in a neighborhood of  $(a_0, \bar{x}_0)$  because  $\varphi \in \operatorname{KER}^{(2)}$ , and  $E(a, \bar{x}, \lambda, w) = 0$  if and only if Equations 1.2.6 are satisfied. One can check that:

$$\frac{\partial E}{\partial (a, \bar{x})}(a_0, \bar{x}_0, 0, 0) = \Gamma_{\bar{x}_0}^* \Gamma_{\bar{x}_0} \begin{pmatrix} Id_N & 0 \\ 0 & D_{a_0} \end{pmatrix}$$

where  $D_{a_0}$  is a diagonal matrix whose coefficients are  $a_0$  repeated  $d$ -times ( $D_{a_0} \in \mathbb{R}^{dN \times dN}$ ,  $d$  is the dimension of  $X$ ). Therefore if  $\Gamma_{\bar{x}_0}$  has full column rank then  $\frac{\partial E}{\partial (a, \bar{x})}$  is invertible and one can apply the Implicit Function Theorem and get the expected conclusion.  $\square$

Hence we have, for values of  $(\lambda, w)$  small enough, a measure  $m_{a, \bar{x}}$  (not yet solution of  $\mathcal{P}_\lambda(y)$ ) composed of exactly the same number of spikes as  $m_{a_0, \bar{x}_0}$  such that  $(a, \bar{x}) = g(\lambda, w)$  where  $g$  is  $\mathcal{C}^1$  and for all  $i \in \{1, \dots, N\}$ ,  $\eta_\lambda(x_i) = \operatorname{sign}(a_i)$  and  $\nabla \eta_\lambda(x_i) = 0$  (if  $\lambda \neq 0$ ). In particular, this means that if we are able to prove that  $\|\eta_\lambda\|_{\infty, X} \leq 1$  then automatically  $m_{a, \bar{x}}$  is a solution of the BLASSO.

It turns out that  $p_\lambda$ , defined from  $m_{a, \bar{x}}$  where  $(a, \bar{x}) = g(\lambda, w)$  i.e.  $(a, \bar{x}, \lambda, w)$  verifies Equations 1.2.6, converges in  $\mathcal{H}$  towards some particular  $p_V \in \mathcal{H}$  when  $\max \left( \lambda, \frac{\|w\|_{\mathcal{H}}}{\lambda} \right) \rightarrow 0$ . This means that we may asymptotically obtain information on  $\eta_\lambda = \Phi^* p_\lambda$  (and show  $\|\eta_\lambda\|_{\infty, X} \leq 1$ ) from properties of  $\eta_V \stackrel{\text{def.}}{=} \Phi^* p_V$ . But first let us define  $\eta_V$ .

Following [54] (Section 4.1, Definition 6), we introduce below the so called *vanishing derivatives pre-certificate*  $\eta_V$ , which is a function defined on  $X$  that interpolates the spikes positions and signs with a minimal norm feature. Note that  $\eta_V$  can be computed in closed form by solving the linear system 1.2.12. See Figure 1.2 for an example of  $\eta_V$  in 2D.

**Definition 5** (Vanishing Derivatives Precertificate, [54]). If  $\Gamma_{\bar{x}_0}$  has full column rank, there is a unique solution to the problem

$$\inf \left\{ \|p\|_{\mathcal{H}} ; \forall i = 1, \dots, N, (\Phi^* p)(x_{0,i}) = \operatorname{sign}(a_{0,i}), (\Phi^* p)'(x_{0,i}) = 0_{(\mathbb{R}^N)^d} \right\}.$$

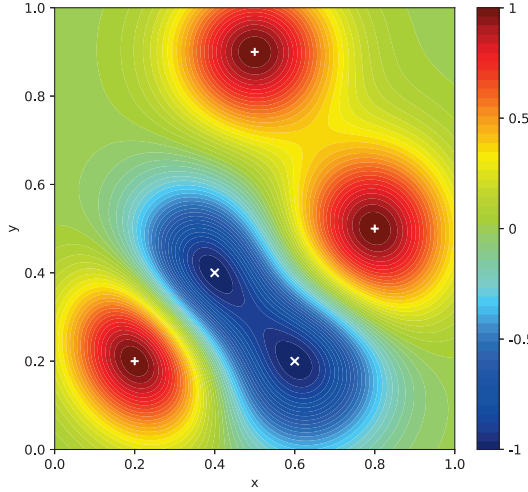
(a)  $\eta_V$  in 2D for a Gaussian with  $\sigma = 0.1$ 

Figure 1.2: Illustration of  $\eta_V$  for a Gaussian convolution in  $\mathbb{R}^2$ . White markers corresponds to the spikes of  $m_{a_0, \bar{x}_0}$ . A "+" (resp "x") is for a positive (resp. negative) spike.  $\eta_V$  satisfies the requirements of Definition 6 (non-degeneracy).

Its solution  $p_V$  is given by

$$p_V = \Gamma_{\bar{x}_0}^{+,*} \begin{pmatrix} \text{sign}(a_0) \\ 0_{\mathbb{R}^d} \end{pmatrix}, \quad (1.2.12)$$

where  $\Gamma_{\bar{x}_0}^+ = (\Gamma_{\bar{x}_0}^* \Gamma_{\bar{x}_0})^{-1} \Gamma_{\bar{x}_0}^*$  is the pseudo-inverse of  $\Gamma_{\bar{x}_0}$ , and we define the vanishing derivatives precertificate as  $\eta_V \stackrel{\text{def.}}{=} \Phi^* p_V$ .

Remark that  $\eta_V$  only depends on the initial measure  $m_{a_0, \bar{x}_0}$  and the kernel  $\varphi$ .

The next Proposition shows, that indeed  $p_\lambda$  converges towards  $p_V$  when  $\lambda$  and  $w$  get smaller with a sufficient signal to noise ratio.

**Proposition 4** ( $p_\lambda \rightarrow p_V$ ). *If  $\Gamma_{\bar{x}_0}$  has full column rank and  $\eta_\lambda = \Phi^* p_\lambda$  is defined as in Equation (1.2.4) where  $(a, \bar{x}) = g(\lambda, w)$  as in Proposition 3 then one has:*

$$p_\lambda \xrightarrow{\max(\lambda, \frac{\|w\|_{\mathcal{H}}}{\lambda}) \rightarrow 0} p_V.$$

In particular  $\eta_\lambda$  converges towards  $\eta_V$  for  $\|\cdot\|_{\infty, X}$  and for  $k \in \{0, 1, 2\}$ :

$$\sup_{x \in X} \|D^k \eta_\lambda(x) - D^k \eta_V(x)\| \xrightarrow{\max(\lambda, \frac{\|w\|_{\mathcal{H}}}{\lambda}) \rightarrow 0} 0.$$

*Proof.* Suppose that  $(\lambda, w) \in V$  and  $(a, \bar{x}) = g(\lambda, w)$ . Then from Equation [1.2.11], we deduce that:

$$\begin{pmatrix} a \\ 0 \end{pmatrix} = \Gamma_{\bar{x}}^{+,*} y - \lambda (\Gamma_{\bar{x}}^* \Gamma_{\bar{x}})^{-1} \begin{pmatrix} \text{sign}(a) \\ 0 \end{pmatrix},$$

hence:

$$\begin{aligned} p_\lambda &= \frac{1}{\lambda} \left( y - \Gamma_{\bar{x}} \Gamma_{\bar{x}}^{+,*} y + \lambda \Gamma_{\bar{x}}^{+,*} \begin{pmatrix} \text{sign}(a) \\ 0 \end{pmatrix} \right), \\ &= p_V + \left( \Gamma_{\bar{x}}^{+,*} \begin{pmatrix} \text{sign}(a) \\ 0 \end{pmatrix} - p_V \right) + (\Gamma_{\bar{x}_0} - \Gamma_{\bar{x}} \Gamma_{\bar{x}}^{+,*} \Gamma_{\bar{x}_0}) \begin{pmatrix} a_0 \\ 0 \end{pmatrix} + \Pi_{\bar{x}} \frac{w}{\lambda}, \end{aligned}$$

where  $\Pi_{\bar{x}} = \text{Id} - \Gamma_{\bar{x}} \Gamma_{\bar{x}}^{+,*}$  is an orthogonal projection of  $\mathcal{H}$ . We have that:

$$\left\| \Gamma_{\bar{x}}^{+,*} \begin{pmatrix} \text{sign}(a) \\ 0 \end{pmatrix} - p_V \right\|_{\mathcal{H}} \rightarrow 0 \quad \text{and} \quad \left\| \Gamma_{\bar{x}_0} - \Gamma_{\bar{x}} \Gamma_{\bar{x}}^{+,*} \Gamma_{\bar{x}_0} \right\| \rightarrow 0,$$

when  $(\lambda, w) \rightarrow (0, 0)$  by continuity at  $(0, 0)$  of the implicit function  $g$ . Therefore, because  $\|\Pi_{\bar{x}}\| \leq 1$ , we deduce that:

$$\|p_\lambda - p_V\|_{\mathcal{H}} \rightarrow 0,$$

when  $(\lambda, \|w\|_{\mathcal{H}}/\lambda) \rightarrow 0$ .  $\square$

Figure [1.3] illustrates the convergence mentioned in the previous proposition in the case of the Dirichlet kernel.

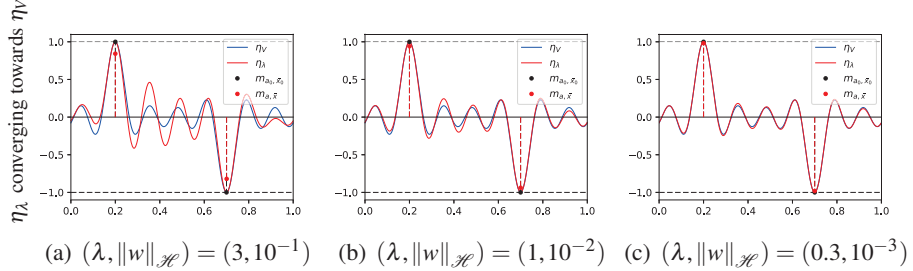


Figure 1.3: Illustration of convergence of  $\eta_{\lambda,t}$  towards  $\eta_V$ , as in Proposition 4, in the case of  $\Phi$  the ideal low pass filter i.e. :  $X = \mathbb{T}$ ,  $\mathcal{H} = L^2(\mathbb{T})$ ,  $\varphi$  is the Dirichlet kernel with cutoff frequency  $f_c = 8$ .

Proposition 4 is crucial to prove the transfer of properties from  $\eta_V$  to  $\eta_\lambda$ . The following definition gives an assumption on  $\eta_V$  in order to prove that  $\|\eta_\lambda\|_{\infty,X} \leq 1$ .

**Definition 6** (Non-Degeneracy of  $\eta_V$ ). *We say that  $\eta_V$  is non-degenerate if:*

$$\begin{cases} \forall x \in X \setminus \bigcup_{i=1}^N \{x_{0,i}\}, \quad |\eta_V(x)| < 1, \\ \forall i \in \{1, \dots, N\}, \quad \det(D^2 \eta_V(x_{0,i})) \neq 0. \end{cases} \quad (1.2.13)$$

where  $D^2 \eta_V(x_{0,i}) \in \mathbb{R}^{d \times d}$  is the Hessian of  $\eta_V$  at  $x_{0,i}$ .

Figure 1.2 shows a case where  $\eta_V$  is non-degenerate. However in Figure 1.4,  $\eta_V$  is degenerate because two of the spikes of  $m_{a_0, \bar{x}_0}$  are not separated enough.

This non-degeneracy assumption on  $\eta_V$  together with Proposition 4 lead to the proof of  $\|\eta_\lambda\|_{\infty, X} \leq 1$  for the measure  $m_{a, \bar{x}}$  built using the implicit function theorem. We summarize this result in the next Proposition.

**Proposition 5.** *If  $\Gamma_{\bar{x}_0}$  has full column rank and if  $\eta_V$  is non-degenerate then provided that  $\max\left(\lambda, \frac{\|w\|_{\mathcal{H}}}{\lambda}\right) \leq C$  for some  $C > 0$  one gets:*

$$\begin{cases} \forall x \in X \setminus \bigcup_{i=1}^N \{x_i\}, \quad |\eta_\lambda(x)| < 1, \\ \forall i \in \{1, \dots, N\}, \quad \det(D^2 \eta_\lambda(x_i)) \neq 0, \end{cases} \quad (1.2.14)$$

where  $\eta_\lambda = \Phi^* p_\lambda$  is defined as in Equation (1.2.4) where  $(a, \bar{x}) = g(\lambda, w)$  as in Proposition 3. In particular  $\|\eta_\lambda\|_{\infty, X} \leq 1$  and  $m_{a, \bar{x}}$  is a solution of the BLASSO.

*Proof.* Knowing that  $\eta_V$  is non-degenerate, the aim is to prove that  $\|\eta_\lambda\|_{\infty, X} \leq 1$  for  $m_{a, \bar{x}}$  with  $(a, \bar{x}) = g(\lambda, w)$  provided sufficient conditions on  $(\lambda, w)$ .

We know from Proposition 4 that if  $\max(\lambda, \|w\|_{\mathcal{H}} / \lambda) \leq C_1$  for some  $C_1 > 0$  then:

$$\forall i \in \{1, \dots, N\}, \quad \det(D^2 \eta_\lambda(x_i)) \neq 0,$$

because  $\eta_V$  is non-degenerate thus  $\det(D^2 \eta_\lambda(x_{0,i})) \neq 0$  by Proposition 4. Therefore, since  $\eta_\lambda(x_i) = \text{sign}(a_i)$  and  $\nabla \eta_\lambda(x_i) = 0$ , we deduce that  $|\eta_\lambda| < 1$  in a neighborhood  $V_i$  of the  $x_i$  for all  $i \in \{1, \dots, N\}$  (except of course at  $x_i$ ).

Finally using again Proposition 4 with the uniform convergence of  $\eta_\lambda$  towards  $\eta_V$ , if  $\max(\lambda, \|w\|_{\mathcal{H}} / \lambda) \leq C_2$  for some  $C_2 > 0$  then:

$$\forall x \in X \setminus \bigcup_{i=1}^N V_i, \quad |\eta_\lambda(x)| < 1,$$

because  $\eta_V$  is non-degenerate thus  $|\eta_V| < 1$  on this set. Taking  $C = \min(C_1, C_2)$ , we obtain the expected result.  $\square$

The previous Proposition proves that if  $\eta_V$  is non-degenerate then  $\|\eta_{\lambda,t}\|_{\infty, X} \leq 1$  which certifies the recovery of the support. However if  $\eta_V$  is degenerate, there may still exist  $m_{a, \bar{x}}$  composed of  $N$  spikes with  $\|\eta_{\lambda,t}\|_{\infty, X} \leq 1$ . This is shown in Figure 1.4.

As a byproduct of this detailed analysis of the convergence of the certificate  $\eta_\lambda$ , we can recover the result of [54] (Theorem 2), but using a very different constructive proof (whereas [54] used compactness arguments). This new proof is important because it is at the heart of our analysis in Chapter I to obtain quantitative super-resolution results as the spikes get close one from each other.

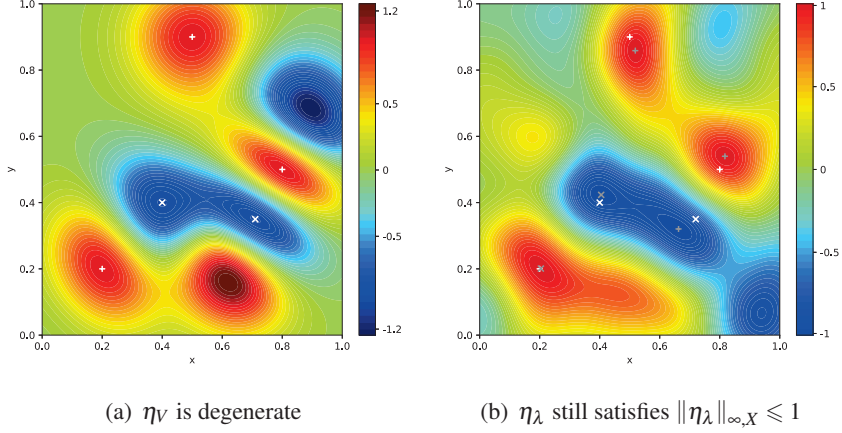


Figure 1.4: Illustration that  $\eta_V$  is not always non-degenerate. Here the spikes at  $(0.72, 0.35)$  and  $(0.8, 0.5)$  are of opposite signs and are too close w.r.t the size of the PSF resulting in oscillations going above 1 in absolute value. However we still recover the support of  $m_{a_0, \bar{x}_0}$  because  $\|\eta_\lambda\|_{\infty,X} \leq 1$  for the measure with gray markers.

**Theorem 1** (Exact Support Recovery). *Assume that  $\varphi \in \text{KER}^{(2)}$ ,  $\Gamma_{\bar{x}_0}$  has full column rank and  $\eta_V$  is non-degenerate. Then there exists  $C > 0$  such that if  $(\lambda, w) \in \mathbb{R}_+^* \times \mathcal{H}$  satisfies:*

$$\max\left(\lambda, \frac{\|w\|_{\mathcal{H}}}{\lambda}\right) \leq C,$$

*then there is a unique solution  $m_{a,\bar{x}}$  to  $\mathcal{P}_\lambda(y)$  composed of  $N$  Dirac masses such that  $(a, \bar{x}) = g(\lambda, w)$  where  $g$  is  $\mathcal{C}^1$ . In particular, by taking the regularization parameter  $\lambda = 1/C \|w\|_{\mathcal{H}}$  proportional to the noise level, one obtains:*

$$|(a, \bar{x}) - (a_0, x_0)|_\infty = O(\|w\|_{\mathcal{H}}),$$

*where  $|\cdot|_\infty$  is the  $\ell^\infty$  norm for vectors.*

*Proof.* The existence of a solution  $m_{a,\bar{x}}$  composed of the same number of spikes as the initial measures, for  $\max(\lambda, \|w\|_{\mathcal{H}}/\lambda) \leq C$ , comes from Proposition 5.

For the uniqueness, we consider the dual problem of  $\mathcal{P}_\lambda(y)$ :

$$\max_{\|\Phi^* p\|_{\infty,X} \leq 1} \langle y, p \rangle_{\mathcal{H}} - \frac{\lambda}{2} \|p\|_{\mathcal{H}}^2,$$

which can be reformulated as follows:

$$\max_{\|\Phi^* p\|_{\infty,X} \leq 1} \left\| \frac{y}{\lambda} - p \right\|_{\mathcal{H}}^2.$$

Since this last problem has a unique solution: the orthogonal projection of  $\frac{y}{\lambda}$  on the closed convex set  $\{p \in \mathcal{H}; \|\Phi^* p\|_{\infty, X} \leq 1\}$ , we get that the dual problem of  $\mathcal{P}_\lambda(y)$  has a unique solution. It is  $p_\lambda = \frac{1}{\lambda}(y - \Phi m_{a, \bar{x}})$  because  $m_{a, \bar{x}}$  is a solution of  $\mathcal{P}_\lambda(y)$  and strong duality holds. Now take any  $m_\lambda$  solution of  $\mathcal{P}_\lambda(y)$ . Then by the optimality conditions, the support of  $m_\lambda$  is included in the saturations points of  $\eta_\lambda$  i.e. the support of  $m_{a, \bar{x}}$ . Let us denote  $\tilde{a} \in \mathbb{R}^N$  the amplitudes of the Dirac masses of  $m_\lambda$ :  $m_\lambda = \sum_{i=1}^N \tilde{a}_i \delta_{x_i}$ . Because  $m_\lambda$  is a solution of  $\mathcal{P}_\lambda(y)$ , one has  $E(\tilde{a}, \bar{x}, \lambda, w) = 0$  so that  $\Phi_{\bar{x}}^* \Phi_{\bar{x}} \tilde{a} = \Phi_{\bar{x}}^* \Phi_{\bar{x}} a$ .  $\Phi_{x_0}^* \Phi_{x_0}$  is invertible because  $\Gamma_{x_0}$  has full column rank. Taking  $C$  smaller if necessary, one can thus assume by continuity of  $g$  that  $\Phi_{\bar{x}}^* \Phi_{\bar{x}}$  is also invertible hence  $\tilde{a} = a$ .

Finally the relation:

$$|(a, \bar{x}) - (a_0, x_0)|_\infty = O(\|w\|_{\mathcal{H}}).$$

is a consequence of the continuity of  $g$  at  $(0, 0)$ .  $\square$

With this theorem, the difficulty of proving that  $\|\eta_\lambda\|_{\infty, X} \leq 1$  for *any*  $m_{a, \bar{x}}$  with  $(a, \bar{x}) = g(\lambda, w)$  is traded with the difficulty of showing that  $\eta_V$  is non-degenerate. However this is a much simpler condition because it only depends on the kernel  $\varphi$  and the initial measure  $m_{a_0, \bar{x}_0}$ . Moreover this theorem shows that  $\eta_V$  governs the support recovery properties of the BLASSO in a low noise regime.

*Remark 2.* It is important to note that the path followed in this Section towards Theorem I is not the one selected in [54]. Although the main ideas are quite similar (implicit function theorem, convergence of  $p_\lambda$ ...), the authors use a more deductive reasoning. Indeed they start with a solution of the BLASSO and then show that this solution must be composed of  $N$  spikes. Instead here, we start with a candidate solution already composed of  $N$  Dirac masses and then show that this is in fact a solution of the problem.

### 1.3 A Result of Non-Degeneracy for $\eta_V$

Before moving to the core of this Chapter (the super-resolution problem), we prove a result of non-degeneracy for  $\eta_V$  provided that the spikes of the initial measure are separated enough.

We consider in this section that  $m_{a_0, x_0} = \sum_{i=1}^N a_{0,i} \delta_{x_{0,i}}$  with  $a_{0,i} \in \mathbb{R}$  and  $x_{0,i} \in X$  where  $X$  is supposed to be unbounded interval of  $\mathbb{R}$ . This choice is made for the sake of simplicity but it can be proved also when  $X$  is as in Definition [I] (dimension  $d \in \mathbb{N}^*$ ) but still unbounded.

We saw in Section [1.2] that if  $\eta_V$  is non-degenerate then  $\mathcal{P}_\lambda(y)$  admits a unique solution composed of exactly the same number of spikes as  $m_{a_0, x_0}$  provided that  $\max(\lambda, \|\frac{w}{\lambda}\|_{\mathcal{H}}) \leq C$  for some constant  $C > 0$ . Moreover the amplitudes and positions of the unique solution of  $\mathcal{P}_\lambda(y)$  are  $\mathcal{C}^1$  functions of the parameters  $\lambda$  and  $w$  if  $\varphi \in \text{KER}^{(2)}$ .

We propose to show here that  $\eta_V$  is non-degenerate provided that the positions  $x_0 = (x_{0,i})_{1 \leq i \leq N}$  of the spikes are separated enough *i.e.*  $\Delta(x_0)$  (see Equation (1.1.1) for the definition) is large enough and some technical assumptions on  $\varphi$ .

A similar result can be found in [15] and used in [13, 14]. The authors have a more quantitative approach by giving an estimation of the constants, in particular the separation of the spikes, with respect to the size of the PSF. The difference with our work is that they did not consider exactly the same certificate (not  $\eta_V$ ). They also made the assumption that the operator  $\Phi$  is a convolution which is not the case here. And finally the authors use the non-degeneracy of their certificate to give a robustness result not for  $\mathcal{P}_\lambda(y)$  but for its discretization on a grid (replacing the TV norm by the  $\ell^1$  norm).

**Theorem 2.** *Let  $X \subset \mathbb{R}$  be an unbounded interval. If the following assumptions are true:*

- (i)  $\varphi \in \mathcal{C}^2(X, \mathcal{H})$ ,
- (ii)  $\varphi, \varphi'$  are not colinear,
- (iii)  $x \in X \mapsto \|D_x^{-1}\|$  where  $D_x = (\varphi(x) \varphi'(x))^*(\varphi(x) \varphi'(x))$  and  $x \in X \mapsto \|\varphi''(x)\|_{\mathcal{H}}$  are bounded above,
- (iv) there exists a function  $\omega : \mathbb{R}_+ \rightarrow \mathbb{R}_+$  satisfying  $\omega(t) \rightarrow 0$  when  $t \rightarrow +\infty$  such that for all  $x, x' \in X$ ,  $|\langle \varphi(x), \varphi(x') \rangle_{\mathcal{H}}|, |\langle \varphi'(x), \varphi(x') \rangle_{\mathcal{H}}|, |\langle \varphi'(x), \varphi'(x') \rangle_{\mathcal{H}}|, |\langle \varphi''(x), \varphi(x') \rangle_{\mathcal{H}}|$  are all upper bounded by  $\omega(|x - x'|)$ ,
- (v) there exists  $C > 0$  and  $r > 0$  such that for all  $x \in X$  and all  $a \in \mathbb{R}^*$ ,  $|\eta_{V,x}''| \geq C$  on  $[x - r, x + r]$  and  $\text{sign}(\eta_{V,x}''(x)) = -\text{sign}(a)$  where  $\eta_{V,x}$  is the vanishing derivatives precertificate for the measure  $a\delta_x$ ,
- (vi) for all open neighborhood  $V$  of 0, there exists  $M > 0$  such that for all  $x \in X$ :

$$\forall x' \in X \setminus (x + V), \quad |\eta_{V,x}(x)| \leq 1 - M,$$

where  $\eta_{V,x}$  is the vanishing derivatives precertificate for the measure  $a\delta_x$ .

Then if  $\Delta(x_0)$  is large enough, then one has:

$$\eta_V(x) = \sum_{i=1}^N \eta_{V,x_{0,i}}(x) + \eta_R(x) \quad \text{with} \quad \|\eta_R\|_{\infty,X} \xrightarrow[\Delta(x_0) \rightarrow +\infty]{} 0,$$

and  $\eta_V$  is non-degenerate i.e. for all  $x \in X \setminus \{x_{0,1}, \dots, x_{0,N}\}$ ,  $|\eta_V(x)| < 1$  and for all  $i \in \{1, \dots, N\}$ ,  $\eta_V''(x_{0,i}) \neq 0$ .

*Proof.* By definition  $\Gamma_{x_0} = (\varphi(x_{0,1}) \dots \varphi(x_{0,N}) \varphi'(x_{0,1}) \dots \varphi'(x_{0,N}))$ . We permute the column of  $\Gamma_{x_0}$ , so that  $\Gamma_{x_0} = (\varphi(x_{0,1}) \varphi'(x_{0,1}) \dots \varphi(x_{0,N}) \varphi'(x_{0,N}))$ . As a result,  $\Gamma_{x_0}^* \Gamma_{x_0} = D_{x_0} + H_{x_0}$  where  $D_{x_0}$  is a block-diagonal matrix whose blocks are for all  $i \in \{1, \dots, N\}$ :

$$D_{x_{0,i}} = \begin{pmatrix} \|\varphi(x_{0,i})\|_{\mathcal{H}}^2 & \langle \varphi(x_{0,i}), \varphi'(x_{0,i}) \rangle_{\mathcal{H}} \\ \langle \varphi'(x_{0,i}), \varphi(x_{0,i}) \rangle_{\mathcal{H}} & \|\varphi'(x_{0,i})\|_{\mathcal{H}}^2 \end{pmatrix},$$

and  $H_{x_0}$  is composed of the blocks for all  $i \neq j$ :

$$\begin{pmatrix} \langle \varphi(x_{0,i}), \varphi(x_{0,j}) \rangle_{\mathcal{H}} & \langle \varphi(x_{0,i}), \varphi'(x_{0,j}) \rangle_{\mathcal{H}} \\ \langle \varphi'(x_{0,i}), \varphi(x_{0,j}) \rangle_{\mathcal{H}} & \langle \varphi'(x_{0,i}), \varphi'(x_{0,j}) \rangle_{\mathcal{H}} \end{pmatrix}.$$

From Assumption (ii), we know that for all  $i \in \{1, \dots, N\}$   $D_{x_{0,i}}$  is invertible hence  $D_{x_0}$  is also invertible. Moreover from Assumption (iv) we deduce that  $\|H_{x_0}\| \rightarrow 0$  when  $\Delta(x_0) \rightarrow +\infty$ . As a result  $\Gamma_{x_0}^* \Gamma_{x_0}$  is invertible when  $\Delta(x_0)$  is large enough and  $\eta_V$  is well defined:

$$\eta_V = \Phi^* p_V = \Phi^* \Gamma_{x_0} (\Gamma_{x_0}^* \Gamma_{x_0})^{-1} \begin{pmatrix} \text{sign}(a_{0,1}) \\ 0 \\ \vdots \\ \text{sign}(a_{0,N}) \\ 0 \end{pmatrix}.$$

We have:

$$(\Gamma_{x_0}^* \Gamma_{x_0})^{-1} = (D_{x_0} + H_{x_0})^{-1} = D_{x_0}^{-1} (I_{2N} + H_{x_0} D_{x_0}^{-1})^{-1},$$

and since from assumption (iii),  $x \in X \mapsto \|D_x^{-1}\|$  is bounded above, we deduce that  $\|H_{x_0} D_{x_0}^{-1}\| \rightarrow 0$  when  $\Delta(x_0) \rightarrow +\infty$ . As a consequence, there exists  $\Delta_0 > 0$  such that if  $\Delta(x_0) \geq \Delta_0$  then

$$(\Gamma_{x_0}^* \Gamma_{x_0})^{-1} = D_{x_0}^{-1} + R(\Delta(x_0)) \quad \text{with} \quad \|R(\Delta(x_0))\| \xrightarrow[\Delta(x_0) \rightarrow +\infty]{} 0.$$

We obtain that  $p_V = p_Z + p_R$  with  $p_Z = \Gamma_{x_0} D_{x_0}^{-1} \begin{pmatrix} \text{sign}(a_{0,1}) \\ 0 \\ \vdots \\ \text{sign}(a_{0,N}) \\ 0 \end{pmatrix} = \sum_{i=1}^N p_{V,i}$  where for all  $i \in \{1, \dots, N\}$   $p_{V,i} = (\varphi(x_{0,i}) \ \varphi'(x_{0,i})) D_{x_0,i}^{-1} \begin{pmatrix} \text{sign}(a_{0,i}) \\ 0 \end{pmatrix}$ , and  $\|p_R\|_{\mathcal{H}} \rightarrow 0$  when  $\Delta(x_0) \rightarrow +\infty$ . Thus:

$$\eta_V = \eta_Z + \eta_R, \quad (1.3.1)$$

$$\text{where } \eta_Z(x) = \Phi_x^* p_Z = \sum_{i=1}^N \eta_{V,i}(x), \quad (1.3.2)$$

$$\text{and } \left\| \eta_R^{(k)} \right\|_{\infty, X} \xrightarrow[\Delta(x_0) \rightarrow +\infty]{} 0, \quad \forall k \in \{0, 1, 2\}, \quad (1.3.3)$$

because for  $k \in \{0, 1\}$ ,  $|\eta_R^{(k)}(x)| \leq \left\| \varphi^{(k)}(x) \right\|_{\mathcal{H}} \|p_R\|_{\mathcal{H}} \leq \sqrt{\omega(0)} \|p_R\|_{\mathcal{H}}$  thanks to Assumption (iv) and  $|\eta_R^{(2)}(x)| \leq K \|p_R\|_{\mathcal{H}}$  thanks to Assumption (iii).

**Step 1:** For all  $i \in \{1, \dots, N\}$ , one has:

$$\eta_Z''(x_{0,i}) = \eta_{V,i}''(x_{0,i}) + \sum_{j \neq i} \eta_{V,j}''(x_{0,i}).$$

From Assumption (iv) and Equation (1.3.3):

$$\begin{aligned} \sum_{j \neq i} \sup_{[x_{0,j}-r, x_{0,j}+r]} |\eta_{V,j}''| &\xrightarrow[\Delta(x_0) \rightarrow +\infty]{} 0 \\ \sup_{[x_{0,j}-r, x_{0,j}+r]} |\eta_R''| &\xrightarrow[\Delta(x_0) \rightarrow +\infty]{} 0. \end{aligned}$$

As a result from Assumption (v),  $\sup_{[x_{0,j}-r, x_{0,j}+r]} |\eta_{V,i}''| \geq C$  and  $\text{sign}(\eta_{V,i}''(x_{0,i})) = -\text{sign}(a_{0,i})$ , we obtain that there exists  $\Delta_1 > \Delta_0$  such that if  $\Delta(x_0) \geq \Delta_1$  then for all  $i \in \{1, \dots, N\}$ :

$$|\eta_V''(x_{0,i})| \geq \frac{C}{2}, \quad (1.3.4)$$

$$\text{sign}(\eta_V''(x_{0,i})) = -\text{sign}(a_{0,i}). \quad (1.3.5)$$

and:

$$\forall x \in \bigcup_{i=1}^N \overline{\mathcal{B}}(x_{0,i}, r), \quad |\eta_V''(x)| \geq \frac{C}{2}, \quad (1.3.6)$$

hence, using Equations (1.3.5) and (1.3.6), we deduce that for all  $x \in \bigcup_{i=1}^N \overline{\mathcal{B}}(x_{0,i}, r)$ ,  $|\eta_V(x)| \leq 1 - \frac{C}{4}(x - x_{0,i})^2$ . In particular:

$$\forall x \in \bigcup_{i=1}^N (\overline{\mathcal{B}}(x_{0,i}, r) \setminus \{x_{0,i}\}), \quad |\eta_V(x)| < 1. \quad (1.3.7)$$

**Step 2:** From Assumption (iv), there exists  $r_1 > r$  such that:

$$\forall i \in \{1, \dots, N\}, \quad \forall x \in X \setminus \mathcal{B}(x_{0,i}, r_1), \quad |\eta_{V,i}(x)| \leq \frac{1}{3N},$$

indeed  $\eta_{V,i}(x) = \langle \varphi(x), p_{V,i} \rangle_{\mathcal{H}} = \alpha_i \langle \varphi(x), \varphi(x_{0,i}) \rangle_{\mathcal{H}} + \beta_i \langle \varphi(x), \varphi'(x_{0,i}) \rangle_{\mathcal{H}}$  for some  $\alpha_i, \beta_i \in \mathbb{R}$ . Hence:

$$\forall x \in X \setminus \bigcup_{i=1}^N \mathcal{B}(x_{0,i}, r_1), \quad |\eta_Z(x)| \leq \frac{1}{3}.$$

From Equation (1.3.3), there exists  $\Delta_2 > \max(2r_1, \Delta_1)$  such that if  $\Delta(x_0) \geq \Delta_2$ , then  $|\eta_R(x)| \leq \frac{1}{3}$  for all  $x \in X \setminus \bigcup_{i=1}^N \mathcal{B}(x_{0,i}, r_1)$ . Thus we get:

$$\forall x \in X \setminus \bigcup_{i=1}^N \mathcal{B}(x_{0,i}, r_1), \quad |\eta_V(x)| \leq \frac{2}{3}. \quad (1.3.8)$$

**Step 3:** From Assumption (vi), there exists  $M > 0$  such that:

$$\forall i \in \{1, \dots, N\}, \quad \forall x \in \overline{\mathcal{B}}(x_{0,i}, r_1) \setminus \mathcal{B}(x_{0,i}, r), \quad |\eta_{V,i}(x)| \leq 1 - M.$$

Moreover, from Assumption (iv):

$$\forall i \in \{1, \dots, N\}, \quad \sup_{x \in \overline{\mathcal{B}}(x_{0,i}, r_1) \setminus \mathcal{B}(x_{0,i}, r)} \sum_{j \neq i} |\eta_{V,j}(x)| \xrightarrow{\Delta(x_0) \rightarrow +\infty} 0.$$

Thus, there exists  $\Delta_3 \geq \Delta_2$  such that if  $\Delta(x_0) \geq \Delta_3$  then for all  $i \in \{1, \dots, N\}$ , for all  $x \in \overline{\mathcal{B}}(x_{0,i}, r_1) \setminus \mathcal{B}(x_{0,i}, r)$ ,  $|\eta_Z(x)| \leq (1 - M) + \frac{M}{3} = 1 - \frac{2M}{3}$  and  $|\eta_R(x)| \leq \frac{M}{3}$  (using again Equation (1.3.3)). As a result:

$$\forall x \in \bigcup_{i=1}^N (\overline{\mathcal{B}}(x_{0,i}, r_1) \setminus \mathcal{B}(x_{0,i}, r)), \quad |\eta_V(x)| \leq 1 - \frac{M}{3}. \quad (1.3.9)$$

Putting Equations (1.3.4), (1.3.7), (1.3.8), (1.3.9) all together, we deduce that if  $\Delta(x_0) \geq \Delta_3$ , then

$$\begin{aligned} \forall x \in X \setminus \{x_{0,1}, \dots, x_{0,N}\}, \quad & |\eta_V(x)| < 1, \\ \forall i \in \{1, \dots, N\}, \quad & \eta_V''(x_{0,i}) \neq 0, \end{aligned}$$

i.e.  $\eta_V$  is non-degenerate.  $\square$

*Remark 3.* i) The statement of Theorem 2 and its proof are made on dimension 1 for clarity but the result can be easily generalize on  $\mathbb{R}^d$ . In particular, in Proposition 6 we show that the assumptions of Theorem 2 hold for the Gaussian convolution and the Cauchy convolution: it is still true in  $\mathbb{R}^d$ .

- ii) The Assumption (ii) in Theorem 2, which states that  $\varphi, \varphi'$  are linearly independent may be replaced by the assumption that  $\Gamma_{x_0}$  has full column rank.

The following Proposition shows that we can apply Theorem 2 in the case of a Gaussian convolution and a Cauchy convolution which means that for these operators  $\eta_V$  is non-degenerate provided that the spikes are separated enough.

**Proposition 6.** *Let  $X = \mathbb{R}$ , then all the assumptions of Theorem 2 holds for a Gaussian convolution and a Cauchy convolution.*

*Proof.* For a Gaussian convolution one has:

$$\forall x \in \mathbb{R}, \quad \varphi_G(x) \stackrel{\text{def}}{=} \frac{1}{\sqrt{2\pi\sigma^2}} e^{-\frac{(\cdot-x)^2}{2\sigma^2}} \quad \text{with } \sigma > 0.$$

For a Cauchy convolution one has:

$$\forall x \in \mathbb{R}, \quad \varphi_C(x) \stackrel{\text{def}}{=} \frac{1}{\pi\sigma} \frac{1}{1 + \frac{(\cdot-x)^2}{\sigma^2}} \quad \text{with } \sigma > 0.$$

We prove the Assumptions of Theorem 4 one by one:

- (i) One has  $\varphi_G, \varphi_C \in \mathcal{C}^2(\mathbb{R}, L^2(\mathbb{R}))$ ,
- (ii) It can be easily check that  $\varphi_G, \varphi'_G$  and  $\varphi_C, \varphi'_C$  are both linearly independent,
- (iii) Let us denote for all  $t \in \mathbb{R}$ ,  $x, x' \in \mathbb{R}$ ,  $\kappa_G(t) = \frac{1}{\sqrt{4\pi\sigma^2}} e^{-\frac{t^2}{4\sigma^2}}$  and  $\kappa_C(t) = \frac{1}{2\pi\sigma} \frac{1}{1 + \frac{t^2}{4\sigma^2}}$ . Then for all  $x, x' \in \mathbb{R}$ ,  $\langle \varphi_G(x), \varphi_G(x') \rangle_{\mathcal{H}} = \kappa_G(x - x')$  and  $\langle \varphi_C(x), \varphi_C(x') \rangle_{\mathcal{H}} = \kappa_C(x - x')$ . One has  $\kappa'_G(t) = -\frac{t}{2\sigma^2} \kappa_G(t)$ ,  $\kappa''_G(t) = (-\frac{1}{2\sigma^2} + \frac{t^2}{4\sigma^4}) \kappa_G(t)$ ,  $\kappa'_C(t) = -\frac{\pi t}{\sigma} \kappa_C(t)^2$  and  $\kappa''_C(t) = -\frac{\pi}{\sigma} \kappa_C(t)^2 - \frac{2\pi t}{\sigma} \kappa'_C(t) \kappa_C(t)$ . As a result for all  $x \in \mathbb{R}$ :

$$\begin{aligned} \|\varphi_G(x)\|_{\mathcal{H}}^2 &= \frac{1}{\sqrt{4\pi\sigma^2}}, \quad \|\varphi'_G(x)\|_{\mathcal{H}}^2 = \frac{1}{2\sigma^2 \sqrt{4\pi\sigma^2}}, \quad \|\varphi''_G(x)\|_{\mathcal{H}}^2 = \kappa_G^{(4)}(0), \\ \|\varphi_C(x)\|_{\mathcal{H}}^2 &= \frac{1}{2\pi\sigma}, \quad \|\varphi'_C(x)\|_{\mathcal{H}}^2 = \frac{1}{2\sigma^2}, \quad \|\varphi''_C(x)\|_{\mathcal{H}}^2 = \kappa_C^{(4)}(0). \end{aligned}$$

Thus for the Gaussian convolution:

$$D_x = \begin{pmatrix} \frac{1}{\sqrt{4\pi\sigma^2}} & 0 \\ 0 & \frac{1}{2\sigma^2 \sqrt{4\pi\sigma^2}} \end{pmatrix},$$

which implies that  $x \mapsto \|D_x^{-1}\|$  is bounded above (because constant, not surprising for a convolution). And for the Cauchy convolution:

$$D_x = \begin{pmatrix} \frac{1}{2\pi\sigma} & 0 \\ 0 & \frac{1}{2\sigma^2} \end{pmatrix},$$

which implies again that  $x \mapsto \|D_x^{-1}\|$  is bounded above (because constant).

- (iv) Consider for all  $t \in \mathbb{R}_+$ ,  $\omega_G(t) = \max(|\kappa_G(t)|, |\kappa'_G(t)|, |\kappa''_G(t)|)$ . Then for all  $x, x' \in \mathbb{R}$ ,  $|\langle \varphi_G(x), \varphi_G(x') \rangle_{\mathcal{H}}|, |\langle \varphi'_G(x), \varphi_G(x') \rangle_{\mathcal{H}}|, |\langle \varphi'_G(x), \varphi'_G(x') \rangle_{\mathcal{H}}|$ , and  $|\langle \varphi''_G(x), \varphi_G(x') \rangle_{\mathcal{H}}|$  are all upper bounded by  $\omega_G(|x - x'|)$ . Moreover  $\omega_G(t) \rightarrow 0$  when  $t \rightarrow 0$ . It is the same argument for the Cauchy convolution.
- (v) For the Gaussian convolution and from the computations above, we deduce that for all  $x \in \mathbb{R}$  and for all  $a \in \mathbb{R}^*$ ,  $\eta_{V,x} = \text{sign}(a)\sqrt{4\pi\sigma^2}\kappa_G(\cdot - x)$ . Hence  $\eta''_{V,x}(x) = \text{sign}(a)\sqrt{4\pi\sigma^2}\kappa''_G(0) = -\frac{\text{sign}(a)}{2\sigma^2}$ . We thus obtain the expected result.  
Similarly for the Cauchy convolution, we have  $\eta_{V,x} = \text{sign}(a)2\pi\sigma\kappa_C(\cdot - x)$  hence  $\eta''_{V,x}(x) = \text{sign}(a)2\pi\sigma\kappa''_C(0) = -\frac{\text{sign}(a)}{2\sigma^2}$  which is again what we want.
- (vi) Let  $V$  a neighborhood of 0. Then for all  $x \in \mathbb{R}$  and for all  $a \in \mathbb{R}^*$ ,

$$|\eta_{V,x}| = \begin{cases} e^{-\frac{(-x)^2}{4\sigma^2}} & \text{for the Gaussian convolution,} \\ \frac{1}{1 + \frac{(-x)^2}{4\sigma^2}} & \text{for the Cauchy convolution,} \end{cases}$$

which are two positive functions equal to 1 at  $x$ , increasing for  $x' \leq x$  and decreasing for  $x' \geq x$ . Thus by taking  $M_G, M_C$  as the minimum of 1 minus these two functions on  $\mathbb{R} \setminus (x + V)$ , we have the expected conclusion.

□

Figure 1.5 and 1.6 show  $\eta_V$  for respectively a Gaussian and a Cauchy convolution for two examples: 3 spikes with an alternation of the signs (first column) and 2 positive spikes (second column). For each example the spikes are progressively brought closer. In the first line, we observe that  $\eta_V$  is non-degenerate and that the approximation of  $\eta_V$  by  $\eta_Z$ , which is used in the proof of Theorem 2, is perfect. When the spikes are too close (third and fourth line), the approximation is no longer valid. In the case of the alternation of signs, we see that  $\eta_V$  is degenerate ( $|\eta_V| > 1$ ) in the last configuration.

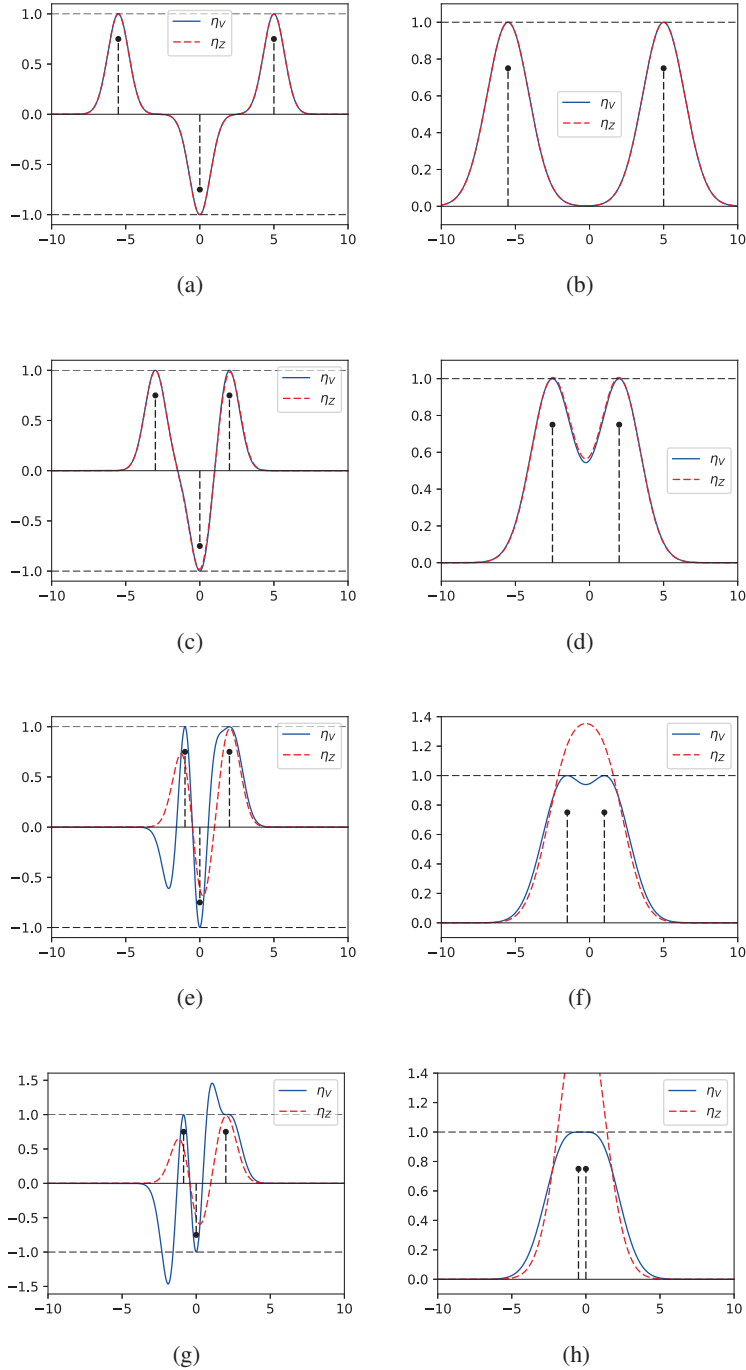


Figure 1.5:  $\eta_V$  for a Gaussian convolution for two examples: 3 spikes with an alternation of the signs (first column) and 2 positive spikes (second column). For each example the spikes are progressively brought closer.

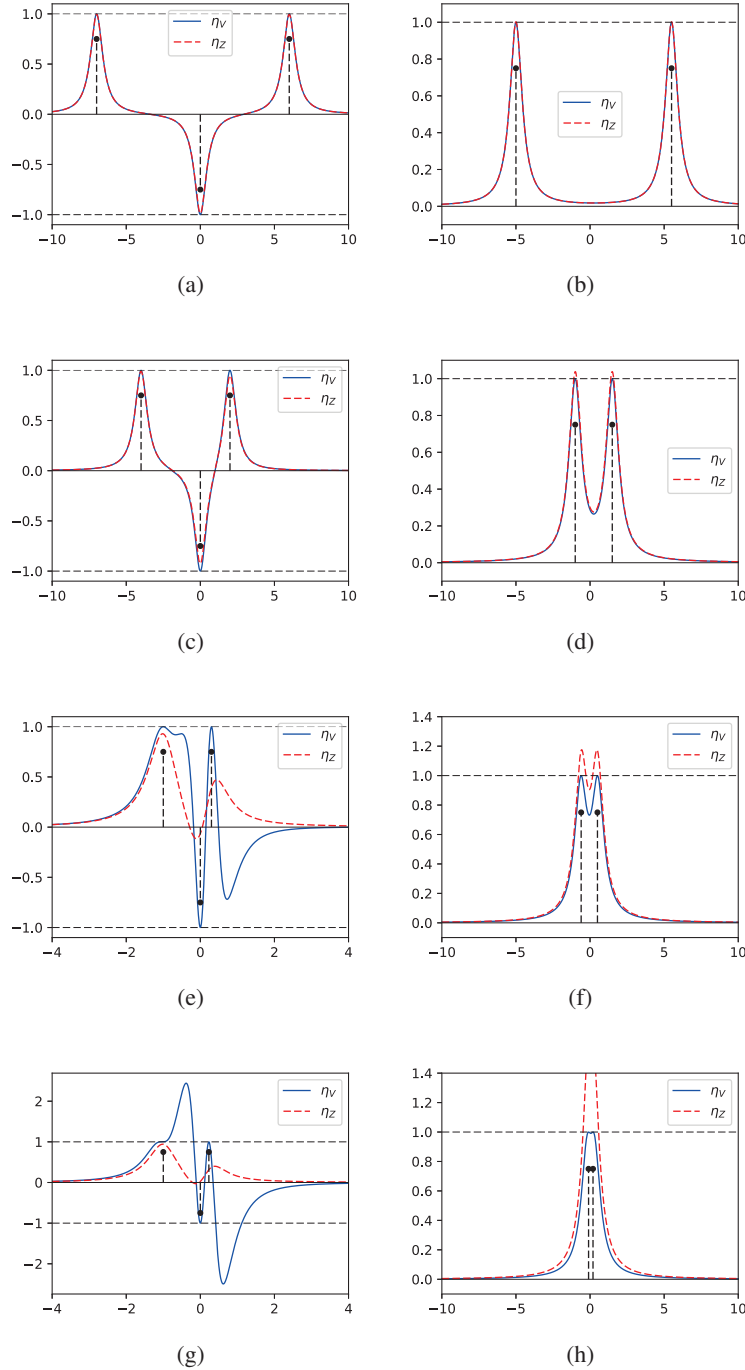


Figure 1.6:  $\eta_V$  for a Cauchy convolution for two examples: 3 spikes with an alternation of the signs (first column) and 2 positive spikes (second column). For each example the spikes are progressively brought closer.

## 1.4 The $(2N - 1)$ -Vanishing Derivatives Pre-Certificate

In Section 1.2, we presented a result of the robustness to noise of the BLASSO (Theorem 1). Proposition 4 proved that recovering a measure with the same number of spikes as the initial measure in a low noise regime  $\lambda \rightarrow 0$  and  $\|w\|_{\mathcal{H}}/\lambda \rightarrow 0$  leads naturally to the definition of the vanishing derivatives pre-certificate  $\eta_V$ .

In this Section, we start to get into the core of this Thesis which is robustness to noise of the super-resolution problem when solving the BLASSO. We recall the framework. The set  $X$  is a smooth manifold of dimension 1 (previously dimension  $d \in \mathbb{N}^*$ ).  $X$  is typically  $\mathbb{R}$ , a compact subset of  $\mathbb{R}$ ,  $\mathbb{T}$  or an interval of  $\mathbb{R}$ . One can assume without loss of generality that  $0 \in \overset{\circ}{X}$ . Let us consider  $a_0 \in (\mathbb{R}_+^*)^N$  and  $z_0 \in X^N$  such that the aim is to recover for all  $t > 0$  small enough:

$$m_{a_0, t z_0} = \sum_{i=1}^N a_{0,i} \delta_{t z_{0,i}},$$

which is a measure whose spikes cluster at  $0 \in \overset{\circ}{X}$ .

As a consequence, interested by the recovery of the support of  $m_{a_0, t z_0}$  when  $t \rightarrow 0$ , it is then natural, given the previous information, to look at  $\eta_{V,t}$  (the  $t$  refers to the  $t$  of initial measure  $m_{a_0, t z_0}$ ) when  $t \rightarrow 0$ .

Figure 1.7 shows  $\eta_{V,t}$  when  $t \rightarrow 0$  in the case of a Gaussian convolution.

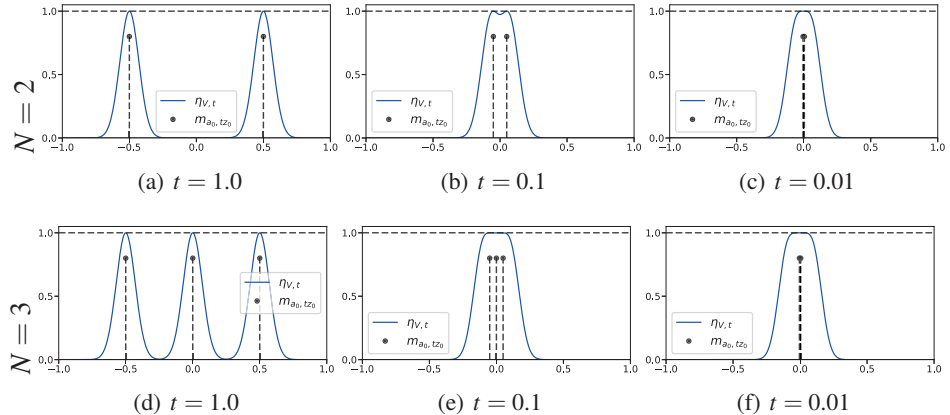


Figure 1.7: Limit of  $\eta_{V,t}$  when  $t \rightarrow 0$  for a discretized Gaussian convolution with 2 or 3 spikes.

We remark that  $\eta_{V,t}$  seems to converge towards some function. Therefore, similarly as in Section 1.2, where  $\eta_V$  was used to show the non-degeneracy of  $\eta_\lambda$  in a low noise regime and hence proving that  $m_{a,\bar{x}}$  was a solution of the BLASSO, this limit function may be helpful to show here the non-degeneracy of  $\eta_{V,t}$ . Note that the limit function seems to get flatter at 0 when  $N$  increases. The reason is, in substance, because  $\eta'_{V,t}$  has  $2N - 1$  zeros, by Rolle's Theorem, which collapse at 0 when  $t \rightarrow 0$ .

This Section is devoted to the formal definition of this particular function, see Proposition 8.

### 1.4.1 Injectivity Hypotheses

But first, one needs to give some definitions. We introduce here an injectivity hypothesis which ensures the invertibility of  $\Phi_{tz}^* \Phi_{tz}$  and  $\Gamma_{tz}^* \Gamma_{tz}$  for  $t > 0$  small enough.

In the case of the ideal low-pass filter  $\Gamma_{\bar{x}}$  has full column rank provided that  $\bar{x} = (x_1, \dots, x_N) \in X^N$  has pairwise distinct coordinates (see [54], Section 3.6, Proposition 6). That property is not true for a general operator  $\Phi$ . However, in this paper we focus on sums of Dirac masses that are clustered around the point  $0 \in X$ , i.e.  $\bar{x} = tz$  for  $t > 0$  and  $z \in \mathbb{R}^N$  with pairwise distinct components. The following assumption, which is crucial to our analysis, shall ensure that  $\Gamma_{tz}$  has full rank at least for small  $t$ .

**Definition 7.** Let  $\varphi : X \rightarrow \mathcal{H}$ . For all  $k \in \mathbb{N}$ , we say that the hypothesis  $\mathcal{I}_k$  holds if and only if

$$\varphi \in \text{KER}^{(k)} \text{ and } (\varphi_0, \dots, \varphi_k) \text{ are linearly independent in } \mathcal{H}, \quad (\mathcal{I}_k)$$

where  $\varphi_k \in \mathcal{H}$  is the  $k^{\text{th}}$  derivative of  $\varphi$  at 0, i.e.

$$\varphi_k \stackrel{\text{def.}}{=} \varphi^{(k)}(0). \quad (1.4.1)$$

In particular,  $\varphi_0 = \varphi(0)$ .

See Definition 4 for the definition of  $\text{KER}^{(k)}$ .

Given  $k \in \mathbb{N}$ , we define:

$$\Psi_k \stackrel{\text{def.}}{=} (\varphi_0 \quad \varphi_1 \quad \dots \quad \varphi_k). \quad (1.4.2)$$

If  $\mathcal{I}_k$  holds, then  $\Psi_k^* \Psi_k$  is a symmetric positive definite matrix, where  $\Psi_k$  is defined in (1.4.2).

To exemplify the meaning of this injectivity hypothesis, Proposition 7 below considers the case  $X = \mathbb{T}$  with  $\Phi$  a convolution operator.

**Proposition 7.** Let  $\tilde{\varphi} \in \mathcal{C}^k(\mathbb{T}, \mathbb{R})$  (where  $\varphi(x) = \tilde{\varphi}(\cdot - x)$ ), then  $\mathcal{I}_k$  holds if and only if  $\varphi_0$  has at least  $k + 1$  non-zeros Fourier coefficients. In particular if  $\Phi$  is the ideal low-pass filter with cutoff frequency  $f_c \in \mathbb{N}^*$ ,  $\mathcal{I}_k$  holds if and only if  $k \leq 2f_c$ .

*Proof.* The functions  $(\varphi_0, \dots, \varphi_k)$  are linearly independent in  $L^2(\mathbb{T})$  if and only if their respective Fourier coefficients are linearly independent in  $\ell^2(\mathbb{Z})$ . If  $(c_n[\varphi_0])_{n \in \mathbb{Z}}$  denotes the Fourier coefficients of  $\varphi_0$ , the Fourier coefficients of  $\varphi_j$  are given by  $((2i\pi n)^j c_n[\varphi_0])_{n \in \mathbb{Z}}$  (with the convention that  $0^0 = 1$ ).

If  $\varphi_0$  has  $k+1$  nonzeros Fourier coefficients corresponding to pairwise distinct frequencies  $(n_0, \dots, n_k)$ , those Fourier coefficients are given by the matrix product

$$\begin{pmatrix} c_{n_0}[\varphi_0] & & 0 \\ & \ddots & \\ 0 & & c_{n_k}[\varphi_0] \end{pmatrix} \begin{pmatrix} 1 & (2i\pi n_0) & (2i\pi n_0)^2 & \dots & (2i\pi n_0)^k \\ 1 & (2i\pi n_1) & (2i\pi n_1)^2 & \dots & (2i\pi n_1)^k \\ \vdots & \vdots & \vdots & \ddots & \vdots \\ 1 & (2i\pi n_k) & (2i\pi n_k)^2 & \dots & (2i\pi n_k)^k \end{pmatrix}$$

Both the diagonal and the Vandermonde matrices are invertible, hence the family of Fourier coefficients of  $(\varphi_0, \dots, \varphi_k)$  is linearly independent.

Conversely, if  $\mathcal{I}_k$  holds, one can find  $k+1$  Fourier coefficients, corresponding to some frequencies  $n_0, \dots, n_k$ , such that the matrix  $(c_{n_\ell}[\varphi_j])_{0 \leq \ell, j \leq k}$  is invertible. From the above factorization, we deduce that each  $c_{n_\ell}[\varphi_0]$  must be nonzero for  $0 \leq \ell \leq k$ .  $\square$

As we shall see in Section 3.4, the conditions  $\mathcal{I}_{N-1}$  and  $\mathcal{I}_{2N-1}$  imply respectively the invertibility of  $\Phi_{tz}^* \Phi_{tz}$  and  $\Gamma_{tz}^* \Gamma_{tz}$ , provided that  $t$  is small enough. According to Proposition 7, in the special case of an ideal low-pass filter, these conditions hold if and only if  $f_c$  is large enough with respect to the number  $N$  of spikes.

#### 1.4.2 Convergence of $\eta_{V,t}$ when $t \rightarrow 0$

Now we can properly define the limit function outlined at the beginning of this Section.

**Proposition 8** (( $2N-1$ )-Vanishing Derivatives Pre-certificate). *If  $\mathcal{I}_{2N-1}$  holds, there is a unique solution to the problem*

$$\inf \left\{ \|p\|_{\mathcal{H}} ; (\Phi^* p)(0) = 1, (\Phi^* p)'(0) = 0, \dots, (\Phi^* p)^{(2N-1)}(0) = 0 \right\}.$$

We denote by  $p_W$  its solution, given by

$$p_W = \Psi_{2N-1}^{+,*} \delta_{2N} \quad (1.4.3)$$

where

$$\delta_{2N} \stackrel{\text{def.}}{=} (1, 0, \dots, 0)^T \in \mathbb{R}^{2N}, \quad (1.4.4)$$

$$(1.4.5)$$

and we define the  $(2N-1)$ -vanishing derivatives pre-certificate as  $\eta_W \stackrel{\text{def.}}{=} \Phi^* p_W$ .

With this proposition, one defines  $\eta_W$  for only one cluster of spikes (all the spikes collapse at 0). This choice, made for the sake of simplicity, is later justified in Section 2.4 where we consider the case of several clusters and shows that it is enough to study the above simpler definition.

The following Proposition, which is a direct consequence of Lemma 7 in Chapter 3, shows that indeed  $\eta_{V,t}$  converges toward  $\eta_W$ .

**Proposition 9.** If  $\mathcal{I}_{2N-1}$  holds and  $\varphi \in \text{KER}^{(K)}$  (for  $K \geq 2N - 1$ ), then for  $t > 0$  small enough  $\Gamma_{tz_0}$  has full column rank. Moreover

$$\lim_{t \rightarrow 0^+} p_{V,t} = p_W \text{ strongly in } \mathcal{H},$$

$$\lim_{t \rightarrow 0^+} \eta_{V,t}^{(k)} = \eta_W^{(k)} \text{ in the sense of the uniform convergence on } X,$$

for all  $0 \leq k \leq K$ .

Figure 1.8 shows graphically this convergence of  $\eta_{V,t}$  toward  $\eta_W$  of  $\Phi$  a convolution by the Dirichlet kernel. Figure 1.9 and 1.10 show  $\eta_W$  for several values of  $N$ . Notice again how it becomes flatter at 0 as  $N$  increases. This implies that  $\eta_{V,t}$  for small  $t$  gets closer to degeneracy as  $N$  increases. This is reflected in our main contribution (Theorem 5) where the signal-to-noise ratio is required to scale with  $t^{2N-1}$ .

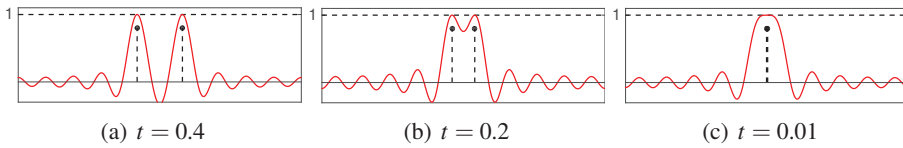


Figure 1.8:  $\eta_{V,t}$  for several values of  $t$ , showing the convergence toward  $\eta_W$ .  $\Phi$  is the ideal low-pass filter with cutoff frequency  $f_c = 10$ .

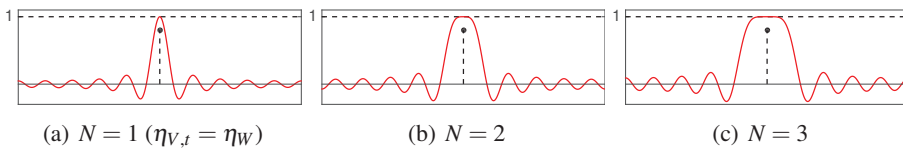


Figure 1.9:  $\eta_W$  for several values of  $N$  when  $\Phi$  is the ideal low-pass filter with a cutoff frequency  $f_c = 10$ .

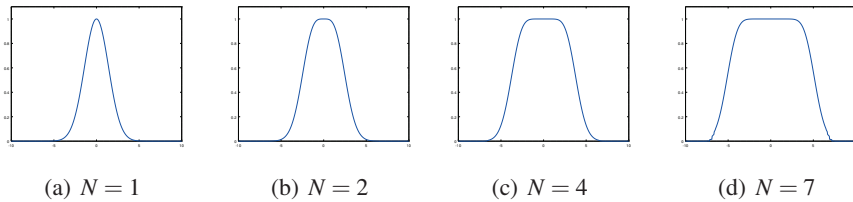


Figure 1.10:  $\eta_W$  for a Gaussian convolution ( $x \in \mathbb{R}$ ,  $\varphi(x) = e^{-\frac{(x-x_0)^2}{2\sigma^2}}$ ) for several numbers of spikes and  $\sigma = 1$ .

## 1.5 Transfer Theorem

From Proposition 9 of the previous Section 1.4, we can infer that the behavior of  $\eta_{V,t}$  is governed by specific properties of  $\eta_W$  for small values of  $t > 0$ .

This is the aim of this Section to study how the relation between  $\eta_{V,t}$  and  $\eta_W$  works and what properties can be transferred from  $\eta_W$  to  $\eta_{V,t}$ . In particular, from the discussion in Section 1.2, we are interested in the non-degeneracy of  $\eta_{V,t}$  (see Definition 6). We define the appropriate notion of non-degeneracy for  $\eta_W$  in Definition 8 and we show in Theorem 3 that this non-degeneracy of  $\eta_W$  implies the non-degeneracy of any sufficiently close  $\eta$  interpolating the signs of the spikes at the associated positions. This is in particular the case for  $\eta_{V,t}$  and it is stated in Corollary 11.

**Definition 8.** Assume that  $\mathcal{I}_{2N-1}$  holds and  $\varphi \in \text{KER}^{(2N)}$ . We say that  $\eta_W$  is  $(2N-1)$ -non-degenerate if  $\eta_W^{(2N)}(0) \neq 0$  and for all  $x \in X \setminus \{0\}$ ,  $|\eta_W(x)| < 1$ .

This is the goal of Chapter 2 to study when  $\eta_W$  is  $(2N-1)$ -non-degenerate.

Figure 1.11 shows some examples of  $\eta_W$  for different convolution operators  $\Phi$  (Dirichlet kernel, Gaussian kernel and Cauchy kernel). One can easily check numerically that these  $\eta_W$  are  $(2N-1)$ -non-degenerate.

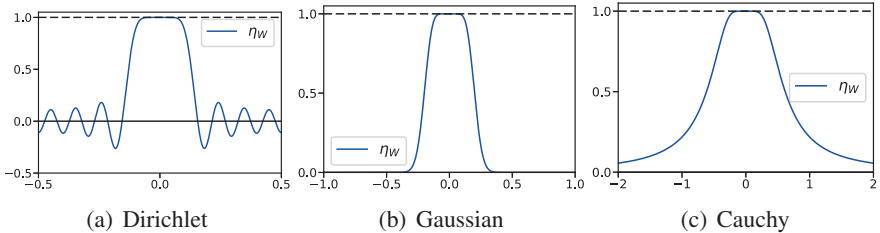


Figure 1.11:  $\eta_W$  for  $N = 4$  and three different convolution operators  $\Phi$ : Dirichlet for  $f_c = 10$ , Gaussian for  $\sigma = 0.05$  and Cauchy for  $\sigma = 0.2$ .

Figure 1.12 shows  $\eta_W$  for a low pass filter with several different choices of Fourier coefficients for the kernel and that it can be degenerate. Note that even when  $|\eta_W| > 1$ ,  $\eta_W$  seems to satisfy the curvature condition  $\eta_W^{(2N)}(0) < 0$ . We prove this result for any convolution operator  $\Phi$  in Chapter 2 with Proposition 11.

We can now state our main result of this Section which shows that any  $\eta$  interpolating  $N$  collapsing spikes to 0 with zero derivatives (i.e.  $\eta(tz_i)$  and  $\eta'(tz_i) = 0$ ), and sufficiently close of  $\eta_W$  is non-degenerate in the sense defined for  $\eta_V$  (Definition 6).

**Theorem 3.** Suppose that  $\eta_W$  is  $(2N-1)$ -non-degenerate (Definition 8). Let  $R_W > 0$ . Then, there exist  $C_W > 0$ ,  $t_W > 0$  such that for all  $t \in (0, t_W)$ , all  $z \in X^N$  with pairwise distinct coordinates and  $|z|_\infty \leq R_W$ , and all  $\eta \in \mathcal{C}^{2N}(X)$  with bounded

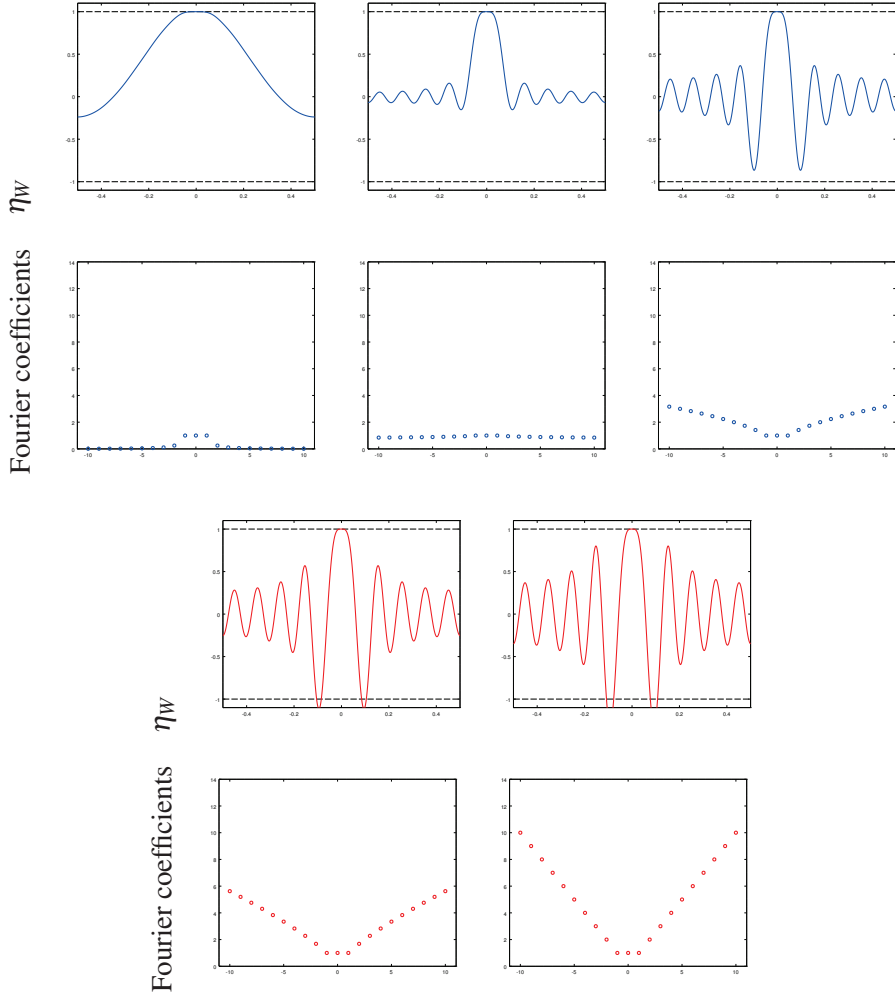


Figure 1.12:  $\eta_W$  for a low pass filter for  $f_c = 10$  with increasing high frequency content. The curve showing  $\eta_W$  is in blue when it is  $(2N-1)$ -non-degenerate and in red when it is degenerate.

derivatives satisfying for  $1 \leq i \leq N$ ,  $\eta(tz_i) = 1$  and  $\eta'(tz_i) = 0$ ,

$$\begin{aligned} & \left( \forall \ell \in \{0, \dots, 2N\}, \quad \left\| \eta^{(\ell)} - \eta_W^{(\ell)} \right\|_{\infty, X} \leq C_W \right) \\ \implies & \left( \forall x \in X \setminus \bigcup_i \{tz_i\}, \quad |\eta(x)| < 1 \quad \text{and} \quad \forall 1 \leq i \leq N, \eta''(tz_i) < 0 \right). \end{aligned}$$

*Proof.* The proof proceeds in two steps. First we show the result locally around 0 in  $X$  thanks to  $\eta_W^{(2N)}(0) < 0$  (because  $\eta_W^{(2N)}(0) \neq 0$  and  $|\eta_W| < 1$  on  $X \setminus \{0\}$ ) and then we extend the result to all  $X$  thanks to  $|\eta_W| < 1$  on  $X \setminus \{0\}$ .

**Locally.** Let us prove that there exist  $C_W > 0$ ,  $t_W > 0$  such that for all  $t \in (0, t_W)$ ,  $z \in \mathbb{R}^N$  with pairwise distinct coordinates and  $|z|_\infty \leq R_W$ , there exist  $r^+ > 0$  with  $r^+ > \max_{1 \leq i \leq N} t_W z_i$  and  $r^- < 0$  with  $r^- < \min_{1 \leq i \leq N} t_W z_i$  such that for all  $\eta \in \mathcal{C}^{2N}(X) \cap W^{2N,\infty}(X)$  satisfying for all  $1 \leq i \leq N$ ,  $\eta(tz_i) = 1$  and  $\eta'(tz_i) = 0$ , the following implication holds,

$$\begin{aligned} & \left( \forall \ell \in \{0, \dots, 2N\}, \left\| \eta^{(\ell)} - \eta_W^{(\ell)} \right\|_{\infty, X} \leq C_W \right) \\ \implies & \left( \forall x \in (r^-, r^+) \setminus \bigcup_i \{tz_i\}, \quad |\eta(x)| < 1 \quad \text{and} \quad \forall 1 \leq i \leq N, \eta''(tz_i) < 0 \right). \end{aligned}$$

First, we prove that, provided  $C_W > 0$ ,  $t_W > 0$  are small enough,  $\eta'$  has exactly  $2N - 1$  zeros in  $(r^-, r^+)$ .

Let  $t > 0$  and  $\eta \in \mathcal{C}^{2N}(X) \cap W^{2N,\infty}(X)$  and  $z \in \mathbb{R}^N$  with pairwise distinct coordinates and  $|z|_\infty \leq R_W$  such that for all  $1 \leq i \leq N$ ,  $\eta(tz_i) = 1$  and  $\eta'(tz_i) = 0$ . We suppose that  $z_1 < z_2 < \dots < z_N$ . By Rolle's Theorem, for all  $1 \leq i \leq N - 1$ , there exists  $c_i(t) \in (tz_i, tz_{i+1})$  such that  $\eta'(c_i(t)) = 0$ . As a result  $\eta'$  has at least  $2N - 1$  zeros in all  $(r^-, r^+)$  satisfying the requirements.

Now, let us assume by contradiction that  $\eta'$  has strictly more than  $2N - 1$  zeros for arbitrarily small values of  $C_W$ ,  $t_W$  and in all  $(r^-, r^+)$  satisfying the requirements. As a result, there are sequences  $(t_k)_{k \in \mathbb{N}}$  where  $t_k \rightarrow 0$ ,  $(z_k)_{k \in \mathbb{N}}$  (where each  $z_k \in \mathbb{R}^N$  has pairwise distinct coordinates and  $|z_k|_\infty \leq R_W$ ),  $(r_k^+)_{k \in \mathbb{N}}$  and  $(r_k^-)_{k \in \mathbb{N}}$  where for all  $k \in \mathbb{N}$ ,  $r_k^+ > 0$ ,  $r_k^+ > \max_{1 \leq i \leq N} t_k(z_k)_i$ ,  $r_k^+ \rightarrow 0$  and  $r_k^- < 0$ ,  $r_k^- < \min_{1 \leq i \leq N} t_k(z_k)_i$  and  $r_k^- \rightarrow 0$ . And there exists  $(\eta_k)_{k \in \mathbb{N}} \in (\mathcal{C}^{2N}(X) \cap W^{2N,\infty}(X))^{\mathbb{N}}$  such that for all  $k \in \mathbb{N}$

$$\begin{aligned} & \forall i \in \{1, \dots, N - 1\}, \eta_k(t_k(z_k)_i) = 1 \quad \text{and} \quad \eta'_k(t_k(z_k)_i) = 0, \\ & \forall \ell \in \{0, \dots, 2N\}, \left\| \eta_k^{(\ell)} - \eta_W^{(\ell)} \right\|_{\infty, X} \leq \frac{1}{k}, \end{aligned}$$

and  $\eta'_k$  has at least  $2N$  zeros in  $(r_k^-, r_k^+)$  (we already know that  $\eta'_k$  has at least  $2N - 1$  zeros in  $(r_k^-, r_k^+)$ ). Thus, for all  $k \in \mathbb{N}$ , by applying successively Rolle's Theorem, we obtain that there exists  $x_k \in (r_k^-, r_k^+)$  such that  $\eta_k^{(2N)}(x_k) = 0$ . Since  $x_k \rightarrow 0$  (because  $r_k^-, r_k^+ \rightarrow 0$ ) and  $\left\| \eta_k^{(2N)} - \eta_W^{(2N)} \right\|_{\infty, X} \leq \frac{1}{k}$ , we deduce that  $\eta_W^{(2N)}(0) = 0$ , which is a contradiction. Hence  $\eta'$  has exactly  $2N - 1$  zeros in some  $(r^-, r^+)$ .

Using the same argument, we may also prove that for all  $i \in \{1, \dots, N\}$ ,  $\eta''(tz_i) \neq 0$ . Let us now observe that, either for all  $1 \leq i \leq N$ ,  $\eta''(tz_i) > 0$  or, for all  $1 \leq i \leq N$ ,  $\eta''(tz_i) < 0$ . Indeed, assume for instance by contradiction that for some  $1 \leq i \leq N - 1$ ,  $\eta''(tz_i) > 0$  and  $\eta''(tz_{i+1}) < 0$ . Then, there exists  $c_i(t) \in (tz_i, tz_{i+1})$  such that  $\eta(c_i(t)) = 1$ . Applying Rolle's Theorem on respectively  $(tz_i, c_i(t))$  and  $(c_i(t), tz_{i+1})$ , we obtain that  $\eta'$  vanishes at least twice in  $(tz_i, tz_{i+1})$ . It is a contradiction with the fact that  $\eta'$  has exactly  $2N - 1$  zeros in  $(r^-, r^+)$  for all  $0 < t < t_W$ .

As a result, there are only two possibilities: either  $\eta''(tz_i) < 0$  for all  $i$  (and then for all  $x \in (r^-, r^+) \setminus \bigcup_i \{tz_i\}$   $\eta(x) < 1$ ), or  $\eta''(tz_i) > 0$  for all  $i$  (and then for all  $x \in (r^-, r^+) \setminus \bigcup_i \{tz_i\}$   $\eta(x) > 1$ ). But since  $\eta_W^{(2N)}(0) < 0$ , there is some  $\tilde{x} \in (r^-, r^+)$  and some  $\varepsilon_0 > 0$  such that  $\eta_W(\tilde{x}) < 1 - \varepsilon_0$ . Choosing  $C_W$  small enough so that  $C_W < \varepsilon_0/2$ , we obtain that  $\eta(\tilde{x}) < 1 - \varepsilon_0/2$ . As a consequence, for all  $x \in (r^-, r^+) \setminus \bigcup_i \{tz_i\}$ ,  $\eta(x) < 1$ . Finally we can suppose that  $\eta_W(x) > -1$  on  $(r^-, r^+)$  by imposing  $0 < C_W < \inf_X \eta_W + 1$ .

To sum up, we have proved the following :

$$\forall x \in (r^-, r^+) \setminus \bigcup_i \{tz_i\}, |\eta(x)| < 1 \quad \text{and} \quad \forall 1 \leq i \leq N, \eta''(tz_i) < 0. \quad (1.5.1)$$

**Globally.** As  $\eta_W$  is non-degenerate, we have  $\sup_{X \setminus (r^-, r^+)} |\eta_W| < 1$ . We can assume that  $0 < C_W < (1 - \sup_{X \setminus (r^-, r^+)} |\eta_W|)/2$  and use  $\|\eta - \eta_W\|_{\infty, X} \leq C_W$  so as to obtain

$$\forall x \in X \setminus (r^-, r^+), \quad |\eta(x)| < 1. \quad (1.5.2)$$

Gathering Equations (1.5.1) and (1.5.2), we obtain the claimed result.  $\square$

A direct corollary of this Theorem is the fact that  $\eta_{V,t}$  is non-degenerate for  $t$  small enough if  $\eta_W$  is  $(2N-1)$ -non-degenerate.

**Corollary 1.** *If  $\eta_W$  is  $(2N-1)$ -non-degenerate then there exists  $t_0 > 0$  such that for all  $m_{a_0, tz_0}$  (positive amplitudes) with  $t \leq t_0$  and  $|z_0|_\infty \leq R_W$ , the  $\eta_{V,t}$  defined for  $m_{a_0, tz_0}$  is non-degenerate i.e. :*

$$\forall x \in X \setminus \bigcup_i \{tz_{0,i}\}, \quad |\eta_{V,t}(x)| < 1 \quad \text{and} \quad \forall 1 \leq i \leq N, \eta''(tz_{0,i}) < 0.$$

*Proof.* From Proposition 9, we know that  $\eta_{V,t}$  converges towards  $\eta_W$  when  $t \rightarrow 0$  so that  $\eta_{V,t}$  satisfies all the assumptions of Theorem 3. Hence the conclusion.  $\square$

Knowing that  $\eta_{V,t}$  is always non-degenerate when  $t \rightarrow 0$  means that (thanks to Theorem 1) one can recover by solving the BLASSO a unique measure composed of the same number of spikes as the original measure  $N$  in presence of noise for any  $t > 0$ . This is stated in the next Proposition.

**Proposition 10** (Exact support recovery for positive spikes when  $t \rightarrow 0$ ). *Assume that  $\mathcal{I}_{2N-1}$  holds and  $\varphi \in \text{KER}^{(2N)}$ . If  $\eta_W$  is  $(2N-1)$ -non-degenerate then for any  $z_0 \in X^N$  there exists  $t_0 > 0$  such that for all  $0 < t < t_0$ , the BLASSO  $\mathcal{P}_\lambda(y)$  has a unique solution  $m_{a,tz}$  composed of the same number of spikes as  $m_{a_0, tz_0}$  if  $(\lambda, w) \in \mathbb{R}_+^* \times \mathcal{H}$  satisfies:*

$$\max \left( \lambda, \frac{\|w\|_{\mathcal{H}}}{\lambda} \right) \leq C_t,$$

for some  $C_t$  (depending on  $t$ ).

This is an interesting result which directly comes from Corollary 1 and Theorem 1. However it does not tell how the constant  $C_t$  evolves with respect to  $t$ , which is an important issue in theory but also in practice. Indeed it states that one can solve a super-resolution problem in presence of noise when solving the BLASSO but without telling whether for a given noise level, it actually works. The main theoretical contribution of this Thesis, see Theorem 5) which is a much stronger result than Proposition 10), consists in quantifying precisely with respect to  $t$  (*i.e.* the separation between the spikes) the constraints on  $\lambda$  and  $w$  to assure the recovery of the support of  $m_{a_0, t z_0}$ . This is the object of Chapter 3.

## Chapter 2

# Non-Degeneracy of $\eta_W$

Super-resolution is a challenging problem but also crucial for many applications (see for example Chapter 5). It corresponds in this thesis to the ability to recover, thanks to the BLASSO, the support of a measure whose spikes cluster at some position. This task is mathematically equivalent to the search of a certificate, namely a continuous function bounded by one in uniform norm that interpolates the sign of the amplitudes at the spikes' positions. While this problem is well understood in absence of noise [42, 30] or with noise but when the spikes are separated enough [54], little is known when the data are noisy and the spikes cluster. Chapter 1 proved that the recovery of the support in this framework amounts to the study of the non-degeneracy of a novel pre-certificate  $\eta_W$  called the  $(2N - 1)$ -vanishing pre-certificate. In this Chapter, we propose to study in depth the  $(2N - 1)$ -non-degeneracy of  $\eta_W$  for several filters. We first prove that  $\eta_W$  is locally non-degenerate for any convolution operator. We also provide a closed-form formula for  $\eta_W$  when the forward operator  $\Phi$  is a Gaussian convolution, which in turn enables to show its non-degeneracy. Then we turn to  $\eta_W$  when  $\Phi$  is not a convolution operator (an advantage of our approach with the BLASSO) with the case of forward operators built on a Laplace-like transform. These models are of particular interest to us because they are involved in the MA-TIRF fluorescent microscopy model (see Chapter 5). In this framework, we provide again several closed-form formula and show the non-degeneracy of  $\eta_W$ , justifying the use of the BLASSO to solve these classes of problems. Finally, we generalizes  $\eta_W$  to the case of several clusters of spikes and proves that if they are separated enough then the overall non-degeneracy lies on the non-degeneracy of  $\eta_W$  for only one cluster. In particular, this accounts for the restriction of our study to the setup of one cluster.

## 2.1 Introduction

### 2.1.1 Recap and Positioning of this Chapter

In this chapter, we study the  $(2N - 1)$ -non-degeneracy of  $\eta_W$  called the  $(2N - 1)$ -vanishing pre-certificate, for several different forward operators  $\Phi$ . Chapter [1] proved that the recovery of the support of an initial measure

$$m_{a_0, tz_0} = \sum_{i=1}^N a_{0,i} \delta_{tz_{0,i}} \quad \text{where} \quad \forall i, a_{0,i} > 0 \quad \text{and} \quad tz_{0,i} \in X,$$

in a one dimensional domain  $X$ , when the spikes cluster at 0 (*i.e.*  $t \rightarrow 0$ ) and in presence of noise, by solving the BLASSO

$$\min_{m \in \mathcal{M}(X)} \frac{1}{2} \|\Phi m - y_t\|_{\mathcal{H}}^2 + \lambda |m|(X), \quad (\mathcal{P}_\lambda(y_t))$$

depends on particular properties of  $\eta_W$ .  $\eta_W$  is a continuous function defined as follows

$$\eta_W \stackrel{\text{def.}}{=} \Phi^* p_W,$$

with  $p_W$  the solution of

$$\min \left\{ \|p\|_{\mathcal{H}} ; (\Phi^* p)(0) = 1, (\Phi^* p)'(0) = 0, \dots, (\Phi^* p)^{(2N-1)}(0) = 0 \right\}.$$

Note that

$$p_W = \Psi_{2N-1}^{+,*} \delta_{2N}, \quad (2.1.1)$$

so that  $\eta_W$  can be easily computed numerically. See Proposition [8] for the definition of  $\eta_W$ .

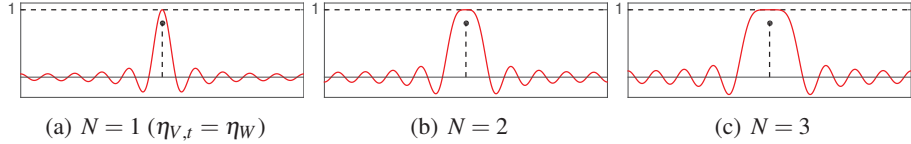


Figure 2.1:  $\eta_W$  for several values of  $N$  when  $\Phi$  is the ideal low-pass filter with a cutoff frequency  $f_c = 10$ .

If  $\eta_W$  is  $(2N - 1)$ -non-degenerate *i.e.*

$$\eta_W^{(2N)}(0) \neq 0 \quad \text{and} \quad \forall x \in X \setminus \{0\}, |\eta_W(x)| < 1,$$

then one proved in Theorem [3] (Section [1.5]) that this non-degeneracy is transferred to any pre-certificate sufficiently close of  $\eta_W$ . Knowing in particular that the vanishing derivatives pre-certificate  $\eta_{V,t}$  (see Definition [5]) converges towards  $\eta_W$  when

$t \rightarrow 0$  (by Proposition 9) this implies the recovery of the support in presence of noise via the BLASSO when  $t \rightarrow 0$  (see Proposition 10).

This transfer theorem (Theorem 3) is therefore an asymptotic way of building certificates (continuous functions assuring that a measure is solution of the BLASSO). Being able to find a certificate for a measure recovering the support of  $m_{a_0, t z_0}$  when the spikes are close ( $t \rightarrow 0$ ) is crucial for the super-resolution problem. There exists other approaches to obtain such functions:

- when the spikes are separated enough, one can show that  $\eta_V$  is non-degenerate (see Theorem 2 in Section 1.3). This is also the case for a slightly different certificate [15].
- By strong algebraic properties based on T-systems, the authors in [128] provide sufficient conditions for the noiseless recovery of spikes without separation for a Gaussian convolution. And in [53], the author shows the non-degeneracy of  $\eta_V$  using similar arguments for a Laplace kernel and two different Gaussian measurements configurations.

However, while these methods provide useful information, the study of the non-degeneracy of  $\eta_W$  gives a systemic approach for any filter to the robustness to noise of the super-resolution problem via the BLASSO. This chapter is devoted to this task in various configurations.

### 2.1.2 Super-Resolution for Laplace Measurements

While in this chapter one presents a study of the non-degeneracy of  $\eta_W$  for convolution operators  $\Phi$  (see Section 2.2), one also looks at the particular case of  $\eta_W$  for operators built on a Laplace-like transform. This class of operators is not translation invariant like convolutions, but recall that it is one of the advantage of our framework to be able to deal with such cases (unlike MUSIC or PRONY). The reason behind the interest for Laplace kernels is the fact that it intervenes in the MA-TIRF fluorescent microscopy model presented in Chapter 5 for the recovery of fluorescent molecules in the 3D volume of a cell. Indeed it enables the recovery of depth information because it models the evanescence of a laser in a sample and its interactions with the fluorophores. As a result, showing the non-degeneracy of  $\eta_W$  for such operators provides theoretical guarantees for the recovery of two or more very close fluorescent molecules aligned along the depth axis. It then backs up, for this application, the use of our algorithm, presented in Chapter 4, to solve the BLASSO.

Solving the inverse problem  $\Phi m = y$  via the BLASSO when  $\Phi$  corresponds to Laplace measurements is a really challenging question. Indeed, Figure 2.2 shows the  $\eta_W$  obtained from Laplace measurements for a varying  $x_0$  ( $\eta_W$  depends on the position of clustering in this setting because the kernel is not invariant under translation) with a fixed number of spikes  $N$  (plus the converse) and one sees that  $\eta_W$  is very flat around  $x_0$ , especially when  $N$  is large or  $x_0$  is far from the origin

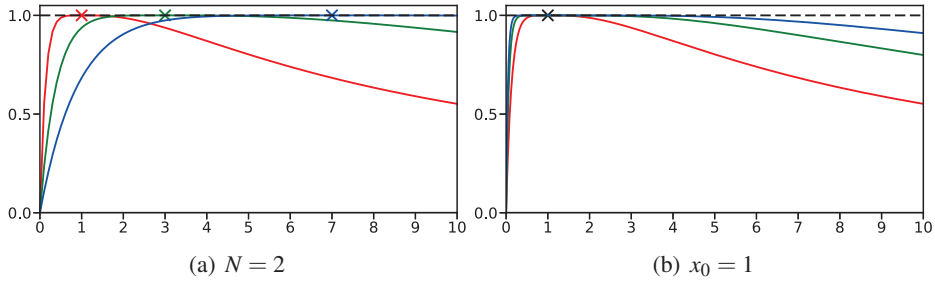


Figure 2.2:  $\eta_W$  for Laplace measurements for a varying  $x_0$  with fixed  $N = 2$  and a fixed  $x_0 = 1$  with varying  $N \in \{2, 4, 6\}$ .

(see Proposition 13 for more details on how this figure is obtained). This indicates that the stability constants are not good. To better understand the difficulty of this problem, one needs to go back to the definition of the Laplace transform.

The bilateral Laplace transform  $\mathcal{L}_b$  is properly defined for distributions  $T \in \mathcal{D}'(\mathbb{R})$  at  $p = \alpha + i\beta \in \mathbb{C}$  if  $e^{-\alpha} T$  is a tempered distribution. Indeed  $\mathcal{L}_b(T)(p)$  is then just the Fourier transform of  $e^{-\alpha} T$  evaluated at  $\beta$ .

$$\mathcal{L}_b(T)(p) = \mathcal{F}(e^{-\alpha \cdot} T)(\beta).$$

This definition gives rigorously the bilateral Laplace transform of for example a locally integrable function or even a Radon measure. For more detail on this matter, see [131]. From the bilateral Laplace transform, using the Heaviside function, one can define the classical Laplace transform of a function  $f$  at  $p \in \mathbb{C}$  by

$$\mathcal{L}(f)(p) = \int_0^{+\infty} f(x) e^{-px} dx.$$

$\mathcal{L}(f)$  is a holomorphic function and an inversion formula exists provided some assumption on  $f$  (see [129, 10]). However in our applications, one only obtains a finite number of values of  $\mathcal{L}(f)$  on  $[0, +\infty[$ , making it impossible to use the inversion formula which requires the knowledge of  $\mathcal{L}(f)$  on some  $\alpha + i\mathbb{R}$  (see [129]). An the inversion of the Laplace transform from values of  $\mathcal{L}(f)$  on  $\mathbb{R}$  is very unstable. Indeed, consider for example (see [10])  $f$  a continuous function and  $g_n(x) = \sin(nx)$ . Then

$$\mathcal{L}(g_n)(p) = \frac{n}{n^2 + p^2},$$

so that

$$\lim_{n \rightarrow +\infty} \mathcal{L}(f + g_n)(p) = \mathcal{L}(f)(p),$$

but

$$\lim_{n \rightarrow +\infty} f + g_n \neq f.$$

### 2.1.3 Contributions

Section 2.2 studies  $\eta_W$  for a convolution operator. We show that in this case,  $\eta_W$  always satisfies the condition  $\eta_W^{(2N)}(0) < 0$  (see Proposition 11). In the particular case of a Gaussian convolution, we provide a formula for  $\eta_W$  (see Proposition 12) and we deduce that

$$\forall x \in \mathbb{R}^*, \quad |\eta_W(x)| < 1.$$

As a result,  $\eta_W$  is  $(2N - 1)$ -non-degenerate.

In Section 2.3, we turn to  $\eta_W$  for Laplace measurements. We show, by providing formulas, that  $\eta_W$  is non-degenerate when  $\Phi$  is the un-normalized and  $L^2$ -normalized Laplace transform (see respectively Proposition 13 and 14).

Finally in Section 2.4, one extends the definition of  $\eta_W$  to the case of several clusters of spikes (Definition 15). Theorem 4 shows that if the clusters are separated enough then the non-degeneracy of the  $\eta_W$  (for several clusters) only depends on the non-degeneracy of the classical  $\eta_W$  (single cluster). This result justifies our choice of defining  $\eta_W$  in Chapter I for spikes collapsing at 0.

## 2.2 $\eta_W$ for a Convolution Operator

In this section, one investigates the  $(2N - 1)$ -non-degeneracy of  $\eta_W$  when  $\Phi$  is a convolution operator *i.e.* :

$$\Phi m \in \mathcal{M}(X) \mapsto \int_X \varphi(x) dm(x) \quad \text{with} \quad \varphi(x) = \tilde{\varphi}(\cdot - x).$$

For the various definitions involving  $\eta_W$  (injectivity hypothesis, non-degeneracy...), see Section 1.4. Moreover we adopt here the same framework.

In the next Section 2.2.1, we prove a general statement on the non-degeneracy of  $\eta_W$  when  $\Phi$  is a convolution: the condition  $\eta_W^{(2N)}(0) < 0$  is always satisfied. Whether the other condition is verified, namely  $|\eta_W| < 1$  (except at 0), has to be checked on a case by case basis.

In Section 2.2.2, we study the particular case of the convolution with a Gaussian. One provides a closed form formula for  $\eta_W$  in this setting and prove that it is  $(2N - 1)$ -non-degenerate (see Proposition 12).

In Section 2.2.3,  $\Phi$  is a convolution by a low pass filter ( $X = \mathbb{T}$ ). One observes numerically that  $\eta_W$  is  $(2N - 1)$ -non-degenerate but we were not able to prove theoretically that  $|\eta_W| < 1$  in  $\mathbb{T} \setminus \{0\}$ .

### 2.2.1 Local Non-Degeneracy of $\eta_W$

Looking at different examples of  $\eta_W$  when  $\Phi$  is a convolution (see Figure 2.3), one sees that  $\eta_W$  seems to always have the right curvature around 0 (concave). This is a general fact stated in the next Proposition.

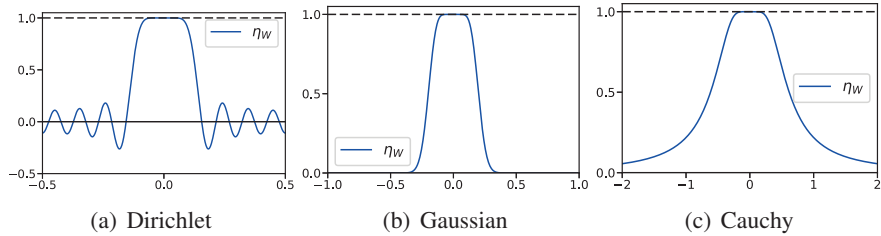


Figure 2.3:  $\eta_W$  for  $N = 4$  and three different convolution operators  $\Phi$ : Dirichlet for  $f_c = 10$ , Gaussian for  $\sigma = 0.05$  and Cauchy for  $\sigma = 0.2$ .

**Proposition 11.** *Assume that  $\Phi$  is a convolution operator (*i.e.* for all  $x \in X$ ,  $\varphi(x) = \tilde{\varphi}(\cdot - x)$  and  $\mathcal{H} = L^2(X)$ ) and  $\mathcal{I}_{2N}$  holds. Suppose also, only in the case when  $X$  is un-bounded, that for all  $0 \leq i \leq 2N - 1$ ,  $\tilde{\varphi}^{(i)}(x) \rightarrow 0$  when  $|x| \rightarrow +\infty$ . Then  $\eta_W^{(2N)}(0) < 0$ .*

The proof of Proposition 11 relies on the study of the structure of the matrices  $\Psi_k^* \Psi_k$  (See Equation (1.4.2) for the definition of  $\Psi_k$ ). One starts by introducing the notion of checkerboard matrices.

**Definition 9.** Let  $n \in \mathbb{N}^*$  and  $A = (a_{i,j})_{i,j} \in \mathbb{R}^{n \times n}$ . We say that  $A$  is a checkerboard matrix if for all  $(i, j)$  such that  $i + j$  is odd,  $a_{i,j} = 0$ .

For an odd  $n$ , such a matrix looks like

$$\begin{pmatrix} a_{1,1} & 0 & a_{1,3} & 0 & \dots & 0 & a_{1,n-2} & 0 & a_{1,n} \\ 0 & a_{2,2} & 0 & a_{2,4} & \dots & a_{2,n-3} & 0 & a_{2,n-1} & 0 \\ \vdots & \vdots & \vdots & \vdots & \ddots & \vdots & \vdots & \vdots & \vdots \\ 0 & a_{n-1,2} & 0 & a_{n-1,4} & \dots & a_{n-1,n-3} & 0 & a_{n-1,n-1} & 0 \\ a_{n,1} & 0 & a_{n,3} & 0 & \dots & 0 & a_{n,n-2} & 0 & a_{n,n} \end{pmatrix}.$$

**Lemma 1.** The set of checkerboard matrices of size  $n \in \mathbb{N}^*$  is an algebra over  $\mathbb{R}$ . As a result the inverse of a checkerboard matrix is also a checkerboard matrix.

*Proof.* The only difficulty is to show that the product of two checkerboard matrices is also a checkerboard matrix. Let  $A = (a_{i,j})_{i,j}$  and  $B = (b_{i,j})_{i,j}$  be two such matrices. Let  $(i, j)$  such that  $i + j$  is odd. Then  $\sum_{k=1}^n a_{i,k} b_{k,j} = 0$  because if  $i + k$  is even then  $(i + j) - (i + k) = j - k$  is odd and  $j - k + 2k = j + k$  is odd, hence  $b_{j,k} = 0$ . On the contrary, if  $i + k$  is odd then  $a_{i,k} = 0$ . So  $AB$  is a checkerboard matrix. The last statement holds because the inverse of any matrix is a polynomial in that matrix.  $\square$

Now we give a more precise result on the structure of some particular checkerboard matrices.

**Lemma 2.** Let  $A = (a_{i,j})_{1 \leq i,j \leq 2n+1}$  be a symmetric positive-definite checkerboard matrix of size  $2n + 1$  such that

$$a_{i,j} = (-1)^{\frac{i-j}{2}} a_{\frac{i+j}{2}, \frac{i+j}{2}}$$

for all  $i, j \in \{1, \dots, 2n + 1\}$  such that  $i + j$  is even, and let  $(b_{i,j})_{1 \leq i,j \leq 2n+1}$  denote the entries of  $A^{-1}$ . Then  $b_{2n+1,2n+1}$  and  $b_{1,2n+1}$  are positive.

*Proof.* The fact that  $b_{2n+1,2n+1}$  is positive, is a direct consequence of the fact that  $A^{-1}$  is symmetric positive-definite because so is  $A$ .

From the expression of the inverse of a matrix using cofactors, one sees that  $b_{1,2n+1} = \det(\hat{A}_{1,2n+1}) / \det(A)$ , where  $\hat{A}_{1,2n+1}$  is the matrix obtained from  $A$  by removing the first row and the last column. Since  $A$  is symmetric positive-definite,  $\det(A) > 0$ , and one needs only show that  $\det(\hat{A}_{1,2n+1}) > 0$ . But one can see that  $\hat{A}_{1,2n+1}$  is a skew symmetric matrix of size  $2n$ , hence

$$\det(\hat{A}_{1,2n+1}) = \text{pf}(\hat{A}_{1,2n+1})^2,$$

where  $\text{pf}(\hat{A}_{1,2n+1})$  is the Pfaffian of the matrix  $\hat{A}_{1,2n+1}$ . For more details on the Pfaffian (definition and proof of the result used here), see [101]. As a result:

$$\det(\hat{A}_{1,2n+1}) \geq 0.$$

Moreover,  $\hat{A}_{1,2n+1}$  is invertible. Indeed if one denotes the columns of  $A$  (resp. the columns  $\hat{A}_{1,2n+1}$ ) by  $C_1, \dots, C_{2n+1}$  (resp.  $\hat{C}_1, \dots, \hat{C}_{2n}$ ), one observes that for  $0 \leq i \leq n-1$ ,  $\hat{C}_{2i+1} \in E_1$  and  $\hat{C}_{2(i+1)} \in E_2$  where

$$\begin{aligned} E_1 &= \text{Span}\{e_{2j+1}; 0 \leq j \leq n-1\}, \\ E_2 &= \text{Span}\{e_{2(j+1)}; 0 \leq j \leq n-1\}, \end{aligned}$$

with  $(e_i)_{1 \leq i \leq 2n}$  is the canonical base of  $\mathbb{R}^{2n}$ . Since  $E_1$  and  $E_2$  are in direct sum, if  $\hat{A}_{1,2n+1}$  is not invertible it means that either  $(\hat{C}_{2i+1})_{0 \leq i \leq n-1}$  or  $(\hat{C}_{2(i+1)})_{0 \leq i \leq n-1}$  is linearly dependent. But it cannot be  $(\hat{C}_{2(i+1)})_{0 \leq i \leq n-1}$  because it would imply that  $(C_{2(i+1)})_{0 \leq i \leq n-1}$  is also linearly dependent, because

$$C_{2(i+1)} = \begin{pmatrix} 0 \\ \hat{C}_{2(i+1)} \end{pmatrix},$$

which would contradict the invertibility of  $A$ .

So it means that  $(\hat{C}_{2i+1})_{0 \leq i \leq n-1}$  must be linearly dependent. However from the structure of the matrix  $A$ , one can see that for all  $0 \leq i \leq n-1$

$$\hat{C}_{2i+1} = \begin{pmatrix} 0 \\ (-1)^{i+1}a_{2i+1,1} \\ 0 \\ -(-1)^{i+1}a_{2i+3,1} \\ \vdots \\ 0 \\ (-1)^{i+1}a_{2(i+n)-1,1} \\ 0 \\ -(-1)^{i+1}a_{2(i+n)+1,1} \end{pmatrix} \quad \text{and} \quad \hat{C}_{2(i+1)} = \begin{pmatrix} (-1)^{i+1}a_{2i+1,1} \\ 0 \\ -(-1)^{i+1}a_{2i+3,1} \\ 0 \\ \vdots \\ (-1)^{i+1}a_{2(i+n)-1,1} \\ 0 \\ -(-1)^{i+1}a_{2(i+n)+1,1} \\ 0 \end{pmatrix}.$$

Thus, a linear combination between the elements of  $(\hat{C}_{2i+1})_{0 \leq i \leq n-1}$  gives the same linear combination between the elements of  $(\hat{C}_{2(i+1)})_{0 \leq i \leq n-1}$ , which contradicts for the same reason as before the invertibility of  $A$ .

Hence  $\hat{A}_{1,2n+1}$  is invertible and  $b_{1,2n+1} > 0$ .  $\square$

The next result describes the structure of the matrices  $\Psi_k^* \Psi_k$  when  $\Phi$  is a convolution operator (*i.e.* for all  $x \in \mathbb{R}$ ,  $\varphi(x) = \bar{\varphi}(\cdot - x)$ ) and  $k \in \mathbb{N}^*$  is odd.

**Lemma 3.** *Suppose that  $\Phi$  is a convolution operator. Then for all  $k \in \mathbb{N}^*$ ,  $\Psi_k^* \Psi_k$  is a checkerboard matrix. Moreover if  $\mathcal{I}_{2N}$  holds, then the entries indexed by  $(1, 2N+1)$  and  $(2N+1, 2N+1)$  of  $(\Psi_{2N}^* \Psi_{2N})^{-1}$  are positive.*

*Proof.* Let  $(i, j)$  such that  $i + j$  is odd and for example  $i > j$  ( $\Psi_k^* \Psi_k$  is symmetric so it does not matter). The entry  $(i, j)$  of  $\Psi_k^* \Psi_k$  is equal to

$$\langle \varphi_{i-1}, \varphi_{j-1} \rangle_{\mathcal{H}}.$$

Recall that in the setting of Proposition 11,  $\mathcal{H} = L^2(X)$  and  $\langle f, g \rangle_{\mathcal{H}} = \int_X f g$ . Successive integrations by parts (we integrate the left term and derive the right term) yield

$$\begin{aligned}\langle \varphi_{i-1}, \varphi_{j-1} \rangle_{\mathcal{H}} &= (-1)^{\frac{i-j+1}{2}} \left\langle \varphi_{\frac{i+j-1}{2}-1}, \varphi_{\frac{i+j+1}{2}-1} \right\rangle_{\mathcal{H}}, \\ \langle \varphi_{i-1}, \varphi_{j-1} \rangle_{\mathcal{H}} &= (-1)^{\frac{i-j-1}{2}} \left\langle \varphi_{\frac{i+j+1}{2}-1}, \varphi_{\frac{i+j-1}{2}-1} \right\rangle_{\mathcal{H}}.\end{aligned}$$

Hence, by the symmetry of the scalar product, one obtains that

$$\langle \varphi_{i-1}, \varphi_{j-1} \rangle_{\mathcal{H}} = -\langle \varphi_{i-1}, \varphi_{j-1} \rangle_{\mathcal{H}}.$$

This implies that  $\langle \varphi_{i-1}, \varphi_{j-1} \rangle_{\mathcal{H}} = 0$  for odd values of  $i + j$ , so that  $\Psi_k^* \Psi_k$  is a checkerboard matrix (see Definition 9).

Moreover, similar computations show that when  $i + j$  is even

$$\langle \varphi_{i-1}, \varphi_{j-1} \rangle_{\mathcal{H}} = (-1)^{\frac{i-j}{2}} \left\langle \varphi_{\frac{i+j}{2}-1}, \varphi_{\frac{i+j}{2}-1} \right\rangle_{\mathcal{H}}.$$

If  $\mathcal{J}_{2N}$  holds,  $\Psi_{2N}^* \Psi_{2N}$  is symmetric positive-definite. As a result  $\Psi_{2N}^* \Psi_{2N}$  satisfies the assumptions of Lemma 2, so the entries  $(1, 2N+1)$  and  $(2N+1, 2N+1)$  of  $(\Psi_{2N}^* \Psi_{2N})^{-1}$  are positive.  $\square$

One can now prove that  $\eta_W^{(2N)}(0) < 0$  when  $\Phi$  is a convolution operator and  $\mathcal{J}_{2N}$  holds.

*Proof of Proposition 11.* Since  $\eta_W = \Phi^* p_W$ , we deduce that

$$\eta_W^{(2N)}(0) = \langle \varphi_{2N}, p_W \rangle_{\mathcal{H}} = \langle \varphi_{2N}, \Psi_{2N-1} (\Psi_{2N-1}^* \Psi_{2N-1})^{-1} \delta_{2N} \rangle_{\mathcal{H}}.$$

Consider the symmetric positive definite matrix

$$\Psi_{2N}^* \Psi_{2N} = \begin{pmatrix} \Psi_{2N-1}^* \Psi_{2N-1} & \Psi_{2N-1}^* \varphi_{2N} \\ [\Psi_{2N-1}^* \varphi_{2N}]^* & \|\varphi_{2N}\|_{\mathcal{H}}^2 \end{pmatrix} \in \mathbb{R}^{2N \times 2N}.$$

Observe that  $\Psi_{2N-1}^* \Psi_{2N-1}$  is invertible, and that

$$S \stackrel{\text{def.}}{=} \|\varphi_{2N}\|_{\mathcal{H}}^2 - \langle \varphi_{2N}, \Psi_{2N-1} (\Psi_{2N-1}^* \Psi_{2N-1})^{-1} \Psi_{2N-1}^* \varphi_{2N} \rangle_{\mathcal{H}} \neq 0.$$

Indeed, since  $(\varphi_0, \dots, \varphi_{2N})$  has full rank, one has

$$S = \|(\text{Id}_{\mathcal{H}} - \Pi_{2N-1}) \varphi_{2N}\|_{\mathcal{H}}^2 > 0$$

where

$$\Pi_{2N-1} \stackrel{\text{def.}}{=} P_{(\text{Im } \Psi_{2N-1})^\perp} = \text{Id}_{\mathcal{H}} - \Psi_{2N-1} (\Psi_{2N-1}^* \Psi_{2N-1})^{-1} \Psi_{2N-1}^*.$$

Thus, we may apply the block inversion formula, and  $(\Psi_{2N}^* \Psi_{2N})^{-1}$  is of the form

$$(\Psi_{2N}^* \Psi_{2N})^{-1} = \frac{1}{\|(\text{Id}_{\mathcal{H}} - \Pi_{2N-1})\varphi_{2N}\|_{\mathcal{H}}^2} \times$$

$$\begin{pmatrix} * * * & -(\Psi_{2N-1}^* \Psi_{2N-1})^{-1} \Psi_{2N-1}^* \varphi_{2N} \\ -[(\Psi_{2N-1}^* \Psi_{2N-1})^{-1} \Psi_{2N-1}^* \varphi_{2N}]^* & 1 \end{pmatrix}$$

Lemma 3 ensures that the entry  $(2N+1, 1)$  of  $(\Psi_{2N}^* \Psi_{2N})^{-1}$  is (strictly) positive. This precisely means that

$$-\frac{\langle \varphi_{2N}, \Psi_{2N-1}(\Psi_{2N-1}^* \Psi_{2N-1})^{-1} \delta_{2N} \rangle_{\mathcal{H}}}{\|(\text{Id}_{\mathcal{H}} - \Pi_{2N-1})\varphi_{2N}\|_{\mathcal{H}}^2} > 0,$$

and as a result  $\eta_W^{(2N)}(0) = \langle \varphi_{2N}, p_W \rangle_{\mathcal{H}} < 0$ .  $\square$

From this result, one can show that the local non-degeneracy of  $\eta_W$  ( $\eta_W^{(2N)}(0) < 0$ ) is transferred to any pre-certificate  $\eta$  sufficiently close of  $\eta_W$  in the sense that  $\eta$  is non-degenerate in a neighborhood of the spikes positions  $tz$ . This is the object of the following Remark.

*Remark 4.* Thanks to Proposition 11 and the first part of the proof of Theorem 3 (which is given in Section 1.5), note that the following is true: there exist  $C_W > 0$ ,  $t_W > 0$  such that for all  $t \in (0, t_W)$ ,  $z \in X^N$  with pairwise distinct coordinates and  $|z|_{\infty} \leq R_W$ , there exists  $r^+ > 0$  with  $r^+ > \max_{1 \leq i \leq N} t_W z_i$  and  $r^- < 0$  with  $r^- < \min_{1 \leq i \leq N} t_W z_i$  such that for all  $\eta \in \mathcal{C}^{2N}(X) \cap W^{2N,\infty}(X)$  satisfying for all  $1 \leq i \leq N$ ,  $\eta(tz_i) = 1$  and  $\eta'(tz_i) = 0$ :

$$\left( \forall \ell \in \{0, \dots, 2N\}, \|\eta^{(\ell)} - \eta_W^{(\ell)}\|_{\infty, X} \leq C_W \right)$$

$$\implies \left( \forall x \in (r^-, r^+) \setminus \bigcup_i \{tz_i\}, |\eta(x)| < 1 \quad \text{and} \quad \forall i \in \{1, \dots, N\}, \eta''(tz_i) < 0 \right).$$

However whether  $\eta$  is globally non-degenerate (i.e.  $|\eta| < 1$  outside the neighborhood) depends on the other part of the definition of the non-degeneracy of  $\eta_W$ :  $|\eta_W| < 1$ . Thus, in general, we need an explicit expression of  $\eta_W$  to assert the global non-degeneracy property.

### 2.2.2 $\eta_W$ for the Gaussian Convolution

For the Gaussian convolution on  $X = \mathbb{R}$ , we prove that  $\eta_W$  is always  $(2N-1)$ -non-degenerate. This is stated in Proposition 12 below.

If one denotes by  $\eta_{W,\sigma}$ , the  $(2N-1)$  vanishing derivatives pre-certificate associated to the filter  $\varphi_{\sigma} : x \in \mathbb{R} \mapsto e^{-\frac{x^2}{2\sigma^2}}$ , then  $\eta_{W,\sigma} = \eta_{W,1}(\frac{\cdot}{\sigma})$ . As a result we only consider the case of  $\sigma = 1$  in Proposition 12.

**Proposition 12.** Assume that  $X = \mathbb{R}$ ,  $\mathcal{H} = L^2(\mathbb{R})$  and  $\Phi$  is a convolution operator, i.e. for all  $x \in \mathbb{R}$ ,  $\varphi(x) = \tilde{\varphi}(\cdot - x)$ , where  $\tilde{\varphi} : x \in \mathbb{R} \mapsto e^{-x^2/2}$  is a Gaussian. Then the associated  $(2N-1)$ -vanishing derivatives pre-certificate is:

$$\forall x \in \mathbb{R}, \quad \eta_W(x) = e^{-\frac{x^2}{4}} \sum_{k=1}^N \frac{x^{2k}}{2^{2k} k!}. \quad (2.2.1)$$

In particular,  $\eta_W$  is  $(2N-1)$ -non-degenerate.

Figure 2.4 shows  $\eta_W$  for the Gaussian filter with an increasing number  $N$  of spikes.

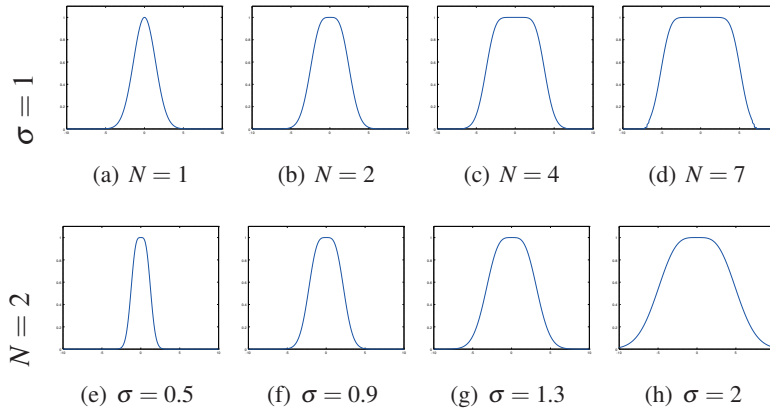


Figure 2.4:  $\eta_W$  for a Gaussian filter.

*Proof of Proposition 12.* Let denote  $(a_k)_{0 \leq k \leq 2N-1}$  the coefficients of the first column of the matrix  $(\Psi_{2N-1}^* \Psi_{2N-1})^{-1}$ . Then one knows that for all  $x \in \mathbb{R}$ ,

$$\eta_W(x) = \sum_{k=0}^{N-1} a_{2k} \varphi \star \varphi^{(2k)}(x).$$

Since  $\varphi \star \varphi = x \rightarrow \sqrt{\pi} e^{-x^2/4}$ , we get that for all  $x \in \mathbb{R}$ ,

$$\eta_W(x) = \sqrt{\pi} e^{-x^2/4} \sum_{k=0}^{N-1} a_{2k} \hat{H}_{2k}(x), \quad (2.2.2)$$

where  $\hat{H}_{2k}$  is the Hermite polynomial of order  $2k$  associated to  $x \rightarrow e^{-x^2/4}$ .

Now let us show (2.2.1) recursively on  $N \in \mathbb{N}^*$ . If  $N = 1$ , we have that  $\eta_W(x) = e^{-x^2/4}$  because  $\Psi_{2N-1}^* \Psi_{2N-1} = (\sqrt{\pi})$ . Suppose that the property is true for some  $N \in \mathbb{N}^*$ , i.e.,

$$\eta_{W,N}(x) = e^{-x^2/4} \sum_{k=0}^{N-1} \frac{x^{2k}}{2^{2k} k!}, \quad (2.2.3)$$

where we use the notation  $\eta_{W,N}$  to recall that this is the function  $\eta_W$  for  $N$  spikes. Then form for all  $x \in \mathbb{R}$ ,

$$\kappa(x) \stackrel{\text{def.}}{=} e^{x^2/4} (\eta_{W,N+1}(x) - \eta_{W,N}(x)).$$

$\kappa$  is a polynomial of degree  $2N$  (thanks to (2.2.2)), it satisfies  $\kappa(0) = 0$  and for all  $1 \leq i \leq 2N-1$ ,  $\kappa^{(i)}(0) = 0$ . As a result for all  $x \in \mathbb{R}$ ,

$$\kappa(x) = \lambda x^{2N},$$

for some  $\lambda \in \mathbb{R}$ .

It remains to show that  $\lambda = \frac{1}{2^{2N}N!}$ . Remark that for all  $x \in \mathbb{R}$ ,  $\kappa^{(2N)}(x) = \lambda(2N)!$  and on the other hand  $\kappa^{(2N)}(0) = -\eta_{W,N}^{(2N)}(0)$  because  $\eta_{W,N+1}^{(2N)}(0) = 0$  by definition of  $\eta_{W,N+1}$ . So it is enough to show that,

$$\eta_{W,N}^{(2N)}(0) = -\frac{(2N)!}{2^{2N}N!}. \quad (2.2.4)$$

Thanks to the Leibniz formula applied to (2.2.3), we have the following formula,

$$\eta_{W,N}^{(2N)}(0) = \sum_{k=0}^{N-1} \binom{2N}{2k} \hat{H}_{2N-2k}(0) \frac{(2k)!}{2^{2k}k!}.$$

Since  $\hat{H}_{2N-2k}(0) = (-1)^{N-k} \frac{(2N-2k-1)!}{2^{2N-2k-1}(N-1-k)!}$ , thanks to Lemma 4 below, one obtains,

$$\begin{aligned} \eta_{W,N}^{(2N)}(0) &= \sum_{k=0}^{N-1} \frac{(2N)!}{(2N-2k)!(2k)!} \cdot (-1)^{N-k} \frac{(2N-2k-1)!}{2^{2N-2k-1}(N-1-k)!} \cdot \frac{(2k)!}{2^{2k}k!} \\ &= -\frac{(2N)!}{2^{2N}N!} \sum_{k=0}^{N-1} \frac{N(N-1)!}{(N-1-k)!k!} \cdot \frac{2 \cdot (-1)^{N-1-k}}{(2N-2k)} \\ &= -\frac{(2N)!}{2^{2N}N!} N \sum_{k=0}^{N-1} \binom{N-1}{k} (-1)^{N-1-k} \int_0^1 x^{N-1-k} dx \\ &= -\frac{(2N)!}{2^{2N}N!} N \underbrace{\int_0^1 (1-x)^{N-1} dx}_{=1/N}. \end{aligned}$$

This ends the recursive proof and thus we have (2.2.1).

To conclude that  $\eta_W$  is  $(2N-1)$ -non-degenerate, it remains to show that for all  $x \in \mathbb{R}^*$ ,  $|\eta_W(x)| < 1$ , since we already know that  $\eta_W^{(2N)}(0) < 0$  thanks to (2.2.4). But we have, thanks to (2.2.1), that for all  $x \in \mathbb{R}^*$ ,  $0 < \eta_W(x) < 1$  since  $\sum_{k=0}^{N-1} \frac{x^{2k}}{2^{2k}k!}$  is the truncated power series of  $e^{x^2/4}$ .  $\square$

**Lemma 4.** One has for all  $k \in \mathbb{N}$ ,

$$\hat{H}_{2k+2}(0) = (-1)^{k+1} \frac{(2k+1)!}{2^{2k+1} k!}. \quad (2.2.5)$$

*Proof.* One knows that  $H_{k+2}(x) = xH_{k+1}(x) - (k+1)H_k(x)$  where  $H_k$  is the Hermite polynomial of order  $k$  associated to  $x \mapsto e^{-x^2/2}$ . Thus  $H_{2k+2}(0) = -(2k+1)H_{2k}(0)$  and then,

$$H_{2k+2}(0) = (-1)^{k+1} \frac{(2k+1)!}{2^k k!}. \quad (2.2.6)$$

Now, remark that  $\hat{H}_k(x) = 2^{-k/2} H_k(x/\sqrt{2})$ , so that together with (2.2.6) we get the expected result (2.2.5).  $\square$

### 2.2.3 $\eta_W$ for a Low-Pass Filter

When  $\Phi$  is a convolution over the 1-D torus ( $X = \mathbb{T}$ ), one knows thanks to Proposition 11 that  $\eta_W^{(2N)}(0) < 0$  and one observes numerically that  $|\eta_W| < 1$  (except at 0) so that  $\eta_W$  is  $(2N-1)$ -non degenerate for the ideal low pass filter for any value  $N$  such that  $N \leq f_c$ .

Figure 2.5 shows  $\eta_W$  for an ideal low pass filter when  $N = 2$  with  $f_c$  increasing.

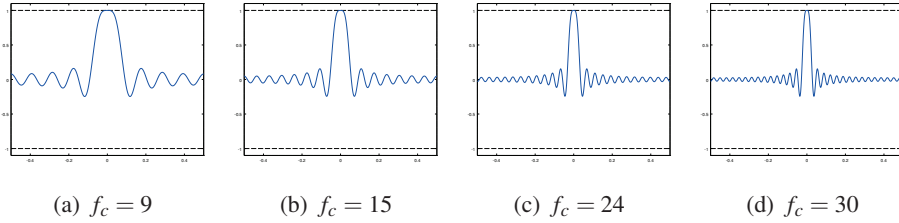


Figure 2.5:  $\eta_W$  for the ideal low pass filter with  $f_c$  increasing with  $N = 2$ .

However, for some filters, the associated  $\eta_W$  might be degenerate. This is illustrated in Figure 2.6 where  $\eta_W$  is displayed for several filters with increasing complexity *i.e.* we consider low pass filters with a fixed cutoff frequency, with increasing extreme Fourier coefficients (starting with a slowly varying filter). Remark that the last two  $\eta_W$  (in red) are degenerate, as they correspond to the filters with the higher complexity (the Fourier coefficients increase the most with the frequency).

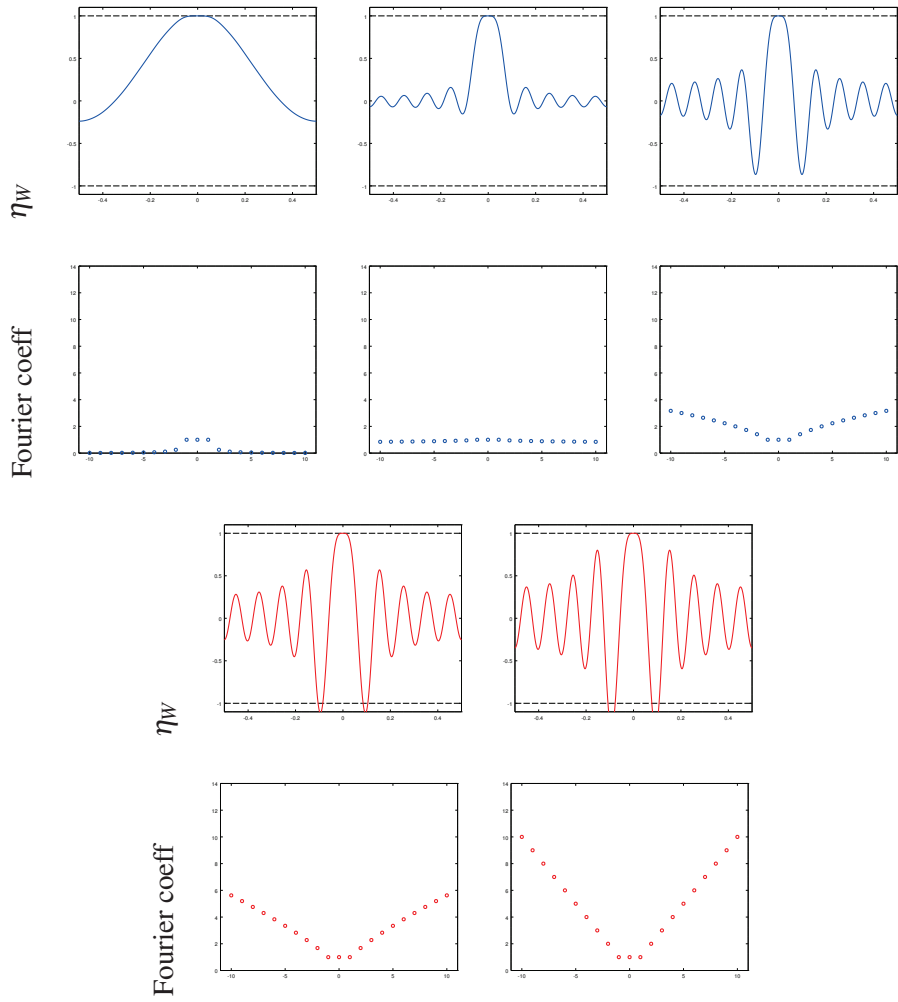


Figure 2.6:  $\eta_W$  for a low pass filter for  $f_c = 10$  with increasing high frequency content. The curve showing  $\eta_W$  is in blue when it is  $(2N - 1)$ -non-degenerate and in red when it is degenerate.

## 2.3 $\eta_W$ for Laplace-like Operators

In this section, we propose to study  $\eta_W$  when  $\Phi$  is not a convolution operator (recall that this is one of the advantage of our approach). One considers a series of operators based on the Laplace transform. The main reason behind our interest for this setup is Chapter 5 where we study a 3D forward model for a fluorescent microscopy problem which uses a Laplace transform for the recovery of depth information. As a result, by looking at  $\eta_W$  for a Laplace transform, we aim at providing some theoretical guarantees concerning the super-resolution problem in this framework which can then back up our numerical experiments in Chapter 5.

In the next Section 2.3.1, we first detail the different models considered. In Section 2.3.2, we give two formulas for  $\eta_W$  in two different setups (continuous) and show that it is  $(2N - 1)$ -non-degenerate.

### 2.3.1 Laplace-Based Forward Models

One considers in the following a Laplace-type transform. For the sake of simplicity, we suppose that in all this section  $X = [\varepsilon, x_b] \subset \mathbb{R}_+^*$  is a compact interval. This choice assures that  $\varphi$  satisfies all the required assumptions for every of the Laplace-like transform models presented below. One supposes also that  $\mathcal{H} = L^2(\mathbb{R}_+, \mu)$  where  $\mu$  is a positive Radon measure on  $X$ . The following kernel is used:

$$\forall x \in X, \quad \varphi(x) = (s \mapsto \xi(x)e^{-sx}) \in \mathcal{H} \quad (2.3.1)$$

with  $\xi \in \mathcal{C}(X)$  is non-negative. In particular here,

$$(\Phi^* p)(x) = \xi(x) \int_{\mathbb{R}_+} e^{-sx} p(s) d\mu(s).$$

Here,  $\mu$  is a weighting function. A high value of  $\mu(s)$  indicates that a high number of measurements have been taken for the measurement indexed by  $s$  (or equivalently that there is less noise in the measurement). A value  $\mu(s) = 0$  indicates that this measurement is not available. In order to model discrete measurements, one can define  $\mu = \sum_{k=1}^K \mu_k \delta_{s_k}$  where  $s_k$  are the sampling values. This corresponds to using  $\mathcal{H} = \mathbb{R}^K$  and  $\varphi(x) \stackrel{\text{def.}}{=} (\xi(x)\mu_k e^{-s_k x})_{k=1}^K \in \mathcal{H}$ .

The normalizing function  $\xi$  can be chosen freely. A common normalization choice is

$$\xi(x)^2 = \frac{1}{\int_{\mathbb{R}_+} e^{-2sx} d\mu(s)}, \quad (2.3.2)$$

which guarantees that  $\|\varphi(x)\|_{\mathcal{H}} = 1$  for all  $x \in X$ . See Section 2.3.2 for more details for this normalization.

Note that both  $\mu$  and  $\xi$  can be chosen freely by the user that wants to solve the acquisition problem, since they act separately on the input and output variables  $x, s$ .

The correlation function reads for these class of operators:

$$\forall x, x' \in X, \quad c_\varphi(x, x') = \xi(x)\xi(x') \int_{\mathbb{R}_+} e^{-(x+x')s} d\mu(s).$$

Note that the choice (2.3.2) of normalization ensures that  $c_\varphi(x, x) = 1$

For instance, for a sampling density of the form  $\mu(s) = e^{-\alpha s}$  for some  $\alpha > 0$ , one obtains

$$\xi(x) = \sqrt{2(x+\alpha)} \quad \text{and} \quad c_\varphi(x, x') = 2 \frac{\sqrt{(x+\alpha)(x'+\alpha)}}{x+x'+2\alpha}. \quad (2.3.3)$$

Note that the parameter  $\alpha$  has only the effect of shifting all Dirac location, i.e. making the change of variable  $x \mapsto x - \alpha$  is equivalent to replacing  $\alpha$  by 0.

We now detail in the following paragraphs, several particular cases covered by Equation 2.3.1. We are particularly interested in this thesis in the last two models presented (discretized un-normalized and discretized  $L^2$ -normalized) because they are involved in Chapter 5.

### Un-normalized Laplace for $\mu = \mathbb{1}_{[0, +\infty)} \mathcal{L}$ .

One supposes that  $\mu = \mathbb{1}_{[0, +\infty)} \mathcal{L}$ , where  $\mathcal{L}$  is the Lebesgue measure on  $\mathbb{R}_+$ , and  $\xi = 1$ . Then  $\varphi(x) = e^{-x}$  and one has:

$$c_\varphi(x, x') = \frac{1}{x+x'} \quad (2.3.4)$$

$$\partial_1^i \partial_2^j c_\varphi(x, x') = (i+j)! \frac{(-1)^{i+j}}{(x+x')^{i+j}} \quad (2.3.5)$$

### $L^2$ -Normalized Laplace for $\mu = \mathbb{1}_{[0, +\infty)} \mathcal{L}$ .

One supposes that  $\mu = \mathbb{1}_{[0, +\infty)} \mathcal{L}$ , where  $\mathcal{L}$  is the Lebesgue measure on  $\mathbb{R}_+$ , and:

$$\forall x \in X, \quad \xi(x) = \sqrt{\frac{1}{\int_{\mathbb{R}_+} e^{-2sx} ds}} = \sqrt{2x},$$

so that for all  $x \in X$ ,  $\varphi(x) : s \mapsto \sqrt{2x}e^{-sx}$  and  $\|\varphi(x)\|_{\mathcal{H}} = 1$ . One gets:

$$\forall x, x' \in X, \quad c_\varphi(x, x') \stackrel{\text{def.}}{=} \langle \varphi(x), \varphi(x') \rangle_{\mathcal{H}} = \frac{2\sqrt{xx'}}{x+x'}.$$

### Un-normalized Band-limited Laplace.

One supposes that  $\mu = \mathbb{1}_{[a, b]} \mathcal{L}$ , where  $0 \leq a < b$  and  $\mathcal{L}$  is the Lebesgue measure on  $\mathbb{R}_+$ , and  $\xi = 1$ .

Then one has

$$c_\varphi(x, x') = \Delta e^{-m(x+x')} \sinhc\left(\Delta \frac{x+x'}{2}\right) \quad \text{where} \quad \sinhc(u) \stackrel{\text{def.}}{=} \frac{\sinh(u)}{u}$$

so that  $\Delta = b - a$  encodes the bandwidth of the measurement, and  $m = (a+b)/2$  the decay of the kernel.

**$L^2$ -normalized Band-limited Laplace.**

One supposes that  $\mu = \mathbb{1}_{[a,b]} \mathcal{L}$ , where  $0 \leq a < b$  and  $\mathcal{L}$  is the Lebesgue measure on  $\mathbb{R}_+$ , and  $\xi$  is defined so that  $\|\varphi(x)\|_{\mathcal{H}} = 1$ .

The normalized Band-limited kernel has correlation:

$$c_\varphi(x, x') = \frac{\sinh\left(\Delta \frac{x+x'}{2}\right)}{\sqrt{\sinh(\Delta x) \sinh(\Delta x')}} \frac{2\sqrt{xx'}}{x+x'}$$

**Discretized Un-normalized Laplace.**

One supposes that  $\mu = \sum_{k=1}^K \delta_{s_k}$  and  $\xi = 1$ . Then  $\varphi(x) = (e^{-s_k x})_{k=1}^K \in \mathbb{R}^K$  and:

$$c_\varphi(x, x') = \sum_{k=1}^K e^{-s_k(x+x')}.$$

If we make the assumption that we discretize uniformly the interval  $[a, b]$  i.e.  $s_k = a + \frac{k}{K-1}(b-a)$  for  $k \in \{0, \dots, K-1\}$ , then:

$$c_\varphi(x, x') = e^{-m(x+x')} \frac{\sinh\left(\Delta \frac{K}{K-1} \frac{x+x'}{2}\right)}{\sinh\left(\Delta \frac{x+x'}{2}\right)},$$

where  $\Delta = b - a$  and  $m = (a+b)/2$ .

**Discretized  $L^2$ -normalized Laplace.**

One supposes that  $\mu = \sum_{k=1}^K \delta_{s_k}$  and  $\xi(x) = (\sum_{k=1}^K e^{-2s_k x})^{-1/2}$ . Then  $\varphi(x) = \xi(x)(e^{-s_k x})_{k=1}^K \in \mathbb{R}^K$ ,  $\|\varphi(x)\|_{\mathcal{H}} = 1$  and:

$$c_\varphi(x, x') = \xi(x)\xi(x') \sum_{k=1}^K e^{-s_k(x+x')}.$$

If we make the assumption that we discretize uniformly the interval  $[a, b]$  i.e.  $s_k = a + \frac{k}{K-1}(b-a)$  for  $k \in \{0, \dots, K-1\}$ , then:

$$c_\varphi(x, x') = \sqrt{\frac{\sinh\left(\Delta \frac{K}{K-1} x\right) \sinh\left(\Delta \frac{K}{K-1} x'\right)}{\sinh\left(\Delta \frac{K}{K-1} x\right) \sinh\left(\Delta \frac{K}{K-1} x'\right)}} \frac{\sinh\left(\Delta \frac{K}{K-1} \frac{x+x'}{2}\right)}{\sinh\left(\Delta \frac{x+x'}{2}\right)},$$

where  $\Delta = b - a$  and  $m = (a+b)/2$ .

**2.3.2 Several Formulas for  $\eta_W$** 

One supposes that  $N$  spikes are clustered at positions  $x_0 \in \overset{\circ}{X}$ . The aim of this section is to provide some explicit formula for the  $(2N-1)$ -vanishing derivatives pre-certificate  $\eta_W$ , in several particular cases. Because the Laplace based kernels  $\varphi$  are not translation invariant, the results provided in this section depends on  $x_0$ .

The knowledge of  $\eta_W$  gives the asymptotic of the dual certificates, and its non-degeneracy provides the error bounds given in Section 3.2 with Theorem 5. It guarantees identifiability and stability for measures that are sufficiently clustered around the point  $x_0 \in X$ .

Let us recall that, if  $\Psi_{2N}$  has full rank,  $\eta_W$  is the unique function of the form

$$\eta_W(x) = \sum_{k=0}^{2N-1} \alpha_k \partial_2^k c_\varphi(x, x_0), \quad \text{where } (\alpha_k)_{0 \leq k \leq 2N-1} \subset \mathbb{R} \quad \text{and} \quad (2.3.6)$$

$$\eta_W(x_0) = 1, \eta'_W(x_0) = 0, \dots, \eta^{(2N-1)}_W(x_0) = 0. \quad (2.3.7)$$

**Preliminaries.** One begins with two elementary lemmas. The first one is a simple consequence of the Faa di Bruno lemma.

**Lemma 5.** *Let  $I, I' \subset \mathbb{R}$  be open intervals, and  $h : I' \rightarrow I$  be a smooth diffeomorphism. Let  $x_0 \in I$ ,  $t_0 := h^{-1}(x_0) \in I'$ , and let  $\eta : I \rightarrow \mathbb{R}$  be a smooth function.*

*Then  $\eta$  satisfies*

$$\eta(x_0) = 1, \eta'(x_0) = 0, \dots, \eta^{(2N-1)}(x_0) = 0, \quad (2.3.8)$$

*if and only if  $v \stackrel{\text{def.}}{=} \eta \circ h$  satisfies*

$$v(t_0) = 1, v'(t_0) = 0, \dots, v^{(2N-1)}(t_0) = 0. \quad (2.3.9)$$

*Moreover, in that case,  $v^{(2N)}(t_0) = \eta^{(2N)}(x_0)(h'(t_0))^{2N}$ .*

The next one follows from the general Leibniz rule.

**Lemma 6.** *Let  $I$  be an open interval,  $t_0 \in I$  and let  $g : I \rightarrow \mathbb{R}$ ,  $\eta : I \rightarrow \mathbb{R}$  be two smooth functions. If  $\eta$  satisfies:*

$$\eta(x_0) = 1, \eta'(x_0) = 0, \dots, \eta^{(2N-1)}(x_0) = 0, \quad (2.3.10)$$

*then  $P \stackrel{\text{def.}}{=} \eta \times g$  satisfies:*

$$P(x_0) = g(x_0), P'(x_0) = g'(x_0), \dots, P^{(2N-1)}(x_0) = g^{(2N-1)}(x_0). \quad (2.3.11)$$

*In particular, if  $P \in \mathbb{R}_{2N-1}[T]$ , then  $P$  is the Taylor expansion of  $g$  at  $x_0$  of order  $2N-1$ , and  $\eta^{(2N)}_W(x_0) = -g^{(2N)}(x_0)/g(x_0)$  provided that  $g(x_0) \neq 0$ .*

One can now provide expressions of  $\eta_W$  and show that it is  $(2N-1)$ -non-degenerate for the following cases.

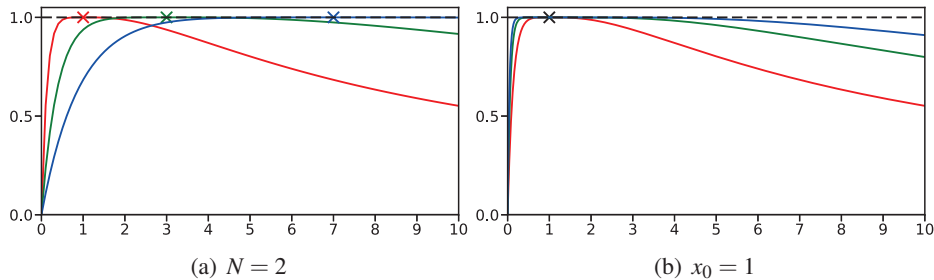


Figure 2.7:  $\eta_W$  for the un-normalized Laplace model for a varying  $x_0$  with fixed  $N = 2$  and a fixed  $x_0 = 1$  with varying  $N \in \{2, 4, 6\}$ .

**Un-normalized Laplace.** The following Proposition provides a formula for  $\eta_W$  in this setting and proves that it is non-degenerate.

**Proposition 13.**  $\eta_W$  is  $(2N - 1)$ -non-degenerate. More precisely, we have the following formula:

$$\forall x \in X, \quad \eta_W(x) = 1 - \left( \frac{x - x_0}{x + x_0} \right)^{2N}. \quad (2.3.12)$$

In Figure 2.7, one sees that when the position  $x_0$  where the spikes cluster increases then the curvature of  $\eta_W$  at  $x_0$  decreases. This means that it is harder in this situation to perform the recovery. It reflects the exponential decay of the kernel  $\varphi$ . Similar observations are made in Chapter 4 and 5 in our numerical experiments. Furthermore when  $N$  increases with a fixed  $x_0$  the curvature at  $x_0$  of  $\eta_W$  also decreases. This is logical because recovering more spikes that cluster at  $x_0$  is harder.

*Proof of Proposition 13.* From Equations (2.3.6) and (2.3.4), one sees that  $\eta_W$  has the form

$$\eta_W(x) = \sum_{k=1}^{2N} \frac{\beta_k}{(x+x_0)^k}, \quad \text{where } \beta_k \in \mathbb{R}.$$

We set  $h : t \mapsto (1/t - x_0)$ ,  $v \stackrel{\text{def.}}{=} \eta \circ h$  so that

$$v(t) = \sum_{k=1}^{2N} \beta_k t^k,$$

is a polynomial with degree at most  $2N$  with  $v(0) = 0$ . By Lemma 5,  $v$  satisfies (2.3.9) at  $t_0 \stackrel{\text{def.}}{=} \frac{1}{2x_0}$ . As a result,  $v(t) = 1 + \beta_{2N}(t - t_0)^{2N}$ . The constant  $\beta_{2N}$  is fixed by the condition  $v(0) = 0$ , so that  $v(t) = 1 - \left(\frac{t-t_0}{t_0}\right)^{2N}$ , and  $\eta_W$  is given by (2.3.12).

The  $2N$  derivative is  $v^{(2N)}(t_0) = -\frac{(2N)!}{(t_0)^{2N}}$ , so that  $\eta_W(x_0) = -\frac{(2N)!}{(2x_0)^{2N}} < 0$ .  $\square$

**$L^2$ -Normalized Laplace.** The following Proposition provides a formula for  $\eta_W$  in this setting and proves that it is non-degenerate.

**Proposition 14.**  $\eta_W$  is  $(2N - 1)$ -non-degenerate. More precisely, we have the following formula:

$$\forall x \in X, \quad \eta_W(x) = \frac{2\sqrt{xx_0}}{x+x_0} \sum_{k=0}^{N-1} \frac{(2k)!}{2^{2k}(k!)^2} \left( \frac{x-x_0}{x+x_0} \right)^{2k}. \quad (2.3.13)$$

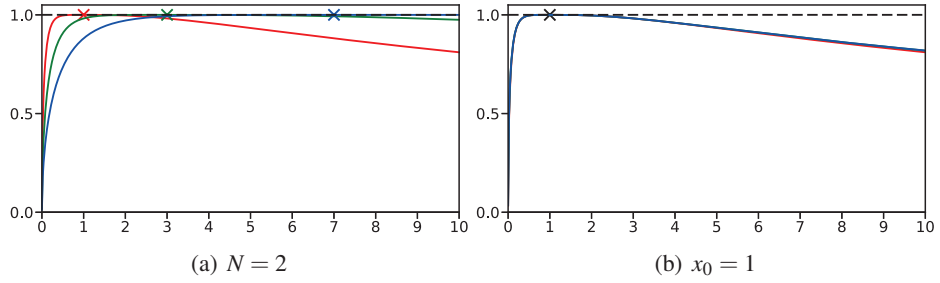


Figure 2.8:  $\eta_W$  for the normalized Laplace model for a varying  $x_0$  with fixed  $N = 2$  and a fixed  $x_0 = 1$  with varying  $N \in \{2, 4, 6\}$ .

In Figure 2.8, one sees that when the position  $x_0$  where the spikes cluster increases then the curvature of  $\eta_W$  at  $x_0$  decreases. The interpretation is the same as in the previous paragraph. When  $N$  increases with a fixed  $x_0$ ,  $\eta_W$  almost does not change.

*Proof of Proposition 14.* From the general Leibniz rule, we have for all  $n \in \{0, \dots, 2N-1\}$  and for all  $x, x' \in X$ :

$$\frac{d^n}{dx'^n} (c_\varphi(x, x')) = 2\sqrt{x} \sum_{k=0}^n \binom{n}{k} \frac{d^{n-k}}{dx'^{n-k}} (\sqrt{x'}) \frac{d^k}{dx'^k} \left( \frac{1}{x+x'} \right)$$

Evaluating this expression at  $x' = x_0$ , one gets that:

$$\partial_2^n c_\varphi(x, x_0) = \sqrt{x} \sum_{k=0}^n \frac{\alpha_k}{(x+x_0)^{k+1}},$$

for some coefficients  $\alpha_k \in \mathbb{R}$ . As a result,  $\eta_W$  is the unique function the form

$$\eta_W(x) = \sqrt{x} \sum_{k=0}^{2N-1} \frac{\beta_k}{(x+x_0)^{k+1}}$$

for some coefficients  $\beta_k \in \mathbb{R}$ , which satisfies (2.3.7). As before, we set  $t = \frac{1}{x+x_0}$ , that is  $x = h(t) \stackrel{\text{def.}}{=} \frac{1}{t} - x_0$ , and  $h$  is a diffeomorphism of  $(0, 1/x_0)$  onto  $(0, +\infty)$ . Then:

$$\eta_W \circ h(t) = \sqrt{\frac{1}{t} - x_0 t} P(t) = \sqrt{t - t^2 x_0} P(t),$$

where  $P(T) = \sum_{k=0}^{2N-1} \beta_k T^k \in \mathbb{R}_{2N-1}[T]$ .

By Lemma 5 and Lemma 6,  $P$  is the Taylor expansion of order  $2N - 1$  of  $g : t \mapsto \frac{1}{\sqrt{t-t^2x_0}}$  at  $t_0 = h^{-1}(x_0) = \frac{1}{2x_0}$ . Setting  $t = u + \frac{1}{2x_0}$ , we note that:

$$\frac{1}{\sqrt{t-t^2x_0}} = \frac{2\sqrt{x_0}}{\sqrt{1-(2ux_0)^2}} \quad \text{and} \quad \frac{1}{\sqrt{1-z^2}} = \sum_{k=0}^{N-1} \frac{(2k)!}{2^{2k}(k!)^2} z^{2k} + o(z^{2N-1}).$$

One deduces that

$$\frac{1}{\sqrt{t-t^2x_0}} = 2\sqrt{x_0} \sum_{k=0}^{N-1} \frac{(2k)!}{2^{2k}(k!)^2} [2x_0(t-t_0)]^{2k} + o((t-t_0)^{2N-1}).$$

As a result,  $P$  is given by  $P(t) = 2\sqrt{x_0} \sum_{k=0}^{N-1} \frac{(2k)!}{2^{2k}(k!)^2} [2x_0(t-t_0)]^{2k}$  and

$$\eta_W \circ h(t) = \sqrt{t-t^2x_0} P(t) \tag{2.3.14}$$

$$= 1 - \frac{\sum_{k=M}^{+\infty} \frac{(2k)!}{2^{2k}(k!)^2} [2x_0(t-t_0)]^{2k}}{\sum_{k=0}^{+\infty} \frac{(2k)!}{2^{2k}(k!)^2} [2x_0(t-t_0)]^{2k}}. \tag{2.3.15}$$

One sees that  $|\eta_W \circ h(t)| < 1$  for all  $t \in (0, \frac{1}{x_0}) \setminus \{\frac{1}{2x_0}\}$ , and by Lemma 6,

$$(\eta_W \circ h)^{(2N)}(t_0) = -g^{(2N)}(t_0)/g(t_0) = -\frac{((2N)!)^2}{(N!)^2} x_0^{2N} < 0 \tag{2.3.16}$$

so that  $\eta_W \circ h$  (hence  $\eta_W$ ) is  $(2N - 1)$ -non-degenerate. One recovers  $\eta_W$  by composing with  $h^{-1}$ , noting that  $2x_0(t-t_0) = \frac{x_0-x}{x+x_0}$ .  $\square$

## 2.4 The Case of Several Clusters of Spikes

In this section, we propose to generalize the definition of  $\eta_W$  seen in Section 1.4 to the case of several clusters of spikes instead of one (all the spikes that cluster at 0). Then we show in Theorem 4 that if the  $\eta_W$  for one cluster is  $(2N - 1)$ -non-degenerate then it is also the case for  $\eta_W$  for several clusters provided that there are separated enough. This result uses the same arguments than the one proved for  $\eta_V$  (see Theorem 1.3 in Section 2).

The framework of this section is similar as the one of Section 1.4.

Consider a measure  $m(t) = \sum_{k=1}^K \left( \sum_{i=1}^{N_k} a_{k,i} \delta_{x_k + t z_{k,i}} \right)$ . We suppose that  $a_{k,i} \in \mathbb{R}$  such that for all  $k \in \{1, \dots, K\}$ ,  $\text{sign}(a_{k,i}) = s_k$  depends only on  $k$ . For all  $k \in \{1, \dots, K\}$ ,  $x_k \in X$  are pairwise distinct and for all  $i \in \{1, \dots, N_k\}$   $z_{k,i} \in X$  are also pairwise distinct. As a result for  $t > 0$  small enough, all the positions of the spikes of  $m(t)$  are pairwise distinct and  $m(t)$  is composed of  $\sum_{k=1}^K N_k$  spikes. The spikes of  $m(t)$  cluster around the positions  $x_k$  when  $t \rightarrow 0$ , so that  $m(t)$  is composed of  $K$  clusters. An example of such a measure is given in Figure 2.9.

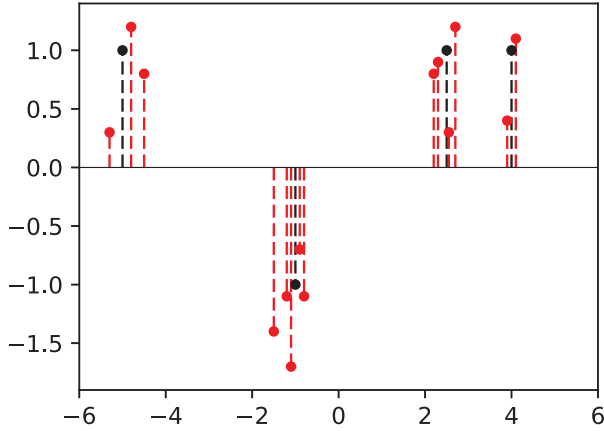


Figure 2.9: An example of a measure composed of several clusters of spikes. In red, the measure  $m(t)$  and in black the positions  $(x_k)_{1 \leq k \leq K}$  where the spikes of  $m(t)$  cluster. Here  $K = 4$ ,  $N_1 = 3$ ,  $N_2 = 5$ ,  $N_3 = 4$ ,  $N_4 = 2$ .

From now on in this section, in order to avoid confusions, one denotes by  $\eta_{W,x_0}$  the  $(2N - 1)$ -vanishing derivatives pre-certificate for one cluster of  $N$  spikes at position  $x_0 \in X$  (as defined in Section 1.4) and  $\eta_{W,\bar{x}}$  the same object but in the case of several clusters of spikes at positions  $\bar{x} = (x_1, \dots, x_K)$ .

The following Proposition is similar to Proposition 8 in Section 1.4 and defines  $\eta_{W,\bar{x}}$ .

**Proposition 15** ( $\eta_{W,\bar{x}}$  for clusters of spikes). *Let  $K \geq 1$ . One denotes by  $(x_1, \dots, x_K) \in$*

$\overset{\circ}{X}^K$ ,  $(s_1, \dots, s_K) \in \{-1, 1\}^K$  and  $\mathbf{N} = (N_1, \dots, N_K) \in (\mathbb{N}^*)^K$  respectively the positions of the  $K$  clusters, the signs of the amplitudes of the spikes at each cluster and the number of spikes at each cluster.

Suppose that  $\varphi \in \mathcal{C}^{2\|\mathbf{N}\|_\infty - 1}(X, \mathcal{H})$ .

If  $\Psi_{2\mathbf{N}-1} = (\varphi(x_1) \dots \varphi^{(2N_1-1)}(x_1) \dots \varphi(x_K) \dots \varphi^{(2N_K-1)}(x_K))$  has full column rank, then there is a unique solution to the problem

$$\inf \left\{ \|p\|_{\mathcal{H}} ; \forall k \in \{1, \dots, K\}, (\Phi^* p)(x_k) = 1, \dots, (\Phi^* p)^{(2N_k-1)}(x_k) = 0 \right\}.$$

One denotes by  $p_{W, \bar{x}}$  its solution, given by

$$p_{W, \bar{x}} = \Psi_{2\mathbf{N}-1}^{+,*} \delta_{2\mathbf{N}} \quad (2.4.1)$$

where  $\delta_{2\mathbf{N}} = (\underbrace{s_1, 0, \dots, 0}_{\text{size } 2N_1}, \underbrace{s_2, 0, \dots, 0}_{\text{size } 2N_2}, \dots, \underbrace{s_K, 0, \dots, 0}_{\text{size } 2N_K})^T \in \mathbb{R}^{2\sum_{k=1}^K N_k}$ . One defines  $\eta_{W, \bar{x}}$  as  $\eta_{W, \bar{x}} \stackrel{\text{def.}}{=} \Phi^* p_{W, \bar{x}}$ .

**Definition 10** (( $2\mathbf{N}-1$ )-non-degeneracy of  $\eta_{W, \bar{x}}$ ). One uses the same notations as in Proposition 15. We suppose that  $\varphi \in \mathcal{C}^{2\|\mathbf{N}\|_\infty}(X, \mathcal{H})$ .

We say that  $\eta_{W, \bar{x}}$  is ( $2\mathbf{N}-1$ )-non-degenerate if:

$$\begin{aligned} \forall k \in \{1, \dots, K\}, \quad & \eta_{W, \bar{x}}^{(2N_k)}(x_k) \neq 0, \\ \forall x \in X \setminus \{x_1, \dots, x_K\}, \quad & |\eta_{W, \bar{x}}(x)| < 1. \end{aligned}$$

Provided that the positions of the clusters are separated enough and some technical assumptions, we can show similarly as in Theorem 2 that  $\eta_{W, \bar{x}}$  is ( $2\mathbf{N}-1$ )-non-degenerate.

**Theorem 4.** Let  $X \subset \mathbb{R}$  be an unbounded interval. Let  $\bar{x} = (x_1, \dots, x_K) \in X^K$  with pairwise distinct coordinates,  $(s_1, \dots, s_K) \in \{-1, 1\}^K$  and  $\mathbf{N} = (N_1, \dots, N_K) \in (\mathbb{N}^*)^K$  be respectively the positions of the  $K$  clusters, the signs of the amplitudes of the spikes at each cluster and the number of spikes at each cluster. If the following assumptions are true:

- (i)  $\varphi \in \mathcal{C}^{2\|\mathbf{N}\|_\infty}(X, \mathcal{H})$ ,
- (ii)  $\Psi_{2\mathbf{N}-1}$  has full column rank,
- (iii) for all  $(i, j) \in \{0, \dots, 2\|\mathbf{N}\|_\infty\}^2$ ,  $x \in X \mapsto \langle \varphi^{(i)}(x), \varphi^{(j)}(x) \rangle_{\mathcal{H}}$  is constant,
- (iv) there exists a function  $\omega : \mathbb{R}_+ \rightarrow \mathbb{R}_+$  satisfying  $\omega(t) \rightarrow 0$  when  $t \rightarrow +\infty$  such that for all  $x, x' \in X$ , for all for all  $(i, j) \in \{0, \dots, 2\|\mathbf{N}\|_\infty\}^2$ ,

$$|\langle \varphi^{(i)}(x), \varphi^{(j)}(x') \rangle_{\mathcal{H}}| \leq \omega(|x - x'|),$$

- (v) there exists  $C > 0$  and  $r > 0$  such that for all  $N \in \{1, \dots, \|\mathbf{N}\|_\infty\}$  (representing the number of spikes of the cluster), for all  $x_0 \in X$  and for all  $x \in [x_0 - r, x_0 + r]$ ,  $\eta_{W,x_0}^{(2N)}(x) \leq -C$ ,
- (vi) for all open neighborhood  $V$  of 0, there exists  $M > 0$  such that for all  $x_0 \in X$  (corresponding to the position of clustering of  $N \in \{1, \dots, \|\mathbf{N}\|_\infty\}$  spikes) :

$$\forall x \in X \setminus (x_0 + V), \quad |\eta_{W,x_0}(x)| \leq 1 - M.$$

Then if  $\Delta(\bar{x})$  is large enough,  $\eta_{W,\bar{x}}$  is non-degenerate i.e. for all  $x \in X \setminus \{x_1, \dots, x_K\}$ ,  $|\eta_{W,\bar{x}}(x)| < 1$  and for all  $k \in \{1, \dots, K\}$ ,  $\eta_{W,\bar{x}}^{(2N_k)}(x_k) \neq 0$ .

*Proof.* By definition  $\Psi_{2\mathbf{N}-1}^* \Psi_{2\mathbf{N}-1} = (B_{k,l})_{(k,l) \in \{1, \dots, K\}^2}$  is a block matrix such that  $B_{k,l} \in \mathbb{R}^{2N_k \times 2N_l}$ , where:

$$B_{k,l} = \left( \left\langle \varphi^{(i)}(x_k), \varphi^{(j)}(x_l) \right\rangle_{\mathcal{H}} \right)_{0 \leq i \leq 2N_k-1, 0 \leq j \leq 2N_l-1}.$$

From Assumption (ii), one knows that  $\eta_{W,\bar{x}}$  is well defined,  $\Psi_{2\mathbf{N}-1}^* \Psi_{2\mathbf{N}-1}$  is invertible and:

$$\eta_{W,\bar{x}} = \Phi^* p_{W,\bar{x}} = \Phi^* \Psi_{2\mathbf{N}-1} (\Psi_{2\mathbf{N}-1}^* \Psi_{2\mathbf{N}-1})^{-1} \delta_{2\mathbf{N}}.$$

From Assumption (iv), we deduce that  $\Psi_{2\mathbf{N}-1}^* \Psi_{2\mathbf{N}-1} \rightarrow D_{\bar{x}}$  when  $\Delta(\bar{x}) \rightarrow +\infty$ , where:

$$D_{\bar{x}} \stackrel{\text{def.}}{=} \begin{pmatrix} B_{1,1} & & \\ & \ddots & \\ & & B_{K,K} \end{pmatrix} \quad \text{with} \quad B_{k,k} = \Psi_{2N_k-1}^* \Psi_{2N_k-1},$$

is a block diagonal matrix. Indeed, when  $k \neq l$ ,  $\|B_{k,l}\| \rightarrow 0$ . Let us denote  $H_{\bar{x}} = \Psi_{2\mathbf{N}-1}^* \Psi_{2\mathbf{N}-1} - D_{\bar{x}}$ , so one has  $\|H_{\bar{x}}\| \rightarrow 0$  when  $\Delta(\bar{x}) \rightarrow +\infty$ . Moreover:

$$(\Psi_{2\mathbf{N}-1}^* \Psi_{2\mathbf{N}-1})^{-1} = (D_{\bar{x}} + H_{\bar{x}})^{-1} = D_{\bar{x}}^{-1} (I + H_{\bar{x}} D_{\bar{x}}^{-1})^{-1}, \quad (2.4.2)$$

and it turns out from assumption (iii) that  $D_{\bar{x}}$  does not depend on  $\bar{x}$ , hence  $\|H_{\bar{x}} D_{\bar{x}}^{-1}\| \rightarrow 0$  when  $\Delta(\bar{x}) \rightarrow +\infty$ . As a consequence, there exists  $\Delta_0 > 0$  such that if  $\Delta(\bar{x}) \geq \Delta_0$  then:

$$(\Psi_{2\mathbf{N}-1}^* \Psi_{2\mathbf{N}-1})^{-1} = D_{\bar{x}}^{-1} + R(\Delta(\bar{x})) \quad \text{with} \quad \|R(\Delta(\bar{x}))\| \xrightarrow[\Delta(\bar{x}) \rightarrow +\infty]{} 0. \quad (2.4.3)$$

Note that:

$$\Psi_{2\mathbf{N}-1} D_{\bar{x}}^{-1} \delta_{2\mathbf{N}} = \sum_{k=1}^K s_k \Psi_{2N_k-1} (\Psi_{2N_k-1}^* \Psi_{2N_k-1})^{-1} \delta_{2N_k}, \quad (2.4.4)$$

so using the Definition of  $p_{W,\bar{x}}$  (see Equation (2.4.2)) and Equations (2.4.3), (2.4.4), we deduce that  $p_{W,\bar{x}} = \sum_{i=1}^K s_k p_{W,x_k} + p_R$  with  $p_{W,x_k} = \Psi_{2N_k-1} (\Psi_{2N_k-1}^* \Psi_{2N_k-1})^{-1} \delta_{2N_k}$

defines the usual  $(2N_k - 1)$ -vanishing derivatives pre certificate (see Section 1.4) for one cluster of spikes at position  $x_k$ , and  $\|p_R\|_{\mathcal{H}} \rightarrow 0$  when  $\Delta(\bar{x}) \rightarrow +\infty$ . Thus:

$$\eta_{W,\bar{x}} = \eta_Z + \eta_R = \sum_{i=1}^K s_k \eta_{W,x_k} + \eta_R, \quad (2.4.5)$$

$$\text{where } \eta_{W,x_k}(x) = \Phi_x^* p_{W,x_k}, \quad \forall k \in \{1, \dots, K\}, \quad (2.4.6)$$

$$\text{and } \left\| \eta_R^{(i)} \right\|_{\infty, X} \xrightarrow[\Delta(\bar{x}) \rightarrow +\infty]{} 0, \quad \forall i \in \{0, \dots, 2\|\mathbf{N}\|_\infty\}, \quad (2.4.7)$$

because for all  $x \in X$ ,  $|\eta_R^{(i)}(x)| \leq \left\| \varphi^{(i)}(x) \right\|_{\mathcal{H}} \|p_R\|_{\mathcal{H}} \leq A \|p_R\|_{\mathcal{H}}$  for some  $A > 0$  thanks to Assumption (iii).

**Step 1:** For all  $k \in \{1, \dots, K\}$ , one has:

$$\eta_Z^{(2N_k)}(x_k) = s_k \eta_{W,x_k}^{(2N_k)}(x_k) + \sum_{j \neq k} s_j \eta_{W,x_j}^{(2N_k)}(x_k).$$

However:

$$\sum_{j \neq k} s_j \eta_{W,x_j}^{(2N_k)}(x_k) = \sum_{j \neq k} \sum_{i=0}^{2N_j-1} \alpha_{j,i} \left\langle \varphi^{(2N_k)}(x_k), \varphi^{(i)}(x_j) \right\rangle_{\mathcal{H}},$$

for some  $\alpha_{j,i} \in \mathbb{R}$ , so that thanks to Assumption (iv) and Equation (2.4.7):

$$\begin{aligned} \sum_{j \neq k} |\eta_{W,x_j}^{(2N_k)}(x_k)| &\xrightarrow[\Delta(\bar{x}) \rightarrow +\infty]{} 0 \\ |\eta_R^{(2N_k)}(x_k)| &\xrightarrow[\Delta(\bar{x}) \rightarrow +\infty]{} 0. \end{aligned}$$

As a result from Assumption (v),  $\sup_{x \in [x_k-r, x_k+r]} \eta_{W,x_k}^{(2N_k)}(x) \leq -C$ , we obtain that there exists  $\Delta_1 > \Delta_0$  such that if  $\Delta(\bar{x}) \geq \Delta_1$  then for all  $k \in \{1, \dots, K\}$ :

$$|\eta_{W,\bar{x}}^{(2N_k)}(x_k)| \geq \frac{C}{2}, \quad (2.4.8)$$

$$\text{sign}(\eta_{W,\bar{x}}^{(2N_k)}(x_k)) = -s_k. \quad (2.4.9)$$

and:

$$\forall k \in \{1, \dots, K\}, \forall x \in \overline{\mathcal{B}}(x_k, r), \quad |\eta_{W,\bar{x}}^{(2N_k)}(x)| \geq \frac{C}{2}, \quad (2.4.10)$$

hence, using Equations (2.4.9) and (2.4.10), we deduce that for all  $\forall k \in \{1, \dots, K\}$ ,  $x \in \overline{\mathcal{B}}(x_k, r)$ ,  $|\eta_{W,\bar{x}}(x)| \leq 1 - \frac{C}{2(2N_k)!} (x - x_k)^{2N_k}$ . In particular:

$$\forall x \in \bigcup_{k=1}^K \overline{\mathcal{B}}(x_k, r) \setminus \{x_k\}, \quad |\eta_{W,\bar{x}}(x)| < 1. \quad (2.4.11)$$

**Step 2:** From Assumption (iv), there exists  $r_1 > r$  such that:

$$\forall k \in \{1, \dots, K\}, \forall x \in X \setminus \bigcup_{l=1}^K \mathcal{B}(x_l, r_1), \quad |\langle \varphi(x), p_{W, x_k} \rangle_{\mathcal{H}}| \leq \frac{1}{3K},$$

hence  $|\eta_Z(x)| \leq \frac{1}{3}$ . From Equation (2.4.7), there exists  $\Delta_2 > \max(2r_1, \Delta_1)$  such that if  $\Delta(\bar{x}) \geq \Delta_2$ , then  $|\eta_R(x)| \leq \frac{1}{3}$  for all  $x \in X \setminus \bigcup_{l=1}^K \mathcal{B}(x_l, r_1)$ . Thus we get:

$$\forall x \in X \setminus \bigcup_{l=1}^K \mathcal{B}(x_l, r_1), \quad |\eta_{W, \bar{x}}(x)| \leq \frac{2}{3}. \quad (2.4.12)$$

**Step 3:** From Assumption (vi), there exists  $M > 0$  such that:

$$\forall k \in \{1, \dots, K\}, \forall x \in \overline{\mathcal{B}}(x_k, r_1) \setminus \mathcal{B}(x_k, r), \quad |\eta_{W, x_k}(x)| \leq 1 - M.$$

Moreover, from Assumption (iv):

$$\forall k \in \{1, \dots, K\}, \quad \sup_{x \in \overline{\mathcal{B}}(x_k, r_1) \setminus \mathcal{B}(x_k, r)} \sum_{l \neq k} |\eta_{W, x_l}(x)| \xrightarrow{\Delta(\bar{x}) \rightarrow +\infty} 0.$$

Thus, there exists  $\Delta_3 \geq \Delta_2$  such that if  $\Delta(\bar{x}) \geq \Delta_3$  then for all  $k \in \{1, \dots, K\}$ , for all  $x \in \overline{\mathcal{B}}(x_k, r_1) \setminus \mathcal{B}(x_k, r)$ ,  $|\eta_Z(x)| \leq (1 - M) + \frac{M}{3} = 1 - \frac{2M}{3}$  and  $|\eta_R(x)| \leq \frac{M}{3}$  (using again Equation (2.4.7)). As a result:

$$\forall x \in \bigcup_{k=1}^K (\overline{\mathcal{B}}(x_k, r_1) \setminus \mathcal{B}(x_k, r)), \quad |\eta_{W, \bar{x}}(x)| \leq 1 - \frac{M}{3}. \quad (2.4.13)$$

Putting Equations (2.4.8), (2.4.11), (2.4.12), (2.4.13) all together, we deduce that if  $\Delta(\bar{x}) \geq \Delta_3$ , then:

$$\begin{aligned} \forall x \in X \setminus \{x_1, \dots, x_K\}, \quad & |\eta_{W, \bar{x}}(x)| < 1, \\ \forall k \in \{1, \dots, K\}, \quad & \eta_{W, \bar{x}}^{(2N_k)}(x_k) \neq 0, \end{aligned}$$

i.e.  $\eta_{W, \bar{x}}$  is  $(2N - 1)$ -non-degenerate.  $\square$

The following Proposition shows that we can apply Theorem 4 in the case of a Gaussian convolution i.e.  $\eta_{W, \bar{x}}$  is  $(2N - 1)$ -non-degenerate provided that the clusters of spikes are separated enough.

**Proposition 16.** *Let us consider  $X = \mathbb{R}$  and for all  $x \in \mathbb{R}$ ,  $\varphi(x) = \psi(\cdot - x)$  where  $t \mapsto \psi(t) = \frac{1}{\sqrt{2\pi}\sigma^2} e^{-\frac{(t-x)^2}{2\sigma^2}}$  for  $\sigma > 0$ , i.e.  $\Phi$  is a Gaussian convolution. Then all the assumptions of Theorem 4 holds.*

*Proof.* One proves the Assumptions of Theorem 4 one by one.

(i) One has  $\varphi \in \mathcal{C}^\infty(\mathbb{R}, L^2(\mathbb{R}))$ ,

- (ii) one can show by induction that for all  $k \in \mathbb{N}$ ,  $\forall x \in \mathbb{R}$ ,  $\varphi^{(k)}(x) = H_k(\cdot - x)\varphi(x)$  where  $H_k$  is a polynomial of degree  $k$ . As a result

$$(\varphi(x_1), \dots, \varphi^{(2N_1-1)}(x_1), \dots, \varphi(x_K), \dots, \varphi^{(2N_K-1)}(x_K)),$$

is linearly independent in  $L^2(\mathbb{R})$ , so  $\Psi_{2N-1}$  has full column rank,

- (iii) for all  $x, x' \in \mathbb{R}$ ,  $\langle \varphi(x), \varphi(x') \rangle_{\mathcal{H}} = \frac{1}{\sqrt{4\pi\sigma^2}} e^{-\frac{(x-x')^2}{4\sigma^2}} \stackrel{\text{def.}}{=} \kappa(x - x')$ . As a result for all  $(i, j) \in \{0, \dots, 2\|\mathbf{N}\|_{\infty}\}^2$ :

$$\forall (x, x') \in \mathbb{R}^2, \quad \left\langle \varphi^{(i)}(x), \varphi^{(j)}(x') \right\rangle_{\mathcal{H}} = (-1)^j \kappa^{(i+j)}(x - x'), \quad (2.4.14)$$

in particular, for all  $x \in \mathbb{R}$ ,  $\left\langle \varphi^{(i)}(x), \varphi^{(j)}(x) \right\rangle_{\mathcal{H}} = (-1)^j \kappa^{(i+j)}(0)$  does not depend of  $x$ ,

- (iv) thanks to Equation 2.4.14, for all  $(i, j) \in \{0, \dots, 2\|\mathbf{N}\|_{\infty}\}^2$ :

$$\forall (x, x') \in \mathbb{R}^2, \quad |\left\langle \varphi^{(i)}(x), \varphi^{(j)}(x') \right\rangle_{\mathcal{H}}| \leq \underbrace{\sup_{(i,j) \in \{0, \dots, 2\|\mathbf{N}\|_{\infty}\}^2} |\kappa^{(i+j)}(x - x')|}_{\stackrel{\text{def.}}{=} \omega(|x - x'|)}$$

and  $\omega(t) \rightarrow 0$  when  $t \rightarrow +\infty$ ,

- (v) From (iii), for all  $N \in \{1, \dots, \|\mathbf{N}\|_{\infty}\}$  (representing the number of spikes of the cluster) and  $x_0 \in \mathbb{R}$ ,  $\eta_{W,x_0}^{(2N)}(x_0)$  does not depend on  $x_0$  because

$$\eta_{W,x_0}^{(2N)}(x_0) = \sum_{i=0}^{N-1} \alpha_i \left\langle \varphi^{(2N)}(x_0), \varphi^{(2i)}(x_0) \right\rangle_{\mathcal{H}},$$

for some  $\alpha_i \in \mathbb{R}$ . As a result,  $\eta_{W,x_0}^{(2N)}(x_0) = \eta_{W,0}^{(2N)}(0)$  and one knows from Proposition 12 that:

$$\eta_{W,0}^{(2N)}(0) = -\frac{(2N)!}{\sigma^{2N} 2^{2N} N!}.$$

Let  $C \stackrel{\text{def.}}{=} \min_{i \in \{1, \dots, \|\mathbf{N}\|_{\infty}\}} \frac{(2N)!}{\sigma^{2N} 2^{2N} N!}$ , then for all  $N \in \{1, \dots, \|\mathbf{N}\|_{\infty}\}$  and  $x_0 \in \mathbb{R}$ ,  $\eta_{W,x_0}^{(2N)}(x_0) \leq -C$ ,

- (vi) one knows from Proposition 12 that for all  $N \in \{1, \dots, \|\mathbf{N}\|_{\infty}\}$  (representing the number of spikes of the cluster) and  $x_0 \in \mathbb{R}$ :

$$\forall x \in \mathbb{R}, \quad \eta_{W,x_0}(x) = e^{-\frac{(x-x_0)^2}{4\sigma^2}} \sum_{i=0}^{N-1} \frac{(x-x_0)^{2i}}{\sigma^{2i} 2^{2i} i!}.$$

$\eta_{W,x_0}$  is increasing on  $\mathbb{R}_-$ , decreasing on  $\mathbb{R}_+$ ,  $\eta_{W,x_0} > 0$  and  $\eta_{W,x_0}(x_0) = 1$ . Let  $V$  be an open neighborhood of 0, then we deduce that:

$$m_{N,x_0} \stackrel{\text{def.}}{=} \sup_{x \in \mathbb{R} \setminus (x_0 + V)} |\eta_{W,x_0}(x)| < 1.$$

$m_{N,x_0}$  does not depend on  $x_0$  because  $\eta_{W,x_0} = \eta_{W,x_1}(\cdot - (x_0 - x_1))$ . Let:

$$M \stackrel{\text{def.}}{=} 1 - \max_{N \in \{1, \dots, \|\mathbf{N}\|_\infty\}} m_N,$$

then for all  $N \in \{1, \dots, \|\mathbf{N}\|_\infty\}$  and  $x_0 \in \mathbb{R}$ :

$$\sup_{x \in \mathbb{R} \setminus (x_0 + V)} |\eta_{W,x_0}(x)| \leqslant 1 - M.$$

□

Figure 2.10 shows  $\eta_{W,\bar{x}}$  for a Gaussian convolution for the example of Figure 2.9 i.e.  $K = 4$ ,  $\bar{x} = (-5, -1, 2.5, 4)$ ,  $s = (1, -1, 1, 1)$ ,  $\mathbf{N} = (3, 5, 4, 2)$ .  $\eta_{W,\bar{x}}$  has been computed numerically by using its definition in Proposition 15. One knows from Proposition 16 and Theorem 4 that provided the clusters are separated enough ( $\Delta(\bar{x})$  large enough), then  $\eta_{W,\bar{x}}$  is  $(2\mathbf{N} - 1)$ -non-degenerate. One sees numerically that indeed  $\eta_{W,\bar{x}}$  is non-degenerate.

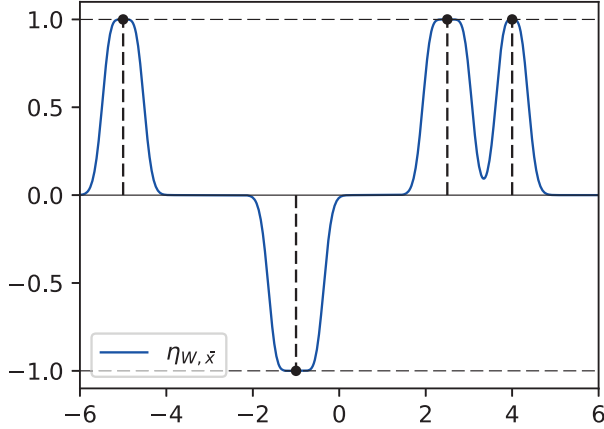


Figure 2.10:  $\eta_{W,\bar{x}}$  for the Gaussian convolution with  $\sigma = 0.15$ , corresponding to the example of Figure 2.9. The black spikes are only here to represent the positions and signs of the different clusters of spikes. As a reminder, here:  $N_1 = 3, N_2 = 5, N_3 = 4, N_4 = 2$ . One sees that  $\eta_{W,\bar{x}}$  is flatter around the clusters where  $N_i$  is larger. This a direct consequence of the definition of  $\eta_{W,\bar{x}}$ : when  $N_i$  is larger then there are more derivatives of  $\eta_{W,\bar{x}}$  at  $x_i$  that are zero.

Figure 2.11 shows  $\eta_{W,\bar{x}}$  for a Gaussian convolution for two typical examples: three clusters with an alternation of signs and two positive clusters. The clusters are progressively brought closer. At some point, one sees as expected that in the case of the alternation of signs that  $\eta_{W,\bar{x}}$  becomes degenerate ( $|\eta_{W,\bar{x}}| > 1$ ). When the clusters are separated enough, one sees that the approximation of  $\eta_{W,\bar{x}}$  by  $\eta_Z$  used

in the proof of Theorem 4 is almost perfect. This is due to the fact that  $x \mapsto e^{-x^2}$  decreases to 0 very quickly. In the case of the two positive clusters, we remark as expected that  $\eta_{W,\bar{x}}$  is always non-degenerate. From Proposition 16 and Theorem 4, one knows that when the clusters are separated enough then  $\eta_{W,\bar{x}}$  is non-degenerate. This situation can be seen on the first line, second column of Figure 2.11 where the approximation by  $\eta_Z$  is almost perfect. However when the two clusters are brought closer, the approximation is no longer valid (theoretically and numerically). But we could prove that  $\eta_{W,\bar{x}}$  converges towards the classical  $\eta_W$  (only one cluster) with  $N = N_1 + N_2$ , which one knows is non-degenerate for a Gaussian convolution thanks to Proposition 12.  $\eta_W$  would then transfer its non-degeneracy to  $\eta_{W,\bar{x}}$  when the two clusters are close enough.

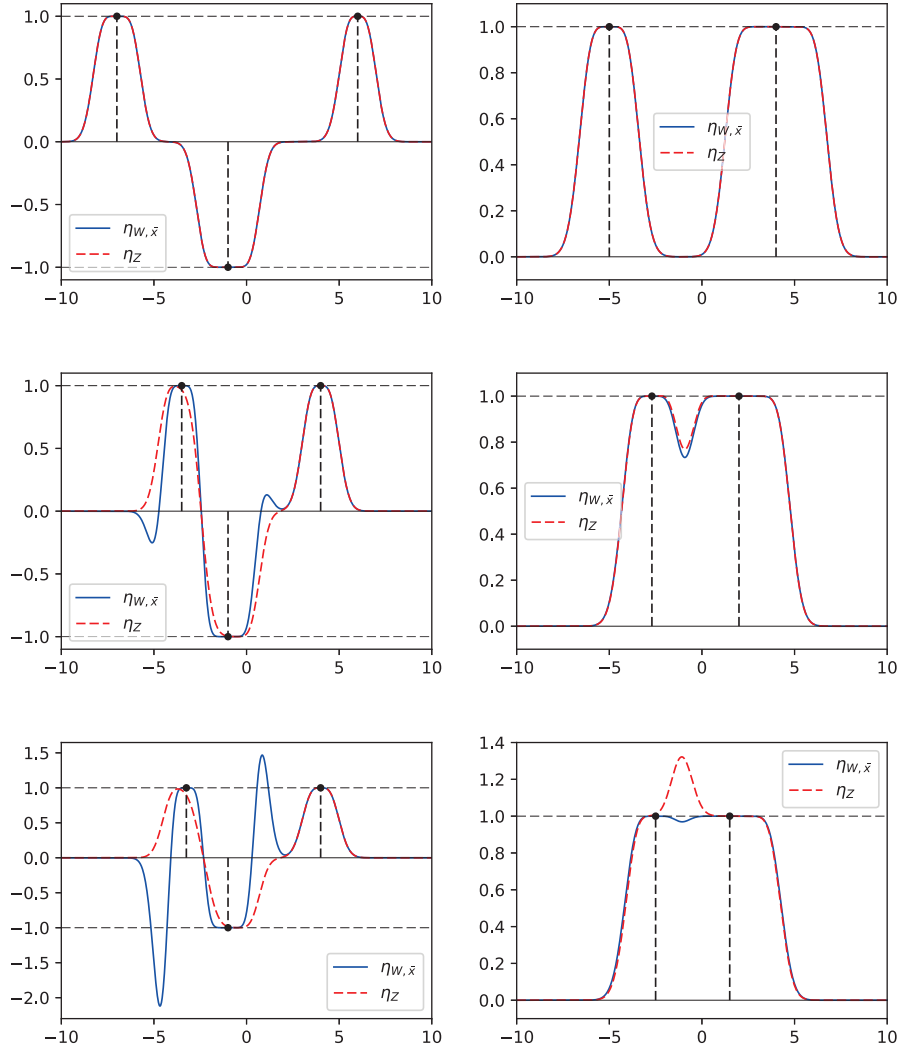


Figure 2.11:  $\eta_{W,\bar{x}}$  (in blue on the figures) for the Gaussian convolution for two typical examples. The black spikes are only here to represent the positions and signs of the different clusters of spikes.  $\eta_Z$ , which is used in the proof of Theorem 4 to approximate  $\eta_{W,\bar{x}}$  and prove its non-degeneracy, is also represented (in dashed red lines). For both examples, the spikes are progressively brought closer. The first column corresponds to three clusters with one negative in the middle,  $N = (3, 5, 2)$  and  $\sigma = 0.4$ . One sees in the more distant configuration that  $\eta_{W,\bar{x}}$  is  $(2N - 1)$ -non-degenerate and is approximated perfectly by  $\eta_Z$ . In the intermediate configuration  $\eta_{W,\bar{x}}$  is still non-degenerate but the approximation by  $\eta_Z$  is less precise for the first two clusters. In the last configuration, only the first two clusters are brought closer a slightly more than in the previous configuration, leading to the degeneracy of  $\eta_{W,\bar{x}}$ . The second column corresponds to two positive clusters,  $N = (3, 8)$  and  $\sigma = 0.5$ . One sees that  $\eta_{W,\bar{x}}$  is always non-degenerate and in the more distant configuration, the approximation by  $\eta_Z$  is almost perfect.

## Chapter 3

# Separation and Robustness of BLASSO

Super-resolution theory is the question of analyzing the dependency between a maximum allowable noise and a minimum separation characteristic distance. This chapter studies the signal-to-noise ratio required to assure the recovery of the support via the BLASSO of an initial measure composed of a sum of Dirac masses, whose minimum separation distance is controlled by a parameter  $t$ . It can be seen as a quantitative counterpart of the recovery theory derived in the previous chapter using the  $\eta_W$  pre-certificate. More precisely, our main contribution proves that if  $\eta_W$  is  $(2N - 1)$ -non-degenerate and if  $w/\lambda$ ,  $w/t^{2N-1}$  and  $\lambda/t^{2N-1}$  are small enough (where  $\lambda$  is the regularization parameter,  $w$  the noise and  $N$  the number of spikes of the initial measure), then the BLASSO has a unique solution composed of  $N$  spikes whose amplitudes and positions converge towards those of the initial measure when the noise level drops faster than  $t^{2N-1}$ . We prove also that the non-degeneracy condition on  $\eta_W$  is almost sharp. The proof techniques rely on the construction, from the first order optimality conditions of the BLASSO, of a candidate solution assured to be an actual solution with the appropriate constraints on  $\lambda$  and  $w$ , thanks to precise estimations of expansions of several involved operators depending on  $t$ .

### 3.1 Introduction

#### 3.1.1 Recap and Positioning of this Chapter

Chapter 1 presented the asymptotic analysis of the support recovery in presence of noise of the BLASSO *i.e.* the study of

$$\min_{m \in \mathcal{M}(X)} \frac{1}{2} \|\Phi m - y_t\|_{\mathcal{H}}^2 + \lambda |m|(X), \quad (\mathcal{P}_\lambda(y_t))$$

when  $t \rightarrow 0$  and where

$$y_t \stackrel{\text{def.}}{=} \Phi m_{a_0, t z_0} + w \quad \text{with} \quad m_{a_0, t z_0} = \sum_{i=1}^N a_0 \delta_{t z_{0,i}},$$

The positions of the spikes are in the one dimensional space  $X$  and the amplitudes are positive. This analysis is motivated by the fact that for positive spikes, exact support recovery without noise holds whatever the minimum separation between the spikes if the kernel satisfies some injectivity assumption, see [42]. This led us to define the  $(2N - 1)$ -vanishing derivatives  $\eta_W$  (Definition 8) and one proved in Corollary 1 that its  $(2N - 1)$ -non-degeneracy (see Definition 8) assures the recovery of the support when solving  $\mathcal{P}_\lambda(y_t)$  with  $t \rightarrow 0$ .

Chapter 2 studied precisely the non-degeneracy of  $\eta_W$  for several filters (general convolution, Gaussian convolution, low pass filter but also different Laplace transform based operators).

However up to now, one lacks a quantitative description of the constraints on the regularization parameter  $\lambda$  and the noise  $w$ , with respect to the distance between the spikes  $t$ , so as to ensure the super-resolution in presence of noise via the BLASSO. Indeed recall that in Corollary 1, one has only the existence of a domain in which the recovery is possible, with no indication whatsoever of its size with respect to  $t$  (which is, both in practice and in theory, a critical information).

The goal of this chapter is to fill this gap.

#### 3.1.2 Previous Works

In [113], the authors shows that stable recovery is obtained, in a discrete framework, if the signal-to-noise ratio grows faster than  $O(1/t^{2N})$ , closely matching optimal lower bounds of  $O(1/t^{2N-1})$  obtained by combinatorial methods, see [45].

Spectral Methods such as MUSIC [130, 100] provide, in the noiseless case, exact reconstruction of the initial signal as long as there are enough observations compared to the number of distinct frequencies [106]. Stability to noise is known to hold under a minimum separation distance similar to the one of the BLASSO [106]. However, contrary to the BLASSO, numerical observations [39] and [45] prove that this stability continues to hold regardless of the sign of the amplitudes, as soon as the signal-to-noise ratio scales like  $O(1/t^{2N-1})$ . It matches, when  $w$  follows a Gaussian distribution, the Cramer-Rao lower bound achievable by any unbiased

estimator [18]. But it is important to note that they are restricted to forward models  $\Phi$  that are convolutions with a low-pass filter, which is not the case of our analysis for the BLASSO.

### 3.1.3 Contributions

Section 3.2.1 presents our main theoretical contribution of Part I of this thesis. Theorem 5 shows that the recovery of the support (*i.e.* the recovery of a measure composed of the same number of spikes as the original measure), when the spikes of the initial measure collapse at 0 ( $t \rightarrow 0$ ), is possible when solving the BLASSO, if the  $(2N - 1)$ -vanishing derivatives pre-certificate  $\eta_W$  is  $(2N - 1)$ -non-degenerate and if the regularization parameter  $\lambda$  and the noise  $w$  are in a domain whose size is quantified with respect to  $t$ . In sharp contrast to the (simpler and less precise) Corollary 1, this result provides quantitative estimate of the required signal-to-noise ratio as a function of the separation distance  $t$ . Proposition 17 in Section 3.2.2 proves that the  $(2N - 1)$ -non-degeneracy of  $\eta_W$  is almost a sharp condition.

The proof of Theorem 5 relies on precise estimations, that are gathered in Section 3.4, of different operators built upon  $\Phi_{tz}$  and  $\Gamma_{tz}$  when  $t \rightarrow 0$  and on a convergence result of  $\eta_{\lambda,t} \stackrel{\text{def.}}{=} \frac{1}{\lambda} \Phi^*(y_t - \Phi m_{a,tz})$  towards  $\eta_W$  (which is an extension of Proposition 4 seen in Section 1.2) proved in Proposition 22 of Section 3.6.

## 3.2 Separation Influence on Robustness of Super-Resolution

Section [3.2.1] presents Theorem [5] which is our main theoretical contribution of Part I of this thesis. Theorem [5] provides quantitative sufficient conditions to guarantee the recovery of the support of  $m_{a_0, t z_0}$  when solving  $\mathcal{P}_\lambda(y_t)$  when  $t \rightarrow 0$ .

### 3.2.1 Main Result

This section states Theorem [5], whose proof is spanned in Sections [3.4], [3.5] and [3.6]. Section [3.3] gives a sketch of the proof to guide the reader through the remaining of the chapter.

**Theorem 5.** *Suppose that  $\varphi \in \text{KER}^{(2N+1)}$  and that  $\eta_W$  is  $(2N-1)$ -non-degenerate. Then there exist constants  $(t_1, t_W, C, C_R, M)$  (depending only on  $\varphi$ ,  $a_0$  and  $z_0$ ) such that for all  $0 < t < \min(t_1, t_W)$ , for all  $(\lambda, w) \in B(0, C_R t^{2N-1})$  with  $\left\| \frac{w}{\lambda} \right\|_{\mathcal{H}} \leq C$ ,*

- the problem  $\mathcal{P}_\lambda(y_t)$  admits a unique solution,
- that solution has exactly  $N$  spikes, and it is of the form  $m_{a, t z}$ , with  $(a, z) = g_t^*(\lambda, w)$  (where  $g_t^*$  is a  $\mathcal{C}^{2N}$  function defined on  $B(0, C_R t^{2N-1}) \subset \mathbb{R} \times \mathcal{H}$ ),
- the following inequality holds

$$|(a, z) - (a_0, z_0)|_\infty \leq M \left( \frac{|\lambda|}{t^{2N-1}} + \frac{\|w\|_{\mathcal{H}}}{t^{2N-1}} \right).$$

The values of the constants involved can be found in the proof of the theorem, more precisely,  $(t_1, C)$  are defined in Equation [3.6.1],  $C_R$  is defined in Proposition [20],  $t_W$  is defined in Theorem [3] and  $M$  is given in Corollary [2].

Some comments on Theorem [5]:

- i) the fact that  $\eta_W$  must be  $(2N-1)$ -non-degenerate (see Definition [8]) implies that the injectivity hypothesis  $\mathcal{I}_{2N-1}$  is satisfied (see Definition [7]) and in particular  $\varphi \in \text{KER}^{(2N-1)}$ . However for this theorem to hold, one requires a bit more regularity, namely  $\varphi \in \text{KER}^{(2N+1)}$ . This is because we perform Taylor expansions in our proof up to the order  $2N+1$  (see Lemma [9]).
- ii) The size of the domain in  $(\lambda, w)$  in which one can perform the recovery of the support is proportional to  $t^{2N-1}$ . We believe that this ratio is optimal because it corresponds to the Cramer-Rao lower bound achievable by any unbiased estimator [18]. In [113], the authors show that stable recovery is obtained if the signal-to-noise ratio grows faster than  $O(1/t^{2N})$ , closely matching optimal lower bounds of  $O(1/t^{2N-1})$  obtained by combinatorial methods, as also proved in [45]. When  $N$  increases, it enforces that the domain gets smaller and logically that the recovery is harder to perform. This is reflected in the fact that  $\eta_W$  gets flatter around 0 when  $N$  increases (more derivatives equal to 0).

- iii) If  $\lambda \sim \|w\|_{\mathcal{H}}$  so that  $\|w\|_{\mathcal{H}}/\lambda \leq C$  and  $\|w\|_{\mathcal{H}}$  goes to 0 faster than  $t^{2N-1}$  then the amplitudes and positions (rescaled by  $t$ ) of the recovered measure  $m_{a,tz}$  converge towards those of  $m_{a_0,tz_0}$  when  $t \rightarrow 0$ .

### 3.2.2 Necessary Condition for the Recovery in the Limit $t \rightarrow 0$

Theorem 5 states that under a non-degeneracy property which involves  $\eta_W$ , it is possible to perform the recovery of the support of a measure  $m_{a_0,tz_0}$  in the limit  $t \rightarrow 0$  when the data are contaminated by some noise, provided that

$$\max(|\lambda|/t^{2N-1}, \|w\|_{\mathcal{H}}/t^{2N-1}, \|w\|_{\mathcal{H}}/\lambda) \leq C,$$

for some constant  $C > 0$  depending only on the filter  $\varphi$  and  $(a_0, z_0)$ . It is natural to ask whether the non-degeneracy condition on  $\eta_W$ , in order to get the recovery of the support in some low noise regime, is sharp.

The following Proposition shows that the  $(2N - 1)$ -non-degeneracy assumption on  $\eta_W$  is almost sharp in the sense that the recovery of the support in a low noise regime leads to  $\|\eta_W\|_{\infty,X} \leq 1$ .

**Proposition 17.** *Suppose that  $\mathcal{I}_{2N-1}$  holds and  $\varphi \in \text{KER}^{(2N+1)}$ . Suppose also that there exists a sequence  $(t_n)_{n \in \mathbb{N}}$  such that  $t_n \rightarrow 0$  and satisfying*

$$\forall n \in \mathbb{N}, \exists (\lambda_n, w_n), \exists (a_n, z_n) \in \mathbb{R}^N \times \mathbb{R}^N, m_{a_n, t_n z_n} \text{ is solution of } \mathcal{P}_{\lambda_n}(y_{t_n}),$$

where  $y_{t_n} \stackrel{\text{def.}}{=} \Phi m_{a_0, t_n z_0} + w_n$ ,  $(\lambda_n, w_n) \rightarrow 0$  with  $\frac{\|w_n\|_{\mathcal{H}}}{\lambda_n} \rightarrow 0$ . Then

$$\|\eta_W\|_{\infty,X} \leq 1. \tag{3.2.1}$$

The proof of this result can be found at the end of this chapter.

Proposition 17 tells us in particular that if one wants to solve the super-resolution problem in presence of noise by solving the BLASSO for a given acquisition operator  $\Phi$  and if the associated  $\eta_W$  (which only depends on  $\Phi$ ) satisfies  $\|\eta_W\|_{\infty,X} > 1$ , then it is impossible to recover the support of the initial measure in a low noise regime when the spikes cluster at some point. This shows that this  $\eta_W$ -based analysis of super-resolution via support stability is almost necessary and sufficient.

### 3.3 Sketch of Proof

Section [3.3.1] details the main ideas of the proof of Theorem [5]. In Section [3.3.2], one gives the proof of Theorem [5] by gathering all the intermediary results proved in the remaining sections of this chapter.

#### 3.3.1 Main Steps

The elements of the proof are divided in three main steps. The path followed is similar to the one already seen in Section [I.2]. The goal is to build a candidate solution to  $\mathcal{P}_\lambda(y_t)$  satisfying some first order optimality conditions and then show, by performing several expansions and controlling precisely the terms involved, that it is indeed a solution of the BLASSO.

**Step 1 (Section [3.5.1] and [3.5.2]).** We start with the first order optimality equation that any solution  $m_{a,tz}$ , for fixed  $t > 0$ , of  $\mathcal{P}_\lambda(y_t)$  must satisfy *i.e.*

$$\Gamma_{tz}^* (\Phi_{tz}a - \Phi_{tz_0}a_0 - w) + \lambda \begin{pmatrix} \mathbb{1}_N \\ 0 \end{pmatrix} = 0.$$

where

$$\mathbb{1}_N \stackrel{\text{def.}}{=} (1, 1, \dots, 1)^T \in \mathbb{R}^N. \quad (3.3.1)$$

It is obtained by applying Fermat's rule to the problem  $\mathcal{P}_\lambda(y_t)$ . Since the parameters  $(a, z, \lambda, w) = (a_0, z_0, 0_{\mathbb{R}}, 0_{\mathcal{H}})$  are a solution of the equation, the idea is to parametrize, in a neighborhood of  $(\lambda, w) = (0_{\mathbb{R}}, 0_{\mathcal{H}})$ , the amplitudes and positions  $(a, z)$  in terms of  $(\lambda, w)$  by applying the implicit function theorem so that  $(a, z, \lambda, w)$  is a solution of the first order equation. This process is detailed in Section [3.5.1] and [3.5.2]. The rest of the proof consists in proving that the measure  $m_{a,tz}$  is the unique solution of the problem  $\mathcal{P}_\lambda(y_t)$ . But, before, we have to deal with the domain of existence of the above parametrization.

**Step 2 (Section [3.5.3]).** The implicit function theorem only provides the existence of a neighborhood in  $(\lambda, w)$  of  $(0_{\mathbb{R}}, 0_{\mathcal{H}})$  where the parametrization holds, but we do not know how its size depends on the parameter  $t$ . This issue is important because one of our aims is to determine the constraints on  $t$  (corresponding roughly to the minimum distance between the spikes of the original measure), on the noise level and on the regularization parameter  $\lambda$  so that the recovery of the support is possible. Section [3.5.3] is devoted to show that the parametrization, which writes  $(a, z) = g_t^*(\lambda, w)$  (see Equation [3.5.3] for the definition of the implicit function  $g_t^*$ ), of the solutions of the first order optimality equation holds in a neighborhood of  $(0_{\mathbb{R}}, 0_{\mathcal{H}})$  and of size proportional to  $t^{2N-1}$ . This result corresponds to Proposition [20]. The proof uses an upper bound of  $dg_t^*$  which is stated in Corollary [2]. Proposition [20] relies on asymptotic expansions (of  $\Gamma_{tz}$  for example), when  $t \rightarrow 0$ ,

gathered and used in the proof of Lemma 11. Section 3.4 is devoted to these asymptotic expansions and it may be skipped at first reading.

**Step 3 (Section 3.6).** Up to now, we have constructed a candidate solution  $m_{a,tz}$  (composed of  $N$  spikes) where  $(a, z) = g_t^*(\lambda, w)$  is built by parametrizing the solutions of the first order optimality equation. Moreover this parametrization holds for all  $(\lambda, w)$  in a ball of radius proportional to  $t^{2N-1}$ . It remains to prove that  $m_{a,tz}$  is indeed the unique solution of  $\mathcal{P}_\lambda(y_t)$ . To prove that  $m_{a,tz}$  is a solution, it is equivalent to check that

$$0 \in \partial \left( m \mapsto \frac{1}{2} \|\Phi m - y_{0,t} - w\|_{\mathcal{H}}^2 + \lambda |m|(X) \right) (m_{a,tz}),$$

where  $y_{0,t} = \Phi m_{a,tz_0}$  and which reformulates into  $\eta_{\lambda,t} \stackrel{\text{def.}}{=} \frac{1}{\lambda} \Phi^*(y_{0,t} + w - \Phi m_{a,tz}) \in \partial |m_{a,tz}|(X)$ . This is done by first showing the convergence of  $\eta_{\lambda,t}$  towards  $\eta_W$  when  $(t, \lambda, w) \rightarrow 0$  in a well chosen domain, see Proposition 22, and then using Theorem 3 and the fact that  $\eta_W$  is ensured to be  $(2N-1)$ -non-degenerate (which is one of the hypotheses of Theorem 5) to get the non-degeneracy of  $\eta_{\lambda,t}$  and the conclusion.

### 3.3.2 Putting all together

After this sketch, we now give the detailed proof. It uses Proposition 20 (parametrization of the solution of the first order optimality equation on a ball, for the parameter  $(\lambda, w)$ , of radius proportional to  $t^{2N-1}$ ), Proposition 22 (convergence of  $\eta_{\lambda,t}$  towards  $\eta_W$ ), Theorem 3 (use of the  $(2N-1)$ -non-degeneracy of  $\eta_W$  to transfer it to  $\eta_{\lambda,t}$ ), and Proposition 21 (upper bound on the error of  $m_{a,tz}$  with respect to  $m_{a_0,tz_0}$ ).

*Proof of Theorem 5.* Let us first introduce a few notations. One denotes

$$\Delta_0 \stackrel{\text{def.}}{=} \Delta(z_0), \quad (3.3.2)$$

where  $\Delta(z_0)$  is introduced in (1.1.1). One denotes by  $\overline{B}(\bar{x}, r)$  (resp.  $B(\bar{x}, r)$ ) the closed (resp. open)  $\ell^\infty$  ball in  $X^N$  with center  $\bar{x}$  and radius  $r$ . One defines neighborhoods of respectively  $z_0$  and  $a_0$  as

$$\mathcal{B}_{z_0} \stackrel{\text{def.}}{=} \overline{B}\left(z_0, \frac{\Delta_0}{4}\right) \quad \text{and} \quad \mathcal{B}_{a_0} \stackrel{\text{def.}}{=} \overline{B}\left(a_0, \frac{\min_i(a_{0,i})}{4}\right). \quad (3.3.3)$$

When  $X = \mathbb{T}$ , depending on the context, we may consider any  $\bar{x}$  as its unique representative in  $(-\frac{1}{2}, \frac{1}{2})^N$  of its class in  $\mathbb{T}^N$  or as an element of  $\mathbb{T}^N$  (*i.e.* the entire equivalence class). Moreover we make the assumption that for any  $z_0 \in \mathbb{T}^N$ , one has in fact  $z_0 \in (-\frac{1}{4}, \frac{1}{4})^N$  (*i.e.* its unique representative in  $(-\frac{1}{2}, \frac{1}{2})^N$  is in  $z_0 \in (-\frac{1}{4}, \frac{1}{4})^N$ ).

Let us take  $t, \lambda, w$  as in the hypotheses of the Theorem 5. Let  $(a, z) = g_t^*(\lambda, w)$ , where  $g_t^*$  is the function constructed in Section 3.5. Let us define

$$p_{\lambda,t} \stackrel{\text{def.}}{=} \frac{1}{\lambda} (\Phi_{tz_0} a_0 + w - \Phi_{tz} a) \quad \text{and} \quad \eta_{\lambda,t} \stackrel{\text{def.}}{=} \Phi^* p_{\lambda,t}.$$

By Proposition 22 combined with Theorem 3 where we take

$$R_W \stackrel{\text{def.}}{=} \sup\{|z|_\infty ; z \in \overline{\mathcal{B}}_{z_0}\}, \quad (3.3.4)$$

we have for  $0 < t < \min(t_W, t_1)$ ,

$$\forall x \in X \setminus \bigcup_i \{tz_i\}, |\eta_{\lambda,t}(x)| < 1 \quad \text{and} \quad \forall 1 \leq i \leq N, \eta''_{\lambda,t}(tz_i) < 0, \quad (3.3.5)$$

while  $\eta_{\lambda,t}(tz_i) = 1 = \text{sign}(a_i)$  by definition.

We deduce that  $\eta_{\lambda,t}$  is in the subdifferential of the total variation at  $m_{a,tz}$  because

- $\eta_{\lambda,t} \in \mathcal{C}_0$ ,
- $\|\eta_{\lambda,t}\|_{\infty,X} \leq 1$  thanks to Equation 3.3.5,
- $\forall 1 \leq i \leq N, \eta_{\lambda,t}(tz_i) = 1 = \text{sign}(a_i)$  by definition of  $\eta_{\lambda,t}$  (recall that  $(a, z) = g_t^*(\lambda, w)$ ).

As a result  $m_{a,tz}$  is a solution to  $\mathcal{P}_\lambda(y_t)$  and  $p_{\lambda,t}$  is the unique solution to the dual problem associated to  $\mathcal{P}_\lambda(y_t)$  (see Section 2.4 of [54] for details on dual certificates and optimality conditions for  $\mathcal{P}_\lambda(y_t)$ ).

Let  $m$  be another solution of  $\mathcal{P}_\lambda(y_t)$ . Then the support of  $m$  is included in the saturation points of  $\eta_{\lambda,t} = \Phi^* p_{\lambda,t}$  i.e. in  $\{tz_1, \dots, tz_N\}$ . As a result  $m = m_{a',tz}$  for some  $a' \in \mathbb{R}^N$  and  $m$  satisfies the first order optimality equation

$$\Gamma_{tz}^* (\Phi_{tz} a' - \Phi_{tz_0} a_0 - w) + \lambda \begin{pmatrix} \mathbf{1}_N \\ 0 \end{pmatrix} = 0.$$

Hence  $\Phi_{tz}^* \Phi_{tz} a' = \Phi_{tz}^* \Phi_{tz} a$  and since  $\Phi_{tz}$  has full rank (by assumption  $t$  is chosen sufficiently small, see Lemma 7 for the proof),  $\Phi_{tz}^* \Phi_{tz}$  is invertible and  $a' = a$ . So  $m = m_{a,tz}$  and  $\mathcal{P}_\lambda(y_t)$  admits a unique solution:  $m_{a,tz}$ .

The bound on the error between  $(a, z)$  and the amplitudes and positions of the initial measure  $(a_0, z_0)$  is a direct consequence of Proposition 21.  $\square$

### 3.4 Preliminaries

The proof of Theorem 5 relies to a large extent on the asymptotic behavior of quantities built upon  $\Phi_{tz}$  and  $\Gamma_{tz}$  for  $t > 0$  small, such as  $(\Phi_{tz}^* \Phi_{tz})^{-1}$  or  $(\Gamma_{tz}^* \Gamma_{tz})^{-1}$ . In this section, we gather several preliminary results that enable us to control that behavior.

**Approximate Factorizations.** Our asymptotic estimates are based on an approximate factorization of  $\Phi_{\bar{x}}$  and  $\Gamma_{\bar{x}}$  using Vandermonde and Hermite matrices. It enables us to study the asymptotic behavior of the optimality conditions of  $\mathcal{P}_\lambda(y_t)$  when  $t \rightarrow 0^+$ . For  $z \in \mathbb{R}^N$ , we let

$$H_z \stackrel{\text{def.}}{=} \begin{pmatrix} 1 & \dots & 1 & 0 & \dots & 0 \\ z_1 & \dots & z_N & 1 & \dots & 1 \\ \vdots & & \vdots & \vdots & & \vdots \\ \frac{(z_1)^{2N-1}}{(2N-1)!} & \dots & \frac{(z_N)^{2N-1}}{(2N-1)!} & \frac{(z_1)^{2N-2}}{(2N-2)!} & \dots & \frac{(z_N)^{2N-2}}{(2N-2)!} \end{pmatrix} \in \mathbb{R}^{2N \times 2N}, \quad (3.4.1)$$

so that  $H_z^{*, -1}$  is the matrix of the Hermite interpolation at points  $z_1, \dots, z_N$  when  $\mathbb{R}_{2N-1}[X]$  is equipped with the basis  $\left(1, X, \dots, \frac{X^{2N-1}}{(2N-1)!}\right)$ .

In the following, we consider  $z \in \overline{\mathcal{B}}_{z_0}$  (see (3.3.3)) and  $t \in (0, 1]$ , so that  $H_{tz}$  is always invertible. Moreover, we shall always assume that at least  $\varphi \in \text{KER}^{(2N)}$ .

**Proposition 18.** *The following expansion holds*

$$\Gamma_{tz} = \Psi_{2N-1} H_{tz} + \Lambda_{t,z} D_t, \quad (3.4.2)$$

where  $\Psi_{2N-1}$  is defined in (1.4.2),  $H_{tz}$  is defined in (3.4.1), and where

$$\begin{aligned} \Lambda_{t,z} &\stackrel{\text{def.}}{=} \left( \left( \int_0^1 (z_i)^{2N} \varphi^{(2N)}(stz_i) \frac{(1-s)^{2N-1}}{(2N-1)!} ds \right)_{1 \leq i \leq N}, \right. \\ &\quad \left. \left( \int_0^1 (z_i)^{2N-1} \varphi^{(2N)}(stz_i) \frac{(1-s)^{2N-2}}{(2N-2)!} ds \right)_{1 \leq i \leq N} \right) \\ D_t &\stackrel{\text{def.}}{=} \text{diag}(t^{2N}, \dots, t^{2N}, t^{2N-1}, \dots, t^{2N-1}). \end{aligned}$$

*Proof.* This expansion is nothing but the Taylor expansions for  $\varphi$  and  $\varphi'$ :

$$\begin{aligned} \varphi(tz_i) &= \varphi_0 + (tz_i)\varphi_1 + \dots + \frac{(tz_i)^{2N-1}}{(2N-1)!} \varphi_{2N-1} \\ &\quad + (tz_i)^{2N} \int_0^1 \varphi^{(2N)}(stz_i) \frac{(1-s)^{2N-1}}{(2N-1)!} ds, \end{aligned} \quad (3.4.3)$$

$$\begin{aligned} \varphi'(tz_i) &= \varphi_1 + (tz_i)\varphi_2 + \dots + \frac{(tz_i)^{2N-2}}{(2N-2)!} \varphi_{2N-1} \\ &\quad + (tz_i)^{2N-1} \int_0^1 \varphi^{(2N)}(stz_i) \frac{(1-s)^{2N-2}}{(2N-2)!} ds. \end{aligned} \quad (3.4.4)$$

□

The above expansion yields a useful factorization for  $\Gamma_{tz}$ ,

$$\Gamma_{tz} = \Psi_{tz} H_{tz} \quad \text{where} \quad \Psi_{tz} \stackrel{\text{def.}}{=} \Psi_{2N-1} + \Lambda_{t,z} D_t H_{tz}^{-1}.$$

The rest of this section is devoted to the consequence of that factorization for the asymptotic behavior of  $\Gamma_{tz}$  and its related quantities. The main ingredient of this analysis is the factorization of  $H_{tz}$  as

$$H_{tz} = \text{diag}(1, t, \dots, t^{2N-1}) H_z \text{diag}\left(1, \dots, 1, \frac{1}{t}, \dots, \frac{1}{t}\right). \quad (3.4.5)$$

Let us emphasize that our Taylor expansions are uniform in  $z \in \overline{\mathcal{B}}_{z_0}$ . More precisely, given two quantities  $f(z, t), g(z, t)$ , we say that  $f(z, t) = g(z, t) + O(t^k)$  if

$$\limsup_{t \rightarrow 0^+} \sup_{z \in \overline{\mathcal{B}}_{z_0}} \left| \frac{f(z, t) - g(z, t)}{t^k} \right| < +\infty.$$

**Lemma 7.** *The following expansion holds for  $t \rightarrow 0^+$ ,*

$$\Psi_{tz} = \Psi_{2N-1} + O(t). \quad (3.4.6)$$

Moreover, if  $\mathcal{I}_{2N-1}$  holds then  $\Psi_{tz}$  and  $\Gamma_{tz}$  have full column rank for  $t > 0$  small enough and

$$(\Psi_{tz}^* \Psi_{tz})^{-1} = (\Psi_{2N-1}^* \Psi_{2N-1})^{-1} + O(t) \quad (3.4.7)$$

$$\Gamma_{tz}^{+,*} \begin{pmatrix} \mathbb{1}_N \\ 0 \end{pmatrix} = \Psi_{2N-1}^{+,*} \delta_{2N} + O(t). \quad (3.4.8)$$

*Proof.* We begin by noticing that

$$\begin{aligned} \Lambda_{t,z} D_t H_{tz}^{-1} &= t^{2N} \Lambda_{t,z} H_z^{-1} \text{diag}(1, 1/t, \dots, 1/t^{2N-1}) \\ &= \Lambda_{t,z} H_z^{-1} \text{diag}(t^{2N}, t^{2N-1}, \dots, t). \end{aligned}$$

The function  $z \mapsto H_z^{-1}$  is  $\mathcal{C}^\infty$  and uniformly bounded on  $\overline{\mathcal{B}}_{z_0}$ , and  $(z, t) \mapsto \Lambda_{t,z}$  is  $\mathcal{C}^0$  on the compact set  $\overline{\mathcal{B}}_{z_0} \times [0, 1]$  hence uniformly bounded too. As a result, we get (3.4.6).

Assume now that  $\mathcal{I}_{2N-1}$  holds. Since  $\Psi_{2N-1}^* \Psi_{2N-1}$  is invertible, there is some  $R > 0$  such that for every  $A$  in the closed ball  $\overline{B}(\Psi_{2N-1}^* \Psi_{2N-1}, R) \subset \mathbb{R}^{(2N-1) \times (2N-1)}$ ,  $A$  is invertible. By the mean value inequality

$$\begin{aligned} \|(\Psi_{2N-1}^* \Psi_{2N-1})^{-1} - A^{-1}\| &\leqslant \sup_{B \in \overline{B}(\Psi_{2N-1}^* \Psi_{2N-1}, R)} \|B^{-1}(A - \Psi_{2N-1}^* \Psi_{2N-1})B^{-1}\| \\ &\leqslant \left( \sup_{B \in \overline{B}(\Psi_{2N-1}^* \Psi_{2N-1}, R)} \|B^{-1}\| \right)^2 \|A - \Psi_{2N-1}^* \Psi_{2N-1}\|. \end{aligned}$$

Applying that to  $A = \Psi_{tz}^* \Psi_{tz} = \Psi_{2N-1}^* \Psi_{2N-1} + O(t)$  (since each term in the product is uniformly bounded), we get (3.4.7).

Now, for the last point, we infer from  $\Gamma_{tz} = \Psi_{tz} H_{tz}$  and the fact that  $H_{tz}$  is invertible that  $\Gamma_{tz}^{+,*} = \Psi_{tz}^{+,*} H_{tz}^{-1,*}$ . Hence

$$\Gamma_{tz}^{+,*} \begin{pmatrix} \mathbb{1}_N \\ 0 \end{pmatrix} = \Psi_{tz}^{+,*} \delta_{2N} = \Psi_{tz} (\Psi_{tz}^* \Psi_{tz})^{-1} \delta_{2N}$$

where  $\delta_{2N}$  is defined in (1.4.4).

Each factor below being uniformly bounded in  $\overline{\mathcal{B}}_{z_0} \times [0, 1]$ , we get

$$\begin{aligned} \Gamma_{tz}^{+,*} \begin{pmatrix} \mathbb{1}_N \\ 0 \end{pmatrix} &= (\Psi_{2N-1} + O(t)) ((\Psi_{2N-1}^* \Psi_{2N-1})^{-1} + O(t)) \delta_{2N} \\ &= \Psi_{2N-1} (\Psi_{2N-1}^* \Psi_{2N-1})^{-1} \delta_{2N} + O(t). \end{aligned}$$

□

**Projectors.** In this paragraph, we shall always suppose that  $\mathcal{I}_{2N-1}$  holds. Another important quantity in our study is the orthogonal projector  $P_{(\text{Im } \Gamma_{tz})^\perp}$  (resp.  $P_{(\text{Im } \Psi_{2N-1})^\perp}$ ) onto  $(\text{Im } \Gamma_{tz})^\perp$  (resp.  $(\text{Im } \Psi_{2N-1})^\perp$ ). We define

$$\begin{aligned} \Pi_{tz} &\stackrel{\text{def.}}{=} P_{(\text{Im } \Gamma_{tz})^\perp} = \text{Id}_{\mathcal{H}} - \Gamma_{tz} (\Gamma_{tz}^* \Gamma_{tz})^{-1} \Gamma_{tz}^*, \\ \Pi_{2N-1} &\stackrel{\text{def.}}{=} P_{(\text{Im } \Psi_{2N-1})^\perp} = \text{Id}_{\mathcal{H}} - \Psi_{2N-1} (\Psi_{2N-1}^* \Psi_{2N-1})^{-1} \Psi_{2N-1}^*. \end{aligned}$$

Observing that  $P_{(\text{Im } \Gamma_{tz})^\perp} = P_{(\text{Im } \Psi_{tz})^\perp}$ , we immediately obtain from the previous Lemma that  $\Pi_{tz} = \Pi_{2N-1} + O(t)$ .

By construction,  $\Pi_{tz} \Phi_{tz} = \Pi_{tz} \Phi'_{tz} = 0$ , but the following proposition shows that this quantity is also small if we replace  $\Phi_{tz}$  with  $\Phi''_{tz}$ .

**Lemma 8.** *There exists a constant  $L_1 > 0$  (which only depends on  $\varphi$ ,  $a_0$  and  $z_0$ ) such that*

$$\|\Pi_{tz} \Phi''_{tz}\|_{\mathcal{H}} \leq L_1 t^{2N-2}$$

uniformly in  $z \in \overline{\mathcal{B}}_{z_0}$ .

*Proof.* Applying a Taylor expansion to  $\varphi^{(2)}$ , we write

$$\Phi''_{tz} = \Psi_{2N-1} \tilde{V}_{tz} + t^{2N-2} \tilde{\Lambda}_{t,z}$$

where

$$\begin{aligned} \tilde{V}_{tz} &= \begin{pmatrix} 0 & \dots & 0 \\ 0 & \dots & 0 \\ 1 & \dots & 1 \\ \vdots & & \vdots \\ \frac{(tz_1)^{2N-3}}{(2N-3)!} & \dots & \frac{(tz_N)^{2N-3}}{(2N-3)!} \end{pmatrix}, \\ \tilde{\Lambda}_{t,z} &= \left( (z_i)^{2N-2} \int_0^1 \varphi^{(2N)}(st z_i) \frac{(1-s)^{2N-3}}{(2N-3)!} ds \right)_{1 \leq i \leq N}. \end{aligned} \tag{3.4.9}$$

Hence

$$\begin{aligned}\Pi_{tz}\Phi''_{tz} &= \Pi_{tz}(\Psi_{tz}\tilde{V}_{tz} + (\Psi_{N-1} - \Psi_{tz})\tilde{V}_{tz} + t^{2N-2}\tilde{\Lambda}_{t,z}) \\ &= \Pi_{tz}(-\Lambda_{t,z}D_tH_{tz}^{-1}\tilde{V}_{tz} + t^{2N-2}\tilde{\Lambda}_{t,z}) \text{ since } \Pi_{tz}\Psi_{tz} = 0.\end{aligned}$$

Using (3.4.5), we see that

$$\begin{aligned}D_tH_{tz}^{-1}\tilde{V}_{tz} &= H_z^{-1}\operatorname{diag}(t^{2N}, t^{2N-1}, \dots, t)\tilde{V}_{tz} \\ &= t^{2N-2}H_z^{-1}\tilde{V}_z, \quad \text{hence} \\ \Pi_{tz}\Phi''_{tz} &= t^{2N-2}\Pi_{tz}(-\Lambda_{t,z}H_z^{-1}\tilde{V}_z + \tilde{\Lambda}_{t,z}).\end{aligned}$$

Since  $\|\Pi_{tz}\| \leq 1$  and the continuous function  $(z, t) \mapsto -\Lambda_{t,z}H_z^{-1}\tilde{V}_z + \tilde{\Lambda}_{t,z}$  is uniformly bounded on the compact set  $\overline{\mathcal{B}}_{z_0} \times [0, 1]$ , we obtain

$$\|\Pi_{tz}\Phi''_{tz}\|_{\mathcal{H}} \leq \left( \sup_{(z', t') \in \overline{\mathcal{B}}_{z_0} \times [0, 1]} \|\Lambda_{t', z'}H_{z'}^{-1}\tilde{V}_{z'} + \tilde{\Lambda}_{t', z'}\|_{\mathcal{H}} \right) t^{2N-2}$$

□

We study further the projector  $\Pi_{tz}$  when it is not evaluated at the same  $z$  as  $\Gamma_{tz}$ .

**Lemma 9.** *If  $\varphi \in \operatorname{KER}^{(2N+1)}$ , then there is a constant  $L_2 > 0$  (which only depends on  $\varphi$ ,  $a_0$  and  $z_0$ ) such that for all  $z \in \overline{\mathcal{B}}_{z_0}$ , all  $t \in (0, 1]$ ,*

$$\left\| \Pi_{tz}\Gamma_{tz_0} \begin{pmatrix} a_0 \\ 0 \end{pmatrix} \right\|_{\mathcal{H}} \leq L_2 t^{2N} |z - z_0|_{\infty}.$$

*Proof.* Let us observe that

$$\begin{aligned}\Pi_{tz}\Gamma_{tz_0} &= \Pi_{tz}(\Psi_{2N-1}H_{tz_0} + \Lambda_{t,z_0}D_t) \\ &= \Pi_{tz}(\Psi_{tz}H_{tz_0} + (\Psi_{2N-1} - \Psi_{tz})H_{tz_0} + \Lambda_{t,z_0}D_t) \\ &= \Pi_{tz}(-\Lambda_{t,z}D_tH_{tz}^{-1}H_{tz_0} + \Lambda_{t,z_0}D_t) \text{ since } \Pi_{tz}\Psi_{tz} = 0.\end{aligned}$$

Observing that

$$D_tH_{tz}^{-1}H_{tz_0} = t^{2N}H_z^{-1}H_{z_0} \operatorname{diag}(1, \dots, 1, 1/t, \dots, 1/t) = H_z^{-1}H_{z_0}D_t,$$

we get

$$\Pi_{tz}\Gamma_{tz_0} = \Pi_{tz}(\Lambda_{t,z_0}(\operatorname{Id}_{2N} - H_z^{-1}H_{z_0}) + (\Lambda_{t,z_0} - \Lambda_{t,z})H_z^{-1}H_{z_0})D_t.$$

For  $k \in \{2N-1, 2N\}$ , the function  $(u, s, t) \mapsto u^k \varphi^{(2N)}(stu)$  is defined and  $\mathcal{C}^1$  on the compact sets (since  $\varphi \in \operatorname{KER}^{(2N+1)}$ )

$$\forall 1 \leq i \leq N, \quad \left[ z_{0i} - \frac{\Delta_0}{4}, z_{0i} + \frac{\Delta_0}{4} \right] \times [0, 1] \times [0, 1],$$

where  $\Delta_0$  is defined in (3.3.2). Thus there is a constant  $C > 0$  (which does not depend on  $t$  nor  $z \in \overline{\mathcal{B}}_{z_0}$ ) such that

$$\left| \int_0^1 \left( (z_i)^k \varphi^{(2N)}(st z_i) - (z_{0i})^k \varphi^{(2N)}(st z_{0i}) \right) \frac{(1-s)^{k-1}}{(k-1)!} ds \right| \leq C |z_i - z_{0i}|,$$

hence       $\|\Lambda_{t,z_0} - \Lambda_{t,z}\| \leq C |z - z_0|_\infty.$

As a result, since  $\|\Pi_{tz}\| \leq 1$  and  $z \mapsto H_z^{-1} H_{z_0}$  is bounded on  $\overline{\mathcal{B}}_{z_0}$ ,

$$\|\Pi_{tz}(\Lambda_{t,z_0} - \Lambda_{t,z})H_z^{-1}H_{z_0}\|_{\mathcal{H}} \leq C \sup_{z' \in \overline{\mathcal{B}}_{z_0}} \|H_{z'}^{-1}H_{z_0}\| |z - z_0|_\infty.$$

As for the left term,  $\Lambda_{t,z_0}$  is bounded uniformly in  $t \in [0, 1]$ , and the mapping  $z \mapsto H_z^{-1}H_{z_0}$  is  $\mathcal{C}^1$  on  $\overline{\mathcal{B}}_{z_0}$ . As a result, there is a constant  $\tilde{C} > 0$  such that

$$\forall z \in \overline{\mathcal{B}}_{z_0}, \quad \|\mathrm{Id}_N - H_z^{-1}H_{z_0}\| \leq \tilde{C} |z - z_0|_\infty.$$

To conclude, we observe that  $D_t \begin{pmatrix} a_0 \\ 0 \end{pmatrix} = t^{2N} \begin{pmatrix} a_0 \\ 0 \end{pmatrix}$ , and we combine the above inequalities to obtain

$$\left\| \Pi_{tz} \Gamma_{t,z_0} \begin{pmatrix} a_0 \\ 0 \end{pmatrix} \right\|_{\mathcal{H}} \leq \left( C \sup_{z' \in \overline{\mathcal{B}}_{z_0}} \|H_{z'}^{-1}H_{z_0}\| + \tilde{C} \sup_{t \in [0,1]} \|\Lambda_{t,z_0}\| \right) t^{2N} |z - z_0|_\infty.$$

□

**Asymptotics of the vanishing derivatives precertificate.** We end this section devoted to the asymptotic behavior of quantities related to  $\Gamma_{tz}$  by studying the second derivative of the vanishing derivatives precertificate  $\eta_{V,t}$  (see Definition 5 and [54] for more details). Theorem 3 ensures that the second derivatives of  $\eta_{V,t}$  do not vanish at  $z_{0,i}$ ,  $1 \leq i \leq N$ . However, it does not provide any estimation of those second derivatives. That is the purpose of the next proposition.

In view of Section 3.5, it will be useful to study those second derivatives not only for the precertificates that are defined by interpolating the sign at  $t z_0$  but more generally for the precertificates that are defined to interpolate the sign at  $t z$  for any  $z \in \overline{\mathcal{B}}_{z_0}$ .

**Proposition 19.** *Assume that  $\varphi \in \mathrm{KER}^{(2N+1)}$  and that  $\mathcal{J}_{2N-1}$  holds. Then*

$$\Phi''_{tz}^* \Gamma_{tz}^{+,*} \begin{pmatrix} \mathbb{1}_N \\ 0 \end{pmatrix} = t^{2N-2} \eta_W^{(2N)}(0) d_z + O(t^{2N-1}), \quad (3.4.10)$$

$$\text{where } d_z \in \mathbb{R}^N, \quad d_{z,i} \stackrel{\text{def.}}{=} \frac{2}{(2N)!} \prod_{j \neq i} (z_i - z_j)^2 \text{ for } 1 \leq i \leq N. \quad (3.4.11)$$

*Proof.* We proceed as in the proof of Lemma 8 by writing  $\Phi''_{tz} = \Psi_{2N-1}\tilde{V}_{tz} + t^{2N-2}\tilde{\Lambda}_{tz}$  (see (3.4.9)) and  $\Psi_{tz} = \Gamma_{tz}H_{tz}^{-1}$ . We obtain

$$\Phi''_{tz} = \Psi_{tz}\tilde{V}_{tz} + t^{2N-2}\tilde{\Lambda}_{tz} - t^{2N-2}\Lambda_{tz}H_z^{-1}\tilde{V}_z.$$

The first term yields

$$\tilde{V}_{tz}^*\Psi_{tz}^*\Gamma_{tz}^{+,*} \begin{pmatrix} \mathbb{1}_N \\ 0 \end{pmatrix} = \tilde{V}_{tz}^*\Psi_{tz}^*\Psi_{tz}(\Psi_{tz}^*\Psi_{tz})^{-1}H_{tz}^{-1,*} \begin{pmatrix} \mathbb{1}_N \\ 0 \end{pmatrix} = \tilde{V}_{tz}^*\delta_{2N} = 0. \quad (3.4.12)$$

As for the second term, we take the Taylor expansion a little further (using integration by parts),

$$\int_0^1 \varphi^{(2N)}(stz_i) \frac{(1-s)^{2N-3}}{(2N-3)!} ds = \frac{\varphi_{2N}}{(2N-2)!} + t z_i \int_0^1 \varphi^{(2N+1)}(stz_i) \frac{(1-s)^{2N-2}}{(2N-2)!} ds,$$

so as to obtain

$$\tilde{\Lambda}_{tz} = (\varphi_{2N}, \dots, \varphi_{2N}) \text{diag}(e_z) + O(t), \text{ where } e_z \stackrel{\text{def.}}{=} \left( \frac{(z_i)^{2N-2}}{(2N-2)!} \right)_{1 \leq i \leq N} \in \mathbb{R}^N$$

and, as usual,  $O(t)$  is uniform in  $z \in \overline{\mathcal{B}}_{z_0}$ . From Lemma 7, we also know that  $\Gamma_{tz}^{+,*} \begin{pmatrix} \mathbb{1}_N \\ 0 \end{pmatrix} = p_W + O(t)$ , hence

$$\tilde{\Lambda}_{tz}^*\Gamma_{tz}^{+,*} \begin{pmatrix} \mathbb{1}_N \\ 0 \end{pmatrix} = \text{diag}(e_z) \begin{pmatrix} \langle \varphi_{2N}, p_W \rangle_{\mathcal{H}} \\ \vdots \\ \langle \varphi_{2N}, p_W \rangle_{\mathcal{H}} \end{pmatrix} + O(t) = \eta_W^{(2N)}(0)e_z + O(t). \quad (3.4.13)$$

Now, we proceed with the last term. Similarly, by integration by parts,

$$\Lambda_{tz} = (\varphi_{2N} \ \dots \ \varphi_{2N}) \text{diag}(f_z) + O(t).$$

where  $f_z$  is defined by

$$f_z \stackrel{\text{def.}}{=} \left( \frac{(z_1)^{2N}}{(2N)!}, \dots, \frac{(z_N)^{2N}}{(2N)!}, \frac{(z_1)^{2N-1}}{(2N-1)!}, \dots, \frac{(z_N)^{2N-1}}{(2N-1)!} \right) \in \mathbb{R}^{2N}. \quad (3.4.14)$$

Hence,

$$\Lambda_{tz}^*\Gamma_{tz}^{+,*} \begin{pmatrix} \mathbb{1}_N \\ 0 \end{pmatrix} = \text{diag}(f_z) \begin{pmatrix} \langle \varphi_{2N}, p_W \rangle_{\mathcal{H}} \\ \vdots \\ \langle \varphi_{2N}, p_W \rangle_{\mathcal{H}} \end{pmatrix} + O(t) = \eta_W^{(2N)}(0)f_z + O(t).$$

To conclude, we study  $\tilde{V}_z^* H_z^{-1,*}$  (which is uniformly bounded on  $\overline{\mathcal{B}}_{z_0}$ ). In  $\mathbb{R}_{2N-1}[X]$  endowed with the basis  $(1, X, \dots, \frac{X^{2N-1}}{(2N-1)!})$ ,  $H_z^*$  is the matrix of the linear map which evaluates a polynomial and its derivatives at  $\{z_1, \dots, z_N\}$ . On the other hand  $\tilde{V}_z^*$  represents the evaluation of the second derivative at  $\{z_1, \dots, z_N\}$ . Thus,

$$\tilde{V}_z^* H_z^{-1,*} f_z = (P''(z_i))_{1 \leq i \leq N},$$

where  $P$  is the unique polynomial in  $\mathbb{R}_{2N-1}[X]$  which satisfies

$$\forall i = 1, \dots, N, \quad P(z_i) = \frac{(z_i)^{2N}}{(2N)!} \quad \text{and} \quad P'(z_i) = \frac{(z_i)^{2N-1}}{(2N-1)!}.$$

One may check that

$$P(X) = \frac{X^{2N}}{(2N)!} - \frac{1}{(2N)!} \prod_{i=1}^N (X - z_i)^2$$

$$\text{and} \quad P''(z_i) = \frac{z_i^{2N-2}}{(2N-2)!} - \frac{2}{(2N)!} \prod_{j \neq i} (z_i - z_j)^2.$$

As a result,

$$-\tilde{V}_z^* H_z^{-1,*} \Lambda_{t,z}^* \Gamma_{tz}^{+,*} \begin{pmatrix} \mathbb{1}_N \\ 0 \end{pmatrix} = \eta_W^{(2N)}(0)(d_z - e_z) + O(t), \quad (3.4.15)$$

where  $O(t)$  is uniform in  $z \in \overline{\mathcal{B}}_{z_0}$ . We obtain the claimed result by summing (3.4.12), (3.4.13) and (3.4.15).  $\square$

## 3.5 Building a Candidate Solution

Now that the technical issues regarding the asymptotic behavior of  $\Gamma_{tz}$  have been settled, we are ready to tackle the study of the BLASSO. In this section, we build a candidate solution for  $\mathcal{P}_\lambda(y_t)$  by relying on its optimality conditions.

### 3.5.1 First Order Optimality Conditions

The optimality conditions for  $\mathcal{P}_\lambda(y_t)$  (see [54]) state that any measure of the form  $m_{a,tz} = \sum_{i=1}^N a_i \delta_{tz_i}$  is a solution to  $\mathcal{P}_\lambda(y_t)$  if and only if the function defined by  $\eta_{\lambda,t} \stackrel{\text{def}}{=} \Phi^* p_{\lambda,t}$  with  $p_{\lambda,t} \stackrel{\text{def}}{=} \frac{1}{\lambda} (\Phi_{tz_0} a_0 + w - \Phi_{tz} a)$  satisfies  $\|\eta_{\lambda,t}\|_{\infty,X} \leq 1$  and  $\eta_{\lambda,t}(tz_i) = \text{sign}(a_i)$  for all  $1 \leq i \leq N$ .

Observe that we must have  $\eta'_{\lambda,t}(tz_i) = 0$  for all  $1 \leq i \leq N$ . Moreover, in our case, since we assume that  $a_{0,i} > 0$  we have in fact  $\eta_{\lambda,t}(tz_i) = 1$ .

In order to build such a function  $\eta_{\lambda,t}$ , let us consider the function  $f_t$  defined for some fixed  $t > 0$  on  $(\mathbb{R}^N)^2 \times \mathbb{R} \times \mathcal{H}$  by

$$f_t(u, v) \stackrel{\text{def}}{=} \Gamma_{tz}^* (\Phi_{tz} a - \Phi_{tz_0} a_0 - w) + \lambda \begin{pmatrix} \mathbb{1}_N \\ 0 \end{pmatrix} \quad (3.5.1)$$

$$\text{where } u = (a, z) \quad \text{and} \quad v = (\lambda, w). \quad (3.5.2)$$

Now, let us write  $u_0 \stackrel{\text{def}}{=} (a_0, z_0)$ . Notice that  $m_{a,tz}$  is a solution to  $\mathcal{P}_\lambda(y_t)$  if and only if  $f_t(u, v) = 0$  and  $\|\eta_{\lambda,t}\|_{\infty,X} \leq 1$ . Our strategy is therefore to construct solutions of  $f_t(u, v) = 0$  and to prove that  $\|\eta_{\lambda,t}\|_{\infty,X} \leq 1$  provided  $(\lambda, w)$  and  $\eta_W$  satisfy certain properties. More precisely we start by parametrizing the solutions of  $f_t(u, v) = 0$ , in a neighborhood of  $(u_0, 0)$ , using the Implicit Function Theorem.

The following Lemma 10 (whose proof is omitted and corresponds to simple computations) shows that  $f_t$  is smooth and gives its derivatives.

**Lemma 10.** *If  $\varphi \in \text{KER}^{(k+1)}$  for some  $k \in \mathbb{N}^*$  then  $f_t$  is of class  $\mathcal{C}^k$  and for all  $(u, v) \in (\mathbb{R}^N)^2 \times (\mathbb{R} \times \mathcal{H})$*

$$\begin{aligned} \partial_u f_t(u, v) &= \Gamma_{tz}^* \Gamma_{tz} J_{ta} + t \begin{pmatrix} 0 & \text{diag}(\Phi_{tz}^* (\Phi_{tz} a - \Phi_{tz_0} a_0 - w)) \\ 0 & \text{diag}(\Phi_{tz}^* (\Phi_{tz} a - \Phi_{tz_0} a_0 - w)) \end{pmatrix} \\ \partial_v f_t(u, v) &= \left( \begin{pmatrix} \mathbb{1}_N \\ 0 \end{pmatrix}, -\Gamma_{tz}^* \right) \end{aligned}$$

$$\text{where } J_{ta} \stackrel{\text{def}}{=} \begin{pmatrix} \text{Id}_N & 0 \\ 0 & t \text{diag}(a) \end{pmatrix}.$$

### 3.5.2 Implicit Function Theorem

Suppose that  $\mathcal{I}_{2N-1}$  holds and  $\varphi \in \text{KER}^{(2N+1)}$ . By the results of Section 3.4, there exists  $0 < t_0 < 1$  such that for  $0 < t < t_0$  and all  $z \in \overline{\mathcal{B}}_{z_0}$ ,  $\Gamma_{tz}^* \Gamma_{tz}$  is invertible.

In the following we shall consider a fixed value of such  $t_0$  provided by Lemma 11 below which also ensures additional properties.

Now, let  $t \in (0, t_0)$  be fixed. By Lemma 10,  $f_t$  is  $\mathcal{C}^{2N}$ ,  $\partial_u f_t(u_0, 0) = \Gamma_{t z_0}^* \Gamma_{t z_0} J_{t a_0}$  is invertible and  $f_t(u_0, 0) = 0$ . Hence by the Implicit Function Theorem, there exists  $V_t$  a neighborhood of 0 in  $\mathbb{R} \times \mathcal{H}$ ,  $U_t$  a neighborhood of  $u_0$  in  $(\mathbb{R}^N)^2$  and  $g_t : V_t \rightarrow U_t$  a  $\mathcal{C}^{2N}$  function such that

$$\forall (u, v) \in U_t \times V_t, \quad f_t(u, v) = 0 \iff u = g_t(v).$$

Moreover, denoting  $dg_t$  the differential of  $g_t$ , we have

$$\forall v \in V_t, \quad dg_t(v) = -(\partial_u f_t(g_t(v), v))^{-1} \partial_v f_t(g_t(v), v).$$

### 3.5.3 Extension of the Implicit Function $g_t$

Our goal is to prove that  $m_{a, t z}$  is the solution of the BLASSO, where  $(a, z) = u = g_t(v)$ . To this end, we shall exhibit additional constraints on  $v \in V_t$ , such as the scaling of the noise  $\|w\|_{\mathcal{H}}$  or  $\lambda$  with respect to  $t$ , in order to ensure that  $\|\eta_{\lambda, t}\|_{\infty, X} \leq 1$ . However, the size of the neighborhood  $V_t$  provided by the Implicit Function Theorem is *a priori* unknown, and it might implicitly impose even stronger conditions on  $\lambda$  and  $w$  as  $t \rightarrow 0^+$ .

Hence, before studying whether  $\|\eta_{\lambda, t}\|_{\infty, X} \leq 1$ , we show in this section that we may replace  $V_t$  with some ball with radius of order  $t^{2N-1}$  and still have a parametrization of the form  $u = g_t(v)$  satisfying  $f_t(g_t(v), v) = 0$  where  $f_t$  is defined in (3.5.1).

Let  $V_t^* = \bigcup_{V \in \mathcal{V}} V$ , where  $\mathcal{V}$  is the collection of all open sets  $V \subset \mathbb{R} \times \mathcal{H}$  such that

- $0 \in V$ ,
- $V$  is star-shaped with respect to 0,
- $V \subset B(0, C_T t^{2N-2})$ , where  $C_T > 0$  is a constant defined by Lemma 11 below,
- there exists a  $\mathcal{C}^{2N}$  function  $g : V \rightarrow (\mathbb{R}^N)^2$  such that  $g(0) = u_0$  and  $f_t(g(v), v) = 0$  for all  $v \in V$ ,
- $g(V) \subset \mathcal{B}_{a_0} \times \mathcal{B}_{z_0}$ .

Observe that  $\mathcal{V}$  is nonempty (by the Implicit Function Theorem in Section 3.5.2) and stable by union, so that  $V_t^* \in \mathcal{V}$ . Indeed, all the properties defining  $\mathcal{V}$  are easy to check except possibly the last two. Let  $V, \tilde{V} \in \mathcal{V}$  and  $g, \tilde{g}$  be corresponding functions. The set  $\{v \in V \cap \tilde{V} ; g(v) = \tilde{g}(v)\}$  is nonempty (because  $g(0) = u_0 = \tilde{g}(0)$ ) and closed in  $V \cap \tilde{V}$ . Moreover, it is open since for any  $v \in V \cap \tilde{V}$ ,  $v \in B(0, C_T t^{2N-2})$  and, by Lemma 11 below, the Implicit Function Theorem applies at  $(g(v), v)$ , yielding an open neighborhood in which  $g$  and  $\tilde{g}$  coincide. By connectedness of  $V \cap \tilde{V}$ ,

$g$  and  $\tilde{g}$  coincide in the whole set  $V \cap \tilde{V}$ . As a result, the function  $g_t^* : V_t^* \rightarrow (\mathbb{R}^N)^2$ , defined by

$$g_t^*(v) \stackrel{\text{def.}}{=} g(v) \text{ if } v \in V, V \in \mathcal{V}, \text{ and } g \text{ is a corresponding function,} \quad (3.5.3)$$

is well defined. Moreover,  $g_t^*$  is  $\mathcal{C}^{2N}$  and  $g_t^*(V_t^*) \subset \mathcal{B}_{a_0} \times \mathcal{B}_{z_0}$ .

Before proving that  $V_t^*$  contains a ball of radius of order  $t^{2N-1}$  and studying the variations of  $g_t^*$ , we state Lemma II mentioned above.

**Lemma 11.** *If  $\mathcal{I}_{2N-1}$  holds and  $\varphi \in \text{KER}^{(2N+1)}$  then there exists  $t_0 \in (0, 1)$  and  $C_T > 0$  (which only depend on  $\varphi$  and  $u_0$ ) such that for all  $t \in (0, t_0)$ , if*

$$u = (a, z) \in \overline{\mathcal{B}}_{a_0} \times \overline{\mathcal{B}}_{z_0} \quad \text{and} \quad v = (\lambda, w) \in B(0, C_T t^{2N-2}), \quad (3.5.4)$$

then the matrix

$$G_{tz}(\lambda, w) \stackrel{\text{def.}}{=} \Psi_{tz}^* \Psi_{tz} + t H_{tz}^{*, -1} F_{tz} J_{ta}^{-1} H_{tz}^{-1}, \quad (3.5.5)$$

$$\text{where } F_{tz} \stackrel{\text{def.}}{=} \begin{pmatrix} 0 & 0 \\ 0 & -\text{diag}(\Phi_{tz}'' q_{tz}) \end{pmatrix}, \quad (3.5.6)$$

$$\text{and } q_{tz} \stackrel{\text{def.}}{=} \lambda \Gamma_{tz}^{*, +} \begin{pmatrix} \mathbb{1}_N \\ 0 \end{pmatrix} + \Pi_{tz} w + \Pi_{tz} \Gamma_{tz} \begin{pmatrix} a_0 \\ 0 \end{pmatrix}, \quad (3.5.7)$$

is invertible and the norm of its inverse is less than  $3 \|(\Psi_{2N-1}^* \Psi_{2N-1})^{-1}\|$ .

If, moreover,  $f_t(u, v) = 0$ , then

$$\partial_u f_t(u, v) = H_{tz}^* G_{tz}(\lambda, w) H_{tz} J_{ta}$$

and this is an invertible matrix.

Let us precise that by  $(\lambda, w) \in B(0, C_T t^{2N-2})$ , we mean that  $|\lambda| < C_T t^{2N-2}$  and  $\|w\|_{\mathcal{H}} < C_T t^{2N-2}$ .

*Proof.* We consider  $t_0 \in (0, 1)$  small enough so that for  $0 < t < t_0$  and all  $z \in \overline{\mathcal{B}}_{z_0}$ ,  $\Gamma_{tz}^* \Gamma_{tz}$  is invertible and

$$\|(\Psi_{tz}^* \Psi_{tz})^{-1}\| \leq 2 \|(\Psi_{2N-1}^* \Psi_{2N-1})^{-1}\| \text{ by Lemma } \text{II}, \quad (3.5.8)$$

$$\left| \lambda \Phi_{tz}'' \Gamma_{tz}^{*, +} \begin{pmatrix} \mathbb{1}_N \\ 0 \end{pmatrix} \right|_{\infty} \leq \frac{4(2R_W)^{2N}}{(2N)!} |\lambda \eta_W^{(2N)}(0)| t^{2N-2} \text{ by Proposition } \text{I9}. \quad (3.5.9)$$

In the last equation, we have used the fact that  $|\prod_{j \neq i} (z_i - z_j)^2| \leq (2R_W)^{2N}$  (where  $R_W = \sup\{|z|_{\infty}; z \in \overline{\mathcal{B}}_{z_0}\}$  is defined in Equation (3.3.4)).

We also know that for some constants  $L_1, L_2 > 0$  which only depend on  $\varphi$  and  $u_0$ ,

$$|\Phi_{tz}'' \Pi_{tz} w|_{\infty} \leq \|w\|_{\mathcal{H}} L_1 t^{2N-2} \text{ by Lemma } \text{II},$$

$$\text{and } \left| \Phi_{tz}'' \Pi_{tz} \Gamma_{tz} \begin{pmatrix} a_0 \\ 0 \end{pmatrix} \right|_{\infty} \leq L_1 L_2 \frac{\Delta_0}{4} t^{4N-2} \text{ by Lemma } \text{II} \text{ and Lemma } \text{I9},$$

for all  $z \in \overline{\mathcal{B}}_{z_0} = \overline{B}\left(z_0, \frac{\Delta_0}{4}\right)$ ,  $t \in (0, t_0)$ , where  $\Delta_0$  is defined in (3.3.2).

Combining those inequalities with (3.5.9), we see that

$$\begin{aligned} |\Phi_{tz}'' q_{tz}|_\infty &= \left| \lambda \Phi_{tz}'' \Gamma_{tz}^{*,+} \begin{pmatrix} \mathbb{I}_N \\ 0 \end{pmatrix} + \Phi_{tz}'' \Pi_{tz} w + \Phi_{tz}'' \Pi_{tz} \Gamma_{tz_0} \begin{pmatrix} a_0 \\ 0 \end{pmatrix} \right|_\infty \\ &\leq |\lambda| \frac{4}{(2N)!} \left| \eta_W^{(2N)}(0) \right| t^{2N-2} + \|w\|_{\mathcal{H}} L_1 t^{2N-2} + L_1 L_2 \frac{\Delta_0}{4} t^{4N-2} \end{aligned}$$

On the other hand, since

$$\begin{aligned} H_{tz}^{*, -1} &= \text{diag}(1, \dots, 1/t^{2N-1}) H_z^{*, -1} \text{diag}(1, \dots, 1, t, \dots, t), \\ \text{and } F_{tz} &= \begin{pmatrix} 0 & 0 \\ 0 & -\text{diag}(\Phi_{tz}'' q_{tz}) \end{pmatrix}, \end{aligned}$$

we get

$$\begin{aligned} H_{tz}^{*, -1} F_{tz} J_{ta}^{-1} H_{tz}^{-1} &= t \text{diag}(1, \dots, \frac{1}{t^{2N-1}}) H_z^{*, -1} F_{tz} \\ &\quad J_a^{-1} H_z^{-1} \text{diag}(1, \dots, \frac{1}{t^{2N-1}}) \end{aligned}$$

so that

$$\begin{aligned} \|t H_{tz}^{*, -1} F_{tz} J_{ta}^{-1} H_{tz}^{-1}\| &\leq \frac{|a|^{-1}|_\infty}{t^{4N-4}} \|H_z^{*, -1}\| \|H_z^{-1}\| |\Phi_{tz}'' q_{tz}|_\infty \\ &\leq C \left( \frac{|\lambda|}{t^{2N-2}} \frac{4(2R)^{2N}}{(2N)!} \left| \eta_W^{(2N)}(0) \right| \right. \\ &\quad \left. + \frac{\|w\|_{\mathcal{H}} L_1 + L_2 L_1 \frac{\Delta_0}{4} t^2}{t^{2N-2}} \right) \end{aligned}$$

with  $C = \sup_{(a,z) \in \overline{\mathcal{B}}_{a_0} \times \overline{\mathcal{B}}_{z_0}} \|H_z^{*, -1}\| \|H_z^{-1}\| |a|^{-1}|_\infty$ .

Possibly choosing  $t_0$  a bit smaller, we may assume that

$$0 \leq CL_2 L_1 \frac{\Delta_0}{4} t_0^2 < \frac{1}{8 \|(\Psi_{2N-1}^* \Psi_{2N-1})^{-1}\|}.$$

As a consequence, there exists  $C_T > 0$  such that for all  $t \in (0, t_0)$ , and all  $(a, z) \in \overline{\mathcal{B}}_{a_0} \times \overline{\mathcal{B}}_{z_0}$ ,

$$\begin{aligned} \left( \max \left( \frac{|\lambda|}{t^{2N-2}}, \frac{\|w\|_{\mathcal{H}}}{t^{2N-2}} \right) \leq C_T \right) \\ \implies \|t H_{tz}^{*, -1} F_{tz} J_{ta}^{-1} H_{tz}^{-1}\| \leq \frac{1}{4 \|(\Psi_{2N-1}^* \Psi_{2N-1})^{-1}\|}. \end{aligned}$$

Then, recalling (3.5.8) and setting

$$\begin{aligned} r &\stackrel{\text{def.}}{=} \left\| t (\Psi_{tz}^* \Psi_{tz})^{-1} H_{tz}^{*, -1} F_{tz} J_{ta}^{-1} H_{tz}^{-1} \right\| \\ &\leq 2 \|(\Psi_{2N-1}^* \Psi_{2N-1})^{-1}\| \frac{1}{4 \|(\Psi_{2N-1}^* \Psi_{2N-1})^{-1}\|} = \frac{1}{2}, \end{aligned}$$

we see that the matrix (3.5.5) is invertible, and

$$\left\| \left( \text{Id}_{2N} + t (\Psi_{tz}^* \Psi_{tz})^{-1} H_{tz}^{*, -1} F_{tz} J_{ta}^{-1} H_{tz}^{-1} \right)^{-1} \right\| \leq \sum_{k=0}^{+\infty} r^k = \frac{1}{1-r} \leq \frac{3}{2}.$$

Eventually, using (3.5.8) again, we obtain that the norm of the inverse of (3.5.5) is less than  $3 \|(\Psi_{2N-1}^* \Psi_{2N-1})^{-1}\|$ .

Now, if  $f_t(u, v) = 0$ , then  $\Phi_{tz}'^*(\Phi_{tz}a - \Phi_{tz_0}a_0 - w) = 0$ , so that thanks to Lemma 10 we obtain

$$\partial_u f_t(u, v) = \Gamma_{tz}^* \Gamma_{tz} J_{ta} + t \begin{pmatrix} 0 & 0 \\ 0 & \text{diag}(\Phi_{tz}''^*(\Phi_{tz}a - \Phi_{tz_0}a_0 - w)) \end{pmatrix}.$$

Moreover,

$$\begin{aligned} \Phi_{tz}a - \Phi_{tz_0}a_0 - w &= \Gamma_{tz} \begin{pmatrix} a \\ 0 \end{pmatrix} - \Gamma_{tz_0} \begin{pmatrix} a_0 \\ 0 \end{pmatrix} - w \\ &= \Gamma_{tz}^{*,+} \Gamma_{tz}^* \Gamma_{tz_0} \begin{pmatrix} a_0 \\ 0 \end{pmatrix} + \Gamma_{tz}^{*,+} \Gamma_{tz}^* w - \lambda \Gamma_{tz}^{*,+} \begin{pmatrix} \mathbb{1}_N \\ 0 \end{pmatrix} - \Gamma_{tz_0} \begin{pmatrix} a_0 \\ 0 \end{pmatrix} - w \\ &= -\Pi_{tz} \Gamma_{tz_0} \begin{pmatrix} a_0 \\ 0 \end{pmatrix} - \Pi_{tz} w - \lambda \Gamma_{tz}^{*,+} \begin{pmatrix} \mathbb{1}_N \\ 0 \end{pmatrix} = -q_{tz}. \end{aligned}$$

As a result,

$$\begin{aligned} \partial_u f_t(u, v) &= H_{tz}^* \Psi_{tz}^* \Psi_{tz} H_{tz} J_{ta} + t \begin{pmatrix} 0 & 0 \\ 0 & \text{diag}(\Phi_{tz}''^* q_{tz}) \end{pmatrix} \\ &= H_{tz}^* G_{tz}(\lambda, w) H_{tz} J_{ta}, \end{aligned}$$

and  $\partial_u f_t(u, v)$  is invertible.  $\square$

We may now study the variations of  $g_t^*$ .

**Corollary 2.** *If  $\mathcal{I}_{2N-1}$  holds and  $\varphi \in \text{KER}^{(2N+1)}$  then there exists  $M > 0$  (which only depends on  $\varphi$  and  $u_0$ ), such that for  $0 < t < t_0$ , for all  $v \in V_t^*$*

$$\|\text{dg}_t^*(v)\| \leq \frac{M}{t^{2N-1}}.$$

*Proof.* Let us recall that by construction,  $V_t^* \subset B(0, C_T t^{2N-2})$ . Thus, from Lemma 11, we know that for all  $v \in V_t^*$ ,  $\partial_u f_t(g_t(v), v) = H_{tz}^* G_{tz}(\lambda, w) H_{tz} J_{ta}$ , where  $(a, z) = g_t^*(v)$ . Since  $\text{dg}_t^*(v) = -(\partial_u f_t(g_t^*(v), v))^{-1} \partial_v f_t(g_t^*(v), v)$ , we get

$$\begin{aligned} \text{dg}_t^*(v) &= -J_{ta}^{-1} H_{tz}^{-1} G_{tz}(\lambda, w)^{-1} H_{tz}^{*, -1} \left( \begin{pmatrix} \mathbb{1}_N \\ 0 \end{pmatrix}, -H_{tz}^* \Psi_{tz}^* \right) \\ &= J_a^{-1} H_z^{-1} \text{diag} \left( 1, \dots, \frac{1}{t^{2N-1}} \right) G_{tz}(\lambda, w)^{-1} (\delta_{2N}, \Psi_{tz}^*), \end{aligned}$$

Using Lemma 11 and the fact that  $J_a^{-1}, H_z^{-1}, \Psi_{tz}$  are uniformly bounded on  $\overline{\mathcal{B}}_{a_0} \times \overline{\mathcal{B}}_{z_0}$ , we obtain the claimed upper bound of  $\|\text{dg}_t^*(v)\|$  for all  $v \in V_t^*$ .  $\square$

We are now in position to prove that  $V_t^*$  contains a ball of radius of order  $t^{2N-1}$ .

**Proposition 20.** *If  $\mathcal{I}_{2N-1}$  holds and  $\varphi \in \text{KER}^{(2N+1)}$ , there exists  $C_R > 0$  such that for all  $t \in (0, t_0)$ ,*

$$B(0, C_R t^{2N-1}) \subset V_t^* \quad \text{with} \quad C_R \geq \min\left(\frac{\Delta_0}{4M}, \frac{\min_i(a_{0,i})}{4M}, \frac{C_T}{t_0}\right).$$

*Proof.* Let  $v \in \mathbb{R} \times \mathcal{H}$  with unit norm (i.e.  $\max(\lambda, \|w\|_{\mathcal{H}}) = 1$ ), and define

$$R_v \stackrel{\text{def.}}{=} \sup \{r \geq 0 ; rv \in V_t^*\}.$$

Clearly  $0 < R_v \leq C_T t^{2N-2}$ . Assume that  $R_v < C_T t^{2N-2}$ . Then by Corollary 2,  $g_t^*$  is uniformly continuous on  $V_t^*$ , so that the value of  $g_t^*(R_v v)$  can be defined as a limit, and  $f_t(g_t^*(R_v v), R_v v) = 0$ .

By contradiction, if  $g_t^*(R_v v) \in \mathcal{B}_{a_0} \times \mathcal{B}_{z_0}$ , then by Lemma 11, we may apply the Implicit Function Theorem to obtain a neighborhood of  $(g_t^*(R_v v), R_v)$  in which  $g_t^*$  may be extended. This enables us to construct an open set  $V \in \mathcal{V}$  (in particular we may ensure that  $V$  is star-shaped with respect to 0) such that  $V_t^* \subsetneq V$ , which contradicts the maximality of  $V_t^*$ .

Hence,  $g_t^*(R_v v) \in \partial(\mathcal{B}_{a_0} \times \mathcal{B}_{z_0}) = (\partial(\mathcal{B}_{a_0}) \times \overline{\mathcal{B}}_{z_0}) \cup (\overline{\mathcal{B}}_{a_0} \times \partial(\mathcal{B}_{z_0}))$ . Assume for instance that  $g_t^*(R_v v) \in \overline{\mathcal{B}}_{a_0} \times \partial(\mathcal{B}_{z_0})$  (the other case being similar). Then, for  $(a, z) = g_t^*(R_v v)$ ,

$$\frac{\Delta_0}{4} = |z - z_0|_\infty \leq \int_0^1 |\mathrm{d}g_t^*(sR_v v) \cdot R_v v|_\infty \, ds \leq \frac{M}{t^{2N-1}} R_v,$$

which yields  $R_v \geq \frac{\Delta_0}{4M} t^{2N-1}$ . Similarly, if  $g_t^*(R_v v) \in \partial(\mathcal{B}_{a_0}) \times \overline{\mathcal{B}}_{z_0}$ , we may prove that  $R_v \geq \frac{\min_i(a_{0,i})}{4M} t^{2N-1}$ .

Eventually, we have proved that for all  $v \in \mathbb{R} \times \mathcal{H}$  with unit norm,

$$R_v \geq \min\left(\frac{\Delta_0}{4M} t^{2N-1}, \frac{\min_i(a_{0,i})}{4M} t^{2N-1}, C_T t^{2N-2}\right),$$

and the claimed result follows.  $\square$

### 3.5.4 Continuity of $g_t^*$ at 0

Before moving to Section 3.6 and to the proof of  $\|\eta_{\lambda,t}\|_{\infty,X} \leq 1$  (which ensures that  $m_{a,tz}$  is a solution to the BLASSO), we give a first order expansion of our candidate solution  $u = g_t^*(v)$  for all  $v \in B(0, C_R t^{2N-1})$ .

**Proposition 21.** *If  $\mathcal{I}_{2N-1}$  holds and  $\varphi \in \text{KER}^{(2N+1)}$  then for all  $t \in (0, t_0)$ ,  $v \in B(0, C_R t^{2N-1})$ ,*

$$\|g_t^*(v) - g_t^*(0)\| \leq M \left( \frac{|\lambda|}{t^{2N-1}} + \frac{\|w\|_{\mathcal{H}}}{t^{2N-1}} \right). \quad (3.5.10)$$

*Proof.* To show Equation (3.5.10), it suffices to write

$$g_t^*(v) = g_t^*(0) + \int_0^1 dg_t^*(sv) \cdot v ds,$$

and use Corollary 2 to conclude.  $\square$

### 3.6 Convergence of $\eta_{\lambda,t}$ to $\eta_W$

In our scheme of proving Theorem 5 (recall that its proof using all the elements detailed in Section 3.4, 3.5 and 3.6 can be found in Section 3.3.2), it remains to show that  $m_{a,tz}$  where  $(a,z) = g_t^*(v)$  is indeed a solution to  $\mathcal{P}_\lambda(y_t)$ . To demonstrate this statement, we prove in this section with Proposition 22, that  $\eta_{\lambda,t}$  converges towards  $\eta_W$  when  $(t,\lambda,w/\lambda) \rightarrow 0$ . This proposition is similar to the one already proved in Section 1.2 (see Proposition 4) where one shows that  $\eta_{\lambda,t} \rightarrow \eta_V$  when  $(\lambda,w/\lambda) \rightarrow 0$ . It was crucial in the proof of the robustness to noise of the BLASSO (see Theorem 1). The convergence proved in Proposition 22 plays a similar role for Theorem 5 because it uses this convergence result, the assumption that  $\eta_W$  is  $(2N-1)$ -non-degenerate and the transfer theorem (see Theorem 3) to conclude.

**Proposition 22.** Assume that  $\varphi \in \text{KER}^{(2N+1)}$  and that  $\mathcal{I}_{2N-1}$  holds, and let  $C_W > 0$  be the constant defined in Theorem 3,  $g_t^*$ ,  $t_0 > 0$  and  $C_R > 0$  be the function and constants defined in Section 3.5.

Then there exist constants  $t_1 \in (0, t_0)$  and  $C > 0$  (which depend only on  $\varphi$  and  $u_0$ ) such that for all  $t \in (0, t_1)$  and for all  $(\lambda, w) \in B(0, C_R t^{2N-1})$  with  $\left\| \frac{w}{\lambda} \right\|_{\mathcal{H}} \leq C$ , the following inequalities hold

$$\forall \ell \in \{0, \dots, 2N\}, \quad \left\| \eta_{\lambda,t}^{(\ell)} - \eta_W^{(\ell)} \right\|_{\infty, X} \leq C_W,$$

with  $\eta_{\lambda,t} = \Phi^* \left( \frac{1}{\lambda} (\Phi_{tz_0} a_0 + w - \Phi_{tz} a) \right)$  and  $(a,z) = g_t^*(\lambda, w)$ .

*Proof.* Let  $t \in (0, t_0)$ ,  $v \in B(0, C_R t^{2N-1})$ , and  $(a,z) = u = g_t^*(v)$ . Then, using  $f_t(u,v) = 0$  (see (3.5.1)), we get

$$\begin{aligned} p_{\lambda,t} &\stackrel{\text{def.}}{=} \frac{1}{\lambda} (\Phi_{tz_0} a_0 + w - \Phi_{tz} a) \\ &= \frac{1}{\lambda} \left( \Gamma_{tz_0} \begin{pmatrix} a_0 \\ 0 \end{pmatrix} + w - \Gamma_{tz} \begin{pmatrix} a \\ 0 \end{pmatrix} \right) \\ &= \Gamma_{tz}^{*,+} \begin{pmatrix} \mathbb{1}_N \\ 0 \end{pmatrix} + \Pi_{tz} \frac{w}{\lambda} + \frac{1}{\lambda} \Pi_{tz} \Gamma_{tz_0} \begin{pmatrix} a_0 \\ 0 \end{pmatrix}. \end{aligned}$$

Hence,

$$\left\| p_{\lambda,t} - p_W \right\|_{\mathcal{H}} \leq \left\| \Gamma_{tz}^{*,+} \begin{pmatrix} \mathbb{1}_N \\ 0 \end{pmatrix} - p_W \right\|_{\mathcal{H}} + \left\| \Pi_{tz} \frac{w}{\lambda} \right\|_{\mathcal{H}} + \left\| \frac{1}{\lambda} \Pi_{tz} \Gamma_{tz_0} \begin{pmatrix} a_0 \\ 0 \end{pmatrix} \right\|_{\mathcal{H}}$$

From Lemma 7, there exists  $C_V > 0$  and  $t_V > 0$  (which only depends on  $\varphi, u_0$ ) such that for all  $t \in (0, t_V)$  and all  $z \in \mathcal{B}_{z_0}$ ,

$$\left\| \Gamma_{tz}^{*,+} \begin{pmatrix} \mathbb{1}_N \\ 0 \end{pmatrix} - p_W \right\|_{\mathcal{H}} \leq C_V t.$$

Moreover, since  $\Pi_{tz}$  is an orthogonal projector,

$$\left\| \Pi_{tz} \frac{w}{\lambda} \right\|_{\mathcal{H}} \leq \left\| \frac{w}{\lambda} \right\|_{\mathcal{H}},$$

and by Lemma 9, there exists  $L_2 > 0$  (which only depends on  $\varphi, u_0$ ) such that, for all  $t \in (0, t_0)$

$$\begin{aligned} \left\| \frac{1}{\lambda} \Pi_{tz} \Gamma_{tz_0} \begin{pmatrix} a_0 \\ 0 \end{pmatrix} \right\|_{\mathcal{H}} &\leq \frac{L_2}{|\lambda|} t^{2N} |z - z_0|_{\infty} \\ &\leq \frac{L_2}{|\lambda|} t^{2N} \frac{M}{t^{2N-1}} (|\lambda| + \|w\|_{\mathcal{H}}) \text{ by Proposition 21} \\ &\leq L_2 M t \left( 1 + \left\| \frac{w}{\lambda} \right\|_{\mathcal{H}} \right). \end{aligned}$$

Gathering all these upper-bounds, one obtains

$$\begin{aligned} \|p_{\lambda,t} - pw\|_{\mathcal{H}} &\leq (C_V + L_2 M) t + (1 + L_2 M t) \left\| \frac{w}{\lambda} \right\|_{\mathcal{H}} \\ &\leq (C_V + L_2 M) t + (1 + L_2 M) \left\| \frac{w}{\lambda} \right\|_{\mathcal{H}} \end{aligned}$$

Now, denoting by  $\Phi^{(\ell)} : \mathcal{M}(X) \rightarrow \mathcal{H}$  the operator  $m \mapsto \int_X \varphi^{(\ell)}(x) dm(x)$  and by  $\Phi^{(\ell)*} : \mathcal{H} \rightarrow \mathcal{C}_0$  its adjoint (so that  $\eta_{\lambda,t}^{(\ell)} = \Phi^{(\ell)*} p_{\lambda,t}$  and  $\eta_W^{(\ell)} = \Phi^{(\ell)*} p_W$ ), we let

$$K \stackrel{\text{def.}}{=} \max_{0 \leq \ell \leq 2N} \sup_{x \in X} \left\| \varphi^{(\ell)}(x) \right\|_{\mathcal{H}},$$

which satisfies  $K < +\infty$  because  $\varphi \in \text{KER}^{(2N+1)}$ . Then, for all  $\ell \in \{0, \dots, 2N\}$ ,

$$\begin{aligned} \left\| \eta_{\lambda,t}^{(\ell)} - \eta_W^{(\ell)} \right\|_{\infty,X} &\leq K \|p_{\lambda,t} - pw\|_{\mathcal{H}} \\ &\leq K \left( (C_V + L_2 M) t + (1 + L_2 M) \left\| \frac{w}{\lambda} \right\|_{\mathcal{H}} \right). \end{aligned}$$

As a consequence, by taking  $t$  smaller than  $\min(t_0, t_V, \frac{C_W}{2K(C_V + L_2 M)})$  and for all  $(\lambda, w) \in B(0, C_R t^{2N-1})$  such that

$$(1 + L_2 M) \left\| \frac{w}{\lambda} \right\|_{\mathcal{H}} \leq \frac{C_W}{2K},$$

we get

$$\left\| \eta_{\lambda,t}^{(\ell)} - \eta_W^{(\ell)} \right\|_{\infty,X} \leq C_W.$$

□

*Remark 5.* The constants involved in Proposition 22 are

$$t_1 \stackrel{\text{def.}}{=} \min(t_0, t_V, \frac{C_W}{2K(C_V + L_2 M)}) \quad \text{and} \quad C \stackrel{\text{def.}}{=} \frac{C_W}{2K(1 + L_2 M)}. \quad (3.6.1)$$

They only depend on  $\varphi$  and  $u_0$ .

## Necessary Recovery Condition

In this section, we prove Proposition 17 stated in Section 3.2. One recalls it below.

**Proposition 23.** Suppose that  $\mathcal{I}_{2N-1}$  holds and  $\varphi \in \text{KER}^{(2N+1)}$ . Suppose also that there exists a sequence  $(t_n)_{n \in \mathbb{N}}$  such that  $t_n \rightarrow 0$  and satisfying

$$\forall n \in \mathbb{N}, \exists (\lambda_n, w_n), \exists (a_n, z_n) \in \mathbb{R}^N \times \mathbb{R}^N, m_{a_n, t_n z_n} \text{ is solution of } \mathcal{P}_{\lambda_n}(y_{t_n}),$$

where  $y_{t_n} \stackrel{\text{def.}}{=} \Phi m_{a_0, t_n z_0} + w_n$ ,  $(\lambda_n, w_n) \rightarrow 0$  with  $\frac{\|w_n\|_{\mathcal{H}}}{\lambda_n} \rightarrow 0$ . Then

$$\|\eta_W\|_{\infty, X} \leq 1. \quad (3.6.2)$$

*Proof of Proposition 17* For all  $n \in \mathbb{N}$ , the solution  $m_n \stackrel{\text{def.}}{=} m_{a_n, t_n z_n}$  of  $\mathcal{P}_{\lambda_n}(y_{t_n})$  satisfies the following first order optimality conditions:

$$\Gamma_{t_n z_n}^* (\Phi_{t_n z_n} a_n - \Phi_{t_n z_0} a_0 - w_n) + \lambda_n \begin{pmatrix} \mathbb{1}_N \\ 0 \end{pmatrix} = 0. \quad (3.6.3)$$

Since  $\eta_{\lambda_n, t_n} = \Phi^*(\frac{1}{\lambda_n}(\Phi_{t_n z_0} a_0 + w_n - \Phi_{t_n z_n} a_n))$  satisfies  $\|\eta_{\lambda_n, t_n}\|_{\infty, X} \leq 1$ ,  $\eta_{\lambda_n, t_n} \in \text{Im } \Phi^*$  and  $\eta_{\lambda_n, t_n}(t z_n) = \text{sign}(a_n) = 1$ .

As a result, by taking  $n$  large enough if necessary, we know that  $(a_n, z_n) = g_t^*(\lambda_n, w_n)$  with  $g_t^* \in \mathcal{C}^{2N}(V_t^*)$  so that  $(a_n, z_n) \rightarrow (a_0, z_0)$ . Therefore all the asymptotic results that we established in Chapter 3 are true when applied for  $(a_n, z_n)$  for  $n$  large enough. Observe from (3.6.3), that we get for all  $n \in \mathbb{N}$ :

$$p_{\lambda_n, t_n} = \Gamma_{t_n z_n}^{*,+} \begin{pmatrix} \mathbb{1}_N \\ 0 \end{pmatrix} + \Pi_{t_n z_n} \frac{w_n}{\lambda_n} + \frac{1}{\lambda_n} \Pi_{t_n z_n} \Gamma_{t z_0} \begin{pmatrix} a_0 \\ 0 \end{pmatrix}.$$

As a consequence:

$$\|p_{\lambda_n, t_n} - p_W\|_{\mathcal{H}} \rightarrow 0 \quad \text{when } n \rightarrow +\infty,$$

so that for all  $0 \leq l \leq 2N$ ,

$$\left\| \eta_{\lambda_n, t_n}^{(l)} - \eta_W^{(l)} \right\|_{\infty, X} \rightarrow 0 \quad \text{when } n \rightarrow +\infty. \quad (3.6.4)$$

In particular, since  $\|\eta_{\lambda, t}\|_{\infty, X} \leq 1$ , we deduce (3.6.2):

$$\|\eta_W\|_{\infty, X} \leq 1.$$

□



**Part II**

**Numerical Grid-Less BLASSO  
Solving**



## Chapter 4

# The Sliding Frank-Wolfe BLASSO Solver

Grid-less approaches for super-resolution in presence of noise of sparse signals comes with strong theoretical guarantees (see Part I of the Thesis). This suggests that algorithms that can cope with this grid-less setting may have also nice practical recovery properties. In this Chapter we detail the Sliding Frank-Wolfe algorithm (SFW algorithm), which is a new BLASSO solver. It is an extension of the initial Frank-Wolfe solver of [24] (see also [22]). This algorithm moves continuously the positions and amplitudes of the Dirac masses after each creation of a new spike, taking advantage of the continuous nature of the domain  $X$ . Our main theoretical contribution, notably thanks to this particular update and under some mild assumptions, is that the SFW algorithm converges after only a finite number of newly created spikes, improving drastically the known weak-\* convergence of Frank-Wolfe based algorithms. We then compare the practical recovery performance of the Sliding Frank-Wolfe algorithm on synthetic benchmarks with other algorithms (FISTA and OMP). We show that the SFW algorithm has better performance both for a Optimal Transport based metric and for detection indices based metrics. Finally we study numerically, using our algorithm, some particular properties of the numerical inversion of the Laplace transform using the BLASSO, in view of Chapter 5 where it is involved in a fluorescent microscopy model (PALM+MA-TIRF) in Biology. This experimental study shows that normalizing the kernel (with the  $L^2$  norm) leads to better performance and that the size of the interval containing the discretization points of the Laplace transform influence the ability to recover spikes near or far the origin.

## 4.1 Introduction

In the first part of this thesis (Chapter I and III) we provided theoretical guarantees when solving the BLASSO for the super-resolution problem with noise contaminating the data. Now we move to the study of numerical methods which may use advantageously the continuous setting of the BLASSO and thus efficiently solving the super-resolution problem.

### 4.1.1 Approximation Schemes for the BLASSO

Because the BLASSO is an optimization problem over the space of Radon measures  $\mathcal{M}(X)$  which is an infinite dimensional space, its exact or approximate resolution is delicate. There are several ways to tackle this problem:

**Fixed spatial discretization.** A common approach consists in choosing a grid and constraining the measure to be supported on this set of points. It leads to the well-known LASSO [142]. The link between the BLASSO and the LASSO has already been discussed in Section . The benefit of this approach is that it leads to a finite dimensional convex optimization problem so that many standard solvers can be used (reviewed in Section 4.1.2). However in order to go below the Rayleigh limit and perform super-resolution, the grid must be thin enough. This leads to both theoretical and practical issues. On the theoretical standpoint, in [55, 56], the authors show that pairs of spikes appears around the true ones in a small noise regime. Numerically, the overall complexity increases with the size of the grid.

**Fixed spectral discretization and SDP formulation.** Following [30], where the authors proposed, in the setting of the one dimensional ideal low pass filter (but it easily extends to any filter with compact Fourier support) *i.e.*  $X = \mathbb{T}$ ,  $\mathcal{H} = \mathbb{C}^{2f_c+1}$  and:

$$\varphi(x) = (e^{2i\pi kx})_{-f_c \leq k \leq f_c},$$

to reformulate the Basis Pursuit for measures:

$$\min_{m \in \mathcal{M}(X), \Phi m = y_0} |m|(X),$$

into an equivalent finite dimensional SDP for which standard solvers already exist, one can perform the same process for the BLASSO ( $y = y_0 + w$ ):

$$\min_{m \in \mathcal{M}(X)} \frac{1}{2} \|\Phi m - y\|_{\mathcal{H}}^2 + \lambda |m|(X).$$

It corresponds to a spectral discretization of the forward operator. It can be shown using classical convex analysis tools that the dual problem of the BLASSO [54, 141] is given by:

$$\max_{p \in \mathcal{H}} \Re(\langle y, p \rangle_{\mathcal{H}}) - \frac{\lambda}{2} \|p\|_{\mathcal{H}}^2 \quad \text{s.t.} \quad \|\Phi^* p\|_{\infty, X} \leq 1, \quad (4.1.1)$$

and that strong duality holds. Then, because  $\Phi^* p$  is a trigonometric polynomial, the constraint  $\|\Phi^* p\|_{\infty, X} \leq 1$  can be recast as a sum of squares constraint and using a result of [52], it can be rewritten as the intersection of the cone of positive semi-definite matrices with an affine space, leading to the following equivalent optimization problem:

$$\begin{aligned} & \max_{p \in \mathbb{C}^{2f_c+1}, Q \in \mathbb{C}^{(2f_c+1) \times (2f_c+1)}} \Re(\langle y, p \rangle_{\mathcal{H}}) - \frac{\lambda}{2} \|p\|_{\mathcal{H}}^2, \\ & \text{s.t. } \begin{pmatrix} Q & p \\ p^* & 1 \end{pmatrix} \succeq 0, \\ & \forall k \in \{-2f_c, \dots, 2f_c\}, \text{Tr}(\Theta_k Q) = \delta_0^k, \end{aligned} \quad (4.1.2)$$

where  $\Theta_k$  is the matrix with only ones at coefficient  $(i, j)$  such that  $i - j = k$  and zeros everywhere else (it is an elementary Toeplitz matrix).

One remarks that the equivalence between this semi-definite program and the BLASSO is only true for specific forward operators  $\Phi$  (here the case of Fourier measurements). But most importantly, the result in [52] used to obtain this semi-definite program is only true in a 1-dimensional setting. To investigate the multivariate case  $d \geq 2$ , one needs to use the so-called Lasserre's hierarchy [103, 102]. The BLASSO belongs to the class of generalized moment problems (GMP) [103] where the goal is to find a representing measure defined on a semi-algebraic sets (*i.e.* described by polynomials inequalities) that is a measure with a sequence of moments prescribed to some values. For these GMP problems, the Lasserre's hierarchy defines a sequence of finite dimensional SDP problems whose sizes increase. This principle has been used for the super-resolution problem in [43]. The difficulty in practice is that one does not know in advance when to stop the hierarchy (collapsing) in order to obtain a measure solution of the BLASSO. Basically, this is because the non-negative trigonometric polynomials in dimension  $d > 1$  are not all sums of squares.

**Adaptive discretization via optimization over the space of measures.** In order to directly solve the BLASSO, one needs to design algorithms that do not use any Hilbertian structure and can instead deals with measures. It can seem complicated but the benefit is the fact that one can exploit advantageously the continuous setting of the problem (typically moving continuously spikes over the domain). In contrast to fixed spatial or spectral discretization methods, these algorithms compute adaptive grids which are progressively refined and can thus be proved to converge to the solution of the BLASSO.

In the next section, we present the existing numerical schemes depending on these three different approaches.

### 4.1.2 Numerical Solvers for the BLASSO

In this section we give an overview of the numerical methods used to solve the BLASSO depending on the approximation considered. They can be roughly divided into three main families although there exists a flurry of generalizations and extensions that must be considered separately. A general study and comparison of the complexity of the following algorithms in the case of the BLASSO (and its approximations) does not exist to our knowledge and it is a challenging question. We give a few elements in the next paragraphs and we provide an estimation of the complexity of a modified Frank-Wolfe algorithm versus FISTA in Section 4.2.4.

**Proximal Methods.** These methods can only be applied to a discretized version of the BLASSO *i.e.* the LASSO (see Equation (2)), because they rely on the fact that the primal problem has an Hilbertian structure (the space of Radon measures is on the contrary a non-reflexive Banach space). Iterative Hard Thresholding (IHT) [19, 20] or Iterative Soft Thresholding (IST) [41, 38] are algorithms which are part of the family of Iterative Shrinkage-Thresholding Algorithms (ISTA) which dates back to the proximal forward-backward method introduced in [25, 114]. Their rates of convergence have been largely studied in the literature [41, 50, 66]. Even if ISTA is simple to implement, it is in general slow to converge (the error in the objective function is typically in  $O(1/k)$ ). FISTA [9] gives a better non-asymptotic rate of convergence ( $O(1/k^2)$ ). With discrete grids, in order to achieve a sharp localization of the spikes of the initial measure, one needs to have a sufficiently small grid step size. But when the size of the grid  $\#\mathcal{G}$  increases it makes each iteration slower and a more correlated dictionaries which in turn deteriorate the constant of convergence. So that in practice, we often obtain a small cluster of non-zero weights in the neighborhood of each true spike. A way to mitigate this issue is to perform a post processing by replacing each cluster of spikes by its center of mass, as proposed in [140]. It drastically reduces the number of false positive spikes but this step is hard to understand theoretically (it does not improve a Optimal Transport based metric, see Section 4.3.3 for more details) and we found in practice that it does not lead to a clear enhancement of the performance. Moreover it has been proved that thin grids lead to unstable support recovery. Indeed in [55, 56], the authors show that pairs of spikes appears around the true ones in a small noise regime.

Finally one remarks that ISTA can also be applied in the case of an SDP lifting (such as in Equation (4.1.2)) resulting of a spectral discretization of the BLASSO. The thresholding of the weights (the amplitudes of the spikes) is replaced by the thresholding of the singular values of a matrix [143].

**Interior Point Methods.** These methods are typically applied to solve an SDP formulation of the BLASSO. In [30], the authors use an Interior Point Method to solve the equivalent (only in 1D) SDP formulation of the BLASSO which is detailed in Section 4.1.1. From the solution obtained  $p \in \mathbb{C}^{2f_c+1}$ , they form the

trigonometric polynomial  $\Phi^* p$ . Then the location of the spikes are just the roots of  $1 - |\Phi^* p|^2$  on the unit circle. One of the drawback of this method is that the root finding step may pose stability issues. Moreover the overall complexity of an interior point method for the SDP is polynomial in  $O(f_c^{2d})$  where  $d$  is the dimension of the domain  $X$ . This has led to recent developments [32] where the authors use a relaxed low rank SDP formulation of the BLASSO in order to use a greedy method (see the associated paragraph). Finally these methods can only be applied to certain type of forward operators (typically Fourier measurements) where Frank-Wolfe and greedy methods and proximal methods can be used for a larger class of operators  $\Phi$ .

To be complete note that interior point methods can also be applied to solve the LASSO.

**Frank-Wolfe and Greedy Methods.** They are particularly well fitted to work directly with measures because they consist of iteratively adding new spikes, *i.e.* Dirac masses, to the recovered measures. They do not fix an a priori grid but rather progressively refine the computational grid by adding spikes one by one. The Matching Pursuit (MP) [109] adds new spikes by finding ones that best correlate with the residual. The Orthogonal Matching Pursuit (OMP) [144, 137, 86] is similar to MP but makes sure that the current estimate of the observations *i.e.*

$$\Phi \left( \sum_{i=1}^k a_i \delta_{x_i} \right),$$

is always orthogonal to the residual. As a result all the amplitudes of the Dirac masses are updated after each new spikes added to the support by an orthogonal projection. There exist many generalizations of OMP. In particular, the results of OMP are improved by a backtracking at each iteration so that non reliable spikes are eventually removed from the support of the reconstructed measure (improving the precision of the adaptive grid) see [91].

The Frank-Wolfe (FW) algorithm [69] also called the Conditional Gradient Method (CGM) [104] solves the following optimization problem:

$$\min_{x \in C} f(x),$$

where  $C$  is a closed, bounded and convex set of a vector space and  $f$  is a differentiable convex function. The algorithm is detailed in Algorithm I. Note that the first step and the main idea of the algorithm consists in iteratively minimizing a linearized version of  $f$ . Moreover no Hilbertian structure is used which makes it well suited to work on space of measures. It has been proven under a curvature condition on  $f$  (which is equivalent to having a Lipschitz gradient on a Banach space) that the rate of convergence of this algorithm in the objective function is  $O(1/k)$ .

Note that the update  $x_{k+1} \stackrel{\text{set.}}{=} \tilde{x}_{k+1}$  can be replaced by any “better” candidate  $x \in C$  such that  $f(x) \leq f(\tilde{x}_{k+1})$  without impacting the convergence proof. This

---

**Algorithm 1** Frank-Wolfe Algorithm

---

```

1: for  $k = 0, \dots, n$  do
2:   Minimize:  $s_k \ni \operatorname{argmin}_{s \in C} f(x_k) + Df(x_k)(s - x_k)$ .
3:   Step research:  $\gamma_k \leftarrow \frac{2}{k+2}$  or  $\gamma_k \ni \operatorname{argmin}_{\gamma \in [0,1]} f(x_k + \gamma(s - x_k))$ .
4:   Tentative update:  $\tilde{x}_{k+1} \leftarrow x_k + \gamma_k(s - x_k)$ .
5:   Final update:  $x_{k+1} \leftarrow \tilde{x}_{k+1}$  or  $x_{k+1} \leftarrow x \in C$  with  $f(x) \leq f(\tilde{x}_{k+1})$ .
6: end for

```

---

simple idea has led to several variations on the basic algorithm which have been shown in practice to be very successful and sometimes crucial. Indeed in [24], the authors proposed to consider the Frank-Wolfe algorithm for the BLASSO but where the final update is determined by a gradient descent on a non-convex optimization problem. This technique has been used later in [22] and provide state of the art numerical results in many sparse inverse problems such as in the matrix completion problem with the Netflix Prize dataset or in super-resolution fluorescence microscopy with the Single Molecule Localization Microscopy (SMLM) challenge [88, 125]. In this particular example where the data are 2D images obtained from the stochastic readout of a sample (PALM-STORM model, see Section 5.1 for more details on this matter), new spikes are iteratively added to the support of the reconstructed measure by minimizing the linearized version of the objective function and then the amplitudes and positions of the spikes are updated by performing a local descent. Moving the spikes positions takes advantage of the continuous framework of the problem (the domain  $X$  is not discretized) which is the main ingredient that leads to a typical  $N$ -step convergence observed. Recently in [58], the authors proved the  $N$ -step convergence for Fourier measurements when  $f_c \rightarrow +\infty$  when minimizing the quadratic error. This modified Frank-Wolfe algorithm has also been used lately [32] for an SDP relaxation, promoting low rank matrices, of the BLASSO using Lasserre's hierarchy, leading to an overall complexity of  $O(f_c^d \log(f_c))$  per iteration (where  $f_c$  is the cutoff frequency of the Fourier measurements and  $d$  the dimension) of the Frank-Wolfe algorithm instead of a classical complexity polynomial in  $f_c^{2d}$  for SDP. The algorithm in this case adds a rank one matrix at each iteration instead of a spikes but a  $N$ -step convergence has also been observed if the initial measure is composed of  $N$  spikes. Note however, in dimension larger than one, that the theoretical link between this problem (relaxed SDP lifting) and the BLASSO on measures is not fully understood yet.

**Other algorithms.** There exist many more different solvers, in particular for the LASSO. One can cite for example the block-coordinate descent (BCD) algorithm [145, 150] or the homotopy/LARS algorithm [57, 138]. To reduce the negative impact on stability and speed of a thin grid for the LASSO solved by FISTA or BCD, one can also consider the methods based on safe rules [62] which perform a progressive pruning of the grid and keep only active sets of weights [112].

### 4.1.3 Contributions

We detail the Sliding Frank-Wolfe (SFW) algorithm which is a modification of [24], in Section 4.2.1. The code can be found in <https://github.com/qdenoyelle>.

We prove in Section 4.2.2 with Proposition 24 that this algorithm, used to solve the BLASSO, enjoys the same convergence property as the classical Frank-Wolfe algorithm (weak-\* convergence with a rate in the objective function of  $O(1/k)$ ).

Our main theoretical contribution is Theorem 6 which proves that our algorithm converges towards the unique solution of the BLASSO in a finite number of iterations. This implies as a corollary that the SFW algorithm solves the super-resolution problem in presence of noise in a finite number of steps by recovering the unique measure solution of the BLASSO (and composed of the same number of spikes) if  $\eta_W$  is  $(2N - 1)$ -non-degenerate, see Corollary 7.

We compare numerically the SFW algorithm with FISTA and OMP in Section 4.3 and we show that it outperforms them in a Optimal Transport based metric but also in a metric based on detection indices.

Finally Section 4.4 deals with the properties of the numerical inversion of the Laplace transform using our algorithm by solving the BLASSO. In particular we show that one obtains better results when normalizing the kernel and that the size of the interval containing the discretization points of the Laplace transform influence the ability to recover spikes near or far the origin. This provides crucial information for the experimentalists in order to design new imaging techniques based on the MA-TIRF model, as detailed in Chapter 5.

## 4.2 The SFW Algorithm

In this section one presents in detail our version (see Algorithm 3) of the modified Frank-Wolfe algorithm introduced first in [24] and one proves in Theorem 6 that it converges in a finite number of steps under mild assumptions. As already mentioned in Section 4.1.2, this algorithm can deal with measures (no need of an Hilbertian structure). It adds iteratively new spikes and following recent developments [24, 22, 58] it moves the spikes positions, benefiting from the continuous framework, to further decrease the objective function. While in the literature it was proved that the classical Frank-Wolfe algorithm has a general rate of convergence of  $O(1/k)$ , little is known about its modified version except that it has state of the art numerical results in several applications (see the Introduction of this Chapter) and that it keeps in the worst case scenario the same  $O(1/k)$  rate of convergence [24, 22]. In [58], the authors proved a  $N$ -step convergence property when minimizing the quadratic error (so not the BLASSO) in the case of Fourier measurements and when  $f_c \rightarrow +\infty$ . This is our formulation of the added update (changing the amplitudes in the same time as moving the positions) that guarantees the convergence in a finite number of steps both theoretically and numerically.

### 4.2.1 The Algorithm

We suppose in this section that  $X \subset \mathbb{R}^d$  is compact, or  $X = \mathbb{T}^d$  with  $d \in \mathbb{N}^*$  and  $\varphi \in \text{KER}^{(2)}$  (see Definition 4, Section 1.2).

**The FW algorithm for the BLASSO.** First one details how the classical Frank-Wolfe algorithm (Algorithm I, see Section 4.1.2) operates in the case of the BLASSO. It turns out that it requires some modification with respect to Algorithm I in order to deal with an optimization problem over  $\mathcal{M}(X)$  which is not bounded and most importantly the objective function:

$$\forall m \in \mathcal{M}(X), \quad T_\lambda(m) \stackrel{\text{def.}}{=} \frac{1}{2} \|\Phi m - y\|_{\mathcal{H}}^2 + \lambda |m|(X), \quad (4.2.1)$$

is not differentiable. In [22], the authors do not have these issues because they consider the Ivanov regularization (constraint formulation) of the inverse problem  $\Phi m = y$ , which implies that they minimize an objective function whose differential is Lipschitz continuous over a closed bounded subset of a Banach space. In [24], the authors consider the Tikhonov regularization of  $\Phi m = y$  (*i.e.* the BLASSO) but they apply a tweaked FW algorithm (partial linearization of the objective function) to obtain in the end a similar rate of convergence of  $O(1/k)$ . We follow a different approach here since we show that one can directly apply the FW algorithm but to an equivalent problem to the BLASSO, which we present in the following Lemma 12.

**Lemma 12.** *The BLASSO:*

$$\min_{m \in \mathcal{M}(X)} \frac{1}{2} \|\Phi m - y\|_{\mathcal{H}}^2 + \lambda |m|(X). \quad (\mathcal{P}_\lambda(y))$$

where  $y = \Phi m_{a_0, x_0} + w \in \mathcal{H}$  with  $m_{a_0, x_0} = \sum_{i=1}^N a_{0,i} \delta_{x_{0,i}}$ , is equivalent (same solutions and same optimal value) to:

$$\min_{\begin{cases} (t, m) \in \mathbb{R}_+ \times \mathcal{M}(X) \\ |m|(X) \leq t, t \leq M \end{cases}} \frac{1}{2} \|\Phi m - y\|_{\mathcal{H}}^2 + \lambda t, \quad (\tilde{\mathcal{P}}_{\lambda}(y))$$

where  $M \stackrel{\text{def.}}{=} \frac{\|y\|_{\mathcal{H}}^2}{2\lambda}$ . In the following we denote by  $T_{\lambda}$  and  $\tilde{T}_{\lambda}$  the objective functions of respectively these two problems and by  $C \stackrel{\text{def.}}{=} \{(t, m) \in \mathbb{R}_+ \times \mathcal{M}(X); |m|(X) \leq t \leq M\}$ .

*Proof.* If  $m_*$  is a minimizer of  $T_{\lambda}$  on  $\mathcal{M}(X)$  then:

$$T_{\lambda}(m_*) \leq T_{\lambda}(0) = \lambda M,$$

so one can restrict the BLASSO to the set of  $m \in \mathcal{M}(X)$  such that  $|m|(X) \leq M$  and then  $\tilde{\mathcal{P}}_{\lambda}(y)$  is obtained using an epigraphical representation.  $\square$

$\tilde{\mathcal{P}}_{\lambda}(y)$  is an optimization problem over  $C$  a weak-\* compact and convex subset of a Hausdorff locally convex topological vector space whose objective function has a differential:

$$D\tilde{T}_{\lambda}(t, m)(t', m') = \int_X \Phi^*(\Phi m - y) dm' + \lambda t',$$

which is Lipschitz continuous (because  $\varphi \in \text{KER}^{(2)}$ ). As a result, one can translate directly Algorithm 1 to  $\tilde{\mathcal{P}}_{\lambda}(y)$ . We obtain Algorithm 2 and by [46] we get in Lemma 13 the classical  $O(1/k)$  rate of convergence (in the objective function).

---

**Algorithm 2** Frank-Wolfe Algorithm for the BLASSO

---

- 1: **for**  $k = 0, \dots, n$  **do**
  - 2:     Minimize:  $(t'_k, m'_k) \ni \operatorname{argmin}_{(t', m') \in C} \int_X \Phi^*(\Phi m_k - y) dm' + \lambda t'$ .
  - 3:     Step research:  $\gamma_k \leftarrow \frac{2}{k+2}$  or  $\gamma_k \ni \operatorname{argmin}_{\gamma \in [0, 1]} \tilde{T}_{\lambda}(t_k + \gamma(t'_k - t_k), m_k + \gamma(m'_k - m_k))$ .
  - 4:     Tentative update:  $(\tilde{t}_{k+1}, \tilde{m}_{k+1}) \leftarrow (t_k, m_k) + \gamma_k((t'_k, m'_k) - (t_k, m_k))$ .
  - 5:     Final update:  $(t_{k+1}, m_{k+1}) \leftarrow (\tilde{t}_{k+1}, \tilde{m}_{k+1})$  or  $(t_{k+1}, m_{k+1}) \leftarrow (t, m) \in C$  with  $\tilde{T}_{\lambda}(t, m) \leq \tilde{T}_{\lambda}(\tilde{t}_{k+1}, \tilde{m}_{k+1})$ .
  - 6: **end for**
- 

**Lemma 13.** Let  $(t_k, m_k)_{k \in \mathbb{N}}$  a sequence obtained thanks to Algorithm 2. Then there exists  $C_1 > 0$  such that for any  $(t_*, m_*)$  solution of  $\tilde{\mathcal{P}}_{\lambda}(y)$  (so  $m_*$  also solution of  $\mathcal{P}_{\lambda}(y)$ ), one has:

$$\forall k \in \mathbb{N}, \quad \tilde{T}_{\lambda}(t_k, m_k) - \tilde{T}_{\lambda}(t_*, m_*) \leq \frac{C_1}{k}.$$

In particular we deduce that:

$$\forall k \in \mathbb{N}, \quad T_\lambda(m_k) - T_\lambda(m_*) \leq \frac{C_1}{k}.$$

We present now our version of the Frank-Wolfe which we call the Sliding Frank-Wolfe algorithm (SFW), see Algorithm 3 for the resolution of the BLASSO. The SFW algorithm is a transcription of the Frank-Wolfe Algorithm for the BLASSO detailed above (see Algorithm 2) where the final update is replaced by the minimization of a non-convex problem.

---

**Algorithm 3** Sliding Frank-Wolfe Algorithm

---

```

1: Initialize with  $m_0 = 0$  and  $k = 0$ .
2: for  $k = 0, \dots, n$  do
3:    $m_k = \sum_{i=1}^{N_k} a_i^k \delta_{x_i^k}$ ,  $a_i^k \in \mathbb{R}$ ,  $x_i^k$  pairwise distincts, find  $x_*^k \in X$  s.t.:
   
$$x_*^k \in \operatorname{argmax}_{x \in X} |\eta_k(x)| \quad \text{where} \quad \eta_k \stackrel{\text{def.}}{=} \frac{1}{\lambda} \Phi^*(y - \Phi m_k),$$

4:   if  $|\eta_k(x_*^k)| \leq 1$  then
5:      $m_k$  solution of  $\mathcal{P}_\lambda(y)$ . Stop.
6:   else
7:     Obtain  $m_{k+1/2} = \sum_{i=1}^{N_k} a_i^{k+1/2} \delta_{x_i^k} + a_{N_k+1}^{k+1/2} \delta_{x_*^k}$ , s.t.:
     
$$(a_i^{k+1/2})_{1 \leq i \leq N_k+1} \ni \operatorname{argmin}_{a \in \mathbb{R}^{N_k+1}} \frac{1}{2} \|\Phi \mathcal{G} a - y\|_{\mathcal{H}}^2 + \lambda \|a\|_1$$

     where  $\mathcal{G} = (x_1^k, \dots, x_{N_k}^k, x_*^k)$ 
8:     Obtain  $m_{k+1} = \sum_{i=1}^{N_k+1} a_i^{k+1} \delta_{x_i^{k+1}}$ , s.t.:
     
$$((a_i^{k+1}), (x_i^{k+1})) \ni \operatorname{argmin}_{(a,x) \in \mathbb{R}^{N_k+1} \times X^{N_k+1}} \frac{1}{2} \|\Phi_x a - y\|_{\mathcal{H}}^2 + \lambda \|a\|_1.$$

9:   Eventually remove zero amplitudes Dirac masses from  $m_{k+1}$ .
10:  end if
11: end for
```

---

On the paper, Algorithm 1 and the SFW algorithm may seem different. Here is the link between the two:

- Step 3 is obtained from Step 2 of Algorithm 1. Indeed solving:

$$\min_{(t', m') \in C} \int_X \Phi^*(\Phi m_k - y) dm' + \lambda t',$$

leads to  $(t'_k, m'_k) = \left( M, \text{sign}(\eta_k(x_*^k))M\delta_{x_*^k} \right)$  (an extreme point of  $C$ ) where:

$$x_*^k \in \operatorname{argmax}_{x \in X} |\eta_k(x)|. \quad (4.2.2)$$

We drop the sequence  $(t_k)_{k \in \mathbb{N}}$ , in the rest of the algorithm (we are only interested in  $(m_k)_{k \in \mathbb{N}}$ ). So one has thanks to Algorithm 1 the following update

$$\tilde{m}_{k+1} = m_k + \gamma_k(a_*^k \delta_{x_*^k} - m_k),$$

for a certain  $\gamma_k$ . As a result one just adds a new Dirac mass to  $m_k$  with an amplitude  $a_*^k$ , whose position solves (4.2.2).

- We add to the algorithm the natural stopping condition  $|\eta_k(x_*^k)| \leq 1$  because if it is satisfied, then  $\|\eta_k\|_{\infty, X} \leq 1$  which is equivalent to  $m_k$  solution of the BLASSO. Said otherwise, if the SFW algorithm stops in a finite number of iterations then it means that  $m_k$  is solution of the BLASSO.
- We do not compute  $\gamma_k$  in the SFW because after Step 7, one has

$$T_\lambda(m_{k+1/2}) \leq T_\lambda(m_k + \gamma_k(a_*^k \delta_{x_*^k} - m_k)),$$

for any  $\gamma_k \in [0, 1]$ .

- Step 7 and Step 8 exploits the final update step of the FW (Step 5) by moving the positions and the amplitudes in the same time to further decrease  $T_\lambda$ .

#### Differences and similarities with the existing equivalent algorithms.

- Step 3 of our Algorithm 3, corresponds to the step of creation of a new spike. This is the greedy step that one can find in the classical Frank-Wolfe algorithm (see Step 2 of Algorithm 1). It can be identically find in [24] and [22].
- Step 4, which is our stopping condition, is up to our knowledge new in the literature. This condition is quite natural if one seeks a convergence towards a solution of the BLASSO in a finite number of iterations. This indeed plays a major role in the proof of the convergence speed of the SFW algorithm, see Theorem 6.
- Step 7 and Step 8 are also new in the literature. Even if they can be found on other forms first in [24] and later in [22], it is crucial to write them precisely as presented above (particularly Step 8) to prove the convergence of this algorithm in a finite number of iterations, see Theorem 6. As already mentioned before, these steps are behind the recent new development on the use of the Frank-Wolfe algorithm for sparse inverse problems on spaces of measures, which have dramatically improve the overall performance of the

algorithm (see the Introduction of this Chapter). They turn to benefit from the degree of freedom let by Step 5 of Algorithm 1, by updating the amplitudes and most importantly the positions of the spikes so as to decrease further the objective function. This procedure is notably well adapted here because the spikes live on a continuum. In [22], the authors update separately the amplitudes and the positions. With this choice, it is not possible to prove a convergence in a finite number of iterations because it does not guarantee that

$$\forall i, \quad \eta_k(x_i^k) = \text{sign}(a_i^k) \quad \text{and} \quad \eta'_k(x_i^k) = 0.$$

Instead here one performs these updates at the same time in Step 8. In [24], the authors only perform Step 7 but they mention that one can also move the positions following the trajectories of a gradient flow.

Note that after Step 7, one has thanks to the optimality conditions:

$$\forall i \in \{1, \dots, N_k\}, \quad \eta_{k+1/2}(x_i^k) = \text{sign}(a_i) \quad \text{and} \quad \eta_{k+1/2}(x_*^k) = 1,$$

where  $\eta_{k+1/2} = 1/\lambda\Phi^*(y - \Phi m_{k+1/2})$  and after Step 8, one gets:

$$\forall i \in \{1, \dots, N_k + 1\}, \quad \eta_{k+1}(x_i^{k+1}) = \text{sign}(a_i) \quad \text{and} \quad (\eta_{k+1})'(x_i^{k+1}) = 0.$$

which is a necessary condition for  $m_{k+1}$  to be a solution of  $\mathcal{P}_\lambda(y)$ .

Before continuing with the theoretical study of the convergence of our algorithm, we detail in the next paragraph the practical implementation choices made.

**Implementation details.** Let us review for the main steps of Algorithm 4 how we perform it in practice:

- Step 3: the goal is to find the maximum of  $|\eta_k|$  over the compact domain  $X$ . We have implemented a Newton method initialized first by a grid search. The size of the grid on  $X$  usually depends on the size of the PSF considered in the application. For example in the case of  $\Phi$  the convolution by the Dirichlet kernel with cutoff frequency  $f_c$ , the number of points on the grid is proportional to  $f_c$ .
- Step 7: the goal is to solve the LASSO. We use FISTA.
- Step 8: the goal is to minimize the same objective function as Step 7 but where we also optimize over the position vector  $x$ . It is thus a non-convex optimization problem. We solve it using a Bounded BFGS, enforcing the positions to stay in the compact domain  $X$ , the negative amplitudes in  $a \leq 0$  and the positive amplitudes to  $a \geq 0$  so that the objective function is differentiable (requirement to apply the BFGS).

### 4.2.2 Study of the Convergence of the SFW Algorithm

We now study the convergence properties of the Sliding Frank-Wolfe algorithm presented last section (see Algorithm 3). Our main result is Theorem 6 where it is shown that if  $\eta_\lambda = \frac{1}{\lambda} \Phi^*(y - \Phi m_{a,x})$ , where  $m_{a,x} = \sum_{i=1}^N a_i \delta_{x_i}$  is the unique solution of  $\mathcal{P}_\lambda(y)$ , is non-degenerate (see Equation (1.2.13)) then Algorithm 3 recovers  $m_{a,x}$  in a finite number of iterations. But first one shows that our algorithm produces a sequence of measures  $(m_k)_{k \in \mathbb{N}}$  that converges towards  $m_*$  (if  $m_* \in \mathcal{M}(X)$  is the unique solution of the BLASSO) for the weak-\* topology on  $\mathcal{M}(X)$ .

**Proposition 24.** *Let  $(m_k)_{k \in \mathbb{N}}$  be the sequence obtained from the Sliding Frank-Wolfe algorithm. Then it has an adherence value for the weak-\* topology on  $\mathcal{M}(X)$  that is solution of  $\mathcal{P}_\lambda(y)$ .*

*Proof.* Because Step 7 and Step 8 decrease  $T_\lambda$ , one has:

$$T_\lambda(m_{k+1}) \leq T_\lambda(m_{k+1/2}) \leq T_\lambda(\tilde{m}_{k+1}).$$

As a result using Lemma 13, one gets, for any  $m_*$  solution of  $\mathcal{P}_\lambda(y)$ , that:

$$\forall k \in \mathbb{N}, \quad T_\lambda(m_k) - T_\lambda(m_*) \leq \frac{C_1}{k}.$$

As a result  $(m_k)$  is a bounded minimizing sequence. One can extract from it a subsequence that converges towards some  $m \in \mathcal{M}(X)$  (with  $|m|(X) \leq M$ ) for the weak-\* topology. Since  $T_\lambda$  is convex and l.s.c (lower semi-continuous), it is also weak-\* l.s.c so that one gets:

$$T_\lambda(m) = T_\lambda(m_*).$$

Hence  $m$  is a solution of  $\mathcal{P}_\lambda(y)$ . □

From this Proposition, one easily deduces the following Corollary.

**Corollary 3.** *If  $m_* \in \mathcal{M}(X)$  is the unique solution of  $\mathcal{P}_\lambda(y)$  then  $(m_k)_{k \in \mathbb{N}}$  weak-\* converges towards  $m_*$ .*

One can now show that our algorithm in fact converges towards a solution of the BLASSO in a finite number of iterations, by fully exploiting the displacement of the spikes over the continuous domain  $X$ . For the sake of clarity, one writes and prove this Theorem in the case of  $d = 1$  but the changes for  $d \in \mathbb{N}^*$  can be easily done.

**Theorem 6.** *Suppose that  $\varphi \in \text{KER}^{(2)}$  and that  $m_{a,\bar{x}} = \sum_{i=1}^N a_i \delta_{x_i}$  is the unique solution of  $\mathcal{P}_\lambda(y)$  and that  $\eta_\lambda = \frac{1}{\lambda} \Phi^*(y - \Phi m_{a,\bar{x}})$  is non-degenerate i.e. :*

$$\forall x \in X \setminus \bigcup_{i=1}^N \{x_i\}, \quad |\eta_\lambda(x)| < 1 \quad \text{and} \quad \forall i \in \{1, \dots, N\}, \quad \eta_\lambda''(x_i) \neq 0.$$

*Then Algorithm 3 recovers  $m_{a,\bar{x}}$  after a finite number of steps i.e. there exists  $k \in \mathbb{N}$  such that  $m_k = m_{a,\bar{x}}$ .*

*Proof.* Since  $m_{a,\bar{x}}$  is the unique solution of  $\mathcal{P}_\lambda(y)$ , one knows by Corollary 3 that the sequence  $(m_k)_{k \in \mathbb{N}}$  produced by Algorithm 3 converges for the weak-\* topology towards  $m_{a,\bar{x}}$ .

$\Phi$  is weak-\* to weak continuous thus defining  $p_k \stackrel{\text{def.}}{=} \frac{1}{\lambda}(y - \Phi m_k)$ , one gets that  $(p_k)_{k \in \mathbb{N}}$  converges for the weak topology on  $\mathcal{H}$  towards  $p_\lambda = 1/\lambda(y - \Phi m_{a,\bar{x}})$  and  $\eta_k \stackrel{\text{def.}}{=} \Phi^* p_k$  converges pointwise towards  $\eta_\lambda$ . But  $\Phi^*$  is a compact operator. Indeed, take any bounded subset  $A \in \mathcal{H}$ , then one can check easily that  $\Phi^* A$  is equicontinuous and pointwise relatively compact so that by Ascoli theorem  $\Phi^* A$  is relatively compact for the strong topology of  $\mathcal{C}(X, \mathbb{R})$ . As a result one can extract a subsequence of  $(\eta_k)_{k \in \mathbb{N}}$  that converges towards  $\eta_\lambda$  in uniform norm.  $\eta_\lambda$  is then the unique adherence value for the uniform norm of the bounded sequence  $(\eta_k)_{k \in \mathbb{N}}$  hence the convergence towards  $\eta_\lambda$  in uniform norm. One can repeat this argument for  $(\eta'_k)_{k \in \mathbb{N}}$  and  $(\eta''_k)_{k \in \mathbb{N}}$  (since  $\varphi \in \text{KER}^{(2)}$ ), obtaining for all  $j \in \{0, 1, 2\}$ :

$$(\eta_k)^{(j)} \xrightarrow[k \rightarrow +\infty]{\|\cdot\|_{\infty, X}} \eta_\lambda^{(j)}, \quad (4.2.3)$$

Since  $\eta_\lambda$  is non-degenerate, there exists a small neighborhood around each  $x_i$  such that on these sets  $\eta_\lambda'' \neq 0$ . As a result one deduces from Equation (4.2.3) that there exists  $\varepsilon > 0$  and  $k_1 \in \mathbb{N}$  such that:

$$\forall k \geq k_1, \forall i \in \{1, \dots, N\}, \forall x \in ]x_i - \varepsilon, x_i + \varepsilon[, \quad \eta_k''(x) \neq 0.$$

We denote in the following:

$$\forall i \in \{1, \dots, N\}, \quad I_{x_i, \varepsilon} \stackrel{\text{def.}}{=} ]x_i - \varepsilon, x_i + \varepsilon[.$$

Because  $m_k$  converges for the weak-\* topology towards  $m_{a,\bar{x}}$ , one gets that:

$$\forall i \in \{1, \dots, N\}, \quad m_k(I_{x_i, \varepsilon}) \rightarrow m_{a,\bar{x}}(I_{x_i, \varepsilon}) = a_i \neq 0,$$

so that there exists  $k_2 \in \mathbb{N}$  such that for all  $k \geq k_2$ ,  $m_k$  has at least one spike in each  $I_{x_i, \varepsilon}$ . In particular  $m_k$  has at least  $N$  spikes.

Again from Equation (4.2.3), since  $(\eta_k)_{k \in \mathbb{N}}$  converges uniformly towards  $\eta_\lambda$ , one deduces that there exists  $k_3 \in \mathbb{N}$  such that for all  $k \geq k_3$ :

$$\text{Sat}^\pm(\eta_k) \subset (\text{Sat}^\pm(\eta_\lambda)) \oplus (]-\varepsilon, \varepsilon[ \times \{0\}),$$

where the set of saturation points of a given  $\eta \in \mathcal{C}(X, \mathbb{R})$  is defined as:

$$\text{Sat}^\pm(\eta) \stackrel{\text{def.}}{=} \{(x, v) \in X \times \{-1, 1\}; \eta(x) = v\}.$$

Moreover:

$$\forall x \in X \setminus \bigcup_{i=1}^N I_{x_i, \varepsilon}, \quad |\eta_k(x)| < 1.$$

In particular for  $k \geq k_3$ ,  $m_k$  has no spikes in  $X \setminus \bigcup_{i=1}^N I_{x_i, \varepsilon}$  because it would contradict the optimality conditions of Step 8 of Algorithm 3: for all  $i \in \{1, \dots, N_k\}$ ,  $\eta_k(x_i^k) = \text{sign}(a_i^k)$ .

Suppose now that  $k = \max(k_1, k_2, k_3)$ . Then  $m_k$  has at least one spike in each neighborhood of  $x_i$  and no spikes outside. Moreover  $|\eta_k| < 1$  outside the neighborhoods and  $\eta_k'' \neq 0$  inside. Let  $i \in \{1, \dots, N\}$  and denote  $x_j^k \in I_{x_i, \varepsilon}$  a position of a spike of  $m_k$ . From the optimality conditions of Step 8, one has also that  $\eta'_k(x_j^k) = 0$ . But because  $\eta_k'' \neq 0$  in  $I_{x_i, \varepsilon}$ , it means necessary  $|\eta_k| < 1$  except at  $x_j^k$  so that  $m_k$  has in fact exactly one spike in this neighborhood. As a consequence, we proved that  $m_k$  has exactly  $N$  spikes (one inside each neighborhood) and:

$$\forall x \in X \setminus \bigcup_{i=1}^N \{x_i^k\}, \quad |\eta_k(x)| < 1.$$

Hence  $m_k$ , composed of  $N$  spikes, is a solution of  $\mathcal{P}_\lambda(y)$ . Since  $m_{a, \bar{x}}$  is supposed to be the unique solution of  $\mathcal{P}_\lambda(y)$ , one concludes that:

$$m_k = m_{a, \bar{x}},$$

i.e. the algorithm recovers  $m_{a, \bar{x}}$  in a finite number of iterations.  $\square$

Note that one proved the convergence in a *finite* number of iterations but not exactly  $N$  iterations if  $m_{a, \bar{x}}$  is composed of  $N$  spikes. However in practice this is exactly what one observes. See Section 4.2.5 for a few examples.

Combining Theorem 5 and Theorem 6, one can deduce the following result when  $d = 1$  which states that using the SFW algorithm, one can always solve numerically the super-resolution problem in a small noise regime.

**Theorem 7.** Suppose that  $\varphi \in \text{KER}^{(2N+1)}$  and  $\eta_W$  is  $(2N - 1)$ -non-degenerate. Then there exists  $C_1 > 0$  such that if:

$$\max \left( \frac{\lambda}{t^{2N-1}}, \frac{\|w\|_{\mathcal{H}}}{t^{2N-1}}, \frac{\|w\|_{\mathcal{H}}}{\lambda}, t \right) \leq C_1,$$

then  $\mathcal{P}_\lambda(y_t)$  has a unique solution composed of exactly the same number of spikes as the initial measure  $m_{a_0, t z_0}$  and recovered by Algorithm 3 in a finite number of iterations.

### 4.2.3 Adaptation for the Positive BLASSO of SFW

In this section we overview how we implement Algorithm 3. The code can be found in <https://github.com/qdenoyelle>.

From now on and in the following we suppose that one wants to recover numerically a positive measure. As a result, we add a positivity constraint to the BLASSO:

$$\min_{m \in \mathcal{M}(X), m \geq 0} \frac{1}{2} \|\Phi m - y\|_{\mathcal{H}}^2 + \lambda m(X). \quad (\mathcal{P}_\lambda^+(y))$$

A consequence is that this changes the typical optimality condition  $\|\eta\|_{\infty, X} \leq 1$  (for  $\eta_\lambda, \eta_V, \eta_W$ ...) into  $\eta \leq 1$ .

In this setting, Algorithm 3 becomes:

---

**Algorithm 4** Sliding Frank-Wolfe Algorithm (Positivity Constraint)

---

```

1: Initialize with  $m_0 = 0$  and  $k = 0$ .
2: for  $k = 0, \dots, n$  do
3:    $m_k = \sum_{i=1}^{N_k} a_i^k \delta_{x_i^k}$ ,  $a_i^k \in \mathbb{R}_+$ ,  $x_i^k$  pairwise distincts, find  $x_*^k \in X$  s.t.:
      
$$x_*^k \in \operatorname{argmax}_{x \in X} \eta_k(x) \quad \text{where} \quad \eta_k \stackrel{\text{def.}}{=} \frac{1}{\lambda} \Phi^*(y - \Phi m_k),$$

4:   if  $\eta_k(x_*^k) \leq 1$  then
5:      $m_k$  solution of  $\mathcal{P}_\lambda^+(y)$ . Stop.
6:   else
7:     Obtain  $m_{k+1/2} = \sum_{i=1}^{N_k} a_i^{k+1/2} \delta_{x_i^k} + a_{N_k+1}^{k+1/2} \delta_{x_*^k}$ , s.t.:
      
$$(a_i^{k+1/2})_{1 \leq i \leq N_k+1} \ni \operatorname{argmin}_{a \in \mathbb{R}_+^{N_k+1}} \frac{1}{2} \|\Phi_{\mathcal{G}} a - y\|_{\mathcal{H}}^2 + \lambda \sum_{i=1}^{N_k+1} a_i$$

      where  $\mathcal{G} = (x_1^k, \dots, x_{N_k}^k, x_*^k)$ 
8:     Obtain  $m_{k+1} = \sum_{i=1}^{N_k+1} a_i^{k+1} \delta_{x_i^{k+1}}$ , s.t.:
      
$$((a_i^{k+1}), (x_i^{k+1})) \ni \operatorname{argmin}_{(a, x) \in \mathbb{R}_+^{N_k+1} \times X^{N_k+1}} \frac{1}{2} \|\Phi_x a - y\|_{\mathcal{H}}^2 + \lambda \sum_{i=1}^{N_k+1} a_i.$$

9:     Eventually remove zero amplitudes Dirac masses from  $m_{k+1}$ .
10:    end if
11: end for
```

---

Of course the convergence study made in Section 4.2.2 is still valid for Algorithm 4 and Theorem 6 holds.

**Implementation details.** Let us review for the main steps of Algorithm 4 how one performs it in practice:

- Step 3: the goal is now to find the maximum of  $\eta_k$  (the absolute values disappear because of the positivity constraint). One still uses a Newton method initialized by a grid search.
- Step 7: the goal is to solve the LASSO with positivity constraint. We use FISTA.
- Step 8: since one has the positivity constraint  $a \in \mathbb{R}_+^{N_k+1}$ , the  $\ell^1$  norm of  $a$  is just the sum of its coefficients so that the objective function is differentiable. We solve it using a Bounded BFGS, enforcing the positions to stay in the compact domain  $X$  and the amplitudes to remain non-negatives.

#### 4.2.4 Discussion on the Complexity of SFW and FISTA

In this section, one provides a rough estimate of the complexity of respectively the SFW Algorithm and FISTA. It is important to remark that this is a challenging question. For example, for FISTA there is no theory (to our knowledge) of how fast it converges when the grid gets thinner. As a consequence, the estimates given below must be taken with caution and are only here to give a coarse idea of the number of operations performed by the two algorithms.

One denotes by  $N$  the number of spikes,  $\Delta$  the minimum separation between the spikes,  $\sigma$  the typical size of the kernel,  $K$  the number of measurements (for example  $(2f_c + 1)^d$  for Fourier measurements),  $q$  the size of the grid for FISTA and  $r$  the size of the grid search in the SFW Algorithm.

- For FISTA, each iteration costs  $Kq$  operations, one expects that the typical condition number of the correlation matrix is  $\kappa = (\frac{\sigma}{\Delta})^{2N-1}$  and one needs to perform of the order of  $\sqrt{\kappa}$  iterations. This leads to an overall complexity of:

$$O\left(\frac{K}{\Delta} \left(\frac{\sigma}{\Delta}\right)^N\right),$$

when using  $q \simeq 1/\Delta$  (because one wants to be able to capture two close spikes separated by  $\Delta$ ).

- For the SFW algorithm, the grid search requires  $rNK$  operations. The number of operations for the computations of the new amplitudes by solving the LASSO using FISTA is negligible with respect to the next step (BFGS). The condition number of the Hessian for the BFGS is  $\kappa = (\frac{\sigma}{\Delta})^{2N-1}$  so that the number of iterations of the BFGS is roughly  $\simeq \sqrt{\kappa}$  and each iterations cost  $NK$ . If we consider that the algorithm converges in  $N$  iterations, we thus obtain an overall complexity of:

$$O\left(rN^2K + N^2K\left(\frac{\sigma}{\Delta}\right)^N\right).$$

When  $\Delta \rightarrow 0$ ,  $rN^2K$  is negligible with respect to  $N^2K\left(\frac{\sigma}{\Delta}\right)^N$  because  $r$  depends only on the size of the PSF. As a consequence, we end up with a complexity of:

$$O\left(N^2K\left(\frac{\sigma}{\Delta}\right)^N\right).$$

Therefore comparing the two complexities, we see that when the spikes are close  $\Delta \rightarrow 0$ ,  $N^2$  is negligible with respect to  $1/\Delta$  so that the SFW algorithm is expected to perform less operations than FISTA.

#### 4.2.5 A Few Numerical Illustrations of the SFW

In this section one gathers numerical experiments performed using the SFW algorithm. The goal is to give a better idea of how it works in practice.

**Number of Spikes recovered.** First, one compares in Figure 4.1 the number of spikes recovered by the SFW algorithm solving  $\mathcal{P}_\lambda^+(y)$  (Algorithm 4) to the number of spikes recovered by an interior point method to the equivalent SDP formulation of  $\mathcal{P}_\lambda^+(y)$  (see Section 4.1.1 for more details on the SDP formulation of the BLASSO and the section at the end of this chapter for the SDP formulation with the added positivity constraint).

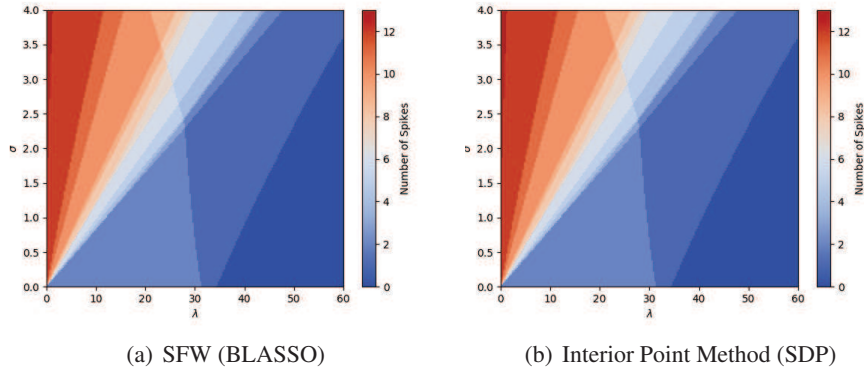


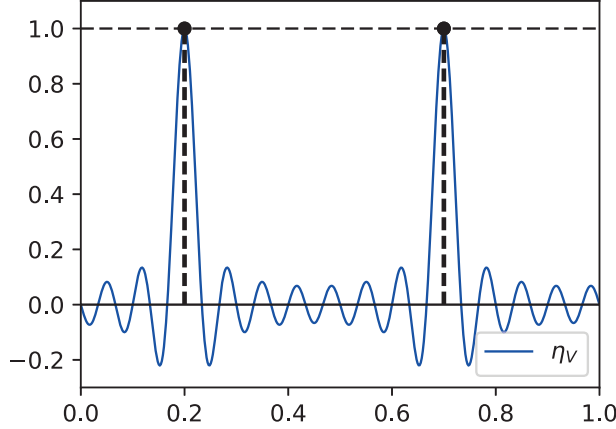
Figure 4.1: Number of spikes recovered for  $\mathcal{P}_\lambda^+(y)$  solved by SFW algorithm and for SDP formulation  $\mathcal{P}_\lambda^+(y)$  solved by interior point method.  $\Phi$  convolution by ideal low pass filter ( $f_c = 15$ ) and  $m_{a_0, x_0} = \delta_{0.2} + \delta_{0.7}$ .  $\sigma$  represents noise level ( $w = \sigma w_0 \in \mathbb{R}^{2f_c+1}$ ).

The setup of this experiment is the 1D torus and  $\Phi$  the convolution with the Dirichlet kernel with cutoff frequency  $f_c = 15$ . The initial measure is composed of two positive spikes and one varies the regularization parameter  $\lambda$  and the noise level  $\sigma > 0$  where  $w = \sigma w_0$  with  $w_0 \in \mathbb{R}^{2f_c+1}$  a fixed vector whose coefficients follow a Gaussian distribution.

One sees that the two graphs are identical, illustrating the fact that the Sliding Frank-Wolfe algorithm recovers exactly the solution of the BLASSO. Moreover we remark that the recovery of the support (2 spikes here) is valid in a triangle satisfying  $\max(\|w\|_{\mathcal{H}}/\lambda, \lambda) \leq C_1$  for some  $C_1 > 0$ . This illustrates the result proved in [54] and the fact that the vanishing derivatives pre-certificate associated to the initial measures and the forward operators  $\Phi$  considered here is non-degenerate (see Figure 4.2).

**N-Steps Convergence.** One now illustrates with two examples how the algorithm works and ones shows that it converges in exactly  $N$  iterations in practice (if of course the noise level and the regularization parameter are appropriate:  $\max(\lambda, \|w\|_{\mathcal{H}}/\lambda)$  is low enough).

The setting that one chooses here is  $X = [0, 1]$  and the kernel  $\Phi$  is a discretiza-

Figure 4.2:  $\eta_V$  for  $m_{a_0, x_0} = \delta_{0.2} + \delta_{0.7}$ .

tion of the convolution by a Gaussian. More precisely, one considers:

$$\Phi : m \in \mathcal{M}(X) \mapsto \int_0^1 \varphi dm \in \mathbb{R}^K \quad \text{where} \quad \varphi(x) = \left( \frac{1}{\sqrt{2\pi\sigma^2}} e^{-\frac{(i-1-x)^2}{2\sigma^2}} \right)_{1 \leq i \leq K}.$$

One chooses  $\sigma = 0.05$  and  $K = 100$ . The data  $y = y_0 + w$  are the same for Figure 4.3, 4.4, 4.5, the initial measure used is  $m_{a_0, x_0} = 1.3\delta_{0.3} + 0.8\delta_{0.37} + 1.4\delta_{0.7}$  and the noise is small ( $w = 10^{-4}w_0$  where  $w_0 = \text{randn}(K)$ ).

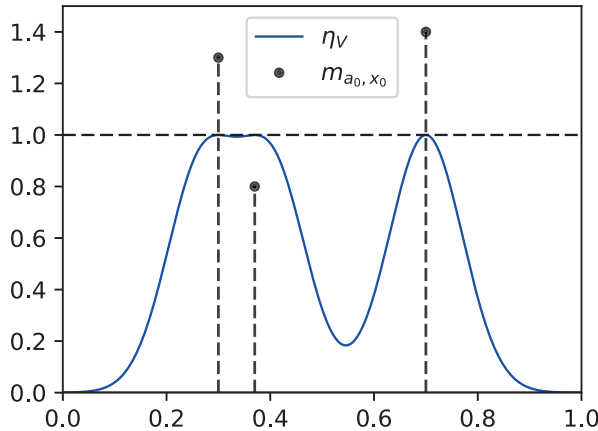
Figure 4.3:  $\eta_V$  for  $m_{a_0, x_0} = 1.3\delta_{0.3} + 0.8\delta_{0.37} + 1.4\delta_{0.7}$ .

Figure 4.3 shows  $\eta_V$  for this configuration. One can see that it is non-degenerate, hence in a small noise now regime with the appropriate choice of  $\lambda$  there is a unique

measure solution of  $\mathcal{P}_\lambda^+(y)$  composed of the same number of spikes as  $m_{a_0, x_0}$  and by Theorem 6, the SFW algorithm recovers it in a finite number of iterations.

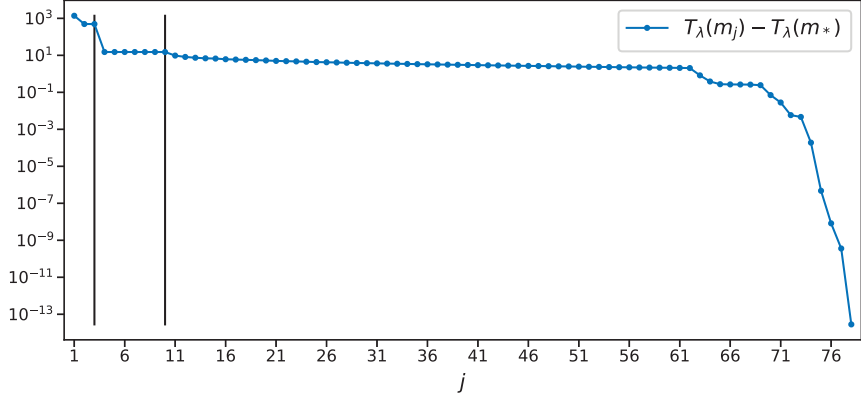


Figure 4.4: Values of the objective function throughout the SFW algorithm (accumulative iterations of the BFGS). The vertical black lines separate the main outer iterations of the algorithm.

In fact the algorithm converges in exactly 3 iterations here (as indicated by the two vertical black lines that shows the intermediate iterations). In Figure 4.4, one sees the decrease of the objective function throughout the algorithm where we display its value for the cumulative iterations of the BFGS. When a spike is added, the objective function decreases suddenly. The BFGS converges with very few iterations when  $k = 0$  and  $k = 1$  (first two spikes added) and the main computational load for the displacements is done when  $k = 2$  (more iterations of the BFGS).

Figure 4.5, shows  $m_k$  and  $\eta_k$  at different times of the algorithm. More precisely for  $k \in \{0, 1, 2\}$  (the three main iterations needed for the recovery of the unique solution of  $\mathcal{P}_\lambda^+(y)$ ) we display the initial measure  $m_{a_0, x_0}$ , the measure recovered after solving the LASSO (Step 7 of Algorithm 4) and after the BFGS (Step 8) with their associated  $\eta$ .

One remarks, as expected, that for all  $i$ ,  $\eta_{k+1/2}(x_i) = 1$ ,  $\eta_{k+1}(x_i) = 1$  and  $\eta'_{k+1}(x_i) = 0$ . In the first two main iterations, the spikes are almost not moved by the BFGS. However the displacement of the positions of the spikes and in the same time of their amplitudes at the last iteration is critical to obtain  $\eta_{k+1} \in \partial|m_{k+1}|(X)$  and thus recover the solution of  $\mathcal{P}_\lambda^+(y)$  in three steps.

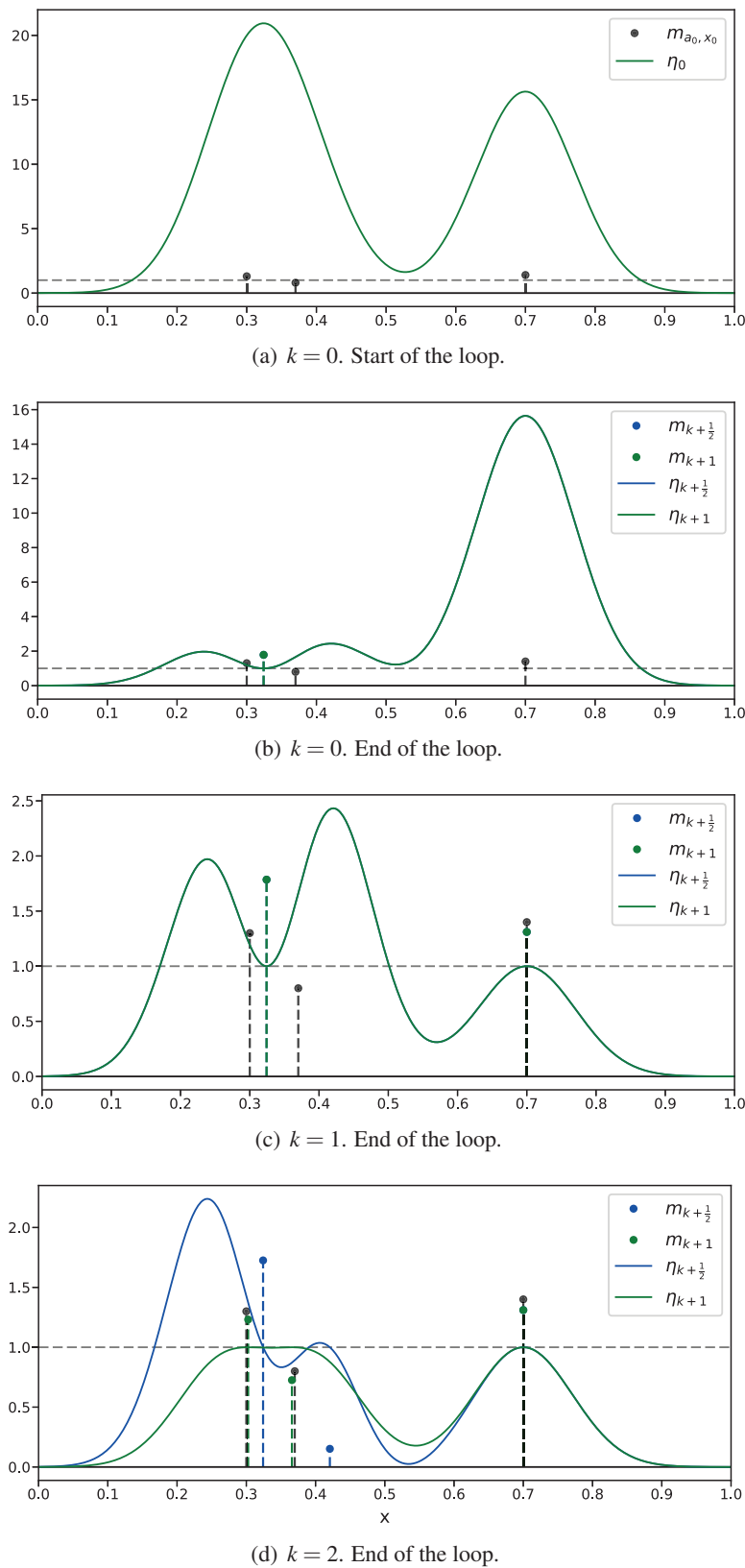


Figure 4.5: Main steps of the SFW algorithm.

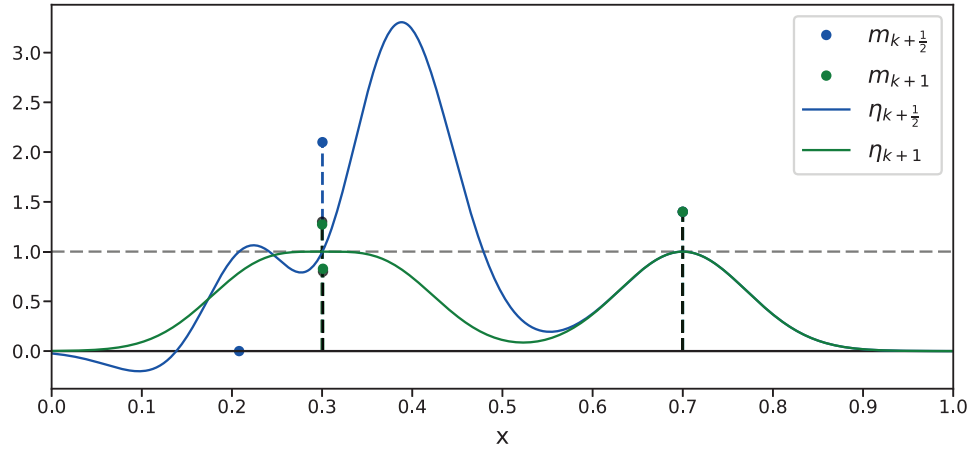


Figure 4.6: Last step of the SFW algorithm for an other initial measure with two very close spikes.

In Figure 4.6, one considers an other initial measure so that the first two spikes are separated by a distance of  $0.02\sigma$ . The noise level is almost zero here because one wants to prove that the SFW algorithm is still able to recover perfectly in a finite number of steps a measure with two very close spikes. If the spikes are closer than  $0.02\sigma$ , the algorithm starts having some difficulty to recover faithfully the amplitudes of the two spikes (but increasing  $K$  helps). We believe this is not a failure of the SFW method but rather numerical instability of the BFGS solver that reaches machine precision.

## 4.3 The SFW Algorithm versus Other Solvers

This Section compares the performance of the Sliding Frank-Wolfe algorithm, detailed in Section 4.2, with FISTA and OMP.

The common setting that one uses to compare these algorithms is the case of the Laplace transform inversion problem. The goal is to give a better insight of the potential of the Sliding Frank-Wolfe algorithm using an operator which is not translation invariant. Indeed the inversion of the Laplace transform is a challenging problem (see Section 2.1.2). Moreover one wants to have guarantees that this solver is better than already existing numerical methods in this particular case, since the Laplace transform is involved in the MA-TIRF model considered in Chapter 5 for the recovery of sparse subsets of fluorescent molecules in cells.

To compare algorithms, one needs metrics to assess the recovery performance. Section 4.3.2 is devoted to this subject. But before, one details more precisely in the following Section the forward models considered here.

### 4.3.1 Laplace Transform Based Forward Models

As mentioned above, one considers here the setting of the Laplace transform. One presented in Section 2.3 various Laplace-like operators (with or without discretization, normalization...). Since this Section is devoted to numerics, one only works with a discretized Laplace transform. As a result the two forward models that one considers are:

1. the discretized un-normalized Laplace transform,
2. the discretized  $L^2$ -normalized Laplace.

We discuss in Section 4.4.1 of the impact on the performance of the normalization.

The domain of the positions of the spikes  $X$  and the Hilbert space of observations  $\mathcal{H}$  are as follows:

- $X = [\varepsilon, x_b] \subset \mathbb{R}$  where  $\varepsilon > 0$  and  $x_b > \varepsilon$  is a bound,
- $\mathcal{H} = \mathbb{R}^K$  equipped with the standard scalar product, where  $K$  is the number of points for the discretization of the Laplace transform (in the MA-TIRF model, it is the number of angles on which the sample is observed, see Chapter 5).

Similar to what was presented in Section 2.3 (the theoretical models of Laplace like operators), here  $X$  is supposed to be a compact subset of  $\mathbb{R}$ . This choice is made mainly for practical numerical reasons because we find that the algorithms are more stable when  $X$  is upper-bounded. Moreover in applications such as the one studied in Chapter 5, the domain is compact.

Finally one recalls that the kernels for both model are given by:

1. for all  $x \in X$ ,  $\varphi(x) = (e^{-s_k x})_{k=1}^K \in \mathcal{H}$ , where  $s_k \in \mathbb{R}_+$ , for the un-normalized transform and the correlation function is:

$$c_\varphi(x, x') = \sum_{k=1}^K e^{-s_k(x+x')},$$

2. for all  $x \in X$ ,  $\varphi(x) = \xi(x)(e^{-s_k x})_{k=1}^K \in \mathcal{H}$ , with  $\xi(x) = (\sum_{k=1}^K e^{-2s_k x})^{-1/2}$ , for the  $L^2$  normalized transform and the correlation function is:

$$c_\varphi(x, x') = \xi(x)\xi(x') \sum_{k=1}^K e^{-s_k(x+x')}.$$

One can check that  $\|\varphi(x)\|_{\mathcal{H}} = 1$ .

In this Section 4.3, the values  $(s_k)_{1 \leq k \leq K}$  are taken uniformly in the interval  $[0, s_{\max}]$ :

$$\forall k \in \{1, \dots, K\}, \quad s_k = \frac{k-1}{K-1} s_{\max}, \quad (4.3.1)$$

where the value  $s_{\max}$  is fixed later. For a study of the influence on the recovery of the value of  $s_{\max}$  see Section 4.4.2.

### 4.3.2 Metrics

One presents now the metrics that one uses to measure the recovery performance of the studied algorithms. These metrics can be divided in two major types:

- metrics based on detection indices,
- metrics that measure how close a solution is from the source signal.

The idea behind the first type of metrics (detection indices) is the fact that the objects that one wants to recover are sums of Dirac masses. As a result it is natural to ask whether a spike has been detected or not. This notion of detection is quite important in many applications such as in Biology and is used in the SMLM challenge<sup>1</sup>, see [125] (Chapter 5 gives more details on these matters). The last type of metrics is more classical. There are many ways to measure distances, but the difficulty here is that one wants to determine a distance between Radon measures which also takes into account their geometry. The choice that we make is to consider the flat norm which is a generalized Optimal Transport distance. But first let us give some more details concerning detection indices.

---

<sup>1</sup><http://bigwww.epfl.ch/smlm/index.html>

**Detection of Spikes.** One details in this paragraph the main metrics used in [125] and the SMLM challenge to measure the performance. They are based on the ability to detect spikes. They all depend on the previous choice of a radius  $r > 0$  of detection. Suppose that such a radius is now fixed, then one has the following Definition:

**Definition 11** (Detected Spike). *We say that a spike  $a_{0,i}\delta_{x_{0,i}}$ , of an initial measure  $m_{a_0,x_0}$ , is detected with a scale  $r$  if there is a spike  $a_j\delta_{x_j}$  of the recovered measure  $m_{a,x}$  that lies in a ball of center  $x_{0,i}$  and radius  $r > 0$ .*

Obviously, the greater  $r$  is, the more there are detected spikes. In practice to determine the list of detected spikes of  $m_{a_0,x_0}$  by  $m_{a,x}$ , one uses the following algorithm:

1. input:  $x_0 \in X^{N_0}$  and  $x \in X^N$ ,
2. compute, store and sort in a list  $\mathcal{D}$  all the distances  $\|x_{0,i} - x_j\|$ ,
3. take the smallest element of  $\mathcal{D}$ , say  $\|x_{0,k} - x_l\|$ , if  $\|x_{0,k} - x_l\| \leq r$  then add  $x_{0,k}$  to the list of detected spikes and remove  $x_{0,k}$  and  $x_l$  from respectively  $x_0$  and  $x$ ,
4. remove all  $\|x_{0,k} - x_{l'}\|$  for all  $l'$  and all  $\|x_{0,k'} - x_l\|$  for all  $k'$  from  $\mathcal{D}$ ,
5. Go back to 3 until the smallest element of  $\mathcal{D}$  is greater than  $r$ ,
6. output: list of detected spikes and of remaining spikes of  $m_{a_0,x_0}$  and  $m_{a,x}$ .

From this algorithm one can define the notion of *true positive*, *false positive* and *false negative* spikes.

**Definition 12** (True positive, false positive, false negative spikes). *We have the following definitions:*

- a *true positive spike* is a detected spike of  $m_{a_0,x_0}$ ,
- a *false positive spike* is a remaining spike of  $m_{a,x}$  that has not been used for a detection,
- a *false negative spike* is a remaining spike of  $m_{a_0,x_0}$  that has not been detected.

The number of true positive, false positive and false negative spike are respectively denoted  $TP$ ,  $FP$  and  $FN$ .

Recall that these notions depend on a previously chosen radius  $r$  of detection. Figure 4.7 shows an illustration of Definition 12.

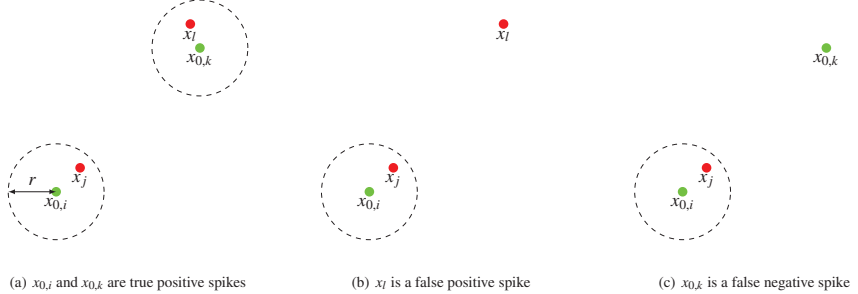


Figure 4.7: Illustration of the notion of true positive, false positive and false negative spike. In green the spikes of  $m_{a_0,x_0}$  and in red the spikes of  $m_{a,x}$ .

**Remark 6.** The ideal case in terms of performance of detection is when TP is equal to the number of spikes of  $m_{a_0,x_0}$ , FP = 0 and FN = 0 i.e.  $m_{a,x}$  has the same number of spikes as  $m_{a_0,x_0}$  and all the spikes of  $m_{a,x}$  are closer than  $r$  of a spike of  $m_{a_0,x_0}$ .

We can now define the indices that one uses in the following to measure the detection performance of the algorithms.

**Definition 13** (Jaccard Index, Recall and Precision). *We define the Jaccard index as:*

$$J \stackrel{\text{def.}}{=} \frac{TP}{TP + FP + FN}, \quad (4.3.2)$$

the Recall as:

$$R \stackrel{\text{def.}}{=} \frac{TP}{TP + FN}, \quad (4.3.3)$$

and finally the Precision as:

$$P \stackrel{\text{def.}}{=} \frac{TP}{TP + FP}. \quad (4.3.4)$$

If  $J = 1$  then it is the ideal case where the recovered measure has the same number of spikes as the original measure and all the spikes of the initial measure are detected.

**Jaccard index.** The Jaccard index measures the overall performance of detection. It was first introduced by Jaccard in 1901 [93] and is used in many fields such as for example in information retrieval, data mining, the study of chemical structures, machine learning [74]. The Jaccard index is in general defined as a way to measure the similarity of sets: let  $E$  be a set and  $(A, B) \in \mathcal{P}(E)^2$ , then:

$$J(A, B) \stackrel{\text{def.}}{=} \frac{|A \cap B|}{|A \cup B|}. \quad (4.3.5)$$

where  $|A|$  is the cardinal of the set  $A$ .

**Proposition 25** (Jaccard Metric). *Let us define:*

$$\forall (A, B) \in \mathcal{P}(E)^2, \quad J_\delta \stackrel{\text{def.}}{=} 1 - J(A, B).$$

*Then  $(\mathcal{P}(E), J_\delta)$  is a metric space.*

The fact that  $J_\delta$  is symmetric and satisfies the identity of indiscernibles is trivial. For the triangle inequality, there exist many proofs [110, 133, 72, 107, 33, 70, 99].

The link between the definition of the Jaccard index in Equation (4.3.2) that one uses in this thesis, and the general definition (4.3.5) is illustrated in Figure 4.8 and is as follows: consider  $m_{a_0, x_0}$  and  $m_{a, x}$  and make the list  $(p_i)_{1 \leq i \leq n}$  containing all the pairs:

- $(x_{0,i}, x_j)$  if  $a_{0,i}\delta_{x_{0,i}}$  is a detected spike by  $a_j\delta_{x_j}$ ,
- $(x_{0,k}, x_{0,k})$  if  $a_{0,k}\delta_{x_{0,k}}$  is a non-detected spike (false negative),
- $(x_l, x_l)$  if  $a_l\delta_{x_l}$  is a spike not used for a detection (false positive).

One has  $\max(N, N_0) \leq n \leq N + N_0$ . We then form the two sets  $M_0$  and  $M$  such that:

$$\forall i \in \{1, \dots, n\}, \quad p_i \in M_0 \Leftrightarrow \text{pr}_1(p_i) \in \text{supp}(m_{a_0, x_0}),$$

and

$$\forall i \in \{1, \dots, n\}, \quad p_i \in M \Leftrightarrow \text{pr}_2(p_i) \in \text{supp}(m_{a, x}),$$

where  $\text{pr}_1$  and  $\text{pr}_2$  are respectively the projection on the first and second coordinates, and  $\text{supp}(m)$  is the support of  $m$ . Then one has finally:

$$J = J(M_0, M),$$

i.e.  $J$  measures the similarity between the sets  $M_0$  and  $M$ . The above equality is true because  $\text{TP} = |M_0 \cap M|$ ,  $\text{FN} = |M_0 \cap M^c|$  and  $\text{FP} = |M \cap M_0^c|$  so that  $|M \cup M_0| = \text{TP} + \text{FP} + \text{FN}$ .

**The Recall.** The Recall ( $R \stackrel{\text{def.}}{=} \frac{\text{TP}}{\text{TP} + \text{FN}}$ ) measures the performance of detection with respect to the number of non-detected spikes. If  $R$  is close to 1, it means that the algorithm has a high ability to detect the spikes of the initial measure. However it does not tell whether it comes from the fact that the solver just produces a lot of spikes (hence a lot of false positives).

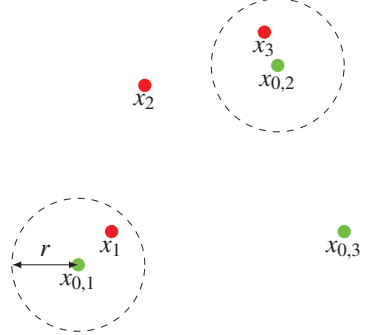


Figure 4.8: Illustration of the equivalence between the two definitions of the Jaccard index. We form the list of pairs from left to right:  $p_1 = (x_{0,1}, x_1)$ ,  $p_2 = (x_2, x_2)$ ,  $p_3 = (x_{0,2}, x_3)$ ,  $p_4 = (x_{0,3}, x_{0,3})$ ,  $p_5 = (x_4, x_4)$ . So  $M_0 = \{p_1, p_3, p_4\}$ ,  $M = \{p_1, p_2, p_3, p_5\}$ . Hence  $|M_0 \cap M| = 2$ ,  $|M_0 \cup M| = 5$  and  $J(M_0, M) = 2/5$ . Moreover one has TP = 2, FN = 1, FP = 2 so that  $J = 2/5$ .

**The Precision.** The Precision ( $P \stackrel{\text{def.}}{=} \frac{\text{TP}}{\text{TP} + \text{FP}}$ ) measures the performance of detection with respect to the number of falsely detected spikes. If  $P$  is close to 1, it means that the spikes of  $m_{a,x}$  are all sufficiently close of those of  $m_{a_0,x_0}$ . However it does not tell whether it comes from the fact that the solver misses a lot of spikes of  $m_{a_0,x_0}$  (hence a lot of false negatives).

To summarize, in the following, in order to assess the overall performance of detection, one uses  $J$  which measures the degree of similarity of the support of  $m_{a_0,x_0}$  and  $m_{a,x}$  and  $(R,P)$  which tells us for a given  $J$  is this level of similarity is obtained thanks to a high recall or a high precision.

Now we turn to the case of the Flat metric which actually measures distance between Radon measure. We show that this particular metric has nice properties for our goals.

**Flat Metric.** Let us consider here  $X = K$  a compact subset of  $\mathbb{R}$ . The total variation norm on  $\mathcal{M}(X)$ ,  $|\cdot|(X)$ , is the dual norm of the norm  $\|\cdot\|_{\infty,X}$  on  $\mathcal{C}(X, \mathbb{R})$ . However the metric and the topology induced by this norm are too strong for our goals. Indeed for example let us consider two Dirac masses denoted respectively  $a\delta_x$  and  $b\delta_y$  with  $a,b > 0$  and  $x \neq y$ . Then:

$$\text{TV}(a\delta_x, b\delta_y) = a + b,$$

where TV is the induced metric by  $|\cdot|(X)$ . This means that the distance between  $a\delta_x$  and  $b\delta_y$  does not depend on their separation. But when comparing two measures composed of Dirac masses, we would like that closer spikes between the two measures means smaller distance for the metric. Wasserstein distances based on the Optimal Transport theory [148], [149] have this property. They are very popular

both for theoretical aspects [3, 94, 31] and applications [2, 40, 12, 77]. In particular the 1-Wasserstein distance also called the Kantorovich-Rubinstein distance is defined as follows for positive Radon measures  $\mu, \nu$  with equal mass:

$$W_1(\mu, \nu) \stackrel{\text{def.}}{=} \sup_{f \in \text{BL}(X, \mathbb{R})} \left\{ \left| \int_X f d(\mu - \nu) \right|; \text{Lip}(f) \leq 1 \right\},$$

where  $\text{BL}(X, \mathbb{R})$  is the set of bounded Lipschitz function on  $X$  and  $\text{Lip}(f)$  denotes the minimal Lipschitz constant for  $f$ . It is easy to check that  $W_1(\delta_x, \delta_y) = |x - y|$ , however  $W_1(\mu, \nu)$  is only defined for measures with equal mass (not our case). That is why one rather considers the following metric called the Flat metric (sometimes also called the Dudley metric).

**Definition 14** (Flat Metric). *We define for all  $\tau > 0$  and for all  $\mu, \nu \in \mathcal{M}(X)$ , the Flat metric between  $\mu$  and  $\nu$  by:*

$$F_\tau(\mu, \nu) \stackrel{\text{def.}}{=} \sup_{f \in \text{BL}(X, \mathbb{R})} \left\{ \left| \int_X f d(\mu - \nu) \right|; \|f\|_{\infty, X} \leq \tau, \text{Lip}(f) \leq 1 \right\}. \quad (4.3.6)$$

$(\mathcal{M}(X), F_\tau)$  is a metric space.

Note that  $F_\tau$  is induced by a norm, called the flat norm, which can be seen as the dual norm of  $W^{1,\infty}(X)$  (Sobolev space) because the bounded Lipschitz functions are dense in  $W^{1,\infty}(X)$ . This norm was already introduced in [63, Section 4.1.12] for currents. It was later used in [78] for the study of Lipschitz spaces.  $F_\tau$  can also be seen as an inc-convolution between the 1-Wasserstein distance and the total variation. Equivalently  $F_\tau$  can be thought as a relaxation of the dynamical formulation of  $W_1$  (*i.e.* a generalization to  $W_1$  of the Benamou-Brenier formulation [11] for the 2-Wasserstein distance) where a source term is added to the equation of conservation of mass and penalized by using the Fisher-Rao metric. This point of view corresponds to the one developed in the theory of Unbalanced Optimal Transport. The reader can find more details on this matter in [36]. As a result this means that  $F_\tau$  measures the cost of moving the mass of  $\mu$  to the mass of  $\nu$  and in the same time authorizing and measuring a creation or destruction of mass by the total variation norm. The tradeoff between the creation (or destruction) of mass and its displacement is controlled by the parameter  $\tau$ .

To have a better understanding of what exactly is measured by  $F_\tau$ , the following Proposition gives the Flat metric between two positive Dirac masses.

**Proposition 26.** *Suppose that  $a, b > 0$ . Then one has:*

$$F_\tau(a\delta_x, b\delta_y) = |a - b|\tau + \min(a, b) \min(2\tau, |x - y|). \quad (4.3.7)$$

Suppose, without loss of generality, that  $a > b$ . Then two cases arises:

- if  $|x - y| > 2\tau$ , then (4.3.7) becomes:

$$F_\tau(a\delta_x, b\delta_y) = (a - b)\tau + 2b\tau = \tau \text{TV}(a\delta_x, b\delta_y),$$

so that  $F_\tau(a\delta_x, b\delta_y)$  can be seen as the cost of destroying the mass of  $b\delta_y$  (*i.e.*  $b\tau$ ) plus the cost of creating a mass  $a$  at  $x$  to form  $a\delta_x$  (*i.e.*  $a\tau$ ). Because the two spikes are too far away from each other ( $|x - y| > 2\tau$ ), no mass is transported here.

- If  $|x - y| \leq 2\tau$ , then (4.3.7) becomes:

$$F_\tau(a\delta_x, b\delta_y) = (a - b)\tau + b|x - y|,$$

so that  $F_\tau(a\delta_x, b\delta_y)$  can be seen as the cost of moving the mass  $b$  from  $y$  to  $x$  (*i.e.*  $b|x - y|$ ) plus the cost of adding mass to  $b\delta_x$  to make  $a\delta_x$  (*i.e.*  $(a - b)\tau$ ). Because the spikes are close enough (separated by less than  $2\tau$ ), in addition to creation of mass, there is also transportation.

In the following when one uses  $F_\tau$  to measure the recovery performance between an initial and a recovered measure, one makes sure that  $\tau$  is large enough so that the spikes that are too far away from each other are well penalized.

**Computation of the Flat metric.** To conclude this paragraph on the Flat metric, let us give details on how we compute it for measures composed of Dirac masses. When  $\mu = m_{a_0, x_0}$  and  $\nu = m_{a, x}$ , so that:

$$\mu - \nu = \sum_{i=1}^{N_0+N} a'_i \delta_{x'_i},$$

then Equation 4.3.6 just becomes:

$$F_\tau(\mu, \nu) = \sup_{f \in \mathbb{R}^{N_0+N}} \left\{ \sum_{i=1}^{N_0+N} f_i a'_i; \forall i, |f_i| \leq \tau, \forall i \neq j, |f_i - f_j| \leq |x'_i - x'_j| \right\},$$

which is a standard linear program that can be solved using a classical optimization toolbox. Note that because the positions are 1 dimensional, one can make the assumption that  $x'_1 \leq x'_2 \leq \dots \leq x'_{N_0+N}$ , so that the constraints on all distinct pairs  $(i, j)$  can be replaced by all successive pairs  $(i, i+1)$ . Thus one obtains:

$$F_\tau(\mu, \nu) = \sup_{f \in \mathbb{R}^{N_0+N}} \left\{ \sum_{i=1}^{N_0+N} f_i a'_i; \forall i, |f_i| \leq \tau, |f_{i+1} - f_i| \leq |x'_{i+1} - x'_i| \right\}.$$

### 4.3.3 Numerical Comparison of the Algorithms

In this Section one details the numerical experiments that we made to compare the SFW Algorithm, FISTA and OMP. We show that the Sliding Frank-Wolfe algorithm has the better performance.

But first in the next paragraph one details the constant values involved in the experiments, the chosen random model of generation of spikes and the noise model.

**Setup of the experiments.** The data used for the comparison are  $n \in \mathbb{N}^*$  vectors of observations:

$$y = \Phi m_{a_0, x_0} + w \in \mathbb{R}^K,$$

obtained from a collection of  $n$  initial measures  $m_{a_0, x_0}$  and where  $\Phi$  is a discretized  $L^2$ -normalized Laplace transform *i.e.*

$$\varphi(x) = \xi(x)(e^{-s_k x})_{k=1}^K \in \mathbb{R}^K \quad \text{with} \quad \xi(x) = \left( \sum_{k=1}^K e^{-2s_k x} \right)^{-1/2}.$$

We detail in Section 4.4.1 why we make this choice rather than the un-normalized version of the discretized Laplace transform.

The collection of  $n$  initial measures  $m_{a_0, x_0}$  used for the comparison of the algorithms are generated randomly thanks to the following process:

1. the positions of the spikes of  $m_{a_0, x_0}$  are chosen in  $[\varepsilon, x_b]$  such that for any two consecutive positions  $x_{0,i}, x_{0,j}$  with  $x_{0,i} < x_{0,j}$  then  $x_{0,j} - x_{0,i}$  follows an exponential law of parameter  $\iota$

$$x_{0,j} - x_{0,i} \sim \mathcal{E}(\iota). \quad (4.3.8)$$

We keep adding new spikes until the last position is greater than  $x_b$ ,

2. once  $x_0 \in X^N$ , for some  $N$ , is fixed the associated amplitudes are uniformly randomly chosen in the interval  $[1, 1.5]$ .

The parameter  $\iota > 0$  controls the density (number of spikes) of the initial measures: the smaller  $\iota$  is the greater the density of the point process is.

The noise  $w \in \mathbb{R}^K$  is obtained from a centered Gaussian distribution with variance  $\sigma^2$ .

Finally the values of the main constants are summarized in the following table 4.9:

Names	Values
$n$	2000
$\varepsilon$	$10^{-4}$
$x_b$	150
$K$	20
$s_{\max}$	0.3

Figure 4.9: Values of numerical constants used in all Section 4.3

**Preliminary discussions concerning FISTA.** Before finally moving to the actual comparison of the SFW algorithm with FISTA and OMP in the setup detailed previously, one needs to deal with a few matters concerning FISTA:

- the question of an eventual post-processing,
- the choice of the size of the grid on the domain  $X$ ,
- the number of iterations performed.

For recall, the domain  $X$  is discretized over a uniform grid  $\mathcal{G}$  of size  $\#\mathcal{G}$  and one solves using FISTA the following optimization problem:

$$\min_{a \in \mathbb{R}^{\#\mathcal{G}}} \frac{1}{2} \|\Phi_{\mathcal{G}} a - y\|_{\mathcal{H}} + \lambda \|a\|_1,$$

which is the LASSO.

**Influence of the clustering for FISTA.** First we discuss about the post-processing clustering step. As already mentioned in the Introduction of this Chapter (see Section 4.1.2), because FISTA often leads to an approximate solution with small clusters of non-zero weights in the neighborhood of each true spike, it might be smart to perform a clustering in order to increase its sparsity. It has been promoted in [140], where the authors proposed for each connected group of spikes of the approximate solution to replace it by a unique spike whose position is the barycenter of the positions of the spikes of the cluster weighted by their amplitudes and whose amplitude is their sum. Figure 4.10 illustrates this idea and Figure 4.11 confirms the enhancement of the Jaccard index. However the Flat Norm performance is slightly better when there is no clustering. Figure 4.11 is obtained by running the algorithms for each values of  $\lambda$  (chosen uniformly in the log scale between  $10^{-4}$  and 1) for the  $n$  observations and taking the mean of the indicator of interest. The table of Figure 4.12 summarizes the choices of parameters for this experiment.

As a result, it is not clear whether the post-processing clustering step is beneficial (it depends on the metric). However because it provides a significant improvement of the Jaccard index and does not impair a lot the flat norm indicator, one chooses in the following to always perform it.

**Influence of the size of the grid for FISTA.** We now study for FISTA the influence of the size of the grid on the performance. Figure 4.13 shows that increasing the sharpness of the grid improves the recovery performance. However going from a grid of 200 points to a grid of 400 points only makes a small difference. The table of Figure 4.14 summarizes the choices of parameters for this experiment.

As a result in the following, one only considers a grid composed of 200 points in order to keep a reasonable convergence speed.

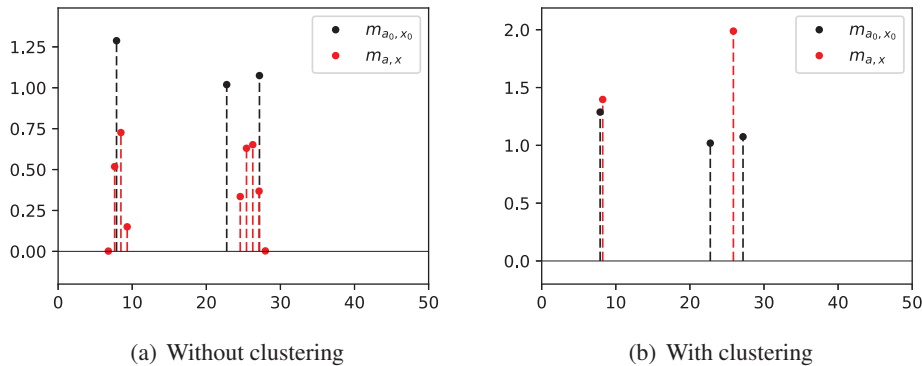


Figure 4.10: Approximate recovered measure from the LASSO solved by FISTA with or without clustering. We see that (b) has much less false positive spikes than (a), hence a better Jaccard index.

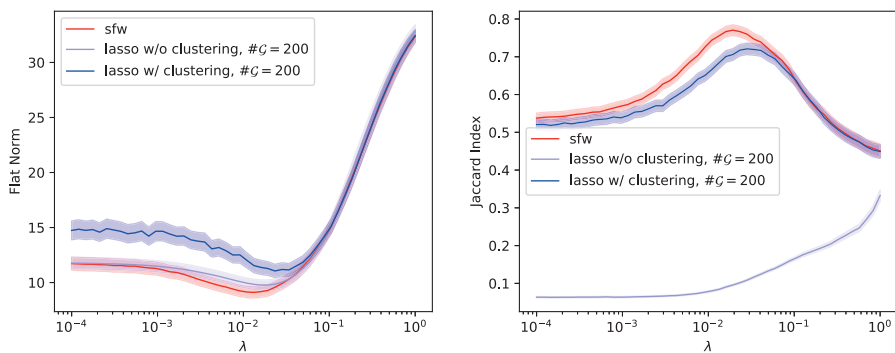


Figure 4.11: Performance comparison in terms of Flat Norm and Jaccard index of FISTA (with  $10^4$  iterations) with and without clustering. The area around the curves corresponds to a 95% confidence interval.

Names	Values
$t$	30
$\sigma$	$5 \cdot 10^{-5}$
$r$	5

Figure 4.12: Numerical constants for the experiment.  $\iota = 30$  corresponds to a rather low density of spikes (see Equation (4.3.8) for the definition of  $\iota$ ).

**Influence of the number of iterations for FISTA.** We now study the influence of the number of iterations on the recovery performance. 50 values of the

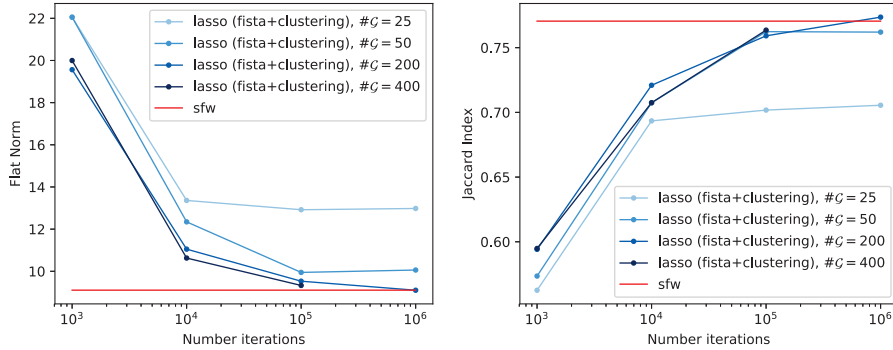


Figure 4.13: Performance comparison in terms of Flat Norm (left) and Jaccard index (right) for the LASSO solved by the FISTA algorithm for an increasing number of iterations and various size of grid. The area around the curves correspond to a 95% confidence interval.

Names	Values
$\iota$	30
$\sigma$	$5 \cdot 10^{-3}$
$r$	5

Figure 4.14: Numerical constants for the experiment.  $\iota = 30$  corresponds to a rather low density of spikes.

regularization parameter  $\lambda$  uniformly distributed in the log-scale between  $10^{-4}$  and 1 were used and only the optimal value (after taking the mean over the  $n$  observations) for both the Flat Norm and the Jaccard index are kept. The table of Figure 4.15 gathers all the main numerical constants used for the experiments of this paragraph.

Names	Values
$\iota$	30
$\sigma$	$5 \cdot 10^{-3}$
$r$	5
#G	200

Figure 4.15: Numerical constants for the experiment.  $\iota = 30$  corresponds to a rather low density of spikes.

We see in Figure 4.16 that the Sliding Frank-Wolfe algorithm performs better whatever the number of iterations for FISTA in terms of Flat Norm although it is slightly beaten for  $10^6$  iterations in terms of Jaccard index (but in the margin of

error). Going from  $10^5$  iterations to  $10^6$  iterations does not significantly improve the recovery performance.

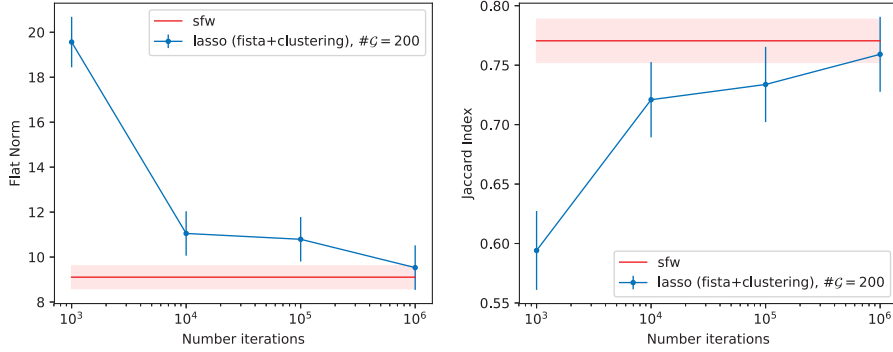


Figure 4.16: Flat norm and Jaccard index for an increasing number of iterations for FISTA. The area around the curves and the error bars correspond to a 95% confidence interval.

Looking at Figure 4.17, one sees that the SFW algorithm is faster than FISTA (with clustering) for better performance (around 25 times faster for approximately the same performance).

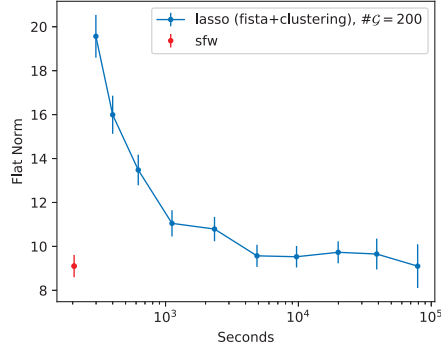


Figure 4.17: Flat norm over computation time for FISTA and SFW. The experiment has been parallelized on 40 cpu. The error bars correspond to a 95% confidence interval.

From now on when one shows results from FISTA, we fix the number of iterations in the order of  $10^4$  because, as shown in Figures 4.16 and 4.17, increasing further the number of iterations does not improve much the performance but increases significantly the computation time.

**Comparison of the three algorithms.** We now compare the SFW algorithm with FISTA and OMP.

Names	Values
$s_{\max}$	0.3
$r$	5
$\#\mathcal{G}$	200
Iterations FISTA	$10^4$

Figure 4.18: Main numerical constants for the comparison of the three algorithms.

Figure 4.19 compares the algorithms with a varying density of spikes controlled by  $\iota$  but with a fixed noise level given by  $\sigma = 5 \cdot 10^{-3}$  (moderate noise).  $\iota = 5$  corresponds to a mean number of spikes of roughly 5 and  $\iota = 30$  to a mean of 1.5.

Instead Figure 4.20 compares the algorithms with a varying noise level but with a fixed density given by  $\iota = 20$  (moderate density).

**Varying density.** We remark as expected that, the higher the density of spikes is, the worse are the performance (both in Jaccard index and in flat norm). Moreover the SFW algorithm always performs better than FISTA. OMP has the worst indicators of the three.

**Varying noise level.** We see as expected that a higher noise level leads to worse performance for the three algorithms. Similarly as in the previous setup (varying density of spikes), the SFW algorithm has the better performance ahead FISTA and finally OMP (for a continuous dictionary). We also remark that the optimal value of  $\lambda$  which gives the higher Jaccard index and the smallest Flat norm follows  $\sigma$  i.e.  $\lambda_{\text{opt}} \sim \sigma$ .

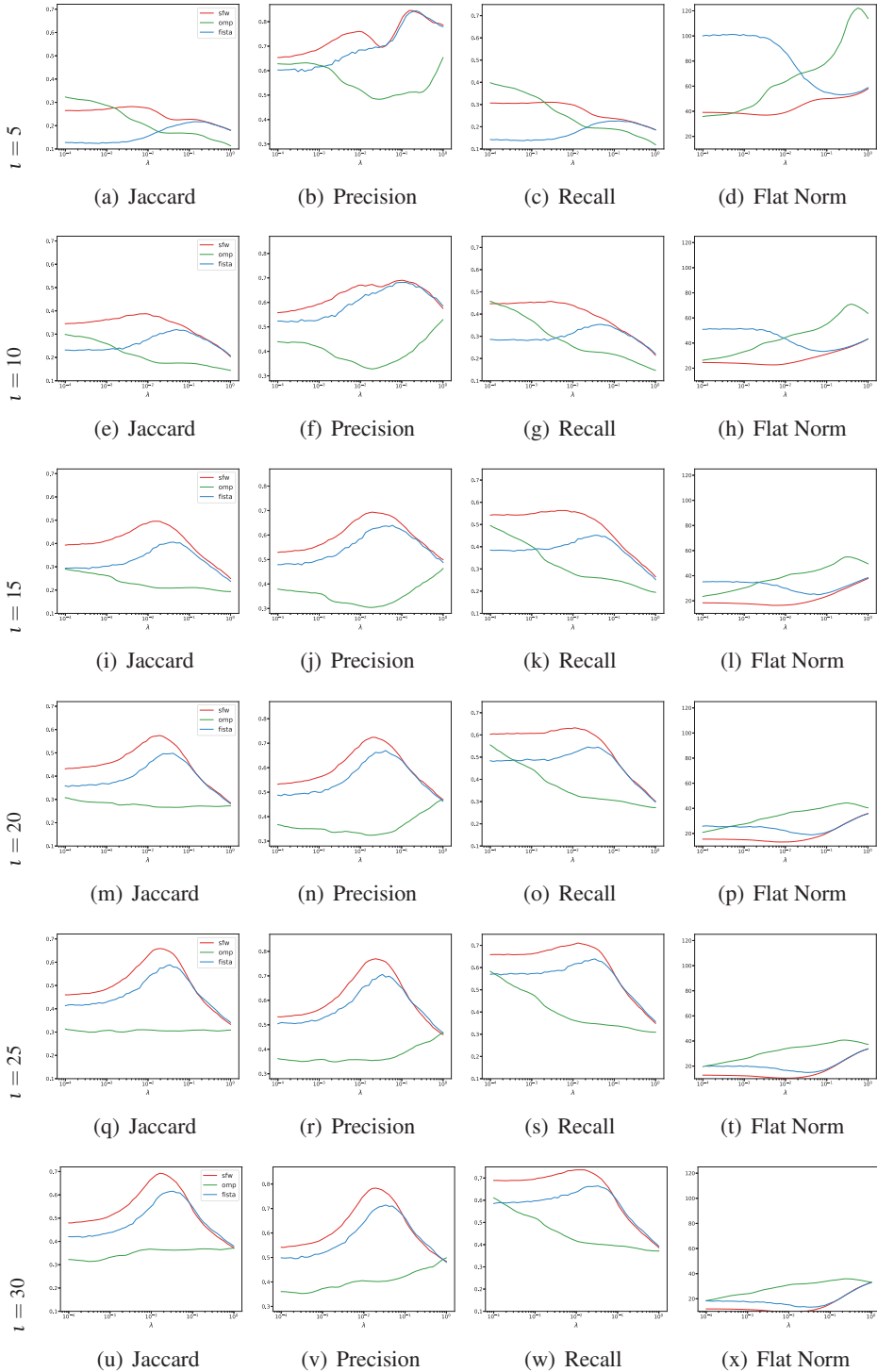


Figure 4.19: Comparison of the algorithms with a varying density of spikes and a fixed noise level ( $\sigma = 5 \cdot 10^{-3}$ ). For OMP, the parameter  $\lambda$  controls the sparsity of the recovered solution.

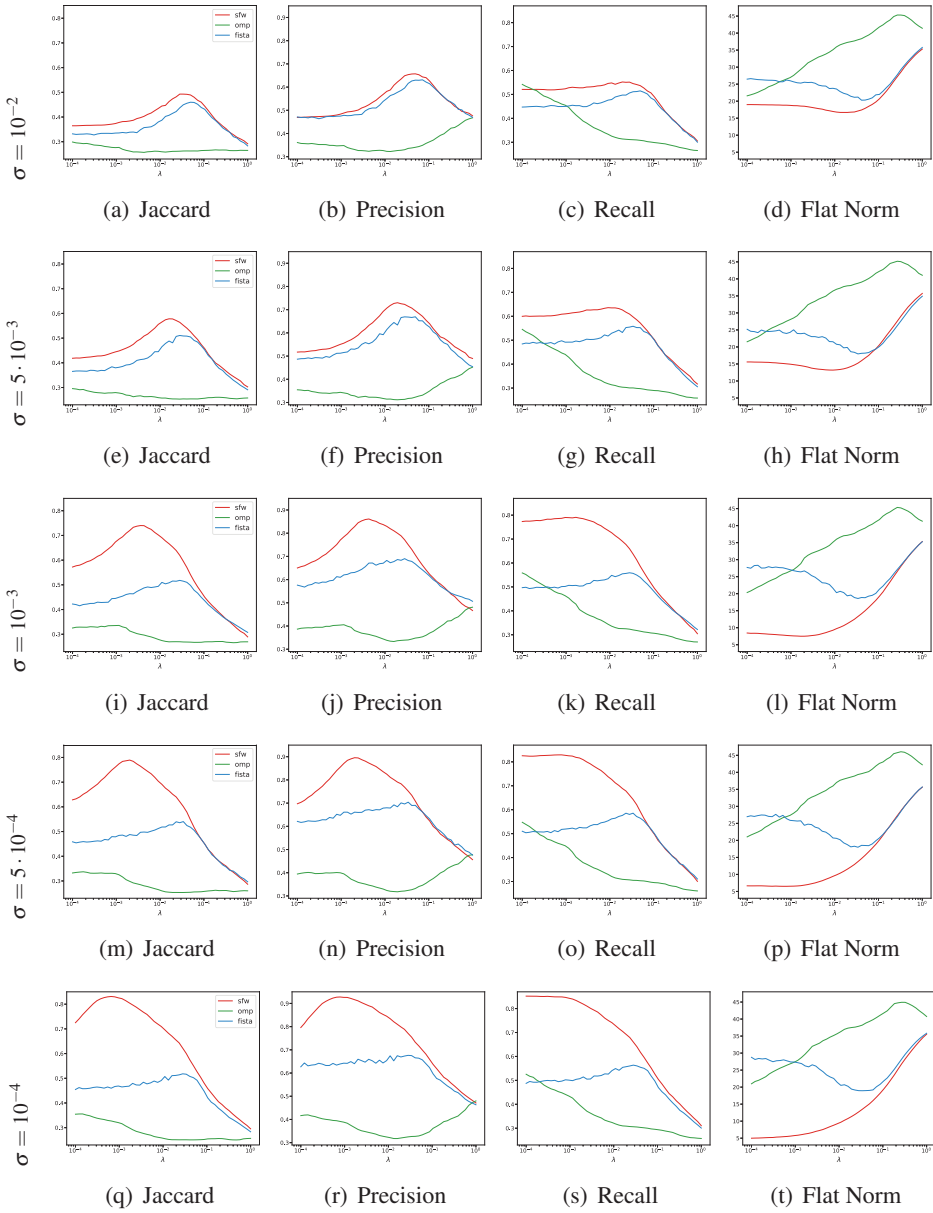


Figure 4.20: Comparison of the algorithms with a varying noise level and a fixed density of spikes ( $\iota = 20$ ). For OMP, the parameter  $\lambda$  controls the sparsity of the recovered solution.

## 4.4 Study of the Laplace Transform Numerical Inversion

One proposes in this section to study the recovery properties of the BLASSO, using the Sliding Frank-Wolfe algorithm, in the case of the Laplace transform. The goal is to get some insight on the numerical inversion of a discretized Laplace transform by solving the BLASSO with our algorithm (see Section 4.4.2), in order to better understand in a simpler setup the numerical results obtained in Chapter 5 where we use (among other models) a Laplace based forward operator to recover fluorophores positions in a 3D volume. Moreover we justify in Section 4.4.1 why we rather consider an  $L^2$ -normalized version of the discretized Laplace transform, in all our numerical experiments (including Chapter 5), even when the data are generated by the un-normalized version of the model.

The setup of this section is similar to the one developed in the last one (see Section 4.3): the forward models are the same, we use the same metrics, the same random model of generation of spikes and the same noise model.

One recalls the two forward operators considered here:

1. Un-normalized discretized Laplace transform: for all  $x \in X$ ,

$$\varphi(x) = (e^{-s_k x})_{k=1}^K \in \mathcal{H},$$

where  $s_k \in \mathbb{R}_+$  and the correlation function is:

$$c_\varphi(x, x') = \sum_{k=1}^K e^{-s_k(x+x')},$$

2.  $L^2$ -normalized discretized Laplace transform: for all  $x \in X$ ,

$$\tilde{\varphi}(x) = \xi(x)(e^{-s_k x})_{k=1}^K \in \mathcal{H} \quad \text{with} \quad \xi(x) = \left( \sum_{k=1}^K e^{-2s_k x} \right)^{-1/2},$$

and the correlation function is:

$$c_{\tilde{\varphi}}(x, x') = \xi(x)\xi(x') \sum_{k=1}^K e^{-s_k(x+x')}.$$

One can check that  $\|\tilde{\varphi}(x)\|_{\mathcal{H}} = 1$ .

### 4.4.1 Influence of the Normalization

In this section we study the influence of the normalization of the kernel of a discretized Laplace transform. One shows that it can be performed even if the data  $y$  are generated using the un-normalized model (the case of the MA-TIRF model detailed in Chapter 5) by rescaling the amplitudes of the spikes and one shows that it leads to better numerical performance.

Normalizing the kernel is quite natural when using a greedy type algorithm (our case here), see details on the Matching Pursuit algorithm [109]. One chooses to normalize it with the norm  $\|\cdot\|_{\mathcal{H}}$  because it arises naturally in the BLASSO (the loss function uses  $\|\cdot\|_{\mathcal{H}}$ ).

Suppose that the data:

$$y = \Phi m_{a_0, x_0} + w = \sum_{i=1}^{N_0} a_{0,i} \varphi(x_{0,i}) + w, \quad (4.4.1)$$

are generated using the un-normalized version of the discretized Laplace transform, then one has:

$$y = \sum_{i=1}^{N_0} \frac{a_{0,i}}{\xi(x_{0,i})} \tilde{\varphi}(x_{0,i}) + w,$$

so that we can just consider  $y$  as input of the SFW algorithm which uses the kernel  $\tilde{\varphi}$  (hence the normalized version of the Laplace transform as our forward operator) instead of  $\varphi$  and as a final step rescale the amplitudes of the recovered measure  $m_{a,\bar{x}}$  and return:

$$m = \sum_{i=1}^N \xi(x_i) a_i \delta_{x_i}.$$

Names	Values
$K$	20
$\iota$	10
$n$	2000
$\sigma$	$5 \cdot 10^{-3}$
$s_{\max}$	0.5
$r$	5

Figure 4.21: Numerical constants for the experiment of Figure 4.22.  $\iota = 10$  corresponds to a high density of spikes.

Figure 4.22 shows that in the normalized case, the recovery performance are better than in the un-normalized case because both in Flat norm and in Jaccard index. One also remarks that the Precision is significantly higher for  $\tilde{\varphi}$  than  $\varphi$ . This means that normalizing the kernel leads to a better localization of the spikes of the initial measure.

The numerical constants used to generate the results of Figure 4.22 can be found in the table of Figure 4.21.

#### 4.4.2 Influence of $s_{\max}$

In this section, we propose to numerically study the influence of the choice of  $s_{\max}$  on the recovery performance when solving the BLASSO with the SFW algorithm where  $\Phi$  is a normalized discretized Laplace transform. One shows that  $s_{\max}$

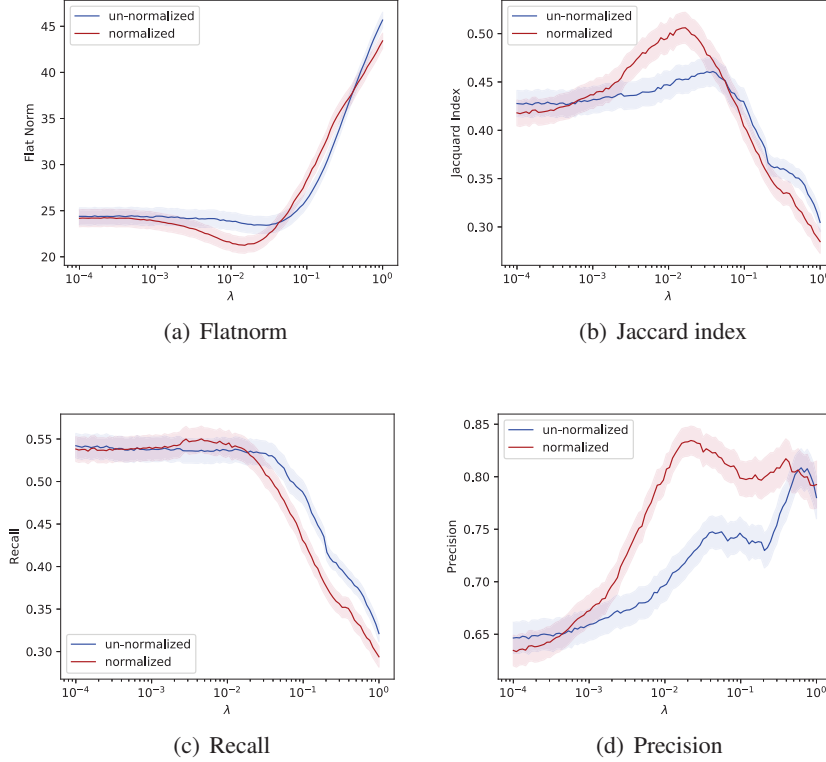


Figure 4.22: Comparison of performance between the un-normalized and normalized forward operator. Note that in both cases the data are the same (see Equation (4.4.1)). The area around the curves correspond to a 95% confidence interval.

needs to be high enough in order to recover precisely two spikes that are close near the origin.

One recalls the values  $(s_k)_{1 \leq k \leq K}$  are taken uniformly in the interval  $[0, s_{\max}]$ :

$$\forall k \in \{1, \dots, K\}, \quad s_k = \frac{k-1}{K-1} s_{\max},$$

In Figure 4.23, we propose to consider an initial measure given by:

$$m_0 = \delta_{\bar{x} - \frac{\Delta}{2}} + \delta_{\bar{x} + \frac{\Delta}{2}},$$

and vary the parameter  $(\bar{x}, \Delta)$  such that  $m_0 \in \mathcal{M}(X)$  is a measure composed of two spikes whose barycenter of positions moves in the domain  $X$  with a changing separation  $\Delta$ . For each value of  $(\bar{x}, \Delta)$  we solve the BLASSO for different  $\lambda$  using our algorithm  $n$  times (each time we randomly choose the noise  $w \in \mathbb{R}^K$ ). One then takes the mean of the Flat norm between the recovered measure and  $m_0$ . This information is displayed, for the optimal  $\lambda$ , in the graphs of Figure 4.23 for  $s_{\max} \in$

$\{0.1, 0.2, 0.3, 0.4, 0.5, 0.6\}$ . The numerical constants involved for this experiment can be found in the table of Figure 4.24.

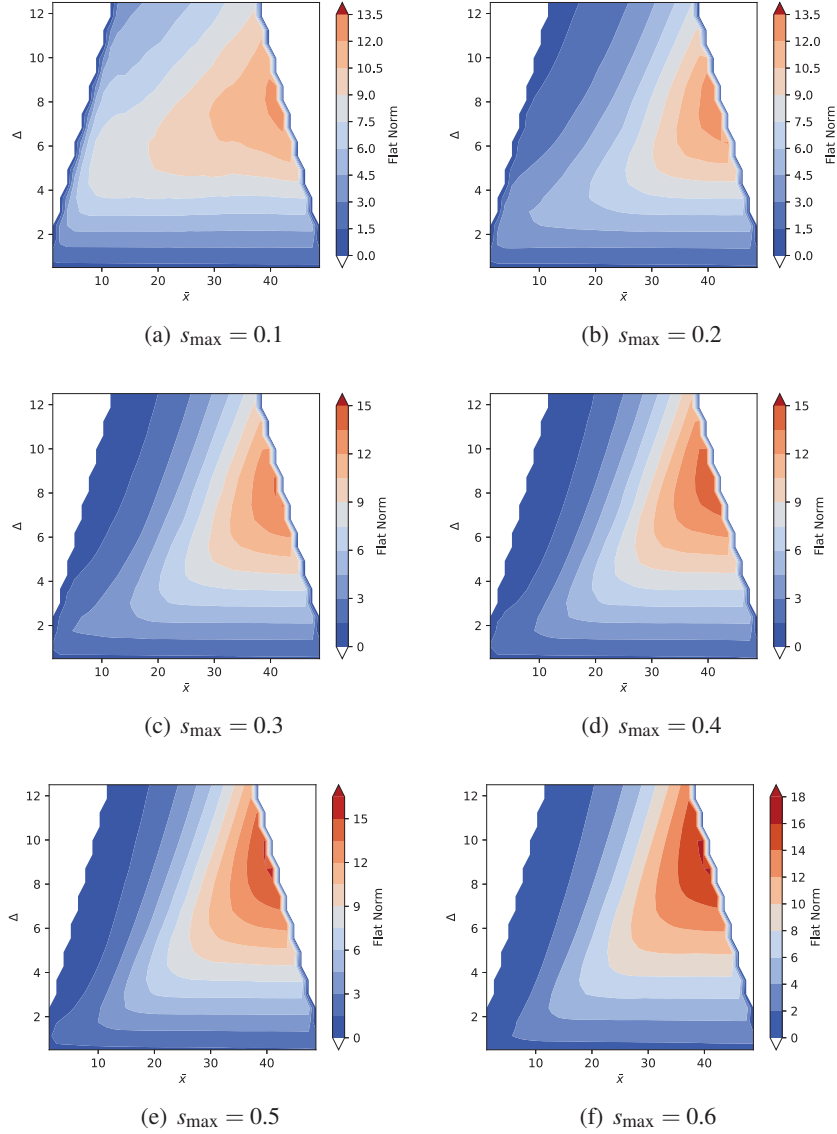


Figure 4.23: Flat norm comparison for different values of  $s_{\max}$  for the recovery of  $m_0 = \delta_{\bar{x}-\frac{\Delta}{2}} + \delta_{\bar{x}+\frac{\Delta}{2}}$ .

One sees in Figure 4.23 that when  $\bar{x}$  increases then the Flat norm gets higher. This phenomenon is due to the exponential decay of the kernel. The worst performance happens when  $(\bar{x}, \Delta) \simeq (40, 8)$  and it deteriorates with  $s_{\max}$ . As a result, in order to recover a measure composed of two spikes far from the origin,

it is better to have a smaller value of  $s_{\max}$ . This can be explained by the fact that a smaller value of  $s_{\max}$  means a slower exponential decay of the kernel. On the contrary when the two spikes are close of the origin (*i.e.*  $\bar{x}$  small), one sees that the performance are worse when  $s_{\max}$  is smaller. This is because in order to recover well the two spikes, the kernel has to decrease fast enough so that the data can reflect separately the contributions of the two spikes.

Since we are performing these experiments with a constant value of  $K$  (here equal to 20), increasing  $s_{\max}$  means that  $s_2 = \frac{s_{\max}}{K-1}$  increases also, so that the recovery performance decreases when  $\bar{x}$  is large. Consequently with  $K$  constant, the choice of the value of  $s_{\max}$  either favors the recovery of measures close of the origin (large  $s_{\max}$ ) or the recovery of measures far from the origin (small  $s_{\max}$ ). Increasing  $K$  in the same time as increasing  $s_{\max}$  keeps the best of both worlds (( $s_k$ ) $_{1 \leq k \leq K}$  contains small and large values). However, often in applications, the smaller  $K$  is the better. Moreover we can also have limitations on the choice of  $s_{\max}$ . It is in particular the case in Chapter 5 ( $K$  smaller is better and  $s_{\max}$  is upper-bounded).

Names	Values
$K$	20
$n$	500
$\sigma$	$5 \cdot 10^{-3}$

Figure 4.24: Numerical constants for the experiment of Figures 4.23, 4.25 and 4.26.

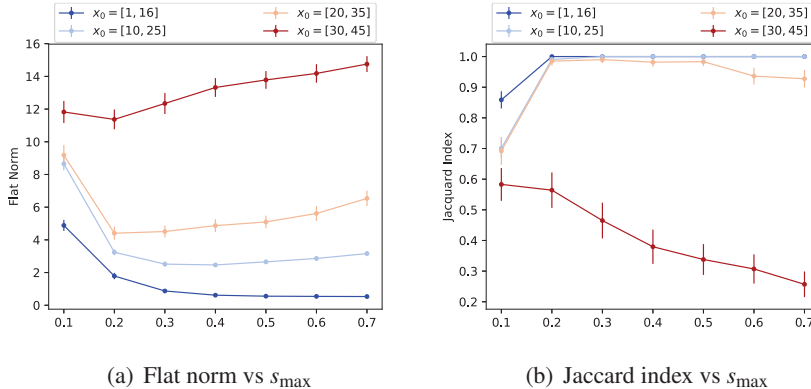


Figure 4.25: Flat Norm and Jaccard Index optimal values with respect to  $s_{\max}$  for different  $m_0$  where  $\Delta = 15$ . The error bars correspond to a 95% confidence interval.

Figure 4.25 is similar to Figure 4.23 (same setup) but only shows the results for  $\Delta = 15$  and a few values of  $\bar{x}$ . The Jaccard index is also provided. The conclusion are the same as above: high values of  $s_{\max}$  for spikes close of the origin and the opposite for spikes far from the origin.

Figure 4.26 shows, for the same setup as detailed above, the recovery perfor-

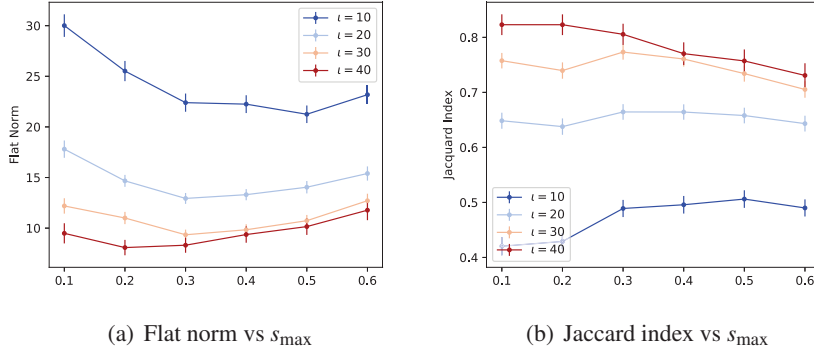


Figure 4.26: Flat Norm and Jaccard Index optimal values with respect to  $s_{\max}$  for different density of spikes  $t$ . The error bars correspond to a 95% confidence interval.

mance in terms of Flat norm and Jaccard index with respect to  $s_{\max}$ , for different density of spikes controlled by  $t$ . One obtains similar conclusions as above where the measures  $m_0$  were fixed (here random but with a fixed density). Indeed one sees in the context of a high density  $t = 10$  that the recovery is better with high values of  $s_{\max}$  which makes sense because in this case there are spikes near the origin. Instead the recovery is better with small values of  $s_{\max}$  in the context of a low density of spikes  $t = 40$  because the initial measures are composed of 1 or 2 spikes that are far from the origin.

To conclude, in order to have the best recovery performance, if one controls the value of  $s_{\max}$  and of the  $(s_k)$ , one needs to have:

- i) a sufficiently high value of  $s_{\max}$  to discriminate close spikes near the origin.  
The closer the spikes are, the higher  $s_{\max}$  needs to be.
- ii)  $K$  large enough because if  $s_{\max}$  is large (see (II)) then  $s_2$  increases when  $K$  has a fixed value (when the  $s_k$  are chosen uniformly) which means that spikes that are far from the origin are not well captured.

In Chapter 5, one looks at the recovery of fluorescent molecules in a 3D volume. One proposes to use the MA-TIRF model (among others) to perform this recovery. The  $L^2$ -normalized discretized Laplace transform studied here is used in this framework to obtain depth information. Considering that our numerical study in 1D is characteristic of what happens for the 3D problem along the  $z$ -axis, one deduces that:

- i) the typical distance (in  $z$ ) between two structures near the origin (the interface) that one aims to recover determine the optimal value of  $s_{\max}$  that the experimenters must choose,

- ii) the size of the domain in  $z$  (maximal depth) and the value of  $s_{\max}$  determine the optimal value of  $K$  to capture well distant fluorescent molecules.

However as one details it in Chapter 5, the experimenters have strong physical constraints on the value  $s_{\max}$  and the lower  $K$  is the better it is in practice.

## SDP Formulation of the BLASSO

In this section, we provide the SDP Formulation of the BLASSO with positivity constraint:

$$\min_{m \in \mathcal{M}(X), m \geq 0} \frac{1}{2} \|\Phi m - y\|_{\mathcal{H}}^2 + \lambda |m|(X), \quad (\mathcal{P}_\lambda^+(y))$$

when  $\Phi$  is the convolution with the Dirichlet kernel with cutoff frequency  $f_c$ :

$$\Phi : m \in \mathcal{M}(\mathbb{T}) \mapsto \int_{\mathbb{T}} \psi(\cdot - x) dm(x) \in \mathcal{H} \quad \text{where} \quad \psi(t) = \sum_{k=-f_c}^{f_c} e^{2i\pi k t},$$

where  $\mathcal{H} = L^2(\mathbb{T})$ .

The case when there is no positivity constraint is recalled in Section 4.1.1 and can be found in [30] (for the basis pursuit).

**Proposition 27.** *The SDP problem:*

$$\begin{aligned} & \min_{p \in \mathbb{R}^{2f_c+1}, Q \in \mathbb{C}^{(f_c+1) \times (f_c+1)}} \left\| \frac{y}{\lambda} - p \right\|_{\mathcal{H}}^2 \\ & \text{s.t. } Q \succeq 0, \\ & \forall k \in \{-f_c, \dots, f_c\}, \operatorname{Tr}(\Theta_k Q) = \delta_0^k - \int_0^1 p(t) e^{-2i\pi t} dt, \end{aligned}$$

is equivalent to  $\mathcal{P}_\lambda^+(y)$ . Recall that  $\Theta_k$  is the matrix with only ones at coefficient  $(i, j)$  such that  $i - j = k$  and zeros everywhere else (it is an elementary Toeplitz matrix).

*Proof.* By standard convex analysis tools, the dual problem of  $\mathcal{P}_\lambda^+(y)$  is equivalent to the problem:

$$\min_{p \in \mathcal{H}, \Phi^* p \leq 1} \left\| \frac{y}{\lambda} - p \right\|_{\mathcal{H}}^2.$$

$1 - \Phi^* p$  can be seen as a trigonometrical polynomial. Indeed there exists  $R(z) = \sum_{k=-f_c}^{f_c} r_k z^k$  with  $r_k = r_{-k} \in \mathbb{R}$  such that:

$$\forall x \in \mathbb{T}, \quad 1 - \Phi_x^* p = R(e^{2i\pi x}).$$

By [52] (Theorem 2.5),  $R \geq 0$  on the unit circle if and only if there exists a positive semi-definite matrix  $Q \in \mathbb{C}^{(f_c+1) \times (f_c+1)}$  such that:

$$\forall k \in \{-f_c, \dots, f_c\}, r_k = \operatorname{Tr}(\Theta_k Q).$$

Since  $r_k = \delta_0^k - \int_0^1 p(t) e^{-2i\pi t} dt$  one deduces the expected result.  $\square$

## Chapter 5

# Super-Resolution Microscopy

Imaging cells at a protein level is a major goal in modern Biology. This challenge requires an imaging process capable of providing a high resolution both laterally and in depth (of the order of 20 nm). Some methods such as PALM (Photo-Activated Localization Microscopy) or STORM (Stochastic Optical Reconstruction Microscopy) already achieve a typical 20 nm but only laterally. We propose to use the SFW algorithm to solve the BLASSO for three different 3D models combining the PALM/STORM technique with three different ways which enable the recovery of depth information: the MA-TIRF (Multi-Angle Total Internal Reflection Fluorescence microscopy), Astigmatism and Double-Helix models. We detail the forward operators for these models. MA-TIRF is based on a Laplace transform for the recovery of depth information. Instead, Astigmatism distorts a 2D Gaussian along the horizontal and vertical axis. And finally Double-Helix consists in the rotation of two Gaussians with the depth. In the particular case of the PALM+Astigmatism and PALM+Double-Helix, we formulate a mathematical framework that can deal with several camera mounted in parallel and acquiring data from several different focal planes at the same time (increasing the total amount of information gathered with respect to the standard case of one focal plane). We design a setup close of the one encountered by experimenters and we show in this context that the SFW algorithm achieves a resolution in all directions lower than 20 nm for the three models, even at a high density of spikes. We demonstrate that the performance plateaus at 4 TIRF angles or 4 focal planes. The model that has the highest performance in this framework is PALM+Double-Helix followed by PALM+MA-TIRF and finally PALM+Astigmatism.

## 5.1 Introduction

### 5.1.1 Classical Microscopy

The ability to recover high resolution images from blurred and noisy measurements is a difficult challenge in imaging sciences such as in astronomy, medicine or geophysics. For example in Biology, key events in cellular trafficking occur at the cell surface and high resolution images are needed to capture them.

However, classical techniques of microscopy which use an optical microscope are all limited by the Abbe diffraction limit. Indeed Ernst Abbe discovered at the end of the nineteenth century, see [1], that a point source of light visualized through an optical microscope makes a spot of radius:

$$r = \frac{\lambda_\ell}{2NA} \quad \text{with} \quad NA = n \sin(\alpha),$$

where  $\lambda_\ell$  is the wavelength of the light, NA is the numerical aperture of the microscope,  $n$  is the index of refraction of the medium being imaged in, and  $\alpha$  is the half-angle subtended by the optical objective lens. Because the numerical aperture of most modern optical systems are around 1.5, the resolution limit is of the order of 200 nm. This limit affects methods such as classical *widefield microscopy* where the whole sample is permanently illuminated or *confocal laser scanning microscopy*, invented by Marvin Minsky, where the light (usually a laser) is focussed on the sample, resulting in a slightly better resolution than widefield microscopy (see [115]). This diffraction phenomenon is not a problem when observing cells whose sizes vary from 1  $\mu\text{m}$  to 100  $\mu\text{m}$ . But to capture events involving viruses or proteins, biologists need a resolution of the order of 10 nm. That is why the development of new solutions of acquisition, which enable to see details below the diffraction limit, is an important milestone.

### 5.1.2 Overcome the Diffraction Limit

In the 2000's, several new acquisition methods were proposed. They provide ways to go below the diffraction limit. They are based on *fluorescence microscopy* which was already widely used in Biology with classical widefield and epifluorescence microscopy or with a confocal laser scanning microscope. Fluorescence microscopy depends on the fluorescence property of some chemical compound called *fluorophore* that is within the sample (either artificially added or naturally present). A source of light (usually a laser) is used to switch on the fluorophores of the sample.

Based on this switching technique of the fluorescent molecules, there are two main families of methods that break the diffraction barrier [82]. The first way relies on specific illuminations, which enables to obtain features below the diffraction limit, over the sample. This approach is used in STED, GSD, SIM/SSIM and SPEM. One presents in the following a quick overview of the STED and SIM methods (GSD and SPEM are based on those two techniques). The second way

consists of letting individual fluorophores switch on and off stochastically in the sample and record all those events. This path is taken in PALM, FPALM, STORM, dSTORM and GSDIM.

**STED:** STimulated Emission Depletion [85, 98] invented in 1994 consists in using the physical principal of stimulated emission (see [60, 61]) by lighting the sample with a first laser beam which activates the fluorophores and a second red-shifted laser beam projected to a doughnut-shape. The second laser beam depletes the emission of the fluorophores laterally leaving only a central spot with a size below the diffraction limit (see Figure 5.1). The typical lateral resolution for living cells is 20 to 30 nm [119, 120, 118]. See Figure 5.2 for an illustration of the gains in resolution between an acquisition using STED and a classical widefield microscope. Note that a similar strategy is used in the GSD [81] method.

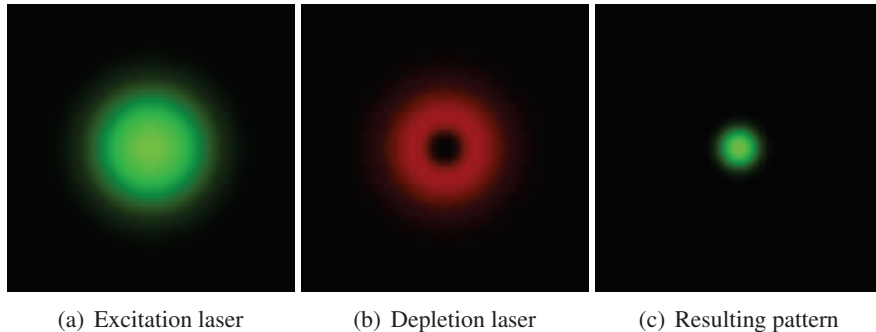


Figure 5.1: Principle of a STED microscope. Diffraction spot produced by the excitation laser (a), the red-shifted depletion laser (b) and the smaller resulting diffraction spot (c). The colors are indicative. In practice the two beams are both in the red spectrum of light.

**SIM:** Structured Illuminated Microscopy [76], invented in 2000, is a widefield technique in which a movable diffraction grid is inserted into the activation beam path. The sample is illuminated with a sequence of excitation light patterns that interfere with the grid at the focal plane of the objective and create an illumination in stripes. The overlap between the high frequency organization of the objects within the sample and the high frequency of the illumination stripes creates a lower frequency signal which can now be captured by the objective. To reconstruct the final image, several raw images must be acquired by translating and rotating the diffraction grid. The typical lateral resolution obtained with this method is 100 nm. Further improvements of the methods with SPEM [80] (Saturated Pattern Excitation Microscopy) and SSIM [71] (Saturated Structured Illuminated Microscopy) give a 50 nm lateral resolution. See Figure 5.3 for an illustration of the gains in resolution between an acquisition using SIM and a classical widefield microscope.

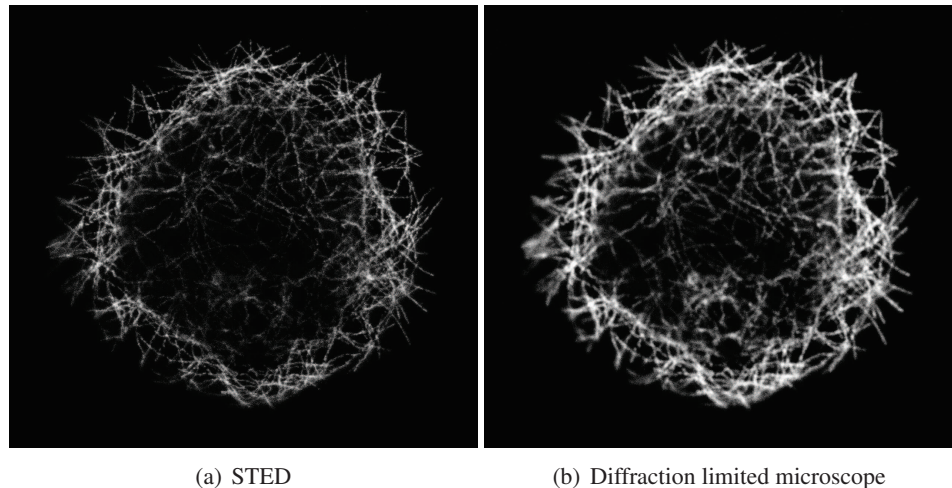


Figure 5.2: Comparison of STED versus a conventional diffraction limited microscope for the imaging of microtubules in a Drosophila S2 cell. Note the increase in spatial resolution in the STED image compared to the diffraction limited image. *Images obtained from the Cell Image Library <http://www.cellimagelibrary.org/images/36148>.*

After this quick overview of the sub-diffraction techniques based on specific illuminations of the sample, we now present sub-diffraction techniques based on a stochastic readout of the sample. Contrary to specific illuminations methods which require a fine tuning of the optical system, stochastic readout techniques are simple to implement (but note that they require more time of preparation of the samples). However as one sees below, they demand expertise to assemble the final image. This is where we aim to step in with this thesis.

**PALM/STORM:** Photoactivation Localization Microscopy (PALM) [16, 132] and Stochastic Optical Reconstruction Microscopy (STORM) [124] are two very similar techniques. They both use a TIRF (Total Internal Reflection Fluorescence) microscope (see Section 5.1.3 for more details on TIRF microscopy). They turn on and off stochastically sparse subsets of fluorophores in the sample with lasers of specific wavelengths. When individual random fluorescent molecules are activated and fluoresce, an image is recorded. A large number of images (often a few thousands), each containing just a few fluorophores, are collected. For each snapshot, a recovery is performed by solving an inverse problem thanks to some numerical method, so as to obtain the coordinates of the fluorophores. The PSF of the system can often be approximated by a 2D Gaussian, thus if the fluorophores are separated enough, the centers of the spots give a nanometer precision on the real positions of the molecules, hence the breaking of the diffraction limit. PALM/STORM can then achieve a resolution of 20 nm [16, 8, 67]. All the coordinates obtained from

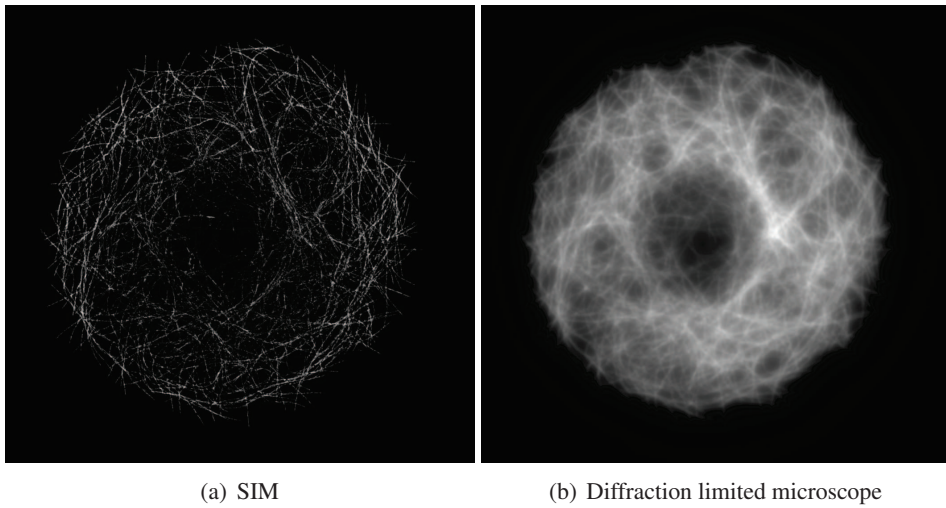


Figure 5.3: Comparison of SIM versus a conventional diffraction limited microscope for the imaging of microtubules in a Drosophila S2 cell. Note the increase in spatial resolution in the SIM image compared to the diffraction limited image. *Images obtained from the Cell Image Library <http://www.cellimagelibrary.org/images/36147>.*

all the snapshots are finally assembled to form the final super-resolved image. See Figure 5.4 for an example of an image obtained thanks to PALM.

Avoiding the accumulation of active fluorophores in time is a key point to keep a good precision. PALM uses photoactivatable protein fluorophores, for example the PA-GFP for Photoactivatable Green Fluorescent Protein (the discovery of the green fluorescent protein (GFP) [146] has been awarded a Chemistry Nobel Prize in 2008<sup>1</sup>), which are first activated by a high frequency laser (typically ultraviolet light). Once activated, they emit fluorescent light (which is captured by a CCD camera) when excited with a lower frequency laser. Then the fluorescent molecules are spontaneously photobleached (see [59] for details on photobleaching for fluorescent microscopy), *i.e.* the fluorophores once they have emitted a given amount of photons are altered such that they are permanently unable to fluoresce, to remove them from the field of view. A new sparse subset of fluorophores can then be activated and imaged, and so on. Since a fluorophore can only be activated once, PALM has the potential to perform a quantization of the number of fluorophores, see [75]. Instead STORM relies on a photo-switchable dye attached to the protein of interest thanks to antibodies binding specifically to given antigens [124]. The fluorophores are turned off by a red laser and turned on by a green laser. In particular a given fluorophore can be detected several times.

As mentioned above, we want the fluorophores of each acquisition to be separated enough in order to achieve the best precision on the localization process.

<sup>1</sup>[https://www.nobelprize.org/nobel\\_prizes/chemistry/laureates/2008/](https://www.nobelprize.org/nobel_prizes/chemistry/laureates/2008/)

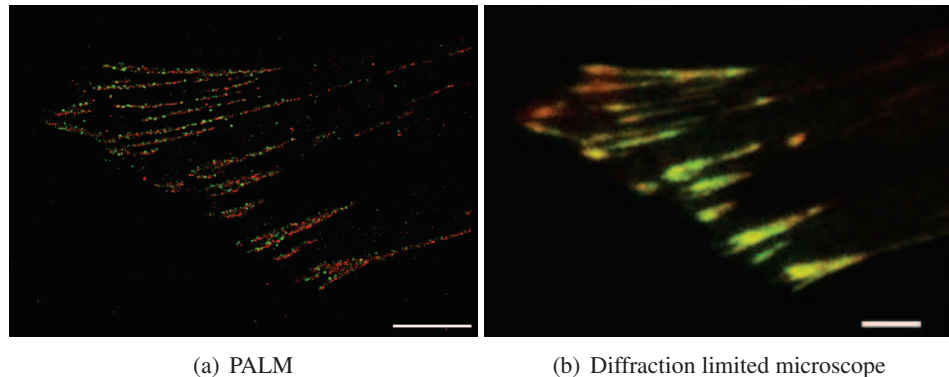


Figure 5.4: Comparison of PALM versus a classical diffraction limited microscope for the imaging of two proteins : tdEos-paxillin (green) and PsCFP20-zyxin (red). It demonstrates that these two focal adhesion proteins have very little overlap when visualized with super-resolution. In contrast, when the same field is visualized with a diffraction limited method, the two proteins appear almost completely colocalized. Bar is 2 microns. *Images obtained from the Cell Image Library <http://www.cellimagelibrary.org/images/38602>.*

However, from time to time, two or more fluorophores can be closer to each other than the size of the PSF of the system. Furthermore, to obtain a detailed final image composed of the stacking of all the recovered fluorophores, one needs to take several thousands of snapshots. Therefore being able to accurately locate more and more fluorescent molecules per activation improves the temporal resolution of the acquisition which is a key factor for imaging rapidly occurring events in Biology. But more fluorophores per snapshot means again more chance of overlapping diffraction spots hence a more challenging inverse problem to solve. That is why PALM/STORM require high performance numerical methods to improve the spatial and temporal resolution (see for example [73] for a method using the CEL0 penalty). The *Single Molecule Localization Microscopy* (SMLM) contest<sup>2</sup> compares different algorithms to locate the fluorescent molecules. One of the main goals of this thesis is, after studying theoretically the super-resolution problem in Chapter 1 and Chapter 3, to provide such a numerical method to tackle these problems. In Chapter 4, we presented a grid-less greedy algorithm to solve the BLASSO inverse problem. In the following, we propose to use this algorithm for the PALM + MA-TIRF model (see Section 5.1.3 for details on MA-TIRF).

To conclude this section, note that there are others methods based on a stochastic readout. FPALM (Fluorescence PALM), see [87], is similar to PALM but uses, instead of a TIRF microscope, a classical confocal microscope. dSTORM (direct STORM), see [79], is a simplified version of STORM (it enables to use conventional photo-switchable fluorescent dyes). GSDIM (Ground State Depletion fol-

<sup>2</sup><http://bigwww.epfl.ch/smlm>

lowed by Individual Molecule return), see [68, 139], is similar to GSD but uses a stochastic readout.

### 5.1.3 Axial Resolution, TIRF and MA-TIRF

So far, we have only discussed about lateral resolution but when looking at a sample, the information is in a 3D volume. Conventional microscopes (widefield, confocal...) have a typical axial resolution of 400 to 700 nm [83, 108] which is, similarly to the 200 nm barrier for lateral resolution of such methods, a important limitation for the imaging of complex living cells phenomena. We have seen in Section 5.1.2 that methods such as STED, PALM or STORM break the diffraction limit and achieve resolutions as small as 20 nm. However these methods offer little improvements of the axial resolution.

To get 3D information on the sample, one can make the PSF dependent of the axial variable and/or take data from several focal planes at the same time. For example, a 3D adaptation of the FPALM method [95] gives a 30 nm lateral resolution and 75nm axial resolution over a range of 800 nm. The authors obtain this improvement in depth resolution by gathering data from two focal planes at the same time and distant of each other of 500 nm. Another method based on PALM, which enables the recovery of axial information can be found in [121]: a double-helix point spread function is used and consists of two spots in the image plane whose angular orientation rotates with the axial position of the fluorophore. It gives a 20 nm depth resolution. In [90], the authors make a 3D adaptation of the STORM method by using optical astigmatism *i.e.* they analyze the ellipticity of the diffraction-limited image which encodes the depth of molecules. They achieve an image resolution of 20 to 30 nm in the lateral dimensions and 50 to 60 nm in the axial dimension. For 3D-STED, in [84] the authors obtained an axial resolution of 30 to 40 nm.

PALM and STORM both use a TIRF (Total Internal Reflection Fluorescence) microscope [4, 5, 6]. This type of microscope can limit the activation of fluorophores to only a small layer of the sample with a dimension inferior to the wavelength. This reduces the background fluorescence compared to classical widefield and confocal microscopes, hence leading to a better signal to noise ratio. In the following, we explain how a TIRF microscope works and how the Multi-Angle TIRF (MA-TIRF) [126, 21] is a method capable, when used in combination with PALM or STORM techniques, of recovering images with both high lateral resolution and high axial resolution. In Section 5.2, we detail the mathematical models that one considers for the PALM + MA-TIRF method along with PALM + Astigmatism and PALM + Double-Helix. In Section 5.3, we compare the recovery performance of fluorophores randomly selected on a generated microtubule structure for these three models when solving the BLASSO by using the numerical method detailed in Chapter 4.

**TIRF:** In a TIRF (Total Internal Reflection Fluorescence) microscope, the incident beam (or excitation beam) first travels through the glass slide. One denotes by

$n_i$  the refractive index of this media. Then the beam goes inside the sample (a cell for example) and we denote by  $n_t$  its refractive index. In this thesis we choose:

$$n_i = 1.515 \quad \text{and} \quad n_t = 1.333, \quad (5.1.1)$$

which correspond respectively to typical indexes for glass and water.

By the Snell-Descartes laws, we know that the incidence angle  $\alpha_i$ , the refraction angle  $\alpha_t$  and the reflection angle  $\alpha_r$  satisfy the following relationships:

$$n_t \sin \alpha_i = n_i \sin \alpha_t \quad \text{and} \quad \alpha_i = \alpha_r. \quad (5.1.2)$$

Let us define the *critical angle*  $\alpha_c$  as:

$$\alpha_c \stackrel{\text{def.}}{=} \arcsin \left( \frac{n_t}{n_i} \right). \quad (5.1.3)$$

It is well defined because here  $n_t < n_i$ , and it corresponds to a refraction angle  $\alpha_t = \frac{\pi}{2}$ . This angle is the angle of incidence above which the *total internal reflection* phenomenon occurs. When  $\alpha_i < \alpha_c$ , a fraction of the incident light travels through the sample with an angle  $\alpha_t$  and the rest is reflected inside the incident media with an angle  $\alpha_r$  according the Snell-Descartes laws. When  $\alpha_i \geq \alpha_c$ , all the incident light is reflected and inside the sample an evanescent wave appears, starting at the interface between the two media and propagating in parallel to the interface. See Figure 5.5.

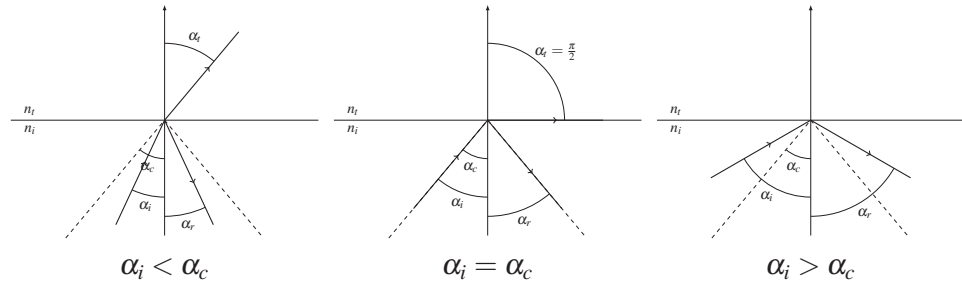


Figure 5.5: Refraction and reflection of an incident light beam according to three different values of  $\alpha_i$ , when  $n_t < n_i$ . When  $\alpha_i > \alpha_c$ , all the incident light is reflected: this corresponds to the total internal reflection phenomenon used in a TIRF microscope.

A TIRF microscope operates when the total internal reflection phenomenon is valid *i.e.*  $\alpha_i \geq \alpha_c$ . A mirror galvanometer deflects the excitation laser and enables to choose the incident angle  $\alpha_i$ . A prism or an objective [6] is used to focus the incident beam on the sample. The angle at which the laser hits the prism or the objective is directly linked to the incident angle  $\alpha_i$ . As a result, when using an objective to focus the light on the sample, one cannot obtain incident angles  $\alpha_i$

greater than a given  $\alpha_{\max}$  defined by the numerical aperture NA of the objective:

$$\alpha_{\max} = \arcsin\left(\frac{\text{NA}}{n_i}\right). \quad (5.1.4)$$

Figure 5.6 summarizes the principle of TIRF microscopy.

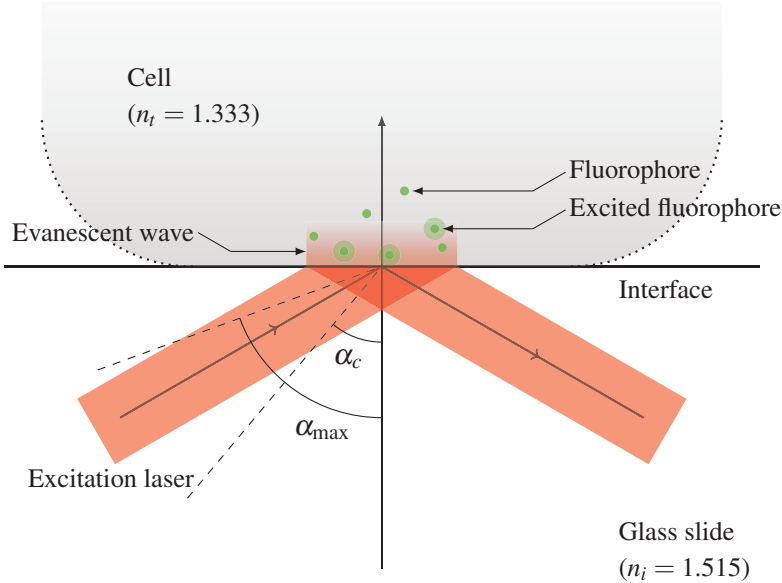


Figure 5.6: TIRF microscopy principle. An excitation laser hits the interface between the glass and the sample with an angle  $\alpha_i \in [\alpha_c, \alpha_{\max}]$ . Since  $\alpha_i \geq \alpha_c$ , all the light is reflected, an evanescent wave in the sample appears and excites some fluorophores only on a thin region located near the interface.

The intensity of the evanescent wave in the sample is given at depth  $z$  with angle  $\alpha$  by (see [6, 111, 134]):

$$I(z, \alpha) = I_0(\alpha) e^{-s(\alpha)z} \quad \text{where} \quad s(\alpha) = \frac{4\pi n_i}{\lambda_\ell} (\sin^2(\alpha) - \sin^2(\alpha_c)). \quad (5.1.5)$$

When  $s(\alpha) \ll 1$ , then  $z \mapsto I(z, \alpha)$  decreases slowly. Hence, by Equation (5.1.5), angle values  $\alpha$  close to  $\alpha_c$  leads to a slow decrease of the evanescent wave. On the contrary angles values  $\alpha$  close to  $\alpha_{\max}$  lead to a quick decrease which means that only the fluorophores localized near the interface can be visualized. Figure 5.7 shows the influence of the angle  $\alpha$  on the evanescence of the wave in the sample, the consequence on the activation of the fluorophores and along with an example of a microtubule structure generated in a 3D volume observed through a simulated TIRF microscope with different angles. Figure 5.8 shows a comparison, for the same 3D microtubule structure, of simulated views of a TIRF microscope with different angles and a classical widefield microscope taking into account the astigmatism phenomenon or with a double helix point spread function for several focal

planes. See Section 5.2 for more details on the mathematical modeling of the TIRF (MA-TIRF), Astigmatism and double helix PSF for PALM/STORM.

One sees in Figure 5.7 that varying the angle  $\alpha_i$  of the excitation laser changes what is visualized (according to the depth) through the microscope. This suggests that recording images for several angles at a time may enable to recover the axial positions of the fluorophores. This is the main principle of the MA-TIRF method.

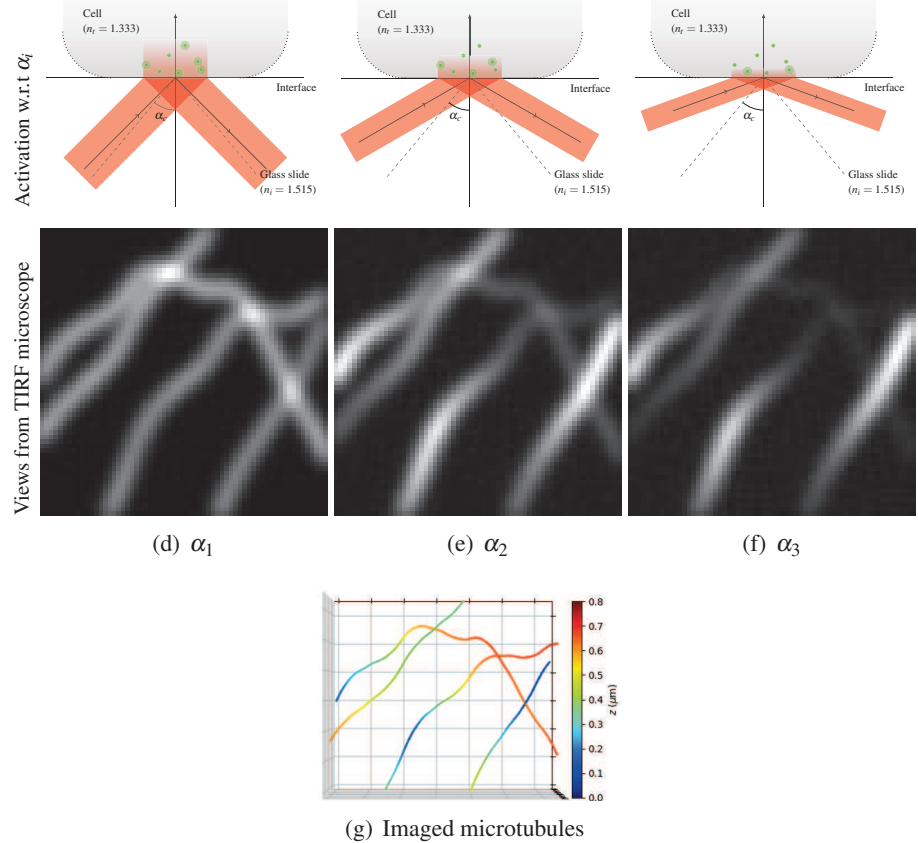


Figure 5.7: Influence of the laser beam incident angle in a (modeled) TIRF microscope on the imaging of the same microtubule structure (g) (numerically generated and composed of four filaments of width 10 nm with a depth range of 800 nm). When the incident angle is close of  $\pi/2$  (f) then only the parts of the microtubules that are near the interface are captured by the microscope. When the incident angle is close of  $\alpha_c$  (d) then all the structure is imaged. Moreover the parts of the structure near the interface have a higher light intensity (f) than when all the structure is imaged (d). This suggests that taking several angles in the acquisition process may enable the recovery of depth information (see Multi-Angle TIRF).

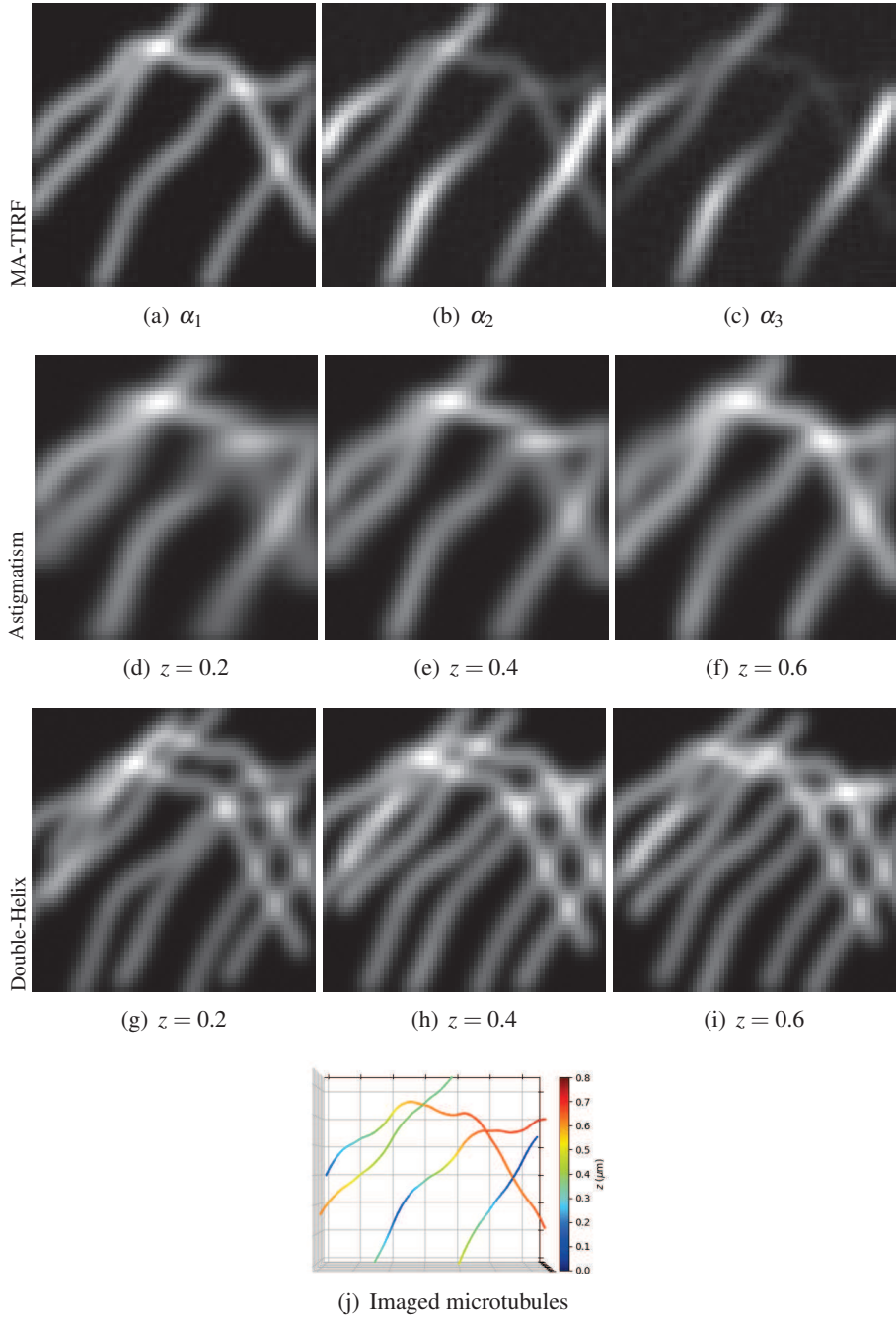


Figure 5.8: Comparison of the simulated imaging of a microtubule structure seen by three different microscopes. For MA-TIRF, the images obtained for three different angles:  $\alpha_c < \alpha_1 < \alpha_2 < \alpha_3 < \alpha_{\max}$ . For Astigmatism and Double-Helix, images obtained for three different focal planes:  $z = 0.2$ ,  $z = 0.4$  and  $z = 0.6$ . When the angles or when the focal planes change, the geometrical structures displayed also vary. This means that we may recover depth information using these data.

**MA-TIRF:** The amount of photons collected by a TIRF microscope at the  $i$ -th pixel of the observed image is proportional to the density of the fluorophores modulated by the lateral impulse response and the intensity of the axial evanescent wave (given in Equation 5.1.5), integrated over the corresponding domain in the sample. As a result, the forward operator  $\Phi_\alpha$  of a TIRF acquisition for a given incident angle  $\alpha \in [\alpha_c, \alpha_{\max}]$  can be modeled by:

$$\Phi_\alpha f \stackrel{\text{def.}}{=} \left( \int_{\Omega_i} \psi(x, y) \left( \int_0^{z_b} I(z, \alpha) f(x, y, z) dz \right) dx dy \right)_{1 \leq i \leq N_x \times N_y},$$

where:

1.  $f$  is the density of fluorophores in the sample,
2.  $\psi$  represents the lateral impulse response (typically a Gaussian) of the microscope. Because of the fast decay of the evanescent wave along  $z$ , the PSF can be assumed constant on the observed layer. Hence we model it as a 2D function,
3.  $I$  is the intensity of light of the evanescent wave in the sample with respect to the angle of the incident laser beam and the depth (see Equation 5.1.5),
4.  $\Omega_i$  is the region in the lateral plane of the sample corresponding to the  $i$ -th pixel of the image obtained thanks to the microscope,
5.  $N_x$  and  $N_y$  are the number of pixels of the observed image along respectively the  $x$ -axis and  $y$ -axis.
6.  $z_b$  defines the axial range (depth) of the sample.

One sees that depending on the decay pattern of the intensity  $I(z, \alpha)$  of the evanescent wave in the sample (which is directly linked to the incident angle  $\alpha$ , see Figure 5.7), the collected data  $\Phi_\alpha f \in \mathbb{R}^{N_x \times N_y}$  change with respect to the axial content ( $z$  axis) of the sample. This is what one observes in Figure 5.7, where only the parts of the microtubule structure near the interface are imaged by a TIRF microscope when the incident angle  $\alpha$  is close of  $\alpha_{\max}$  whereas all the structure is imaged when  $\alpha$  is close of  $\alpha_c$ .

This means that if one considers a set of  $K \in \mathbb{N}^*$  angles

$$\mathcal{A} = \{\alpha_1, \dots, \alpha_K\} \quad \text{with} \quad \alpha_c < \alpha_1 < \dots < \alpha_K \leq \alpha_{\max},$$

then recording at the same time an image for each angles  $\alpha_k$  gives the following data:

$$\Phi f = (\Phi_{\alpha_1} f, \dots, \Phi_{\alpha_K} f) \mathbb{R}^{K \times N_x \times N_y}. \quad (5.1.6)$$

These measures may enable to recover with high precision the axial positions of the fluorophores. Here,  $\Phi$  models the forward operator for the so-called Multi-Angle

TIRF (MA-TIRF) technique. The typical depth resolution achieved by this method is 20 nm over a range of 500 to 800 nm, see [126, 21].

However this method does not give any improvements of the lateral resolution with respect to a classical microscope (because it is based on a standard optical system). The Morpheme team (CNRS/INRIA/UCA) at the Institute of Biology Val-rose (iBV), which works on MA-TIRF [136, 135] and built such a system, is currently working on combining the PALM/STORM techniques with the MA-TIRF technique (*i.e.* using the stochastic activation of sparse subset of fluorophores with a TIRF microscope) to get the best of both worlds: a sub-diffraction lateral and axial resolution of the order of 20 nm. This new technique is not yet available on the market but it is important to investigate the recovery performance of this new method when solving the BLASSO using the Sliding Frank-Wolfe algorithm (see Section 5.3) and compare the results to two other methods: PALM+Astigmatism and PALM+Double-Helix.

#### 5.1.4 Contributions

In Section 5.2, we detail a mathematical framework, close of the one encountered by experimenters, modeling the acquisition of data for the three models PALM+Double-Helix, PALM+MA-TIRF and PALM+Astigmatism. One provides the forward operators  $\Phi$  for these three cases. In the particular case of the Double-Helix and Astigmatism, one gives a formulation that deals with several cameras mounted in parallel and acquiring data in the same time from several focal planes. The number of angles in the MA-TIRF case or of focal planes is denoted  $K$ .

In Section 5.3, one uses our algorithm to solve the BLASSO for these three models in the designed framework of Section 5.2, providing a new way (grid-less approach) to tackle this 3D problem. One shows that the best performance is attained by the PALM+Double-Helix model followed by the PALM+MA-TIRF model and finally the PALM+Astigmatism model. The peak performance is attained in all cases when  $K = 4$ . For the Double-Helix and Astigmatism, we show that considering at least two focal planes ( $K = 2$ ) instead of one (standard in the literature) improves significantly the recovery performance. The resolution attained for both models is under 20 nm in all dimensions.

## 5.2 Modelling of the 3D recovery problem

In this section we explore the mathematics behind the data obtained through three different models of acquisition for optical systems based on a stochastic read-out (PALM/STORM, see Section 5.1.2 for more details), for the 3D recovery problem of fluorophores with a resolution under the diffraction limit.

Using the Sliding Frank-Wolfe algorithm, one wants to solve the BLASSO:

$$\min_{m \in \mathcal{M}(X)} \frac{1}{2} \|\Phi m - y\|_{\mathcal{H}}^2 + \lambda |m|(X),$$

where  $y = \Phi m_{a_0, \bar{x}_0} + w$ , in the case of the PALM+MA-TIRF, PALM+Astigmatism and PALM+Double-Helix models. As a result we need to define:

1.  $X$  and  $m_{a_0, \bar{x}_0}$  are defined in details in Section 5.2.1 where we explain how we generate the ground-truths (*i.e.* the initial measures  $m_{a_0, \bar{x}_0}$ ) that one wants to recover using the algorithm,
2.  $\mathcal{H}$  and  $\Phi$  the forward operator for the three models, detailed in Section 5.2.2,
3.  $w$  the noise on the data, detailed in Section 5.2.3.

### 5.2.1 Model of Generation of Spikes

A typical example of structures that the biologists want to image under the diffraction limit is structures composed of microtubules, which are protein filaments and are the base components of the cytoskeleton of eukaryotic cells. The diameter of a microtubule is around 25 nm, therefore imaging methods such as PALM/STORM which offer a lateral resolution of 20-30 nm seem particularly appropriate. Figure 5.9 shows an example of microtubules in a living cell.

One wants to compare PALM + MA-TIRF with PALM + Astigmatism and PALM + Double-Helix when solving the BLASSO using the Sliding Frank-Wolfe algorithm, for the recovery of fluorophores in a 3D volume. Therefore we propose to use the same numerically generated microtubules structure and try to recover it with all three models and measure various metrics to make comparisons (see Section 5.3 for the numerical results and Section 4.3.2 for more details on the metrics used). Figure 5.10 shows the filaments that we use in the following to generate random sets of spikes.

Let us introduce some notations to detail how the filaments structure of Figure 5.10 is numerically generated and how we produce the initial measures we try to recover with the algorithm for the three models. One denotes by:

$$X = [0, x_b] \times [0, y_b] \times [0, z_b] \subset \mathbb{R}^3 \quad \text{where } x_b = y_b = 6.4, z_b = 0.8,$$

the set where the positions of the spikes (or fluorophores) lie.  $X$  corresponds to the sample being imaged. The unit used here is the micrometer, thus this means that

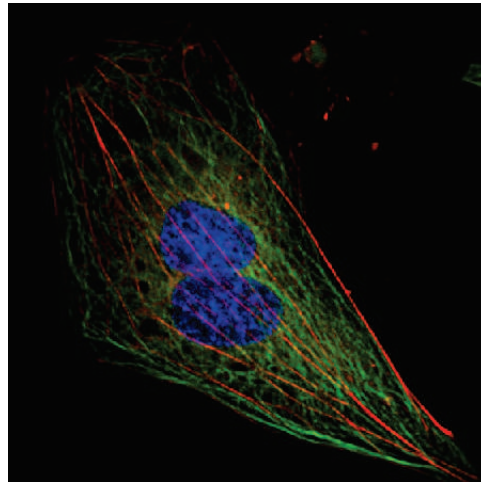


Figure 5.9: Microtubules (in green) and actin microfilaments (in red) of a U2OS human osteosarcoma cell. The typical diameter of a microtubule is 25 nm. *Image obtained from the Cell Image Library, <http://www.cellimagelibrary.org/images/7756>.*

the depth range is 0 to 800 nm. This choice of dimensions for the domain  $X$  ties in with real life applications and datasets used for the Single-Molecule Localization Microscopy challenge, see <http://bigwww.epfl.ch/smlm/challenge2016/index.html?p=datasets>.

The filaments of Figure 5.10 are obtained by scattering many points randomly uniformly sampled along four curves parametrized by polynomial equations. To ensure that the points are equidistributed along the curves, we first parametrize each curve by a piecewise linear function (with very small steps) which is in turn parametrized by the arc length. Finally, in order to give a width to the filaments, each point  $(x, y, z)$  randomly chosen on one of the curves is replaced by a point randomly chosen in a ball of center  $(x, y, z)$  and of radius 0.01 (*i.e.* 10 nm). This gives the diameter of 20 nm for the microtubules showed in Figure 5.10.

An acquisition of the filaments structure of Figure 5.10 for each of the 3D models corresponds to the imaging, using the different PSF (see Section 5.2.2), of every of the  $n \in \mathbb{N}^*$  sparse set of spikes randomly chosen on the microtubules. This process models the stochastic activations of sparse subsets of fluorophores in the sample and the recording of the snapshots. Each sparse set of spikes is modeled by a Radon measure composed of a sum of Dirac masses with positive amplitudes:

$$m_{a_0, \bar{x}_0} = \sum_{i=1}^N a_{0,i} \delta_{\bar{x}_{0,i}} \quad \text{where} \quad a_{0,i} > 0 \quad \text{and} \quad \bar{x}_{0,i} = (x_{0,i}, y_{0,i}, z_{0,i}) \in X.$$

Here we make the assumption that each sparse set of spikes, *i.e.* each  $m_{a_0, \bar{x}_0}$ , is composed of the same number  $N \in \mathbb{N}^*$  of Dirac masses (of course the algorithm has only access to the observations *i.e.*  $y = \Phi m_{a_0, \bar{x}_0} + w$  and not to the value  $N$ ). In

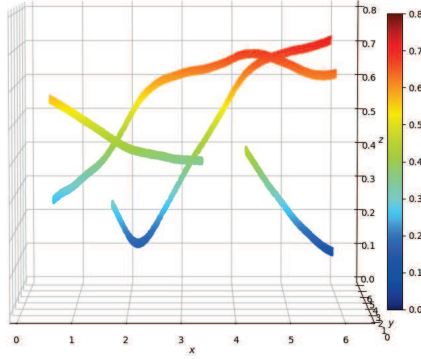


Figure 5.10: Microtubules structure used to generate the ground truths for the comparisons of the three different models. The diameter of the filaments is 20 nm.

general this number is not always the same and instead varies around a given value depending on the power of the excitation laser beam. In Section 5.3, we measure the recovery performance for several values of  $N$  (for the three models) to see the influence of the density of fluorophores. As already explained in Section 5.1.2, an imaging technique based on a stochastic readout which enjoys good recovery performance for a high density of fluorophores on each snapshots results in an improvement of the temporal resolution of the acquisition (which is a key factor for imaging rapidly occurring events in Biology). Figure 5.11 shows an example of an initial measure  $m_{a_0, \bar{x}_0}$  randomly chosen on the filaments structure and used as a ground-truth.

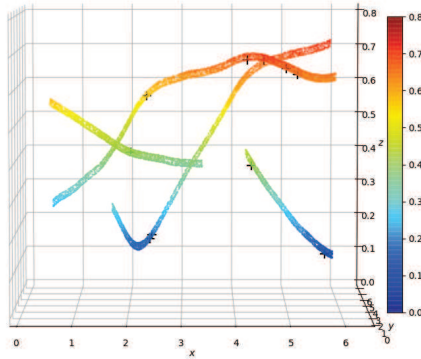


Figure 5.11: Microtubules structure used to generate the ground truths for the comparisons of the three different models with an initial measures  $m_{a_0, \bar{x}_0}$  randomly chosen on it (black cross).

To summarize this section, for each value of  $N$  we generate a set  $\mathcal{M}_0$  of  $n$  measures  $m_{a_0, \bar{x}_0}$ , each composed of  $N$  spikes, randomly chosen on the microtubules

structure of Figure 5.10. The set  $\mathcal{M}_0$  is used, for every of the three models that one wants to compare, to generate the snapshots (*i.e.* the  $\Phi m_{a_0, \bar{x}_0} + w$ ) obtained thanks to their respective PSF and used as the inputs of the Sliding Frank-Wolfe algorithm.

Now that we have our initial measures  $\mathcal{M}_0$ , we need to detail how we compute the forward operators  $\Phi$ .

### 5.2.2 Forward Operators

In this section, we define the forward operators  $\Phi$  for the three models. One has:

$$\forall m \in \mathcal{M}(X), \quad \Phi m = \int_X \varphi(x, y, z) dm(x, y, z).$$

The operator  $\Phi$ , for the three models, is built upon the 2D case where only the variables  $(x, y)$  matter. Therefore let us first study this particular setting.

**$\Phi$  in the 2D case.** This setting corresponds to the well-known PALM/STORM setup. In this setup, the PSF of the system is often approximated by a 2D Gaussian with variance  $\sigma_x^2$  and  $\sigma_y^2$  (for respectively the  $x$ -axis and the  $y$ -axis). Hence one can write:

$$\forall m \in \mathcal{M}(X), \quad \Phi m = \left( p \in \mathbb{R}^2 \mapsto \int_X \psi(p - (x, y)) dm(x, y) \right) \in L^2(\mathbb{R}^2),$$

where for all  $(s, t) \in \mathbb{R}^2$ :

$$\psi(s, t) = \psi_x(s) \psi_y(t) \quad \text{with} \quad \psi_x(s) = \frac{1}{\sqrt{2\pi\sigma_x^2}} e^{\frac{-s^2}{2\sigma_x^2}} \quad \text{and} \quad \psi_y(t) = \frac{1}{\sqrt{2\pi\sigma_y^2}} e^{\frac{-t^2}{2\sigma_y^2}},$$

So  $\Phi$  is a Gaussian convolution in 2D. In order to manipulate  $\Phi m$  with a computer, one integrates the PSF over the camera pixels.

**$\Phi$  in the 2D sampled case.** Let us denote  $N_x$  and  $N_y$  respectively the number of pixels of the camera along the  $x$ -axis and the  $y$ -axis. One considers:

$$\begin{aligned} \forall 1 \leq i \leq N_x, \quad x_i &= \frac{1}{2N_x} + (i-1) \frac{x_b}{N_x}, \\ \forall 1 \leq i \leq N_y, \quad y_i &= \frac{1}{2N_y} + (i-1) \frac{y_b}{N_y}, \end{aligned}$$

uniformly distributed points in  $[0, 6.4]$ , so that for  $(i, j) \in \{1, \dots, N_x\} \times \{1, \dots, N_y\}$ ,  $(x_i, y_j)$  is the center of the domain in the sample corresponding to the pixel  $(i, j)$  of the camera. Thus we consider that the value recorded by the camera for the pixel  $(i, j)$ , *i.e.*  $(\Phi m)_{(i,j)}$ , is the integral of  $p \in \mathbb{R}^2 \mapsto \int_X \psi(p - (x, y)) dm(x, y)$  over the domain  $[x_i - \frac{1}{2N_x}, x_i + \frac{1}{2N_x}] \times [y_j - \frac{1}{2N_y}, y_j + \frac{1}{2N_y}]$ .

As a result, the forward operator  $\Phi$  in the 2D case is  $\Phi m = \int_X \varphi(x, y) dm(x, y)$  where:

$$\varphi(x, y) = (\psi_x(x_i - x) \psi_y(y_i - y))_{(i,j) \in \{1, \dots, N_x\} \times \{1, \dots, N_y\}} \in \mathbb{R}^{N_x \times N_y}.$$

where for all  $(s, t) \in \mathbb{R}^2$ :

$$\begin{aligned}\psi_x(s) &= \frac{1}{2} \left( \operatorname{erf} \left( \frac{s + \frac{1}{2N_x}}{\sqrt{2}\sigma_x} \right) - \operatorname{erf} \left( \frac{s - \frac{1}{2N_x}}{\sqrt{2}\sigma_x} \right) \right), \\ \psi_y(t) &= \frac{1}{2} \left( \operatorname{erf} \left( \frac{t + \frac{1}{2N_y}}{\sqrt{2}\sigma_y} \right) - \operatorname{erf} \left( \frac{t - \frac{1}{2N_y}}{\sqrt{2}\sigma_y} \right) \right),\end{aligned}$$

with  $\operatorname{erf} \stackrel{\text{def.}}{=} \frac{2}{\sqrt{\pi}} \int_0^s e^{-t^2} dt$ .

Now that we have defined a forward operator in the 2D case, in the following we add a particular  $z$  dependency to  $\varphi$  for each of the three 3D models.

**$\Phi$  for the PALM + MA-TIRF model.** Following what was presented in Section 5.1.3, we combine the MA-TIRF setup with the PALM/STORM technique to recover 3D information. The forward operator of this model is based on the forward operator presented in the previous paragraph for the recovery of information in the  $(x, y)$  plane (integration of a Gaussian convolution over the camera pixel domains) and on a normalized discretized Laplace transform, presented in Section 4.3.1, in the  $z$  axis for the recovery of depth information. More precisely, we have:

$$\forall m \in \mathcal{M}(X), \quad \Phi m = \int_X \varphi(x, y, z) dm(x, y, z),$$

where:

$$\varphi(x, y, z) = (\psi_x(x_i - x) \psi_y(y_i - y) \psi_k(z))_{(i,j,k) \in \{1, \dots, N_x\} \times \{1, \dots, N_y\} \times \{1, \dots, K\}} \in \mathbb{R}^{N_x \times N_y \times K}.$$

with for all  $k \in \{1, \dots, K\}$  and for all  $z \in [0, z_b]$ :

$$\psi_k(z) = \xi(z) e^{-s_k z} \quad \text{with} \quad \xi(z) = \left( \sum_{k=1}^K e^{-2s_k z} \right)^{-1/2}.$$

Note that we consider here a normalized Laplace transform even if the data acquired through the experimental setup, see Equation (5.1.6), are not normalized. This is theoretically and numerically justified in Section 4.4.1.

The values of the  $(s_k)_{k \in \{1, \dots, K\}}$  are obtained according to Equation (5.1.5):

$$s_k = \frac{4\pi n_i}{\lambda_\ell} (\sin^2(\alpha_k) - \sin^2(\alpha_c)),$$

where the  $\alpha_k$  are the incident angles of the excitation laser (see Figure 5.6):

$$\mathcal{A} = \{\alpha_1, \dots, \alpha_K\} \quad \text{with} \quad \alpha_c < \alpha_1 < \dots < \alpha_K \leq \alpha_{\max}.$$

One remarks that because  $\alpha_K \leq \alpha_{\max}$ , the values taken by the  $s_k$  are upper bounded by the positive constant:

$$\frac{4\pi n_i}{\lambda_\ell} (\sin(\alpha_{\max})^2 - \sin(\alpha_c)^2).$$

As mentioned in Section 4.4.2, it restricts the ability to recover spikes that are aligned on the  $z$ -axis (same  $(x, y)$ ) near the interface *i.e.*  $z$  small. This observation is confirmed by our 3D numerical experiments, see Section 5.3.

*Remark 7.* On a numerical standpoint, it is worth noting that the kernel  $\varphi$  is separable in the variables  $x, y, z$ , which is not the case for the PALM+Astigmatism and PALM+Double-Helix (see the next paragraphs). This can be advantageously used in the code to reduce the overall complexity.

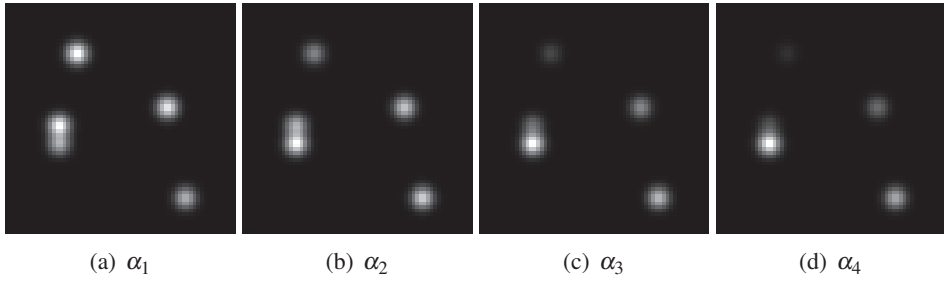


Figure 5.12:  $y_0 = \Phi m_{a_0, \bar{x}_0}$  when  $K = 4$  for the PALM+MA-TIRF model with the constants of table 5.13 and  $m_{a_0, \bar{x}_0}$  given in (5.2.1).

Names	Values	Names	Values
$\sigma_x = \sigma_y$	0.186	NA	1.49
$N_x = N_y$	64	$n_i$	1.515
$x_b = y_b$	6.4	$n_t$	1.333
$z_b$	0.8	$\lambda_\ell$	0.66

Figure 5.13: Numerical constants used in all Chapter 5. They correspond to typical real-life experimental values. For  $\sigma_x, \sigma_y, x_b, y_b, z_b, \lambda_\ell$  the unit the micrometer ( $10^{-6}m$ ).

Figure 5.12 shows the data ( $y_0 = \Phi m_{a_0, \bar{x}_0}$ ) when  $K = 4$  and for the numerical constants given in the table of Figure 5.13. The initial measure considered is:

$$m_{a_0, \bar{x}_0} = \delta_{(1.5, 2.5, 0.1)} + \delta_{(1.5, 3, 0.5)} + \delta_{(2, 5, 0.7)} + \delta_{(4.5, 3.5, 0.4)} + \delta_{(5, 1, 0.2)}. \quad (5.2.1)$$

The angles  $\alpha_1 < \alpha_2 < \alpha_3 < \alpha_4$  are taken uniformly such that  $\alpha_4 = \alpha_{\max}$  and  $\alpha_1 > \alpha_c$  is very close of  $\alpha_c$ . One remarks, as already mentioned, that the spikes far from the interface (here  $\delta_{(1.5, 3, 0.5)}$  and  $\delta_{(2, 5, 0.7)}$ ) are only visible for values of  $\alpha$  close of

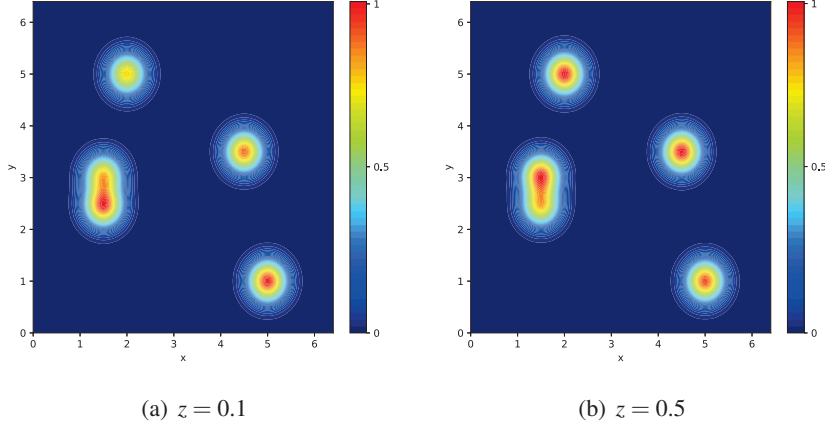


Figure 5.14:  $\eta_V$  for the PALM+MA-TIRF model for  $m_{a_0, \bar{x}_0}$  given in Equation (5.2.1).

$\alpha_c$  (here  $\alpha_1$  and  $\alpha_2$ ) because of the exponential decay. In addition, for angles close of  $\alpha_{\max}$  (here  $\alpha_3$  and  $\alpha_4$ ) only the spikes near the interface are visible.

Figure 5.14 shows  $\eta_V$  for the measure given in Equation (5.2.1) at  $z = 0.1$  and  $z = 0.5$ . One sees that  $\eta_V(1.5, 2.5, 0.1) = \eta_V(1.5, 3, 0.5) = 1$  and is otherwise smaller than 1.  $\eta_V$  is non-degenerate so that one can recover in a low noise regime using our algorithm a measure composed of the same number of Dirac masses as  $m_{a_0, \bar{x}_0}$  (see Theorem 6).

**Φ for the PALM + Astigmatism model.** One now details the forward operator of the PALM+Astigmatism model. To recover depth information, this model considers a deformation along the  $x$  and  $y$  axis of a 2D Gaussian with respect to  $z$ . More precisely, we have:

$$\varphi(x, y, z) = (\psi_x(x_i - x, z) \psi_y(y_i - y, z))_{(i,j) \in \{1, \dots, N_x\} \times \{1, \dots, N_y\}}.$$

with for all  $(s, t) \in \mathbb{R}^2$  and for all  $z \in [0, z_b]$ :

$$\begin{aligned} \psi_x(s, z) &= \frac{1}{2} \left( \operatorname{erf} \left( \frac{s + \frac{1}{2N_x}}{\sqrt{2}\sigma_x(z)} \right) - \operatorname{erf} \left( \frac{s - \frac{1}{2N_x}}{\sqrt{2}\sigma_x(z)} \right) \right), \\ \psi_y(t, z) &= \frac{1}{2} \left( \operatorname{erf} \left( \frac{t + \frac{1}{2N_y}}{\sqrt{2}\sigma_y(z)} \right) - \operatorname{erf} \left( \frac{t - \frac{1}{2N_y}}{\sqrt{2}\sigma_y(z)} \right) \right). \end{aligned}$$

So the size of the 2D Gaussian integrated over the pixel's domains of the camera depends on  $z$ . The dependence of  $\sigma_x$  and  $\sigma_y$  on  $z$  is illustrated in Figure 5.15. It is

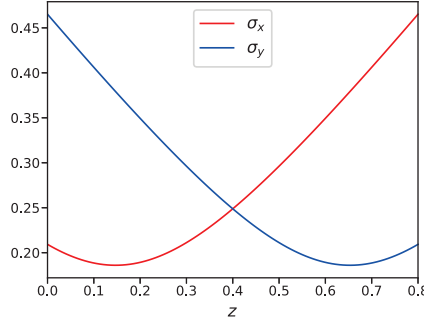


Figure 5.15:  $\sigma_x$  and  $\sigma_y$  with respect to  $z$  when  $f_p = 0.4$ .

given by the following expressions:

$$\begin{aligned}\sigma_x(z) &= \sigma_0 \sqrt{1 + \left( \frac{\alpha(z - f_p) - \beta}{d} \right)^2}, \\ \sigma_y(z) &= \sigma_x(-z + 2f_p),\end{aligned}$$

where the constants involved are given in the table of Figure 5.16. With such choice

Names	Values	Names	Values
$\sigma_0$	$\frac{0.42\lambda_\ell}{NA}$	$\alpha$	-0.79
$\beta$	0.2	$d$	$\frac{\lambda_\ell n_i}{2NA^2}$

Figure 5.16: Numerical constants used in all Chapter 5. They correspond to typical real-life experimental values. The values of  $\lambda_\ell, NA, n_i$  can be found in Figure 5.13.

of constants, one obtains that the minimum value taken by  $\sigma_x$  and  $\sigma_y$  is  $\sigma_0 \simeq 0.186$  (size of the Gaussian for the PALM+MA-TIRF model).

The kernel  $\varphi$  presented above corresponds to the classical astigmatism adjustment. It is made with respect to only one focal plane ( $f_p = 0.4$  in Figure 5.15) because there is only one camera acquiring the data. However one can imagine several cameras focalized at different focal planes and acquiring the data in the same time. This process can be thought as equivalent to acquiring the data for several angles of the excitation laser for the MA-TIRF model. The experimental setup is more difficult to install than with one camera, but it can be done: see for example [92]. One can then expect that this technique improves the recovery performance. This is indeed confirmed in our numerical results presented in Section 5.3. As a result the kernel of the forward operator, for the PALM+Astigmatism model, that we rather consider is given by:

$$\varphi(x, y, z) = (\psi_{x,k}(x_i - x, z) \psi_{y,k}(y_i - y, z))_{(i,j,k) \in \{1, \dots, N_x\} \times \{1, \dots, N_y\} \times \{1, \dots, K\}} \in \mathbb{R}^{N_x \times N_y \times K}.$$

where for all  $(s, t) \in \mathbb{R}^2$ , for all  $z \in [0, z_b]$  and for all  $k \in \{1, \dots, K\}$ :

$$\begin{aligned}\psi_{x,k}(s, z) &= \frac{1}{2} \left( \operatorname{erf} \left( \frac{s + \frac{1}{2N_x}}{\sqrt{2}\sigma_{x,k}(z)} \right) - \operatorname{erf} \left( \frac{s - \frac{1}{2N_x}}{\sqrt{2}\sigma_{x,k}(z)} \right) \right), \\ \psi_{y,k}(t, z) &= \frac{1}{2} \left( \operatorname{erf} \left( \frac{t + \frac{1}{2N_y}}{\sqrt{2}\sigma_{y,k}(z)} \right) - \operatorname{erf} \left( \frac{t - \frac{1}{2N_y}}{\sqrt{2}\sigma_{y,k}(z)} \right) \right),\end{aligned}$$

with:

$$\begin{aligned}\sigma_{x,k}(z) &= \sigma_0 \sqrt{1 + \left( \frac{\alpha(z - f_{p,k}) - \beta}{d} \right)^2}, \\ \sigma_{y,k}(z) &= \sigma_{x,k}(-z + 2f_{p,k}).\end{aligned}$$

In this case  $f_p = (f_{p,k})_{k \in \{1, \dots, K\}} \in \mathbb{R}^K$  is a vector of focal planes. In practice we take:

$$\forall k \in \{1, \dots, K\}, \quad f_{p,k} = \frac{k}{K+1} z_b.$$

Figure 5.17 shows the data ( $y_0 = \Phi m_{a_0, \bar{x}_0}$ ) when  $K = 4$  and for the numerical constants given in the table of Figure 5.13 and 5.16. The same initial measure as in the previous paragraph is considered (see Equation 5.2.1).

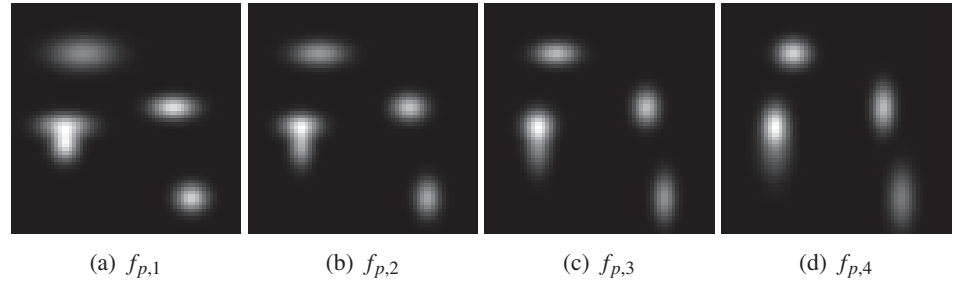


Figure 5.17:  $y_0 = \Phi m_{a_0, \bar{x}_0}$  when  $K = 4$  for the PALM+Astigmatism model with the constants of table 5.13 and 5.16, and  $m_{a_0, \bar{x}_0}$  given in (5.2.1).

One remarks that the Gaussians around the spikes are stretched in the  $x$  and  $y$  axis depending on the focal plane  $f_{p,k}$  and the depth  $z$  of the spike considered. For example, if we look at the particular spike  $\delta_{(1.5, 3, 0.5)}$  we note that the diffraction pattern centered on it forms a disk for  $f_{p,3}$ . This is because 0.5 is close of  $f_{p,3} = 0.48$  and  $\sigma_{x,3}(0.48) = \sigma_{y,3}(0.48)$  (for all  $k$ ,  $\sigma_{x,k}(f_{p,k}) = \sigma_{y,k}(f_{p,k}) = \sigma_0 \sqrt{1 + (\beta/d)^2} \simeq 0.25$ ).

Figure 5.18 shows  $\eta_V$  for the measure given in Equation (5.2.1) at  $z = 0.1$  and  $z = 0.5$ . One sees that  $\eta_V(1.5, 2.5, 0.1) = \eta_V(1.5, 3, 0.5) = 1$  and is otherwise smaller than 1. As a result,  $\eta_V$  seems non-degenerate.

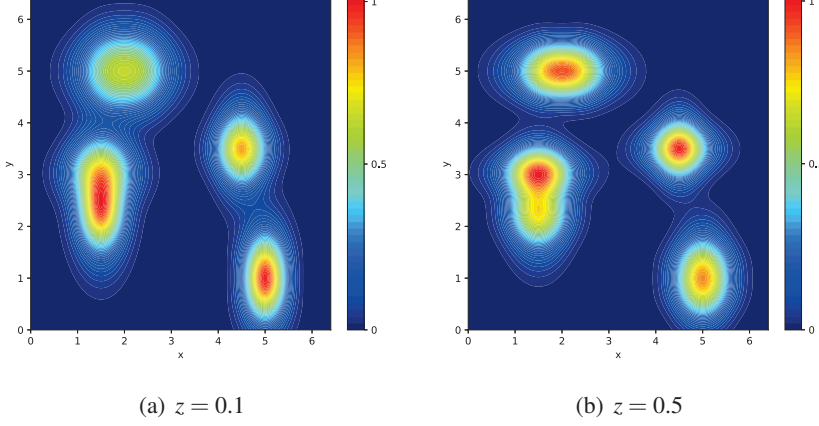


Figure 5.18:  $\eta_V$  for the PALM+Astigmatism model for  $m_{a_0, \bar{x}_0}$  given in Equation (5.2.1).

**Φ for the PALM + Double Helix model.** One now details the forward operator of the PALM+Double-Helix model. To recover depth information, this model considers a rotation controlled by  $z$  of two Gaussians offset by opposite constants. More precisely, we have:

$$\varphi(x, y, z) = (\psi_x^1(x_i - x, z) \psi_y^1(y_i - y, z) + \psi_x^2(x_i - x, z) \psi_y^2(y_i - y, z))_{(i,j)},$$

with for all  $(s, t) \in \mathbb{R}^2$  and for all  $z \in [0, z_b]$ :

$$\begin{aligned} \psi_x^1(s, z) &= \frac{1}{2} \left( \operatorname{erf} \left( \frac{s + \frac{1}{2N_x} - r_x(z)}{\sqrt{2}\sigma_x} \right) - \operatorname{erf} \left( \frac{s - \frac{1}{2N_x} - r_x(z)}{\sqrt{2}\sigma_x} \right) \right), \\ \psi_y^1(t, z) &= \frac{1}{2} \left( \operatorname{erf} \left( \frac{t + \frac{1}{2N_y} - r_y(z)}{\sqrt{2}\sigma_y} \right) - \operatorname{erf} \left( \frac{t - \frac{1}{2N_y} - r_y(z)}{\sqrt{2}\sigma_y} \right) \right) \\ \psi_x^2(s, z) &= \frac{1}{2} \left( \operatorname{erf} \left( \frac{s + \frac{1}{2N_x} + r_x(z)}{\sqrt{2}\sigma_x} \right) - \operatorname{erf} \left( \frac{s - \frac{1}{2N_x} + r_x(z)}{\sqrt{2}\sigma_x} \right) \right), \\ \psi_y^2(t, z) &= \frac{1}{2} \left( \operatorname{erf} \left( \frac{t + \frac{1}{2N_y} + r_y(z)}{\sqrt{2}\sigma_y} \right) - \operatorname{erf} \left( \frac{t - \frac{1}{2N_y} + r_y(z)}{\sqrt{2}\sigma_y} \right) \right), \end{aligned}$$

where:

$$r_x(z) = \frac{\omega}{2} \cos(\theta(z)), \quad (5.2.2)$$

$$r_y(z) = -\frac{\omega}{2} \sin(\theta(z)), \quad (5.2.3)$$

$$\theta(z) = \frac{\pi}{3} \frac{z - f_p}{z_b - f_p}. \quad (5.2.4)$$

So  $\psi_x^1(x_i - x, z) \psi_y^1(y_i - y, z)$  corresponds to a 2D Gaussian, integrated over the pixel's domains of the camera, offset by  $\omega/2$  are rotated by the angle  $\theta(z)$ .  $\psi_x^2(x_i - x, z) \psi_y^2(y_i - y, z)$  is the same thing but offset  $-\omega/2$ . Having two rotating Gaussians instead of one prevents from eventually mis-identifying the position of a spike in the  $(x, y)$  plane.

The numerical constants involved in this model can be found in the tables of Figure 5.13 and 5.19.

Name	Value
$\omega$	1

Figure 5.19: Numerical constant used in all Chapter 5. It corresponds to typical real-life experimental value.

The kernel  $\varphi$  presented above corresponds to the classical and ideal double-helix model. It is made with respect to only one focal plane because there is only one camera acquiring the data. However, similarly to in the case of the astigmatism model, one can imagine several cameras focalized at different focal planes and acquiring the data in the same time. As a result the kernel of the forward operator, for the PALM+double model, that we rather consider is given by:

$$\varphi(x, y, z) = (\psi_{x,k}^1(x_i - x, z) \psi_{y,k}^1(y_i - y, z) + \psi_{x,k}^2(x_i - x, z) \psi_{y,k}^2(y_i - y, z))_{(i,j,k)},$$

$\varphi(x, y, z) \in \mathbb{R}^{N_x \times N_y \times K}$ ,  $(s, t) \in \mathbb{R}^2$ , for all  $z \in [0, z_b]$  and for all  $k \in \{1, \dots, K\}$ :

$$\begin{aligned} \psi_{x,k}^1(s, z) &= \frac{1}{2} \left( \operatorname{erf} \left( \frac{s + \frac{1}{2N_x} - r_{x,k}(z)}{\sqrt{2}\sigma_x} \right) - \operatorname{erf} \left( \frac{s - \frac{1}{2N_x} - r_{x,k}(z)}{\sqrt{2}\sigma_x} \right) \right), \\ \psi_{y,k}^1(t, z) &= \frac{1}{2} \left( \operatorname{erf} \left( \frac{t + \frac{1}{2N_y} - r_{y,k}(z)}{\sqrt{2}\sigma_y} \right) - \operatorname{erf} \left( \frac{t - \frac{1}{2N_y} - r_{y,k}(z)}{\sqrt{2}\sigma_y} \right) \right) \\ \psi_{x,k}^2(s, z) &= \frac{1}{2} \left( \operatorname{erf} \left( \frac{s + \frac{1}{2N_x} + r_{x,k}(z)}{\sqrt{2}\sigma_x} \right) - \operatorname{erf} \left( \frac{s - \frac{1}{2N_x} + r_{x,k}(z)}{\sqrt{2}\sigma_x} \right) \right), \\ \psi_{y,k}^2(t, z) &= \frac{1}{2} \left( \operatorname{erf} \left( \frac{t + \frac{1}{2N_y} + r_{y,k}(z)}{\sqrt{2}\sigma_y} \right) - \operatorname{erf} \left( \frac{t - \frac{1}{2N_y} + r_{y,k}(z)}{\sqrt{2}\sigma_y} \right) \right). \end{aligned}$$

where:

$$\begin{aligned} r_{x,k}(z) &= \frac{\omega}{2} \cos(\theta_k(z)), \\ r_{y,k}(z) &= -\frac{\omega}{2} \sin(\theta_k(z)), \\ \theta_k(z) &= \frac{\pi}{3} \frac{z - f_{p,k}}{f_{p,K}}. \end{aligned}$$

When  $K = 1$ , one sees with Equation (5.2.4) that the rotation angle  $\theta(z)$  varies from  $-\pi/3$  to  $\pi/3$  when  $z$  goes from 0 to  $z_b$ . So the rotation amplitude is in this case  $2\pi/3$ . In the general case that we consider in this thesis (several focal planes) one sees that  $\theta_k$  is designed such that the range of rotation angles changes for every focal plane considered  $f_{p,k}$  but has always the same amplitude given by  $\frac{\pi}{3} \frac{K+1}{K}$ . Of course with this general formulation, we recover the classical model when  $K = 1$ .

Figure 5.20 shows the data ( $y_0 = \Phi m_{a_0, \bar{x}_0}$ ) when  $K = 4$  and for the numerical constants given in the table of Figure 5.13 and 5.19. The same initial measure as before is considered (see Equation 5.2.1).

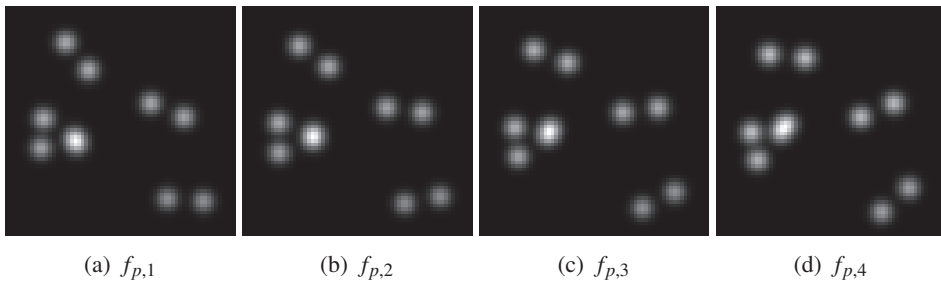


Figure 5.20:  $y_0 = \Phi m_{a_0, \bar{x}_0}$  when  $K = 4$  for the PALM+Double-Helix model with the constants of Table 5.13 and  $m_{a_0, \bar{x}_0}$  given in (5.2.1).

One sees for example by tracking the PSF produced by the spike  $\delta_{(2,5,0.7)}$ , that the two Gaussians rotate progressively throughout the different focal planes. And one remarks that they are almost horizontal for  $f_{p,4}$ . This is because  $f_{p,4} = 0.64$  is close of 0.7 and  $\theta_4(f_{p,4}) = 0$ . More generally, the two Gaussians produced by a Dirac mass appear horizontal for a given focal plane  $f_{p,k}$  if the depth of the Dirac mass is equal to  $f_{p,k}$ , because one has  $\theta_k(f_{p,k}) = 0$ .

Figure 5.21 shows  $\eta_V$  for the measure given in Equation (5.2.1) at  $z = 0.1$  and  $z = 0.5$ . One sees that  $\eta_V(1.5, 2.5, 0.1) = \eta_V(1.5, 3, 0.5) = 1$  and is otherwise smaller than 1. As a result,  $\eta_V$  seems non-degenerate.

### 5.2.3 Noise model

Now that we presented in the last section the forward models involved in this chapter, we give in this section the model of noise that corrupts the data. This model, that we detail below, is directly motivated by the experimental setup.

The noise on the data has two components:

- first a Poisson noise which comes from random emissions of photons by the excited fluorophores (shot noise). One denotes it  $\mathcal{P}(\Phi m_{a_0, \bar{x}_0}) \in \mathbb{R}^{N_x \times N_y \times K}$ , it follows a Poisson distribution whose intensity is controlled by  $n_{\text{photon}} \in \mathbb{R}_+$ , which we call the photon budget. This photon budget is distributed over each image of the sample acquired corresponding to either an angle  $\alpha_k$  (for the PALM+MA-TIRF model) or a focal plane  $f_{p,k}$  (for the PALM+Astigmatism

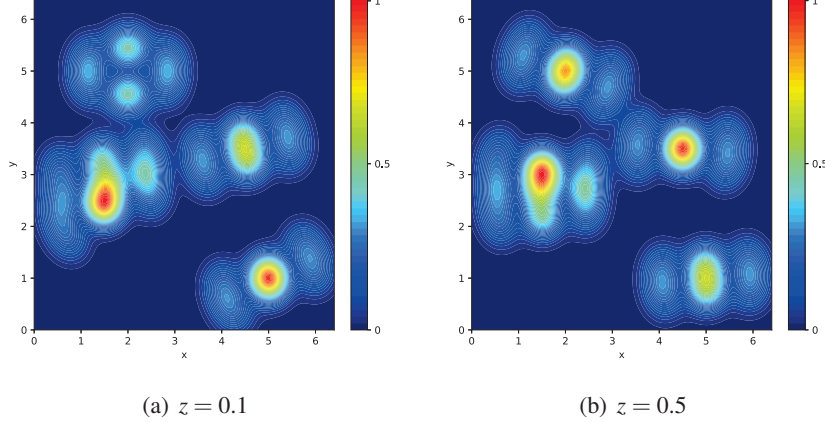


Figure 5.21:  $\eta_V$  for the PALM+Double-Helix model for  $m_{a_0, \bar{x}_0}$  given in Equation (5.2.1).

and double-helix models). As a result the greater  $K$ , the more there is Poisson noise contaminating the data.

- A Gaussian noise which comes from the camera acquiring the incoming signal. One denotes it  $w_G = \sigma w_0$  where  $w_0$  follows a centered Gaussian distribution with variance 1.  $w_G$  is in general negligible with respect to Poisson noise.

So one has:

$$y = \mathcal{P}(\Phi m_{a_0, \bar{x}_0}) + w_G.$$

Note that the noise is not additive anymore. In the next Section 5.3 where we present our numerical results for the three models detailed previously, we consider the numerical values given in the table of Figure 5.22 for the noise on the data. It corresponds to a low noise framework.

Name	Value
$n_{\text{photon}}$	1000
$\sigma$	$1e-4$

Figure 5.22: Numerical constant involved for the noise model and used in Section 5.3.

### 5.3 Numerical Results

In this section, one provides the numerical results that one obtained using our algorithm (the SFW algorithm, see Chapter 4) to solve the BLASSO in the framework of the fluorescent microscopy problem detailed in the introduction of this chapter (see Section 5.1). More precisely one wants to recover fluorophores (fluorescent molecules) in a 3D volume (the sample) for each snapshot taken (several thousands). One compares three different models of acquisition of the data (hence three forward operators  $\Phi$ ). These three models are detailed in Section 5.2, there are:

- the PALM+MA-TIRF model (abbreviated to Laplace in the following),
- the PALM+Astigmatism model (abbreviated to Astigmatism),
- the PALM+Double-Helix model (abbreviated to Double-Helix).

The use of a modified Frank-Wolfe algorithm for these 3D problems based on the PALM/STORM model has never been done before. In [22], the authors applied such an algorithm to the 2D problem and obtained state of the art numerical results (see the page of the SMLM challenge<sup>3</sup>).

One shows in the following that our algorithm applied to each of the models provides a way to achieve a sub 20 nm resolution in the  $(x,y)$  plane but also in the depth dimension  $z$ , when  $K$  is large enough ( $K = 3$  or  $K = 4$ ), even at the highest density ( $N = 15$ ). One shows that in this framework, the performance plateau at  $K = 4$ . But one also proves that it improves significantly the performance to consider at least  $K = 2$  (two focal planes) for the PALM+Astigmatism and PALM+Double-Helix models. One also shows that the PALM+Double-Helix seems to achieve the best performance overall, followed by the PALM+MA-TIRF model and finally the PALM+Astigmatism model.

One recalls that the data used in this section to produce the results are generated first by choosing randomly  $n$  measures  $m_{a_0, \bar{x}_0}$  composed of  $N$  Dirac masses distributed over a numerically generated microtubules structure (see Figure 5.10 and Section 5.2.1 for more details). The numerical constants used for the experiments, already detailed in Section 5.2, are gathered here in the table of Figure 5.23. Moreover one uses the following protocol: for each experiment, *i.e.* the choice of a model and a set of parameters  $n, N, K$ , one chooses the value  $\lambda$  which maximizes the Jaccard index for a radius of  $r = 0.02$  (*i.e.* 20 nm). This radius corresponds to the aim of resolution. The optimal values of  $\lambda$  are gathered in Figure 5.24. The number of  $n$  initial measures for each density ( $N$ ) is taken so that the total number of spikes randomly chosen on the 3D structure is equal to  $10^4$ . For the Double-Helix and Astigmatism models, one considers  $K \in \{1, \dots, 4\}$  because the performance is stabilized for  $K = 3$  and  $K = 4$  and because the computation time becomes unfavorable. For the Laplace model we go up to  $K = 6$  because the computation time is quicker (see Remark 7).

---

<sup>3</sup><http://bigwww.epfl.ch/smlm/>

Names	Values	Names	Values
$\sigma_x = \sigma_y$	0.186	NA	1.49
$N_x = N_y$	64	$n_i$	1.515
$x_b = y_b$	6.4	$n_t$	1.333
$z_b$	0.8	$\lambda_\ell$	0.66
$\sigma_0$	$\frac{0.42\lambda_\ell}{\text{NA}}$	$\alpha$	-0.79
$\beta$	0.2	$d$	$\frac{\lambda_\ell n_i}{2\text{NA}^2}$
$\omega$	1	$n_{\text{photon}}$	1000
$\sigma$	$1e-4$		

Figure 5.23: Numerical constants used in this section. Correspond to typical real-life experimental values. Obtained from [90, 97] and the SMLM challenge webpage.

		PALM+MA-TIRF	PALM+Astigmatism	PALM+Double-Helix
$K = 1$	N=5		$\lambda = 0.04$	$\lambda = 0.12$
	N=10		$\lambda = 0.007$	$\lambda = 0.06$
	N=15		$\lambda = 0.004$	$\lambda = 0.04$
$K = 2$	N=5	$\lambda = 0.03$	$\lambda = 0.012$	$\lambda = 0.05$
	N=10	$\lambda = 0.021$	$\lambda = 0.01$	$\lambda = 0.05$
	N=15	$\lambda = 0.013$	$\lambda = 0.01$	$\lambda = 0.04$
$K = 3$	N=5	$\lambda = 0.016$	$\lambda = 0.012$	$\lambda = 0.04$
	N=10	$\lambda = 0.012$	$\lambda = 0.009$	$\lambda = 0.04$
	N=15	$\lambda = 0.008$	$\lambda = 0.009$	$\lambda = 0.035$
$K = 4$	N=5	$\lambda = 0.012$	$\lambda = 0.012$	$\lambda = 0.04$
	N=10	$\lambda = 0.008$	$\lambda = 0.009$	$\lambda = 0.04$
	N=15	$\lambda = 0.008$	$\lambda = 0.009$	$\lambda = 0.03$
	N=20	$\lambda = 0.005$	$\lambda = 0.003$	$\lambda = 0.01$
$K = 5$	N=5	$\lambda = 0.01$		
	N=10	$\lambda = 0.008$		
	N=15	$\lambda = 0.008$		
$K = 6$	N=5	$\lambda = 0.009$		
	N=10	$\lambda = 0.007$		
	N=15	$\lambda = 0.007$		

Figure 5.24: Optimal values of the regularization parameter  $\lambda$  for all the experiments made.

### 5.3.1 Numerical Results in Terms of Detection Indices

In this section, one presents the performance obtained for all the experiments in terms of Jaccard index, Recall and Precision.

Figure 5.25 shows the Jaccard index, the Recall and the Precision (see Section 4.3.2 for their definitions) for the three models with respect to  $K$  (the number of angles or focal planes considered) and different densities of fluorophores ( $N \in \{5, 10, 15\}$ ).

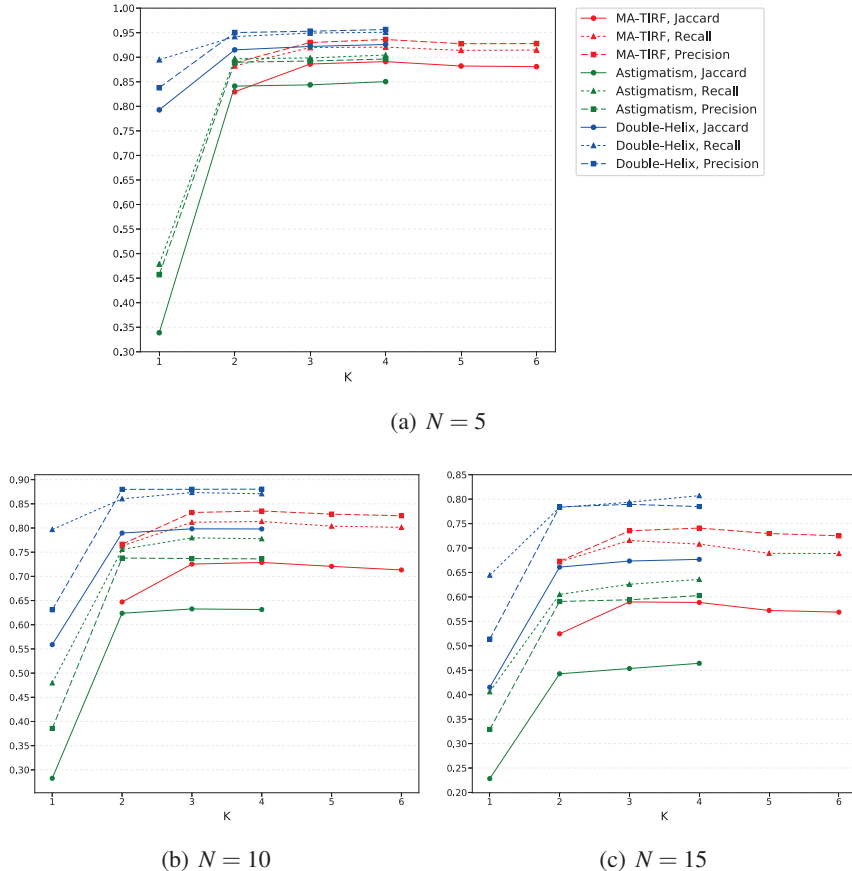


Figure 5.25: Detection indices comparison of the three models w.r.t  $K$  for a radius of detection  $r = 0.02$ .

One remarks that the various indices ( $J, R, P$ ) increase with  $K$ , except for Laplace for which there is a slight decrease when  $K = 5$  and  $K = 6$ . This is expected because a higher  $K$  means more information gathered. Moreover because the photon budget  $n_{\text{photon}}$  is distributed over each frame acquired of a given distribution of fluorophores emitting light (one frame per angle or focal plane), a higher  $K$  means also more Poisson noise contaminating the data. Hence for  $K$  large enough it balances the gain due to the increase of information. Then one sees that going from one focal plane for Astigmatism and Double-Helix to two focal plane, improves significantly the performance.

As expected, the Jaccard index, the Recall and the Precision decrease for the three models for a fixed  $K$  with an increasing density of fluorophores.

Finally, one remarks that the Double-Helix performs better than Laplace which in turn performs better than Astigmatism.

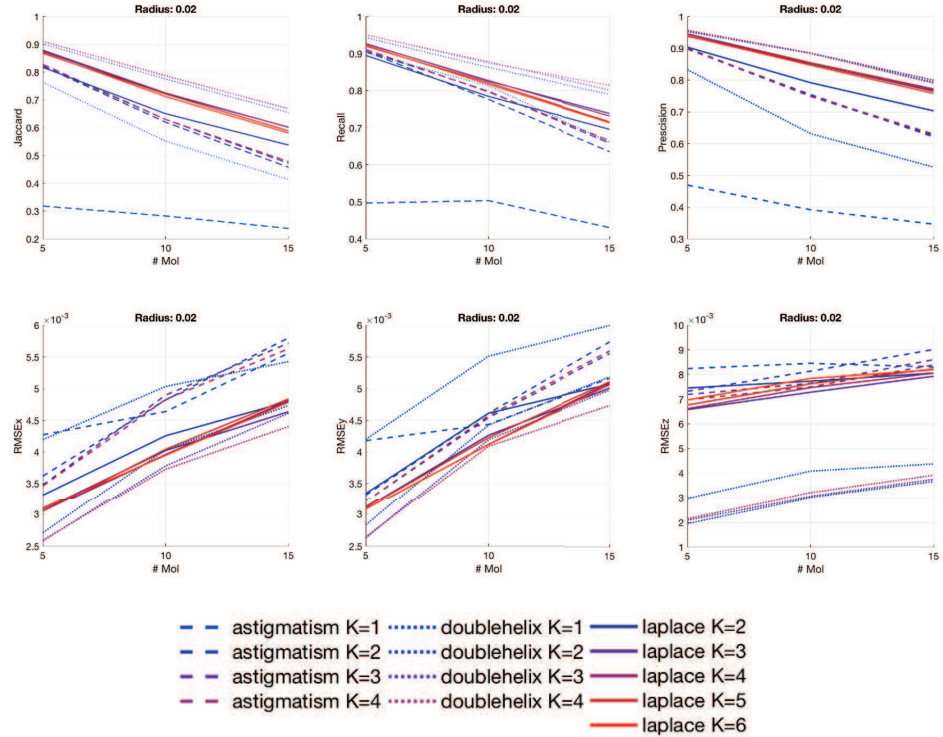


Figure 5.26: Detection indexes and RMSE comparison of the three models w.r.t  $N$  for  $r = 0.02$  (20 nm).

Figures 5.26 and 5.27 show the Jaccard index, the Recall and the Precision for the three models with respect to  $N \in \{5, 10, 15\}$  (all the values of  $K$  for each model are displayed on the same graph). They also show the RMSE, for Root Mean Square Error, which measures the mean of the quadratic errors between detected spikes of the initial measures and the associated spikes of the recovered measures used in the detection. The RMSE is given separately for each axes  $x$ ,  $y$  and  $z$ . The RMSE together with the Jaccard index gives more information than just the Jaccard index alone. Indeed suppose that two models have the same  $J$ , then a difference in the RMSE means that one of the two has a better accuracy than the other. It gives basically an idea of the resolution obtained. The Jaccard, the Recall, the Precision and the RMSE are computed for several radius of detection ( $r \in \{0.02, 0.06, 0.1\}$ ). Note that the RMSE when  $r = 0.02$  is harder to interpret because the radius  $r$  is very small only, the recovered spikes that are very close of a true fluorophore are used to compute the RMSE. On the contrary, for  $r = 0.06$  and  $r = 0.1$ , the mean error also takes into account the spikes that are farther so that it gives a better estimation of the real resolution achieved.

One sees, as already stated for Figure 5.25, that the increase of the density

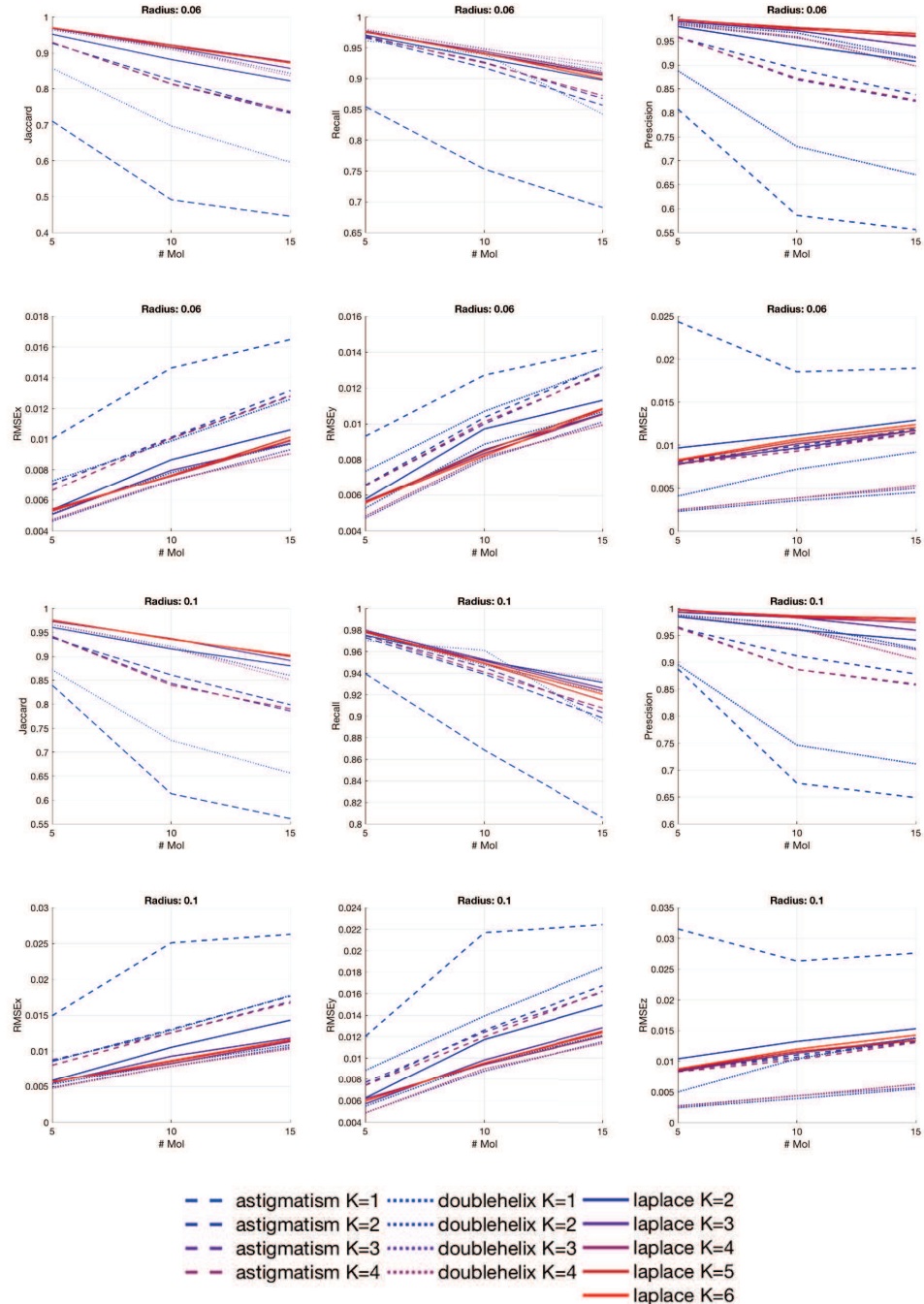


Figure 5.27: Detection indices and RMSE comparison of the three models w.r.t  $N$  for  $r = 0.06$  (60 nm) and  $r = 0.1$  (100 nm).

leads to a decrease of the indices. In the same time and as expected, the RMSE along the different axes increase. One remarks that the RMSE along the  $x$  and  $y$

axes are the same for Laplace and Double-Helix (around 5 nm when  $N = 5$  and 12 nm at the highest density  $N = 15$ ). Astigmatism has a worse RMSE along these axes than Laplace and Double-Helix. Concerning the RMSE along the  $z$  axes, the better performance (around 5 nm) are obtained by the Double-Helix (with even a lower RMSE than along the axes  $x$  and  $y$ ). Laplace and Astigmatism have similar performance, around 10 nm.

To conclude, Double-Helix performs better than the other models because it has the best resolution (equal with Laplace) in the  $(x,y)$  plane and has a significantly better resolution along the  $z$  axes than Laplace and Astigmatism. Then comes Laplace which has a better resolution than Astigmatism in the  $(x,y)$  plane but similar along the  $z$  axes.

### 5.3.2 Recovered 3D Structures

One now gives in this section the recovered structures obtained after each run of an experiment. Figure 5.28 recalls the true microtubular structure that one aims to recover (see Section 5.2.1 for more details on it and how the spikes of the initial measures are generated).

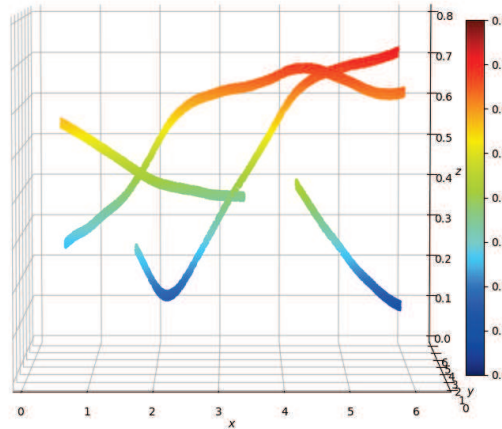


Figure 5.28: Microtubules structure used to generate the ground truths for the comparisons of the three models. The diameter of the filaments is 20 nm.

Figures 5.29, 5.30 and 5.31 present the recovered structures for respectively Laplace, Astigmatism and Double-Helix for all the values of  $K$  and densities.

Figures 5.33, 5.34 and 5.35 present the same thing but with a view of only the  $(x,y)$  plane.

Figures 5.32 and 5.36 give a comparison, for respectively the side view and the view of the  $(x,y)$  plane, of the recovered structure for the different densities, when the models achieve the best performance (*i.e.* when  $K = 4$ ).

Before commenting the results, note that the scale on the  $z$  axes is not the same as on the  $x$  and  $y$  axes.

One remarks visually that the recovery of the structure is better for every model when  $K$  is higher and the density is lower. However it is hard to see any difference for Laplace between the case  $K = 4$ ,  $K = 5$  and  $K = 6$  (it should get slightly worse according to the previous section). Moreover the visual improvement is clear when going from  $K = 1$  to  $K = 2$  for Astigmatism and Double-Helix (especially Astigmatism). One sees in Figure 5.32 that Double-Helix achieves a really nice precision along the  $z$  axes compared to Laplace and Astigmatism. For Laplace and Astigmatism the visual comparison is similar. This confirms the observations made in the previous section.

One remarks that the precision along the  $z$  axes for Laplace is better for spikes near the interface ( $z = 0$ ). This is due to the exponential decay of the kernel. One also notes that for Laplace there are spikes between two microtubules in a cylinder centered on  $(x, y) = (5.7, 2.9)$ . This is because these two microtubules cross each other in the  $(x, y)$  plane with different  $z$ . As a result when an initial measure has (at least) two spikes with roughly the same  $(x, y) = (5.7, 2.9)$  with one spike on each microtubule, the algorithm is not able to recover both spikes and instead puts one between the two. This comes from the fact that the maximum value  $p_K$  in the discretization of the Laplace transform obtained for the angle  $\alpha_K = \alpha_{\max}$  is not large enough. This phenomenon was discussed in Section 4.4.2. The downside is that one cannot increase enough  $p_K$  to deal with this issue because in the best case it is upper bounded by:

$$\frac{4\pi n_i}{\lambda_\ell} (1 - \sin(\alpha_c)^2),$$

when one takes  $\alpha_{\max} = \pi/2$  (one could also imagine take  $n_i$  slightly greater with different objectives but without changing the conclusion).

Concerning the views of the recovered structures from above (the  $(x, y)$  plane), one sees that all the models perform well, even if one can note a slight advantage for Laplace and Double-Helix versus Astigmatism (confirming the observations made in the last section). This difference is particularly visible in the area around  $(x, y) = (4.9, 4.5)$  where two microtubules cross each other at the same  $z$ . In the case of Astigmatism, this area is more noisy than for Laplace and Double-Helix.

### 5.3.3 Limitations and Final Comments

The setup and the experiments presented in this Section 5.3 have several limitations:

- the forward operators modeling the different methods of acquisition are ideal in the sense that they only approximate the real experimental point spread functions. The closest PSF from the reality is the one of the PALM+MA-TIRF model. For example the 2 Gaussians of the PALM+Double-Helix model in practice deteriorate with  $z$ .
- We did not take into account the background noise and the noise level considered here is small.

- We emphasized in the introduction of this chapter (see Section 5.1) the importance of the time resolution: the fact that the experimenters working on a sample have only a limited time to acquire data. Which means that a method able to work with a higher density of spikes (at each snapshot) is better. One proved that solving the BLASSO with our algorithm for the three models still leads (in our ideal setup) to a resolution below 20 nm when  $N = 15$  (which corresponds in practice to a high resolution, see the 3D data for the SMLM challenge). However it is better to integrate time directly to the models.

To conclude, although its setup is simplified and idealized, our study has shown the potential of the SFW algorithm for this 3D problem, that is not yet very studied in the literature (most existing numerical methods focus on the simpler 2D problem). In particular, it highlights the interest of the PALM+MA-TIRF model or PALM+Astigmatism and PALM+Double-Helix with at least two focal planes (*i.e.* two camera mounted in parallel and acquiring data from two different focal planes).

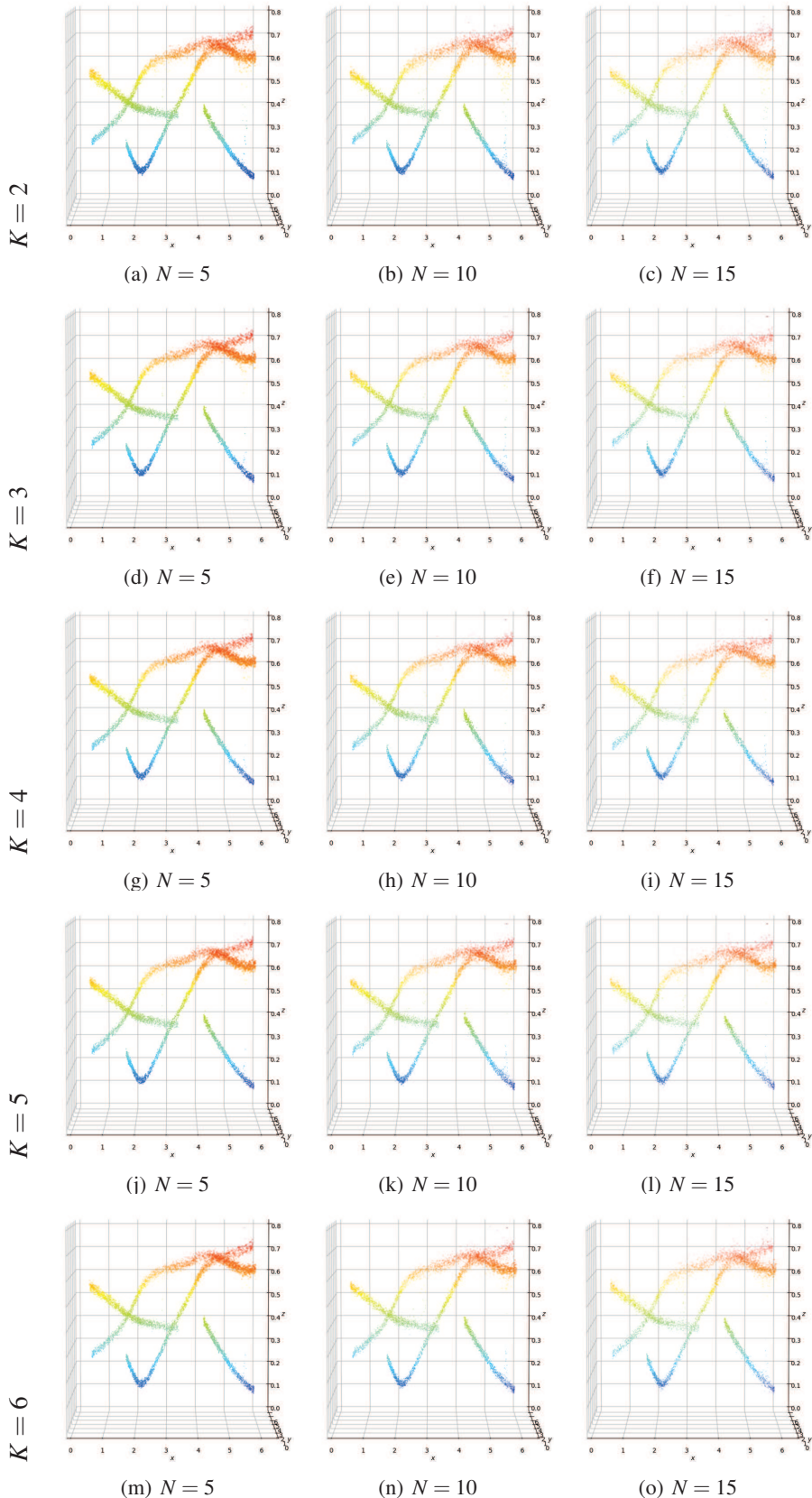


Figure 5.29: Recovered structures for the PALM+MA-TIRF model.

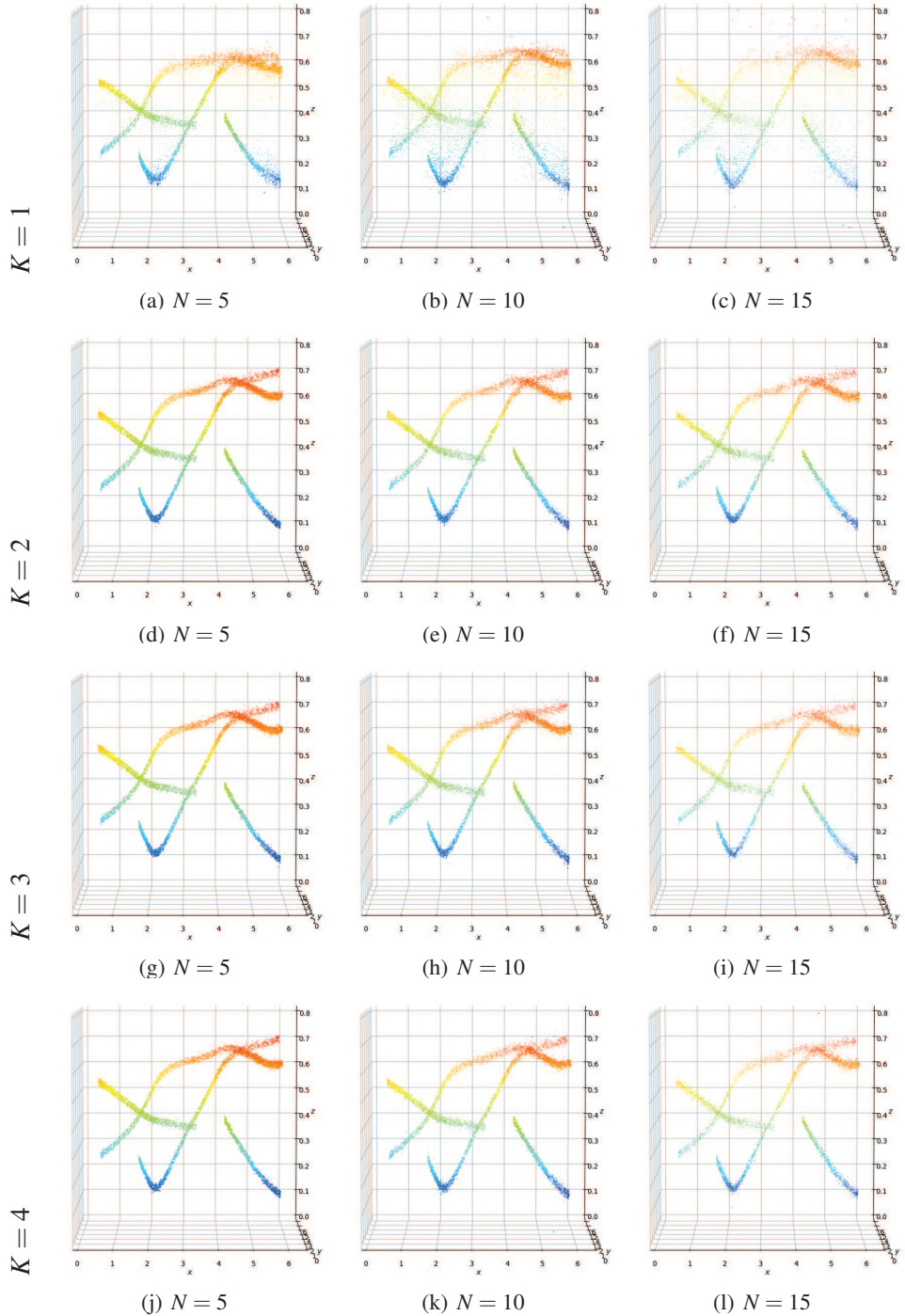


Figure 5.30: Recovered structures for the PALM+Astigmatism model.

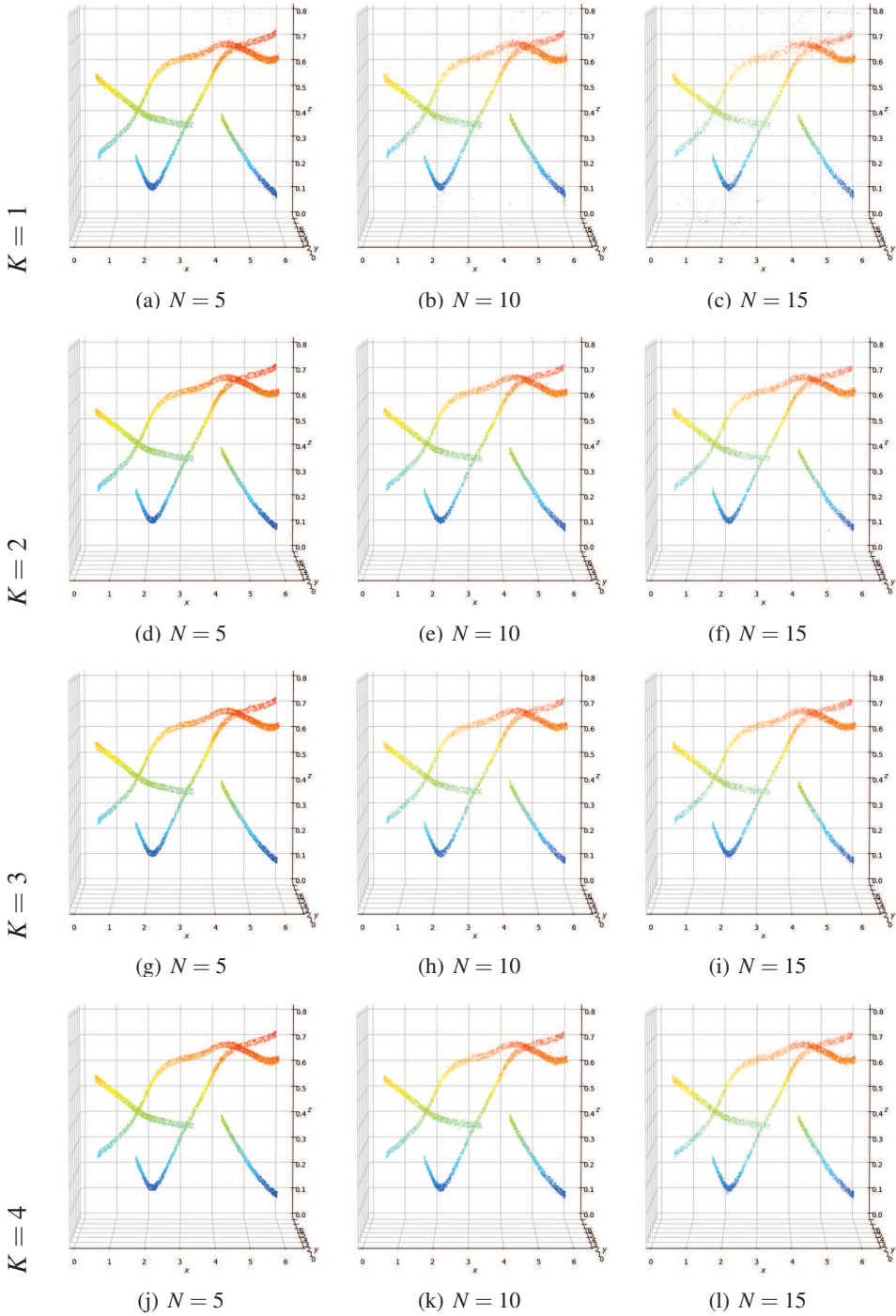


Figure 5.31: Recovered structures for the PALM+Double-Helix model.

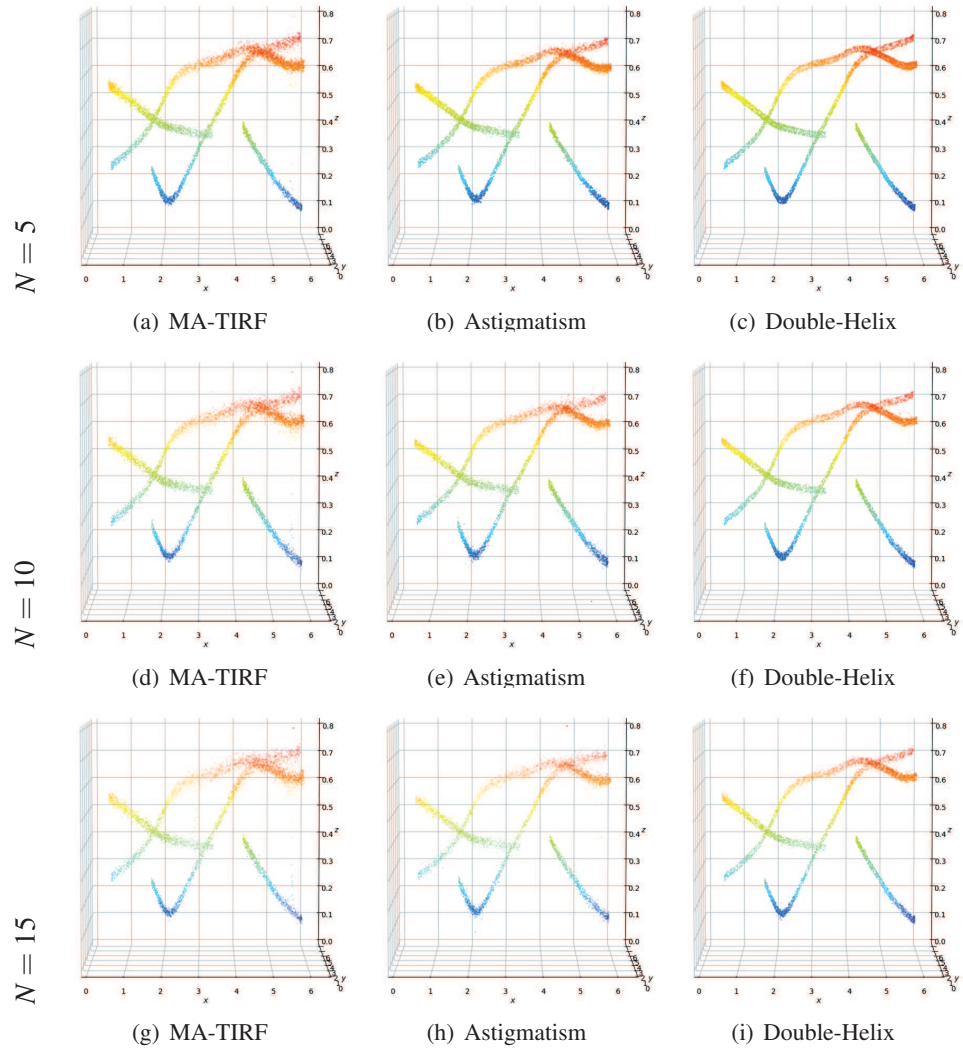


Figure 5.32: Comparison of recovered structures for the three models when  $K = 4$ .

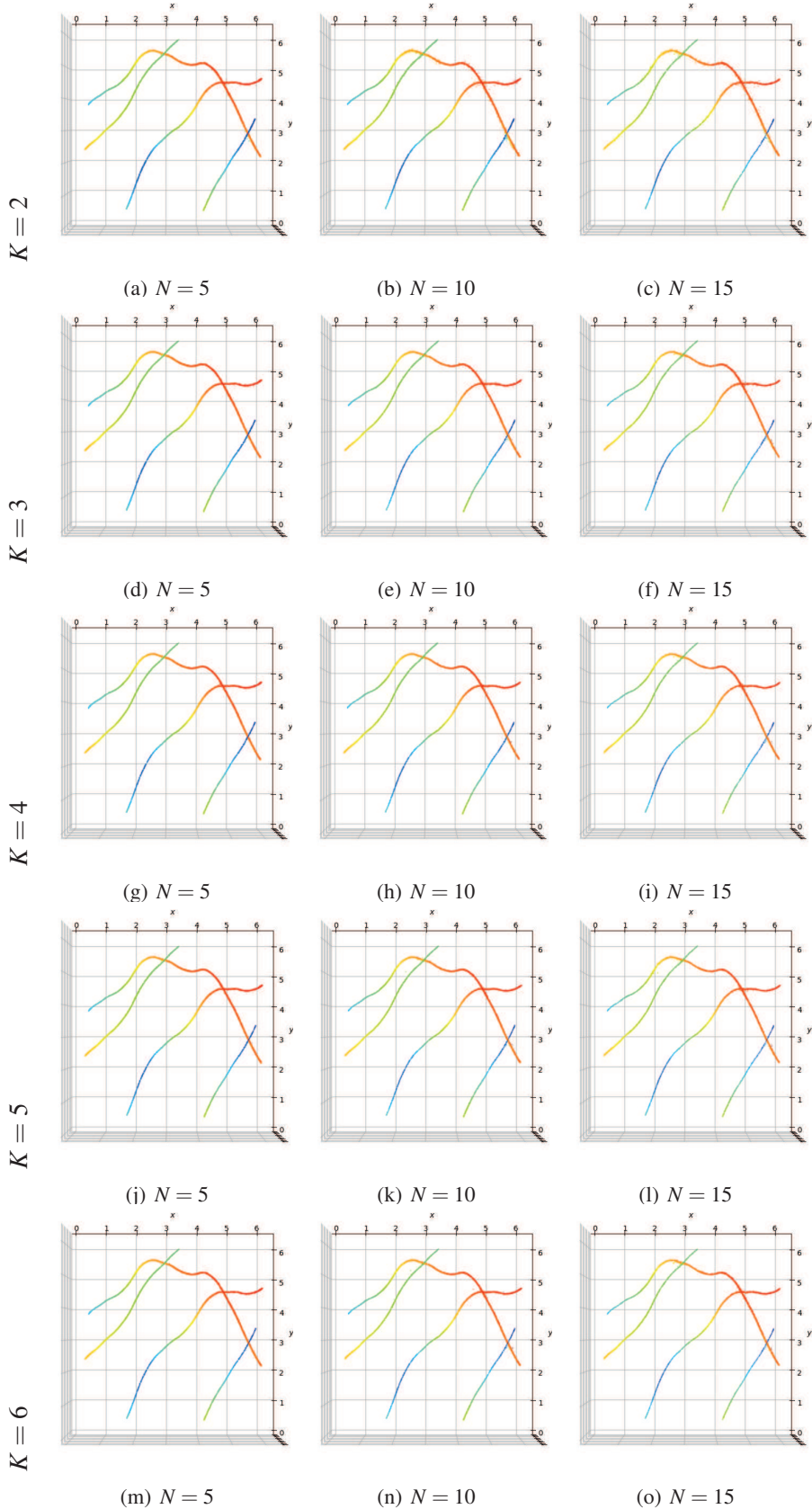


Figure 5.33: Recovered structures for the PALM+MA-TIRF model in the  $(x, y)$  plane.

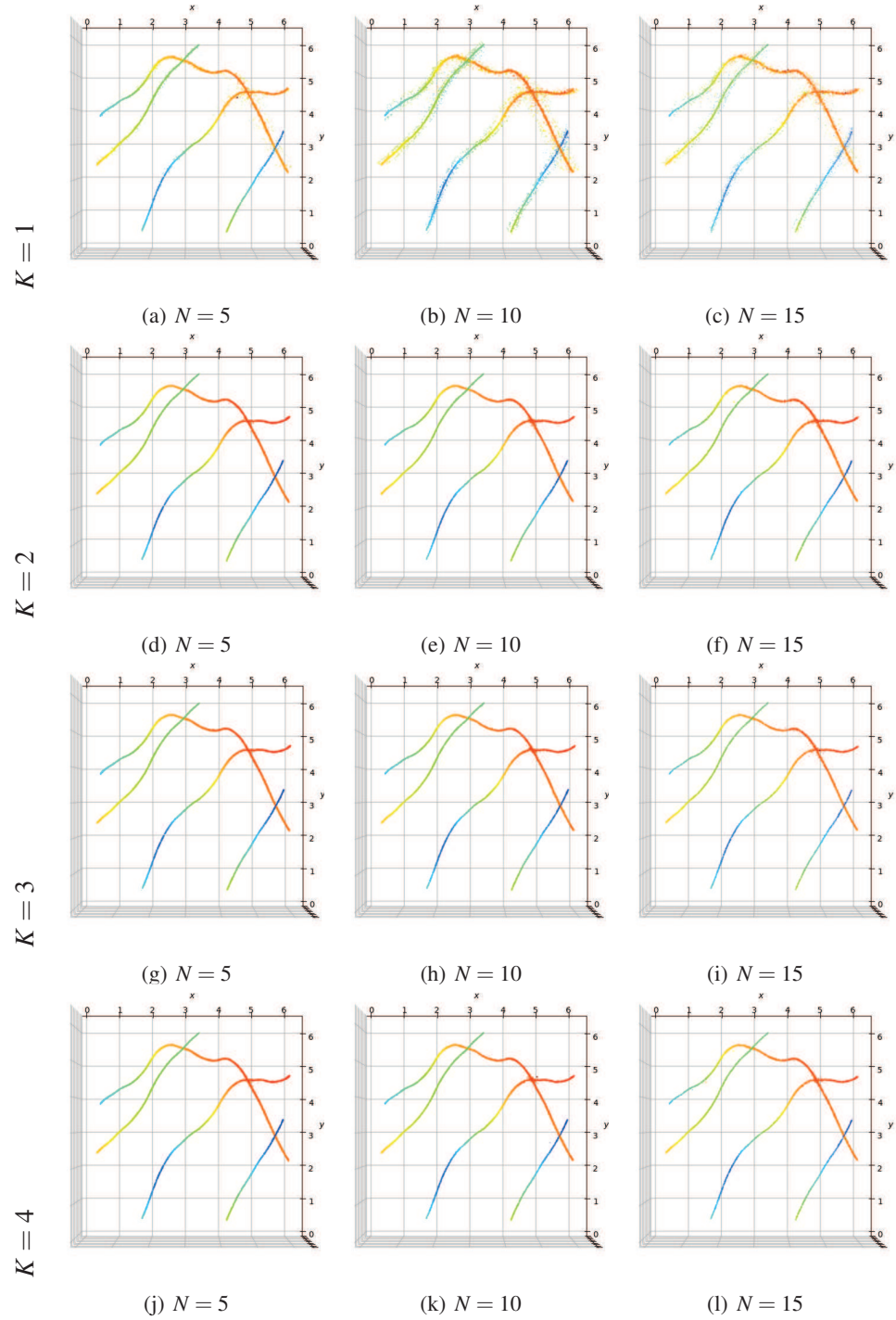


Figure 5.34: Recovered structures for the PALM+Astigmatism model in the  $(x, y)$  plane.

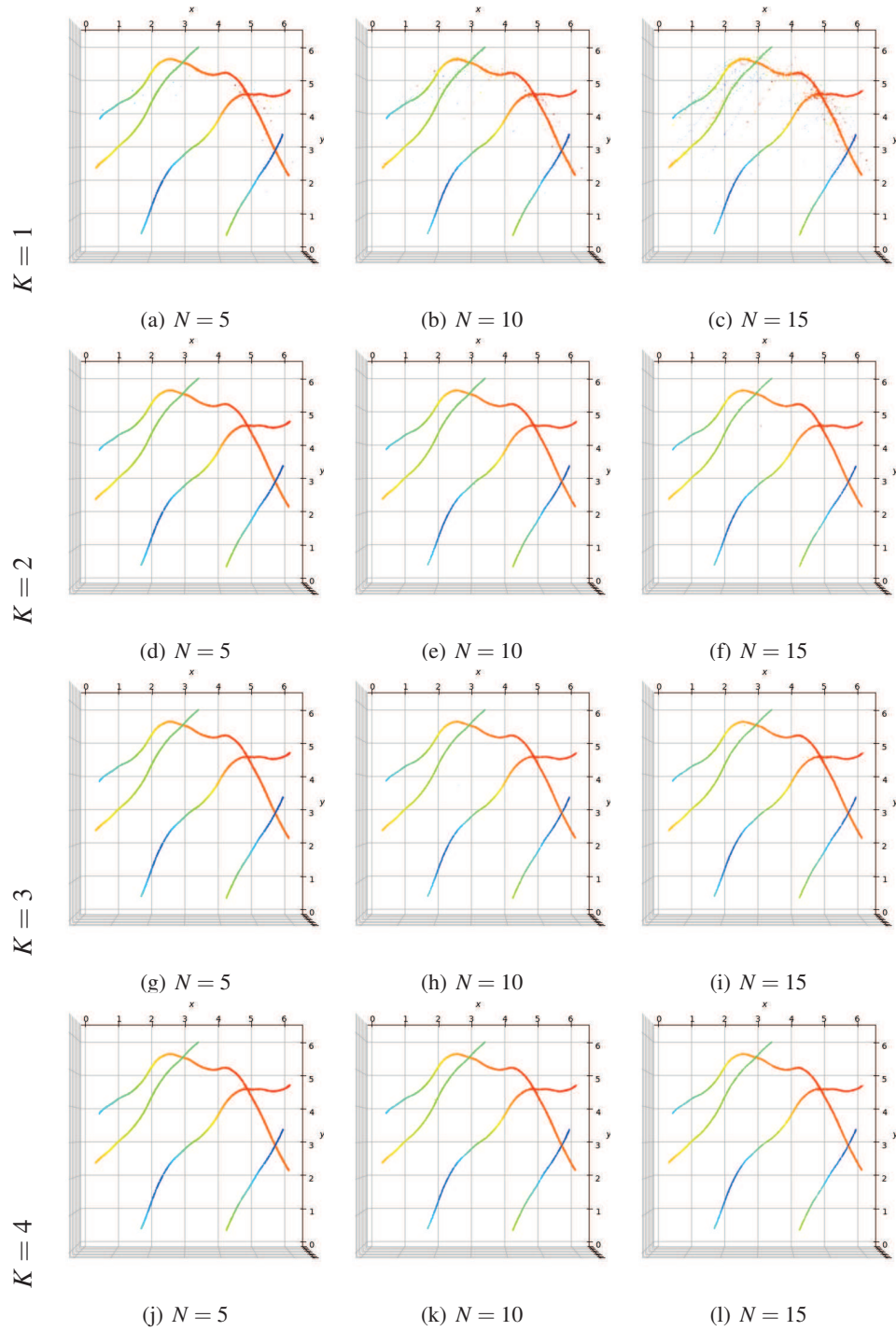


Figure 5.35: Recovered structures for the PALM+Double-Helix model in the  $(x, y)$  plane.

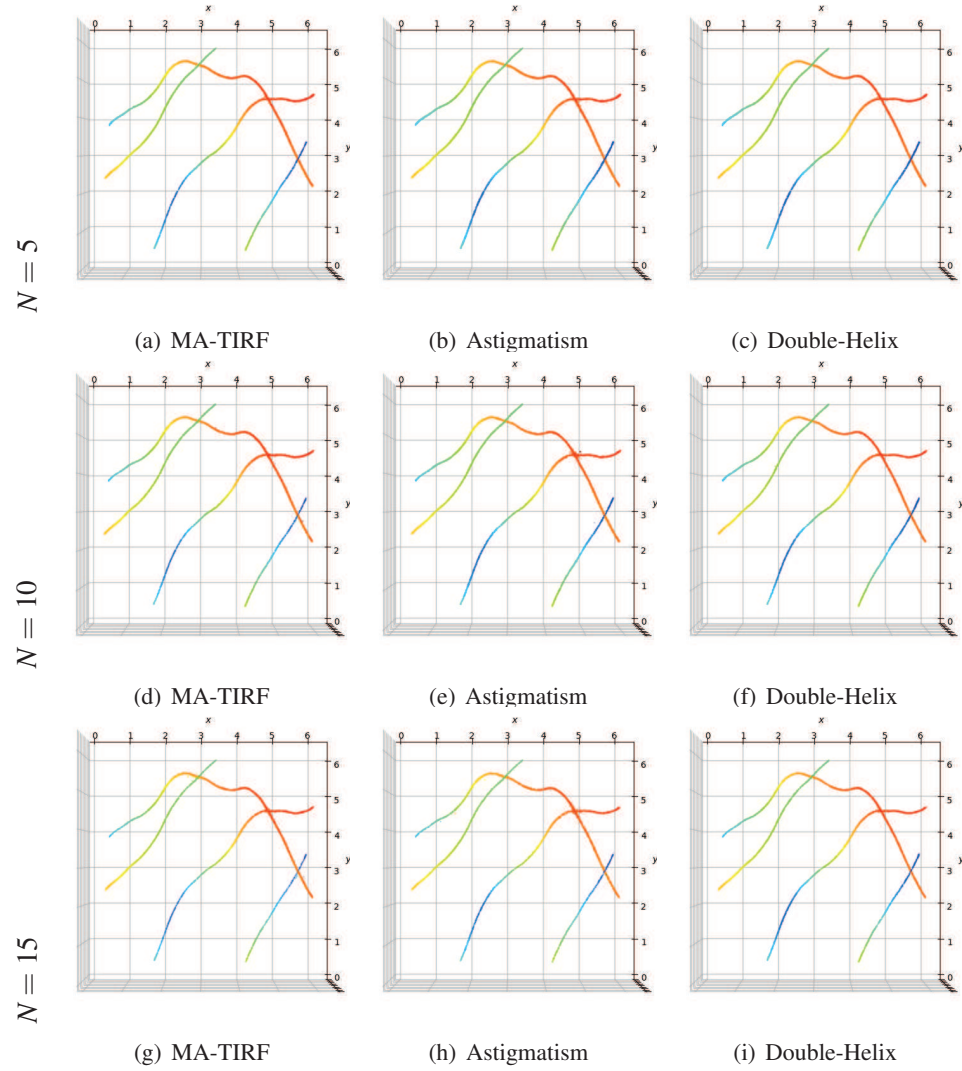


Figure 5.36: Comparison of recovered structures for the three models when  $K = 4$  in the  $(x, y)$  plane.

# Conclusion

This thesis demonstrates the importance of a study that provides in the same time theoretical results which proves insights and numerical algorithms combining guaranteed convergence rates and performance in real life applications.

Looking back on the results proved, we note that two main ingredients take part in almost every major result of this thesis:

1. the first one involves first order optimality conditions, *i.e.* typically

$$\forall i, \quad \eta(x_i) = 1 \quad \text{and} \quad \eta'(x_i) = 0.$$

These conditions are at the core of the proof of Theorem 5 (construction of a candidate solution) but also intervene in the proof of Theorem 6 (to show that the SFW algorithm stops after a finite number of iterations),

2. the second one involves an asymptotic argument using a simpler pre-certificate depending only on the initial measure and the filter ( $\eta_V$ ) or only the filter ( $\eta_W$ ) which transfer its non-degeneracy to any sufficiently close other pre-certificate. This reasoning gives the intuition for the definition of  $\eta_W$  (which is crucial in our theoretical study) and is used in the proof of Theorem 1 and Theorem 5.

Our work opens the way to both new theoretical and numerical questions. On the theoretical standpoint, a question of particular interest is the definition of  $\eta_W$  and the extension of the results developed in this thesis, in a 2D or 3D domain. Partial answers are given in [117], but the case of more than two points is still open.

On the numerical standpoint, the application to fluorescence microscopy detailed in Chapter 5 leads to many future collaborations and exchanges with experimenters and Biologists. First, there is the important question of finding a good metric to measure the recovery performance for synthetic data (Optimal Transport based ?). Moreover our experimental setup can be modified to make it even closer to real conditions (background noise, better modeling of the PSF). Another question that needs to be addressed with the help of experimenters is the possibility to tweak the parameters of the PALM+MA-TIRF model to improve its performance. Then one can imagine merging two or even the three different models studied in this thesis into one, and see if it is tractable and if it enhances the recovery performance.



# Bibliography

- [1] Ernst Abbe. Beiträge zur theorie des mikroskops und der mikroskopischen wahrnehmung. *Archiv für mikroskopische Anatomie*, 9(1):413–418, Dec 1873.
- [2] Martial Aguech and Guillaume Carlier. Barycenters in the Wasserstein space. *SIAM J. Math. Anal.*, 43(2):904–924, 2011.
- [3] Luigi Ambrosio, Nicola Gigli, and Giuseppe Savaré. *Gradient flows in metric spaces and in the space of probability measures*. Lectures in Mathematics ETH Zürich. Birkhäuser Verlag, Basel, second edition, 2008.
- [4] Daniel Axelrod. Cell-substrate contacts illuminated by total internal reflection fluorescence. *The Journal of cell biology*, 89(1):141–145, 1981.
- [5] Daniel Axelrod. Total internal reflection fluorescence microscopy. *Traffic (Copenhagen, Denmark)*, 2:764–74, 12 2001.
- [6] Daniel Axelrod. Total internal reflection fluorescence microscopy. *Methods in cell biology*, 89:169–221, 02 2008.
- [7] Jean-Marc Azaïs, Yohann de Castro, and Fabrice Gamboa. Spike detection from inaccurate samplings. *Appl. Comput. Harmon. Anal.*, 38(2):177–195, 2015.
- [8] Mark Bates, Bo Huang, Graham T Dempsey, and Xiaowei Zhuang. Multicolor super-resolution imaging with photo-switchable fluorescent probes. *Science (New York, N.Y.)*, 317:1749–53, 10 2007.
- [9] Amir Beck and Marc Teboulle. A fast iterative shrinkage-thresholding algorithm for linear inverse problems. *SIAM J. Imaging Sci.*, 2(1):183–202, 2009.
- [10] Richard Bellman and Robert S Roth. *The laplace transform*, volume 3. World Scientific, 1984.
- [11] Jean-David Benamou and Yann Brenier. A computational fluid mechanics solution to the Monge-Kantorovich mass transfer problem. *Numer. Math.*, 84(3):375–393, 2000.

- [12] Jean-David Benamou, Guillaume Carlier, Marco Cuturi, Luca Nenna, and Gabriel Peyré. Iterative Bregman projections for regularized transportation problems. *SIAM J. Sci. Comput.*, 37(2):A1111–A1138, 2015.
- [13] Tamir Bendory. Robust recovery of positive stream of pulses. *IEEE Trans. Signal Process.*, 65(8):2114–2122, 2017.
- [14] Tamir Bendory, Avinoam Bar-Zion, Dan Adam, Shai Dekel, and Arie Feuer. Stable support recovery of stream of pulses with application to ultrasound imaging. *IEEE Trans. Signal Process.*, 64(14):3750–3759, 2016.
- [15] Tamir Bendory, Shai Dekel, and Arie Feuer. Robust recovery of stream of pulses using convex optimization. *J. Math. Anal. Appl.*, 442(2):511–536, 2016.
- [16] Eric Betzig, George H. Patterson, Rachid Sougrat, O. Wolf Lindwasser, Scott Olenych, Juan S. Bonifacino, Michael W. Davidson, Jennifer Lippincott-Schwartz, and Harald F. Hess. Imaging intracellular fluorescent proteins at nanometer resolution. *Science*, 313(5793):1642–1645, 2006.
- [17] Badri Narayan Bhaskar, Gongguo Tang, and Benjamin Recht. Atomic norm denoising with applications to line spectral estimation. *IEEE Trans. Signal Process.*, 61(23):5987–5999, 2013.
- [18] Thierry Blu, Pier-Luigi Dragotti, Martin Vetterli, Pina Marziliano, and Lionel Coulot. Sparse sampling of signal innovations. *IEEE Signal Processing Magazine*, 25(2):31–40, 2008.
- [19] Thomas Blumensath and Mike E. Davies. Iterative thresholding for sparse approximations. *J. Fourier Anal. Appl.*, 14(5-6):629–654, 2008.
- [20] Thomas Blumensath and Mike E. Davies. Iterative hard thresholding for compressed sensing. *Applied and Computational Harmonic Analysis*, 27(3):265 – 274, 2009.
- [21] Jérôme Boulanger, Charles Gueudry, Daniel Münch, Bertrand Cinquin, Perrine Paul-Gilloteaux, Sabine Bardin, Christophe Guérin, Fabrice Senger, Laurent Blanchoin, and Jean Salamero. Fast high-resolution 3d total internal reflection fluorescence microscopy by incidence angle scanning and azimuthal averaging. *Proceedings of the National Academy of Sciences*, 111(48):17164–17169, 2014.
- [22] Nicholas Boyd, Geoffrey Schiebinger, and Benjamin Recht. The alternating descent conditional gradient method for sparse inverse problems. *SIAM J. Optim.*, 27(2):616–639, 2017.
- [23] Claire Boyer, Yohann De Castro, and Joseph Salmon. Adapting to unknown noise level in sparse deconvolution. *Inf. Inference*, 6(3):310–348, 2017.

- [24] Kristian Bredies and Hanna Katriina Pikkarainen. Inverse problems in spaces of measures. *ESAIM Control Optim. Calc. Var.*, 19(1):190–218, 2013.
- [25] Ronald E. Bruck, Jr. On the weak convergence of an ergodic iteration for the solution of variational inequalities for monotone operators in Hilbert space. *J. Math. Anal. Appl.*, 61(1):159–164, 1977.
- [26] Martin Burger and Stanley Osher. Convergence rates of convex variational regularization. *Inverse Problems*, 20(5):1411–1421, 2004.
- [27] Martin Burger, E. Resmerita, and L. He. Error estimation for Bregman iterations and inverse scale space methods in image restoration. *Computing*, 81(2-3):109–135, 2007.
- [28] James A Cadzow. Signal enhancement-a composite property mapping algorithm. *IEEE Transactions on Acoustics, Speech, and Signal Processing*, 36(1):49–62, 1988.
- [29] Emmanuel J. Candès and Carlos Fernandez-Granda. Super-resolution from noisy data. *J. Fourier Anal. Appl.*, 19(6):1229–1254, 2013.
- [30] Emmanuel J. Candès and Carlos Fernandez-Granda. Towards a mathematical theory of super-resolution. *Comm. Pure Appl. Math.*, 67(6):906–956, 2014.
- [31] J. A. Carrillo, M. Di Francesco, and G. Toscani. Strict contractivity of the 2-Wasserstein distance for the porous medium equation by mass-centering. *Proc. Amer. Math. Soc.*, 135(2):353–363, 2007.
- [32] Paul Catala, Vincent Duval, and Gabriel Peyré. A low-rank approach to off-the-grid sparse deconvolution. *PrePrint*, 2017.
- [33] Moses S. Charikar. Similarity estimation techniques from rounding algorithms. In *Proceedings of the Thirty-Fourth Annual ACM Symposium on Theory of Computing*, pages 380–388. ACM, New York, 2002.
- [34] Scott Shaobing Chen, David L. Donoho, and Michael A. Saunders. Atomic decomposition by basis pursuit. *SIAM J. Sci. Comput.*, 20(1):33–61, 1998.
- [35] Yuejie Chi, Louis L Scharf, Ali Pezeshki, and A Robert Calderbank. Sensitivity to basis mismatch in compressed sensing. *IEEE Transactions on Signal Processing*, 59(5):2182–2195, 2011.
- [36] Lénaïc Chizat, Gabriel Peyré, Bernhard Schmitzer, and François-Xavier Vialard. Unbalanced optimal transport: dynamic and Kantorovich formulations. *J. Funct. Anal.*, 274(11):3090–3123, 2018.

- [37] Jon F Claerbout and Francis Muir. Robust modeling with erratic data. *Geophysics*, 38(5):826–844, 1973.
- [38] Patrick L. Combettes and Valérie R. Wajs. Signal recovery by proximal forward-backward splitting. *Multiscale Model. Simul.*, 4(4):1168–1200, 2005.
- [39] Laurent Condat and Akira Hirabayashi. Cadzow denoising upgraded: a new projection method for the recovery of Dirac pulses from noisy linear measurements. *Sampl. Theory Signal Image Process.*, 14(1):17–47, 2015.
- [40] Marco Cuturi. Sinkhorn distances: Lightspeed computation of optimal transportation distances. *Advances in Neural Information Processing Systems*, 26, 06 2013.
- [41] Ingrid Daubechies, Michel Defrise, and Christine De Mol. An iterative thresholding algorithm for linear inverse problems with a sparsity constraint. *Comm. Pure Appl. Math.*, 57(11):1413–1457, 2004.
- [42] Yohann de Castro and Fabrice Gamboa. Exact reconstruction using Beurling minimal extrapolation. *J. Math. Anal. Appl.*, 395(1):336–354, 2012.
- [43] Yohann De Castro, Fabrice Gamboa, Didier Henrion, and Jean-Bernard Lasserre. Exact solutions to super resolution on semi-algebraic domains in higher dimensions. *IEEE Trans. Inform. Theory*, 63(1):621–630, 2017.
- [44] G.C.F.M.R. de Prony. *Essai expérimental et analytique sur les lois de la dilatabilité des fluides élastiques et sur celles de la force expansive de la vapeur de l'eau et de la vapeur de l'alcool à différentes températures, par R. Prony ...* 1795.
- [45] Laurent Demanet and Nam Nguyen. The recoverability limit for superresolution via sparsity. *preprint arXiv:1502.01385*, 2015.
- [46] Vladimir Fedorovich Demyanov and Aleksandr Moiseevich Rubinov. *Approximate methods in optimization problems*, volume 32. Elsevier Publishing Company, 1970.
- [47] AJ Den Dekker and A Van den Bos. Resolution: a survey. *JOSA A*, 14(3):547–557, 1997.
- [48] Samuel Deslauriers-Gauthier and Pina Marziliano. Sampling signals with a finite rate of innovation on the sphere. *IEEE Trans. Signal Process.*, 61(18):4552–4561, 2013.
- [49] David L. Donoho. Super-resolution via sparsity constraints. *SIAM J. Math. Anal.*, 23(5):1309-1331, 9 1992.

- [50] David L. Donoho and Iain M. Johnstone. Adapting to unknown smoothness via wavelet shrinkage. *J. Amer. Statist. Assoc.*, 90(432):1200–1224, 1995.
- [51] Marco F Duarte and Richard G Baraniuk. Spectral compressive sensing. *Applied and Computational Harmonic Analysis*, 35(1):111–129, 2013.
- [52] Bogdan Dumitrescu. *Positive trigonometric polynomials and signal processing applications*. Signals and Communication Technology. Springer, Cham, second edition, 2017.
- [53] Vincent Duval. A characterization of the Non-Degenerate Source Condition in Super-Resolution. December 2017. working paper or preprint.
- [54] Vincent Duval and Gabriel Peyré. Exact support recovery for sparse spikes deconvolution. *Found. Comput. Math.*, 15(5):1315–1355, 2015.
- [55] Vincent Duval and Gabriel Peyré. Sparse regularization on thin grids I: the Lasso. *Inverse Problems*, 33(5):055008, 29, 2017.
- [56] Vincent Duval and Gabriel Peyré. Sparse spikes super-resolution on thin grids II: the continuous basis pursuit. *Inverse Problems*, 33(9):095008, 42, 2017.
- [57] Bradley Efron, Trevor Hastie, Iain Johnstone, and Robert Tibshirani. Least angle regression. *Ann. Statist.*, 32(2):407–499, 2004. With discussion, and a rejoinder by the authors.
- [58] Armin Eftekhari and Michael B Wakin. Greed is super: A fast algorithm for super-resolution. *arXiv preprint arXiv:1511.03385*, 2015.
- [59] C Eggeling, Jerker Widengren, Rudolf Rigler, and Claus Seidel. Photo-bleaching of fluorescent dyes under conditions used for single-molecule detection: Evidence of two-step photolysis. *Analytical chemistry*, 70:2651–9, 07 1998.
- [60] Albert Einstein. Strahlungs-emission und absorption nach der quantentheorie. *Deutsche Physikalische Gesellschaft*, 18, 1916.
- [61] Albert Einstein. Zur quantentheorie der strahlung. *Physikalische Zeitschrift*, 18, 1917.
- [62] Laurent El Ghaoui, Vivian Viallon, and Tarek Rabbani. Safe feature elimination in sparse supervised learning. *Pac. J. Optim.*, 8(4):667–698, 2012.
- [63] Herbert Federer. *Geometric measure theory*. Die Grundlehren der mathematischen Wissenschaften, Band 153. Springer-Verlag New York Inc., New York, 1969.

- [64] C. Fernandez-Granda. Support detection in super-resolution. *Proc. Proceedings of the 10th International Conference on Sampling Theory and Applications*, pages 145–148, 2013.
- [65] Carlos Fernandez-Granda. Super-resolution of point sources via convex programming. *Inf. Inference*, 5(3):251–303, 2016.
- [66] Mário A. T. Figueiredo and Robert D. Nowak. An EM algorithm for wavelet-based image restoration. *IEEE Trans. Image Process.*, 12(8):906–916, 2003.
- [67] J. Folling, Vladimir Belov, R Kunetsky, Rebecca Medda, Andreas Schonle, A Egner, C Eggeling, M L. Bossi, and S W Hell. Photochromic rhodamines provide nanoscopy with optical sectioning. *Angewandte Chemie (International ed. in English)*, 46:6266–70, 08 2007.
- [68] Jonas Folling, Mariano Bossi, Hannes Bock, Rebecca Medda, Christian Wurm, Birka Hein, Stefan Jakobs, Christian Eggeling, and Stefan W Hell. Fluorescence nanoscopy by ground-state depletion and single-molecule return. *Nature methods*, 5:943–5, 10 2008.
- [69] Marguerite Frank and Philip Wolfe. An algorithm for quadratic programming. *Naval Res. Logist. Quart.*, 3:95–110, 1956.
- [70] Osamu Fujita. Metrics based on average distance between sets. *Japan Journal of Industrial and Applied Mathematics*, 30(1):1–19, Feb 2013.
- [71] Mats G L Gustafsson. Nonlinear structured-illumination microscopy: Wide-field fluorescence imaging with theoretically unlimited resolution. *Proceedings of the National Academy of Sciences of the United States of America*, 102:13081–6, 10 2005.
- [72] Andrew Gardner, Jinko Kanno, Christian A. Duncan, and Rastko R. Selmic. Measuring distance between unordered sets of different sizes. In *CVPR*, pages 137–143. IEEE Computer Society, 2014.
- [73] Simon Gazagnes, Emmanuel Soubies, and Laure Blanc-Féraud. High density molecule localization for super-resolution microscopy using cel0 based sparse approximation. *Biomedical Imaging (ISBI 2017), 2017 IEEE 14th International Symposium on*, pages 28–31, 2017.
- [74] John C Gower. Similarity, dissimilarity and distance, measures of. *Encyclopedia of Statistical Sciences*, 12, 2004.
- [75] Derek Greenfield, Ann Mcevoy, Hari Shroff, Gavin E Crooks, Ned S Wingreen, Eric Betzig, and Jan Liphardt. Self-organization of the *Escherichia coli* chemotaxis network imaged with super-resolution light microscopy. *PLoS biology*, 7:e1000137, 07 2009.

- [76] M. G. L. Gustafsson. Surpassing the lateral resolution limit by a factor of two using structured illumination microscopy. *Journal of Microscopy*, 198(2):82–87, 2000.
- [77] Steven Haker, Lei Zhu, Allen Tannenbaum, and Sigurd Angenent. Optimal mass transport for registration and warping. *International Journal of computer vision*, 60(3):225–240, 2004.
- [78] Leonid G. Hanin. Kantorovich-Rubinstein norm and its application in the theory of Lipschitz spaces. *Proc. Amer. Math. Soc.*, 115(2):345–352, 1992.
- [79] Mike Heilemann, Sebastian Van de Linde, Mark Sch $\tilde{A}_{\frac{1}{4}}$ ttpelz, Robert Kasper, Britta Seefeldt, Anindita Mukherjee, Philip Tinnefeld, and Markus Sauer. Subdiffraction-resolution fluorescence imaging with conventional fluorescent probes. *Angewandte Chemie (International ed. in English)*, 47:6172–6, 08 2008.
- [80] Rainer Heintzmann, Thomas M. Jovin, and Christoph Cremer. Saturated patterned excitation microscopy—a concept for optical resolution improvement. *J. Opt. Soc. Am. A*, 19(8):1599–1609, Aug 2002.
- [81] S. W. Hell and M. Kroug. Ground-state depletion fluorescence microscopy: A concept for breaking the diffraction resolution limit. *Applied Physics B*, 60(5):495–497, May 1995.
- [82] Stefan W. Hell. Far-field optical nanoscopy. *Science*, 316(5828):1153–1158, 2007.
- [83] Stefan W. Hell. Microscopy and its focal switch. *Nature methods*, 6:24–32, 02 2009.
- [84] Stefan W Hell, Marcus Dyba, and Stefan Jakobs. Concepts for nanoscale resolution in fluorescence microscopy. *Current opinion in neurobiology*, 14(5):599–609, 2004.
- [85] Stefan W. Hell and Jan Wichmann. Breaking the diffraction resolution limit by stimulated emission: stimulated-emission-depletion fluorescence microscopy. *Opt. Lett.*, 19(11):780–782, Jun 1994.
- [86] Cédric Herzet, Angélique Drémeau, and Charles Soussen. Relaxed recovery conditions for OMP/OLS by exploiting both coherence and decay. *IEEE Trans. Inform. Theory*, 62(1):459–470, 2016.
- [87] Samuel Hess, Thanu P K Girirajan, and Michael Mason. Ultra-high resolution imaging by fluorescence photoactivation localization microscopy. *Bioophysical journal*, 91:4258–72, 01 2007.
- [88] Seamus Holden and Daniel Sage. Super-resolution fight club. 10:152 EP –, 02 2016.

- [89] Yingbo Hua and Tapan K. Sarkar. Matrix pencil method for estimating parameters of exponentially damped/undamped sinusoids in noise. *IEEE Trans. Acoust. Speech Signal Process.*, 38(5):814–824, 1990.
- [90] Bo Huang, Wenqin Wang, Mark Bates, and Xiaowei Zhuang. Three-dimensional super-resolution imaging by stochastic optical reconstruction microscopy. *Science*, 2008.
- [91] Honglin Huang and Anamitra Makur. Backtracking-based matching pursuit method for sparse signal reconstruction. *IEEE Signal Processing Letters*, 18(7):391–394, 2011.
- [92] Jiaqing Huang, Mingzhai Sun, Kristyn Gumper, Yuejie Chi, and Jianjie Ma. 3d multifocus astigmatism and compressed sensing (3d macs) based superresolution reconstruction. *Biomed. Opt. Express*, 6(3):902–917, Mar 2015.
- [93] Paul Jaccard. Etude de la distribution florale dans une portion des alpes et du jura. *Bulletin de la Societe Vaudoise des Sciences Naturelles*, 37:547–579, 01 1901.
- [94] Richard Jordan, David Kinderlehrer, and Felix Otto. The variational formulation of the fokker-planck equation. *SIAM Journal on Mathematical Analysis*, 29, 04 2000.
- [95] Manuel Juette, Travis J Gould, Mark Lessard, Michael Mlodzianoski, Bhupendra S Nagpure, Brian Thomas Bennett, Samuel Hess, and Joerg Bewersdorf. Three-dimensional sub-100 nm resolution fluorescence microscopy of thick samples. *Nature methods*, 5:527–9, 07 2008.
- [96] Thomas Kailath. ESPRIT–estimation of signal parameters via rotational invariance techniques. *Optical Engineering*, 29(4):296, 1990.
- [97] Hagai Kirshner, Cédric Vonesch, and Michael Unser. Can localization microscopy benefit from approximation theory? In *Biomedical Imaging (ISBI), 2013 IEEE 10th International Symposium on*, pages 588–591. IEEE, 2013.
- [98] Thomas A. Klar, Stefan Jakobs, Marcus Dyba, Alexander Egner, and Stefan W. Hell. Fluorescence microscopy with diffraction resolution barrier broken by stimulated emission. *Proceedings of the National Academy of Sciences*, 97(15):8206–8210, 2000.
- [99] Sven Kosub. A note on the triangle inequality for the jaccard distance. *arXiv preprint arXiv:1612.02696*, 2016.
- [100] Hamid Krim and Mats Viberg. Two decades of array signal processing research: the parametric approach. *Signal Processing Magazine, IEEE*, 13(4):67–94, Jul 1996.

- [101] Serge Lang. *Algebra*. Graduate Texts in Mathematics. Springer New York, 2002.
- [102] Jean Bernard Lasserre. Global optimization with polynomials and the problem of moments. *SIAM J. Optim.*, 11(3):796–817, 2000/01.
- [103] Jean Bernard Lasserre. Moments, positive polynomials and their applications. *Imperial College Press Optimization Series*, 1:xxii+361, 2010.
- [104] Evgenii Solomonovich Levitin and Boris Teodorovich Polyak. Constrained minimization methods. *Zhurnal Vychislitel'noi Matematiki i Matematicheskoi Fiziki*, 6(5):787–823, 1966.
- [105] Shlomo Levy and Peter K Fullagar. Reconstruction of a sparse spike train from a portion of its spectrum and application to high-resolution deconvolution. *Geophysics*, 46(9):1235–1243, 1981.
- [106] Wenjing Liao and Albert Fannjiang. MUSIC for single-snapshot spectral estimation: stability and super-resolution. *Appl. Comput. Harmon. Anal.*, 40(1):33–67, 2016.
- [107] Alan H Lipkus. A proof of the triangle inequality for the tanimoto distance. *Journal of Mathematical Chemistry*, 26(1-3):263–265, 1999.
- [108] Laura MacDonald, Giulia Baldini, and Brian Storrie. Does super-resolution fluorescence microscopy obsolete previous microscopic approaches to protein co-localization? *Methods in molecular biology (Clifton, N.J.)*, 1270:255–275, 02 2015.
- [109] Stéphane Mallat and Zhifeng Zhang. Matching pursuit with time-frequency dictionaries. *Signal Processing, IEEE Transactions on*, 41:3397 – 3415, 01 1994.
- [110] Edward Marczewski and Hugo Steinhaus. On a certain distance of sets and the corresponding distance of functions. *Colloquium Mathematicae*, 6(1):319–327, 1958.
- [111] Marisa Martin-fernandez, Christopher Tynan, and Stephen Webb. A pocket guide to total internal reflection fluorescence. *Journal of microscopy*, 252, 07 2013.
- [112] Mathurin Massias, Alexandre Gramfort, and Joseph Salmon. From safe screening rules to working sets for faster lasso-type solvers. *arXiv preprint arXiv:1703.07285*, 2017.
- [113] Veniamin I. Morgenshtern and Emmanuel J. Candès. Super-resolution of positive sources: the discrete setup. *SIAM J. Imaging Sci.*, 9(1):412–444, 2016.

- [114] Gregory B. Passty. Ergodic convergence to a zero of the sum of monotone operators in Hilbert space. *J. Math. Anal. Appl.*, 72(2):383–390, 1979.
- [115] James B. Pawley. *Handbook Of Biological Confocal Microscopy*. Springer-Verlag New York Inc., 2006.
- [116] Thomas Peter, Gerlind Plonka, and Robert Schaback. Prony’s method for multivariate signals. *PAMM*, 15(1):665–666, 2015.
- [117] Clarice Poon and Gabriel Peyré. Multi-dimensional sparse super-resolution. *arXiv preprint arXiv:1709.03157*, 2017.
- [118] Brian R Rankin, Gael Moneron, Christian Wurm, Jessica C Nelson, Arne Walter, Dirk Schwarzer, Jorg Schroeder, Daniel Colón-Ramos, and Stefan W Hell. Nanoscopy in a living multicellular organism expressing gfp. *Bio-physical journal*, 100:L63–5, 06 2011.
- [119] Brian R Rankin, Robert R Kellner, and Stefan W Hell. Stimulated-emission-depletion microscopy with a multicolor stimulated-raman-scattering light source. *Optics letters*, 33:2491–3, 12 2008.
- [120] Brian R Rankin and Stefan W Hell. Sted microscopy with a mhz pulsed stimulated-raman-scattering source. *Optics express*, 17:15679–84, 09 2009.
- [121] Sri Rama Prasanna Pavani, Michael A Thompson, Julie S Biteen, Samuel Lord, Na Liu, Robert Twieg, Rafael Piestun, and William Moerner. Three-dimensional, single-molecule fluorescence imaging beyond the diffraction limit by using a double-helix point spread function. *Proceedings of the National Academy of Sciences of the United States of America*, 106:2995–9, 03 2009.
- [122] Lord Rayleigh. Xxxi. investigations in optics, with special reference to the spectroscope. *The London, Edinburgh, and Dublin Philosophical Magazine and Journal of Science*, 8(49):261–274, 1879.
- [123] Walter Rudin. *Real and Complex Analysis, 3rd Ed.* McGraw-Hill, Inc., New York, NY, USA, 1987.
- [124] Michael J Rust, Mark Bates, and Xiaowei Zhuang. Sub-diffraction-limit imaging by stochastic optical reconstruction microscopy (storm). *Nature methods*, 3(10):793–796, 2006.
- [125] Daniel Sage, Hagai Kirshner, Thomas Pengo, Nico Stuurman, Junhong Min, Suliana Manley, and Michael Unser. Quantitative evaluation of software packages for single-molecule localization microscopy. *Nature methods*, 12, 06 2015.

- [126] Marcelina Cardoso Dos Santos, Régis Déturche, Cyrille Vézy, and Rodolphe Jaffiol. Axial nanoscale localization by normalized total internal reflection fluorescence microscopy. *Opt. Lett.*, 39(4):869–872, Feb 2014.
- [127] Fadil Santosa and William W Symes. Linear inversion of band-limited reflection seismograms. *SIAM Journal on Scientific and Statistical Computing*, 7(4):1307–1330, 1986.
- [128] Geoffrey Schiebinger, Elina Robeva, and Benjamin Recht. Superresolution without separation. *Inf. Inference*, 7(1):1–30, 2018.
- [129] Joel L Schiff. *The Laplace transform: theory and applications*. Springer Science & Business Media, 2013.
- [130] Ralph Schmidt. Multiple emitter location and signal parameter estimation. *IEEE transactions on antennas and propagation*, 34(3):276–280, 1986.
- [131] Laurent Schwartz. Transformation de Laplace des distributions. *Comm. Sémin. Math. Univ. Lund [Medd. Lunds Univ. Mat. Sem.]*, 1952(Tome Supplémentaire):196–206, 1952.
- [132] Hari Shroff, Catherine Galbraith, James Galbraith, and Eric Betzig. Live-cell photoactivated localization microscopy of nanoscale adhesion dynamics. *Nature methods*, 5:417–23, 06 2008.
- [133] Dan A Simovici and Djibrab Chabane. *Mathematical tools for data mining: set theory, partial orders, combinatorics*. Advanced Information and Knowledge Processing. Springer, London, 2008.
- [134] Emmanuel Soubies. *Sur quelques problèmes de reconstruction en imagerie MA-TIRF et en optimisation parcimonieuse par relaxation continue exacte de critères pénalisés en norme- $l_0$* . PhD thesis, Université Nice Sophia-Antipolis, 2016.
- [135] Emmanuel Soubies, Laure Blanc-Féraud, Sébastien Schaub, and Gilles Aubert. A 3d model with shape prior information for biological structures reconstruction using multiple-angle total internal reflection fluorescence microscopy. *Biomedical Imaging (ISBI), 2014 IEEE 11th International Symposium on*, pages 608–611, 2014.
- [136] Emmanuel Soubies, Sébastien Schaub, Agata Radwanska, Ellen Van Obberghen-Schilling, Laure Blanc-Féraud, and Gilles Aubert. A Framework for Multi-angle Tirf Microscope Calibration. In *ISBI - International Symposium on Biomedical Imaging*, page 4, Prague, Czech Republic, April 2016. IEEE.
- [137] Charles Soussen, Rémi Gribonval, Jérôme Idier, and Cédric Herzet. Joint  $k$ -step analysis of orthogonal matching pursuit and orthogonal least squares. *IEEE Trans. Inform. Theory*, 59(5):3158–3174, 2013.

- [138] Charles Soussen, Jérôme Idier, Junbo Duan, and David Brie. Homotopy based algorithms for  $\ell_0$ -regularized least-squares. *IEEE Trans. Signal Process.*, 63(13):3301–3316, 2015.
- [139] Christian Steinhauer, Carsten Forthmann, Jan Vogelsang, and Philip Tinnefeld. Superresolution microscopy on the basis of engineered dark states. *Journal of the American Chemical Society*, 130:16840–1, 12 2008.
- [140] Gongguo Tang, Badri Narayan Bhaskar, and Benjamin Recht. Sparse recovery over continuous dictionaries-just discretize. *Signals, Systems and Computers, 2013 Asilomar Conference on*, pages 1043–1047, 2013.
- [141] Gongguo Tang, Badri Narayan Bhaskar, and Benjamin Recht. Near minimax line spectral estimation. *IEEE Trans. Inform. Theory*, 61(1):499–512, 2015.
- [142] Robert Tibshirani. Regression shrinkage and selection via the lasso. *J. Roy. Statist. Soc. Ser. B*, 58(1):267–288, 1996.
- [143] Kim-Chuan Toh and Sangwoon Yun. An accelerated proximal gradient algorithm for nuclear norm regularized linear least squares problems. *Pac. J. Optim.*, 6(3):615–640, 2010.
- [144] Joel A. Tropp and Anna C. Gilbert. Signal recovery from random measurements via orthogonal matching pursuit. *IEEE Trans. Inform. Theory*, 53(12):4655–4666, 2007.
- [145] Paul Tseng. Convergence of a block coordinate descent method for nondifferentiable minimization. *J. Optim. Theory Appl.*, 109(3):475–494, 2001.
- [146] Roger Y. Tsien. The green fluorescent protein. *Annual Review of Biochemistry*, 67(1):509–544, 1998. PMID: 9759496.
- [147] Jose Antonio Urigüen, Yonina C. Eldar, Pier Luigi Dragotti, and Zvika Ben-Haim. Sampling at the rate of innovation: theory and applications. In *Compressed sensing*, pages 148–209. Cambridge Univ. Press, Cambridge, 2012.
- [148] Cédric Villani. *Topics in optimal transportation*. American Mathematical Soc., 2003.
- [149] Cédric Villani. *Optimal transport: old and new*, volume 338. Springer Science & Business Media, 2008.
- [150] Tong Tong Wu and Kenneth Lange. Coordinate descent algorithms for lasso penalized regression. *Ann. Appl. Stat.*, 2(1):224–244, 2008.

## Résumé

Cette thèse porte sur l'utilisation du BLASSO, un problème d'optimisation convexe en dimension infinie généralisant le LASSO aux mesures, pour la super-résolution de sources ponctuelles. Nous montrons d'abord que la stabilité du support des solutions, pour N sources se regroupant, est contrôlée par un objet appelé pré-certificat aux  $2N-1$  dérivées nulles. Quand ce pré-certificat est non dégénéré, dans un régime de petit bruit dont la taille est contrôlée par la distance minimale séparant les sources, le BLASSO reconstruit exactement le support de la mesure initiale. Nous proposons ensuite l'algorithme Sliding Frank-Wolfe, une variante de l'algorithme de Frank-Wolfe avec déplacement continu des amplitudes et des positions, qui résout le BLASSO. Sous de faibles hypothèses, cet algorithme converge en un nombre fini d'itérations. Nous utilisons cet algorithme pour un problème 3D de microscopie par fluorescence en comparant trois modèles construits à partir des techniques PALM/STORM.

## Abstract

This thesis studies the noisy sparse spikes super-resolution problem for positive measures using the BLASSO, an infinite dimensional convex optimization problem generalizing the LASSO to measures. First, we show that the support stability of the BLASSO for  $N$  clustered spikes is governed by an object called the  $(2N-1)$ -vanishing derivatives pre-certificate. When it is non-degenerate, solving the BLASSO leads to exact support recovery of the initial measure, in a low noise regime whose size is controlled by the minimal separation distance of the spikes. In a second part, we propose the Sliding Frank-Wolfe algorithm, based on the Frank-Wolfe algorithm with an added step moving continuously the amplitudes and positions of the spikes, that solves the BLASSO. We show that, under mild assumptions, it converges in a finite number of iterations. We apply this algorithm to the 3D fluorescent microscopy problem by comparing three models based on the PALM/STORM technics.

## Mots Clés

Super-résolution, parcimonie, BLASSO, LASSO, variation totale, mesures positives, reconstruction exacte du support, algorithme de Frank-Wolfe, microscopie par fluorescence, PALM/STORM, MA-TIRF, double-hélice, astigmatisme

## Keywords

Super-resolution, sparsity, BLASSO, LASSO, total variation, positive measures, exact support recovery, Frank-Wolfe algorithm, fluorescence microscopy, PALM/STORM, MA-TIRF, Double-Helix, Astigmatism